Thermal and Visible Studies of Mars Using the Termoskan Data Set

Thesis by

Bruce Harold Betts

In Partial Fulfillment of the Requirements

for the Degree of

Doctor of Philosophy

California Institute of Technology

Pasadena, California

1994

(Defended September 1993)

To Dad and Mom

and Kathy

Oh, I have slipped the surly bonds of earth
And danced the skies on laughter-silvered wings...
-John Gillespie Magee, Jr.

ACKNOWLEDGMENTS

Many people have helped me during the creation of this thesis, and here I wish to formally thank them. I am grateful to my thesis advisor, Prof. Bruce Murray, who assisted me the most, providing scientific insights and many helpful reviews of the text. I thank him for his advice, vision, and encouragement over the years, and for starting our discussions with what I did right. I also appreciate that he always had an interest in my life outside of science. Lastly, I thank him for the opportunity to try "road kill chicken" and for several other opportunities that went beyond those normally given to graduate students.

The other major research that I carried out while at Caltech was with Prof. Dewey Muhleman. I thank him for the diverse research experiences he introduced me to, for the knowledge and wisdom he imparted, and for his genuine, albeit sometimes hidden, concern for students and devotion to teaching. Thanks to Prof. Arden Albee for his insights over the years and for all that taking and T.A.'ing his Geology/Remote Sensing field trips taught me. For their time and insights, thanks to my thesis committee: Prof. Peter Goldreich, Prof. Andy Ingersoll, UCLA Prof. Dave Paige, Prof. Dewey Muhleman, and Prof. Bruce Murray. Thanks to all of the Planetary Science faculty for their teaching and insights over the years. Thanks to Prof. Bob Sharp and Prof. Kerry Sieh for adding significantly to my knowledge of and interest in Geology.

Thanks to Phil Christensen, Hugh Kieffer, Bruce Jakosky, Dave Paige, Terry Martin, and Frank Palluconi who have all, through many separate discussions, taken the time to teach me about thermal infrared analysis of Mars. Thanks to Tom Duxbury for help in navigating the Soviet space program and for friendly help with many tasks over the years. Thanks to the following for their insightful reviews, both official and unofficial, of

manuscripts that not only became papers, but also part of this thesis: Ken Tanaka, Jeff Plescia, Peter Mouginis-Mark, Bill Anderson, Phil Christensen, Vic Baker, and Doug Nash. I thank Arnold Selivanov, Margarita Naraeva, Vladimir Kharlamov, Yuri Gektin, and all the other members of the ISDE Termoskan team for their help with the instrument and the data. I thank Ruslan Kuzmin for his hospitality and our Termoskan discussions.

I am grateful to the following for significantly helping and educating me on Caltech research that did not directly become part of this thesis: Don Rudy (extensive help right before my orals with his thermal models of the Galilean satellites); Glenn Berge (OVRO and radio astronomy); Gary Neugebauer and Keith Matthews (IR observations using the 200" and cowboy billiards); Jim Westphal (the ins and out of Palomar); Ted Sweetser and Steve Schlaifer, (KPLOT software and orbital sequence planning); Terry Martin and Margaret Cribbs (PDS data standards and formats); and Boris Ivanov, Boris Zhukov, and Leonid Ksanfomaliti (for wonderful hospitality in Moscow and for help with impact processes, VSK, and KRFM, respectively).

I am grateful to my fellow graduate students over the years for their help and friendship. Thanks to Bill Anderson, who along with Mark Hofstadter, sparked the fusing of an explosive 154 South Mudd office triumvirate whose legacy has been marked in vegetation, fumes, and disks that will continue to diffuse for years to come. My Caltech experience was significantly enhanced by our antics, and for that I am profoundly grateful. Thanks to Michelle Santee for being a great friend to commiserate with about school and work, as well as for her help with Russian. Thanks to Tom Svitek for his friendship and all of his technical and scientific help over the years. Special thanks for their help and friendship also go to: Alan Yamamura, Don Banfield, Laurie Leshin Watson, Joel Schwartz, David Herrick, Alden Consolver, Hari Nair, Jim Lyons, and Rich Dissly. Oh yeah, not "'nuff said" about Mark. Late the night before my orals, the morning I proposed to Kathy, the night he toasted Kathy and me: for these and all the other times he was there for me, and for all the fish laughter, thanks.

Thanks to: Mike Black for his friendship and cheerful attitude and for his superb computer support; Coach Clint Dodd, for great coaching, stories, SCUBA, and friendship; the Planetary Science secretarial staff for all their assistance; Doug Nash, for his support and understanding as I was finishing and defending this thesis; Mark Weilert and Todd Olson for Team Physics at Stanford, and for their continued friendship; Mike Melavic, just 'cuz; Joe and Mike at Primo Deli for good brain food; the gang; Jodi Lewis, for assisting with final thesis preparations; and all the great teachers (far too numerous to mention) who paved my way to this thesis through Caleb Greenwood, Sutter, Jesuit, and Stanford.

Thanks to Barbara, Chris, Robyn, Tim, and Bob Reagan, and Jeannette Swinney for their love and for making me feel at home in Pasadena. I thank my grandmother, Alma Betts Pirlet, my siblings, and the rest of my family for their love and support, and I fondly remember my grandparents, Harold and Helen Lang. It is with gratitude and love that I remember Trudea Lovelace, whose goodness and support when I was a child continue to influence me today.

Thanks to my parents, Bert and Barbara Betts, whose never-ending encouragement and love have always inspired me in my education and in all other parts of my life. This never could have happened without them. Finally, I am thankful that coming to Caltech provided me not only with a great education, fabulous experiences, and most excellent friends, but also with an opportunity to re-meet the woman who became my best friend and wife, Kathleen Reagan Betts. I thank her for all the support she has provided me during my graduate career and during the creation of this thesis. Most especially, I thank her for the love, friendship, and happiness she gives me everyday of our life. Woof!

I now return you to my thesis. There will be no further interruptions.

ABSTRACT

In February and March, 1989, the Termoskan instrument on board the Phobos '88 spacecraft of the USSR acquired the highest spatial resolution thermal data ever obtained for Mars, ranging in resolution from 300 m to 3 km per pixel. It simultaneously obtained broad band visible channel data. The panoramas cover a large portion of the equatorial region from 30°S to 6°N. New and unique analyses facilitated by Termoskan are presented here. In addition, this thesis describes the instrument, data, and validation. Termoskan thermal data shows good temperature agreement with Viking IRTM. However, conversion of Termoskan visible data to bolometric albedo is problematic.

Utilizing the Termoskan data, I recognized a new feature on Mars: ejecta blanket distinct in the thermal infrared (EDITH). Virtually all of the more than 100 such features discovered in the Termoskan data are located on the plains near Valles Marineris. I compiled a data base of 110 EDITH and non-EDITH craters ranging in diameter from 4.2 km to 90.6 km. EDITHs have a startlingly clear dependence upon terrains of Hesperian age, and show almost no other correlations within the data base. The Hesperian terrain dependence cannot be explained by either atmospheric or impactor variations. Wind patterns or locally available aeolian material cannot provide a single overall explanation for the observed variations. I postulate that most of the observed EDITHs are due to excavation of thermally distinctive Noachian age material from beneath a relatively thin layer of younger, more consolidated Hesperian volcanic material. The plausibility of this theory is supported by much geological evidence for relatively thin near-surface Hesperian deposits overlying massive Noachian megabreccias on the EDITH-rich plains units. I suggest that absence of thermally distinct ejecta blankets on Noachian and Amazonian terrains is due to absences of distinctive near-surface layering. Thermally distinct ejecta

blankets are excellent locations for future landers and remote sensing because of relatively dust free surface exposures of material excavated from depth.

Also included in the thermal images are observations of several major channel and valley systems including significant portions of Shalbatana, Ravi, Al-Qahira, and Ma'adim Valles, the channel south of Hydraotes Chaos, channel material in Eos Chasma, and small portions Simud, Tiu, and Ares Valles and channel material in Gangis Chasma. Simultaneous broad band visible data exists for all but Ma'adim Vallis. I find that most of the channels and valleys have higher inertias than their surroundings, consistent with previous thermal studies of martian channels. I show for the first time that thermal inertia boundaries closely match all flat channel floor boundaries. Using Viking albedos, Termoskan temperatures, and thermal modelling, I derive lower bounds on typical channel thermal inertias ranging from 8.4 to 12.5 (10^{-3} cal cm^{-2} $s^{-1/2}$ K^{-1}). Lower bounds on inertia differences with the surrounding heavily cratered plains range from 1.1 to 3.5. Atmospheric and geometric effects are not sufficient to cause the inertia enhancements. I agree with previous researchers that localized, dark, high inertia areas within channels are likely aeolian in nature. However, thermal homogeneity and strong correlation of thermal boundaries with the channel floor boundaries lead me to favor non-aeolian overall explanations. Small scale aeolian deposition or aeolian deflation may, however, play some role in the inertia enhancement. Channel floor inertia enhancements are strongly associated with channels showing fretted morphologies such as wide, flat floors and steep scalloped walls. Therefore, I favor fretting processes over catastrophic flooding for explaining the inertia enhancements. Fretting may have emplaced more blocks on channel floors or caused increased bonding of fines due to increased availability of water. Alternatively, post-channel formation water that may have been preferentially present due to the low, flat fretted floors may have enhanced bonding of original fines or dust fallout. The coupling of both EDITHs and channel inertias to morphology is unlike most sharp Martian inertia variations which are decoupled from observed surface morphology.

Termoskan observed morning limb brightening in the thermal channel, but not in the visible channel. The thermal morning limb brightening is likely due to a water ice or dust haze that is warmer than the surface at the time of the observations. A water ice haze with a scale height of 5 km could match the observations. Visible scattering is observed to be significant on morning and evening limbs out to 60 or 70 km. Localized high altitude stratospheric clouds are observed in the visible channel.

The Termoskan data show that the highland-lowland boundary in the Aeolis Quadrangle appears strongly correlated with a high-low thermal inertia boundary. The sharpness of that boundary varies from less than 4 km to more than 50 km. In all cases, inertias continue to decrease gradually for many tens of km into the lowlands. Several other large scale thermal boundaries are also observed in the data.

Termoskan observed fine thermal structure on the flanks of Arsia Mons and elsewhere, which represent examples of interesting and significant thermal variations seen at the limit of Termoskan's spatial resolution. Sharp variations and boundaries imply there cannot be global scale dust blanketing deeper than about one centimeter, if that.

Termoskan obtained the first ever thermal images of Phobos' shadow on the surface of Mars, along with simultaneous visible images. The best observed shadow occurrence was on the flanks of Arsia Mons. For this occurrence, I combined the observed decrease in visible illumination of the surface with the observed decrease in brightness temperature to calculate thermal inertias of the Martian surface. Most of the derived inertias fall within the range 0.9 to 1.4, corresponding to 5 to 10 micron dust particles for a homogeneous surface. Dust at the surface is consistent with previous theories of Tharsis as a current area of dust deposition. Shadow derived inertias are sensitive to mm depths, whereas diurnally derived inertias are sensitive to cm depths. The shadow derived inertias are very similar to *Haberle and Jakosky* [1991] atmospherically corrected *Palluconi and Kieffer* [1981] Viking IRTM diurnally derived inertias. Thus, if near surface layering exists at all in this region, it is not very significant.

TABLE OF CONTENTS

LIST OF FIGURES

LIST OF TABLES

Chapter 1

We shall not cease from exploration
And the end of all our exploring
Will be to arrive where we started
And know the place for the first time.
-T.S. Eliot

INTRODUCTION

Mars: the new frontier? Not yet, but maybe someday. Mars has intrigued man for millennia. Its seasonally advancing and retreating polar caps and the changing patterns on its surface have stirred the imaginations of observers since telescopes were first pointed in its direction. The Red Planet is the most earthlike of any of the planets, although we now know that it has a harsh, dry, frigid, low pressure environment. Nevertheless, as man explores beyond his home planet, Mars holds the best known chance of independent habitation. In addition, Mars is scientifically fascinating. But I probably do not need to tell you that. Since you are reading this, you probably already have an interest in Mars.

Thus, let me direct your attention to the one thread besides Mars that winds its way through this entire thesis: the Termoskan data set. Many theses focus on one topic. In contrast, this thesis focuses on several topics, but one spacecraft data set. In February and March, 1989, the Termoskan instrument on board the Soviet Phobos '88 spacecraft acquired the highest spatial resolution thermal data ever obtained for Mars, ranging in resolution from 300 meters to 3 km/pixel and covering a large portion of the equatorial region. It simultaneously obtained broad band visible channel data.

Two categories of material are presented in this thesis. The first is presented in Chapter 2 and the Appendices and includes descriptions of the instrument, data, data files and data validation. These are included to increase understanding of the rest of the thesis. In addition, these descriptions are intended to serve as a unique archive, particularly for non-Soviet/Russian scientists, that can be used to understand the Termoskan instrument, data, and accuracy. The second category of material is presented throughout the rest of

the thesis. It consists of scientific analyses designed to exploit the new and unique advantages of the Termoskan data.

1.1 Personal Historical Context and Background

My original intended thesis and first involvement with the Soviet Phobos '88 space mission involved the mission's TV camera, called VSK-FREGAT. I developed a series of orbital camera sequences that could be used to study diurnally varying frosts and fogs on Mars. These sequences were proposed to the Soviet camera team and were accepted. I made one trip to Moscow to work out the details. Originally the observations were scheduled to be carried out by the Phobos 2 orbiter while Phobos 1 moved in to encounter the moon Phobos and drop landers onto its surface. However, when Phobos 1 failed en route to Mars, Phobos 2 was then scheduled to take over for Phobos 1 and quickly move towards the Phobos encounter. As a result, I had to design a new set of sequences which were to be taken after the encounter with Phobos. However, contact with Phobos 2 was lost before this encounter, so my observations were never acquired.

So, it was back to Moscow. My thesis advisor, Bruce Murray, and I then made contact with the Termoskan instrument design team from the Institute of Space Devices Engineering (ISDE). Fortunately, Termoskan did obtain Mars data before the failure of Phobos 2. (Termoskan was not flown on Phobos 1, so if the spacecraft had failed in reverse order, even the Termoskan Mars data would not exist!) We developed arrangements with the ISDE people to work with their data. At this time, 1989, this was still the Soviet Union, and this was the first interaction the ISDE group had with western scientists. After months of diplomatic growing pains, we finally obtained the entire data set. After some work with the data, a third trip to Moscow, and four extended meetings with ISDE personnel in the U.S., I had grown to understand Termoskan's power as well as the idiosyncrasies of the instrument and the data. This process was worthwhile, but complicated by diplomacy, distance, and language. Thus, my experience with Termoskan

and the Phobos '88 mission in general has involved far more than just science. It also has been a fascinating, rewarding, and sometimes frustrating odyssey through one aspect of the workings of the former Soviet and current Russian space program.

Note my spelling of Termoskan is historical, following *Murray et al.* [1991]. The instrument name is a Russian abbreviation for thermal scan. Alternate English spellings that have occurred occasionally elsewhere include Termoscan and Thermoscan.

1.2 Termoskan Analyses / Thesis Organization

The first steps with the Termoskan data were to understand the instrument, the observations, and the data. The next step was to validate the data, which in this case was done by comparing with the Viking infrared thermal mapper (IRTM) data. Validation showed the Termoskan temperatures to be in good agreement with IRTM. Lastly, the data were put in a more usable format, aligning thermal and visible channel data and dealing with several problems in the data such as dropped lines. All of these activities are described in Chapter 2. Also, Appendices 1, 2, 3 describe more fully my edited data files as well as the original data files.

Beyond the actual understanding and validation of the data, the next question was what are the most powerful scientific uses for the Termoskan data? The one clear advantage of the Termoskan data over previous data sets is its superior spatial resolution in the thermal channel (better by factors of 10 to 100 for most of the IRTM data). Thus, the major focus of the studies presented in this thesis is upon thermal studies of features that could not be resolved easily with previous thermal data, namely Viking IRTM. Additionally, Termoskan obtained the first ever thermal observations of the Phobos shadow, which is also analyzed in this thesis. The last advantage of Termoskan data is that the data fill a gap in time between Viking and future missions to Mars. Now, the data are perhaps even more valuable for all of these reasons because of the tragic loss of the Mars Observer spacecraft.

Thermally distinct ejecta blankets, analyzed in Chapter 3 and in *Betts and Murray* [1993a], were never before recognized due to the lesser spatial resolution of IRTM. Somewhat surprisingly, I find that they appear strongly dependent upon terrains of Hesperian age (the middle of the three major Martian geologic time periods), and are not well correlated with any other parameter. I postulate that the thermally distinct ejecta blankets are the result of distinctive Noachian aged (the oldest Martian time period) fragmented material being ejected onto younger, more consolidated Hesperian aged volcanics.

Channels and valleys, analyzed in Chapter 4 and in *Betts and Murray* [1993b], were first recognized as often having higher thermal inertias than their surroundings with IRTM data. However, many channels could not be resolved with IRTM data, and none could be resolved and studied with complete spatial coverage. Termoskan shows for the first time that the thermal inertia boundaries very closely match the channel floor boundaries. In addition, I recognized that enhanced inertia channel floors are associated with channels that show fretted morphologies such as wide, flat floors and steep, scalloped walls. The fretted floor inertia enhancements may result from original emplacement of blocks or enhanced bonding of fines due to original or secondary increased availability of water.

Most of the features discussed in Chapter 5, miscellaneous topical studies, also could not be resolved by Viking IRTM. These include fine thermal structure near Arsia Mons and the thermal sharpness of the highland-lowland boundary. In addition to surface features, Termoskan's high spatial resolution allowed the study of the atmospheric limb in both the thermal and visible, which is also discussed in Chapter 5. Termoskan observed morning thermal limb brightening that was likely the result of an ice or dust haze that was at higher temperatures than the surface. Also, visible scattering was observed out to 60 or 70 km above the horizon and localized stratospheric cloud features were observed.

Termoskan fortuitously obtained thermal as well as visible observations of the shadow of Phobos on Mars. This presented the first opportunity ever to study the cooling of the surface of Mars resulting from the passage of the shadow in order to determine thermal inertias of the upper mm of the surface. Shadow studies are discussed in Chapter 6. I found very low thermal inertias for the Arsia Mons occurrence studied, indicative of dust. In addition, the shadow derived inertias are very similar to atmospherically corrected IRTM derived inertias. The IRTM inertias were sensitive to centimeter depths versus the shadow derived millimeter or less depths. Thus, if layering of the upper surface exists at all in this region, it is very minimal.

Chapter 7 provides a summary of major conclusions, proposed future Termoskan research, and proposed studies for future missions based upon insights gained from the Termoskan studies presented in this thesis.

1.3 Publications

Virtually all of the work in this thesis is published, in press, or in preparation for publication. References to these works are described at the beginning of each chapter and are summarized here. Chapter 3 is taken from *Betts and Murray* [1993a], which has been published in the *Journal of Geophysical Research - Planets*. Chapter 4 is essentially *Betts and Murray* [1993b], which has been accepted and is in press, also in *JGR - Planets*. Chapters 2, 5, and 6 expand upon material presented in *Murray et al.* [1991], published in the Phobos '88 special edition of *Planetary and Space Science*. Appendices 1, 2, and 3 are reproduced from *Betts* [1992], which appeared on the Planetary Data System's Phobos '88 CD-ROM. Lastly, new modelling and results presented in Chapter 6 that go beyond the initial Phobos shadow investigation presented in *Murray et al.* [1991] are in preparation for submission.

Chapter 2

Here in a little lonely room
I am master of earth and sea,
And the planets come to me.
-Arthur Symons

THE INSTRUMENT, THE DATA SET, AND VALIDATION

This chapter describes the Termoskan instrument, observations, and data set. Also presented are data validation studies and conclusions. This chapter includes material that was presented in *Murray et al.* [1991], as well as additional materials. The Termoskan digital data files, both raw and edited, that were included on the Planetary Data System Phobos '88 CD-ROM [*Betts*, 1992] are listed in Appendix 1. They are briefly described in this chapter and described in more detail in Appendix 2.

2.1 Introduction

In February and March 1989, the Termoskan instrument on board the Phobos '88 spacecraft of the USSR acquired a limited set of very high spatial resolution simultaneous observations of the reflected solar flux and emitted thermal flux from Mars' equatorial region. The slightly overlapping Termoskan panoramas cover a large portion of the equatorial region from 30°S to 6°N latitude. The Termoskan data are significant because they are the highest spatial resolution thermal data ever obtained for Mars. In addition, they are the only spacecraft imaging observations of Mars in the visible, as well as the thermal, since Viking. They also include unique simultaneous thermal and visible observations of the shadow of Phobos on the surface of Mars.

2.2 The Termoskan Instrument

Termoskan was an optical-mechanical scanning radiometer with one visible channel (0.5-1.0 μm) and one thermal infrared channel (8.5-12.0 μm) [*Selivanov et al.*, 1989; *Murray et al.*, 1991]. Figure 2.1 is an optical diagram of the instrument. Incoming radiation flux reflected off a scanning mirror (1), a parabolic mirror (2), and a mirror with a hole in it (3). It was then filtered by (4) which transmited thermal infrared radiation to

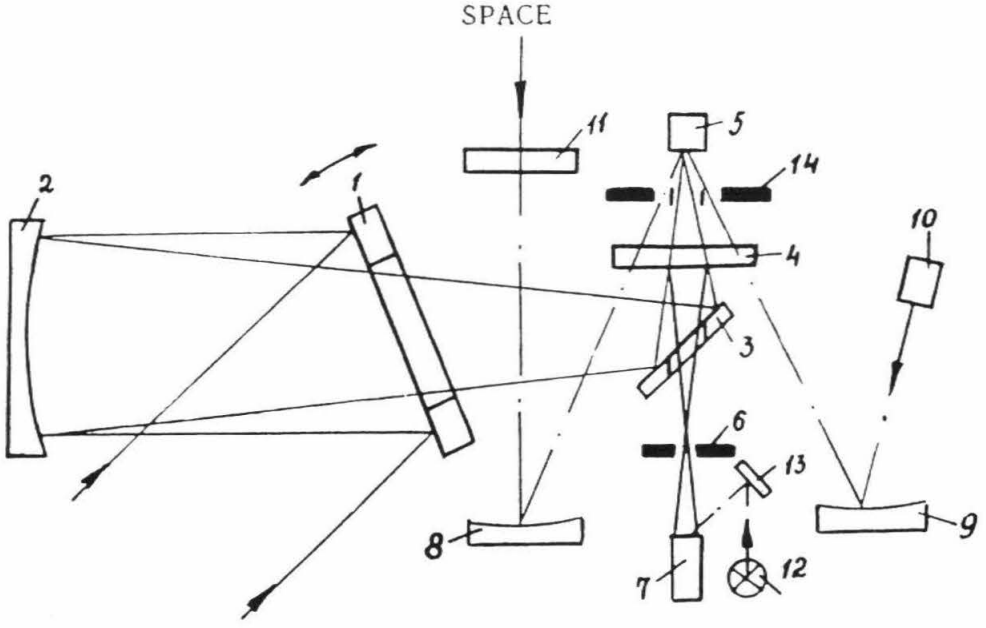

Figure 2.1: Optical block diagram of the Termoskan instrument. 1 - Scanning mirror; 2 - parabolic mirror; 3 - mirror with hole in center; 4 - IR filter, reflects visible light and transmits IR; 5 - thermal infrared detector; 6 - rotating visible channel modulator; 7 - visible channel detector; 8, 9 - spherical mirrors used in the thermal channel calibration process; 10 - black body calibrator; 11 - protective glass over the opening used for thermal channel calibration to space; 12 - visible channel calibration lamp; 13 - mirror; and 14 - rotating modulating chopping wheel for the infrared channel.

the infrared detector (5) and reflected visible radiation to the visible channel detector (7). Figure 2.2 shows Termoskan's spectral response, which is reproduced in tabular form in Appendix 3.

Two dimensional images were acquired one thermal-visible pixel pair at a time through the combined action of the scan mirror and the spacecraft motion. The displacement of the instantaneous field of view by the scanning mirror provided line scanning in the direction perpendicular to the spacecraft motion vector. Frame scanning resulted from the orbital motion of the spacecraft. The instrument was fixed to the spacecraft, i.e., there was no scan platform.

The Termoskan instrument had an instantaneous field of view of 0.9 minutes of arc, a full scan angle of 6.1°, and a scanning frequency of one line per second. Data were only taken in one direction (roughly north to south in the observations). Most of the one second per line involved the actual taking of Mars data. A small fraction of the time was needed to reset the mirror. The instrument arrangement allowed a swath width of 650 km and a best resolution of 1.8 x 1.8 km per pixel from an altitude of 6300 km. The duration of each survey session determined the length of each panorama. Table 2.1 summarizes the optical and signal characteristics of the Termoskan instrument.

The calibration of the infrared channel was fine tuned using an on-board black body (10) at 310 ± 0.1 K, as well as observations to open space (11) to determine a zero level. Sampling of the black body and space were carried out after every eight data pixels via a rotating modulating chopping wheel (14).

The base level for the visible channel calibrations was determined during the return phase of the scan mirror after each line of data was taken, i.e., once per second. This was done using a black area on the rotating visible modulator (6). The amplification factor for the visible channel calibration could be set from the ground to a fixed value, or adjusted according to the signal from the visible calibration lamp (12). The calibration lamp could be viewed once per second using the rotating visible channel modulator (6). In practice,

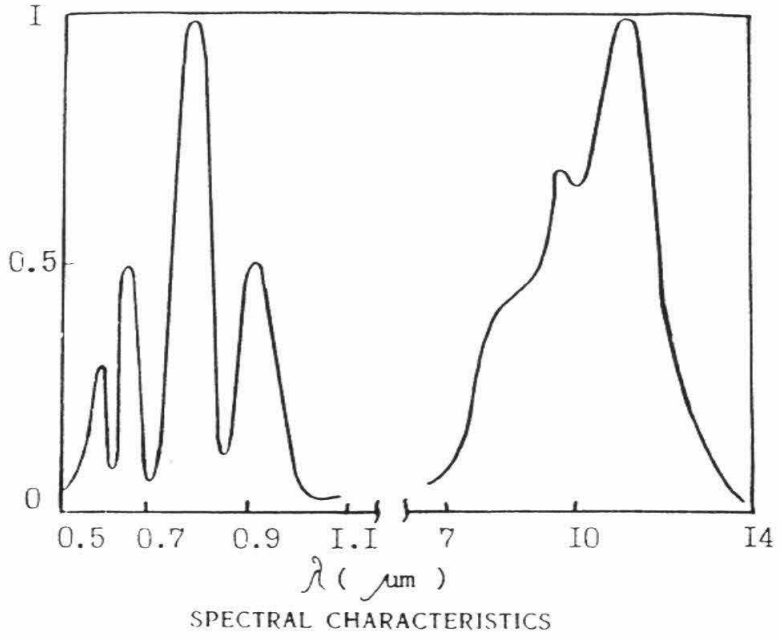

Figure 2.2: Spectral response of the Termoskan visible and infrared channels.

however, the signal from the calibration lamp (12) was never used. Only fixed amplification factors were used. Thus, the calibration of the visible channel was more dependent than the thermal channel upon pre-flight calibration, plus some refinement during the cruise to Mars. Figure 2.3 shows the calibration of the thermal channel, which is reproduced in tabular form in Appendix 3.

TABLE 2.1: Termoskan Instrument and Signal Parameters

Weight	28 kg
Aperture	150 mm
Focal length	375 mm
Scan rate	1 line/second
Scan angle	+ 3.0 degrees
Instantaneous Field of View	0.26 mrad per pixel
Infrared detector	HgCdTe
Visible detector	Photodiode Si
Spectral Bands: Visible	0.5 - 0.95 microns
Infrared	8.5 - 12.0 microns
Data pixels per line	384
Calibration: Visible	Onboard lamp
Calibration: Infrared	Onboard black body and space
Bits per pixel	8
Temperature sensitivity (K)	0.5 at 240 K
Temperature range (K)	170 - 290

There is noise equivalent to approximately 1-2 degrees Kelvin in every 8th sample of the infrared images.

2.3 The Observations

Four Termoskan observing sessions were carried out. Each provided a thermal emission and a visible panoramic view of the surface. Details of the panoramas are summarized in Table 2.2. Originally, the main purpose of the sessions was to refine the calibration of the instrument. When the spacecraft failed, however, their value obviously increased significantly. The four observing sessions were carried out in 1989, one each on

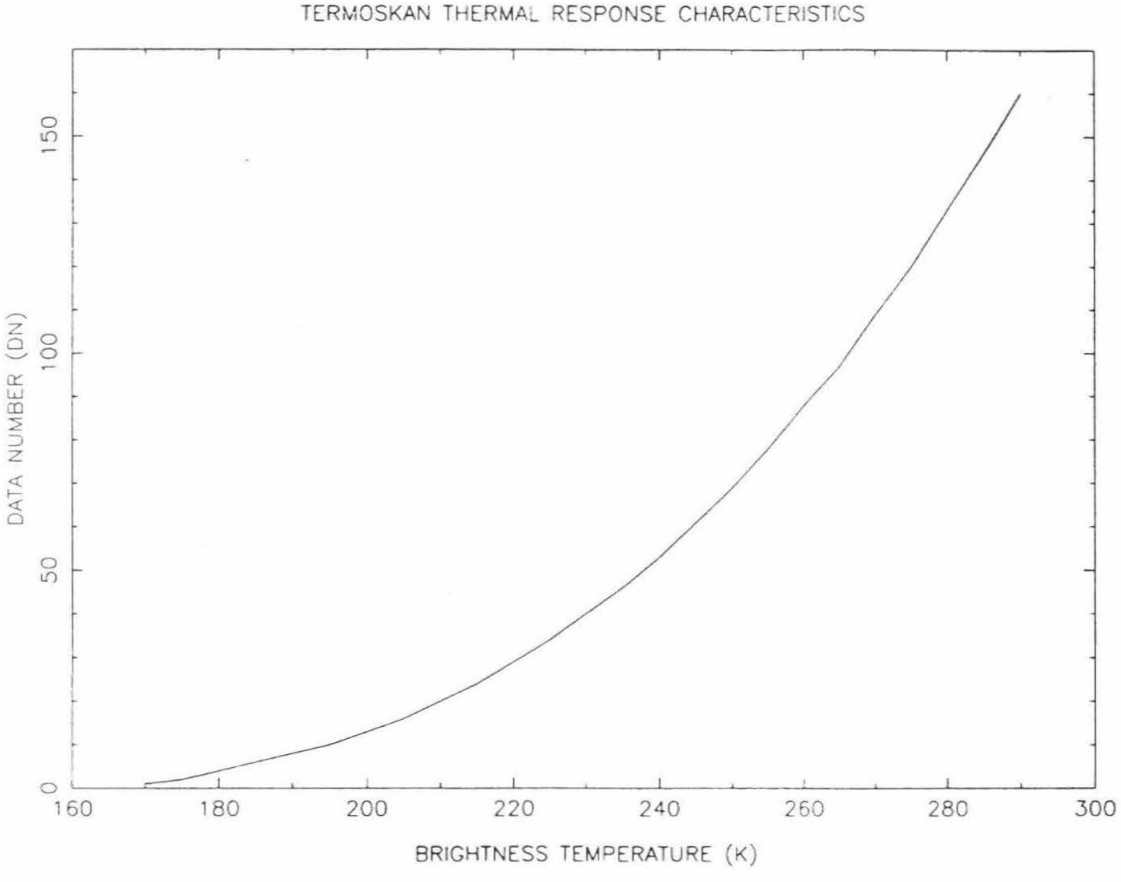

Figure 2.3: Termoskan infrared calibration curve.

TABLE 2: SUMMARY OF TERMOSKAN DATA SET

Scan	Date M-D-Y	Start Time (UT) h	m	s	Stop Time (UT) h	m	s	Ls	West Longitude	Latitude	Local Time of Day	Minimum Altitude (km)	Resolution per pixel (km)	Total Number of Lines	Morning Limb in scan	Evening Limb in scan	Phobos Shadow in scan
1A	2-11-89	10	55	00	11	26	04	357	80-240	6N-4S	6.0-18.0	1150	.3	1864	No	No	No
1B	2-11-89	10	55	00	11	26	04	357	80-240	6N-4S	6.0-18.0	1150	.3	1864	Yes	No	No
2A	3-01-89	13	12	00	13	52	00	6	317-0-49	5N-12S	9.6-16.5	6300	1.8	2400	No	No	No
2B	3-01-89	13	12	00	13	34	50	6	4-49	5N-8S	9.6-13.0	6300	1.8	1370	No	No	No
3A	3-26-89	09	11	29	10	11	29	18	5-170	7S-30S	6.3-17.6	6300	1.8	3600	Yes	Yes	Yes
3B	3-26-89	09	11	29	10	11	29	18	5-170	7S-30S	6.3-17.6	6300	1.8	3600	Yes	Yes	Yes
4A	3-26-89	16	48	30	17	49	50	18	115-280	7S-30S	6.3-17.6	6300	1.8	3680	No	No	Yes
4B	3-26-89	16	48	30	17	23	30	18	185-280	7S-30S	6.3-17.6	6300	1.8	2100	Yes	No	Yes

Termoskan acquired a total of 4 strips across Mars. In the above chart, A designates infrared data, and B designates visible data; e.g., scans 1A and 1B were acquired simultaneously with 1A consisting of infrared data and 1B consisting of data from the visible channel.

Start and stop times given are times at the spacecraft, not ground receive times.

All scans were acquired in 3 axis, sun-star stabilized mode. There was no scan platform. Termoscan looked along the Sun-spacecraft line (i.e., zero phase angle), except for slight rocking motions of the spacecraft.

Because Scan 1 was acquired near the periapse of one of the early elliptical orbits, the scan is very undersampled.

February 11 and March 1, and two on March 26. These dates corresponded to areocentric solar longitudes (L_S) of 356°, 6°, and 18°, respectively. These occur near the beginning of northern spring (L_S = 0°) on Mars. The four slightly overlapping thermal panoramas (also called scans or swaths) cover a large portion of the equatorial region from 30°S to 6°N latitude (Figure 2.4). Simultaneous visible panoramas were taken during each of the four observing sessions; due to spacecraft memory limitations, visible channel processing was stopped early relative to the thermal channel for two of the sessions (panoramas 2 and 4). Thus, the visible panoramas are shorter than the thermal panoramas for these sessions (Table 2.2).

Termoskan's best resolution per pixel was 1.8 km for three of the panoramas acquired and 300 m for the remaining panorama (taken on February 11). These resolutions per pixel are much better than those obtained by the Viking infrared thermal mapper (IRTM) (approximately 5 to 170 km/pixel, with only a small fraction of the data near 5 km/pixel, and with a typical value of 30 km/pixel [*Christensen*, 1986]). Termoskan's spatial resolution is also better than the 3 km/pixel expected for Mars Observer's thermal emission spectrometer (TES), although TES observations will provide global 2 p.m. and 2 a.m. local time as well as spectral coverage.

During the Termoskan observations, the Phobos spacecraft was in the mode of continuous sun - star orientation. Fixed to the spacecraft, Termoskan pointed in the anti-solar direction during all observing sessions. Thus, all observations are at nearly 0° phase angle and only daytime observations were acquired.

Scan lines were acquired going approximately from North to South on the planet at a rate of 1 line per second. Each image consists of 384 samples. The number of lines varied depending upon how long the instrument was on in any given panorama (Table 2.2). Data taking progressed from west to east due to the spacecraft motion. The data are 8 bit data with dn (data number, i.e., signal) values able to range from 0 to 255 for both the thermal and visible channels.

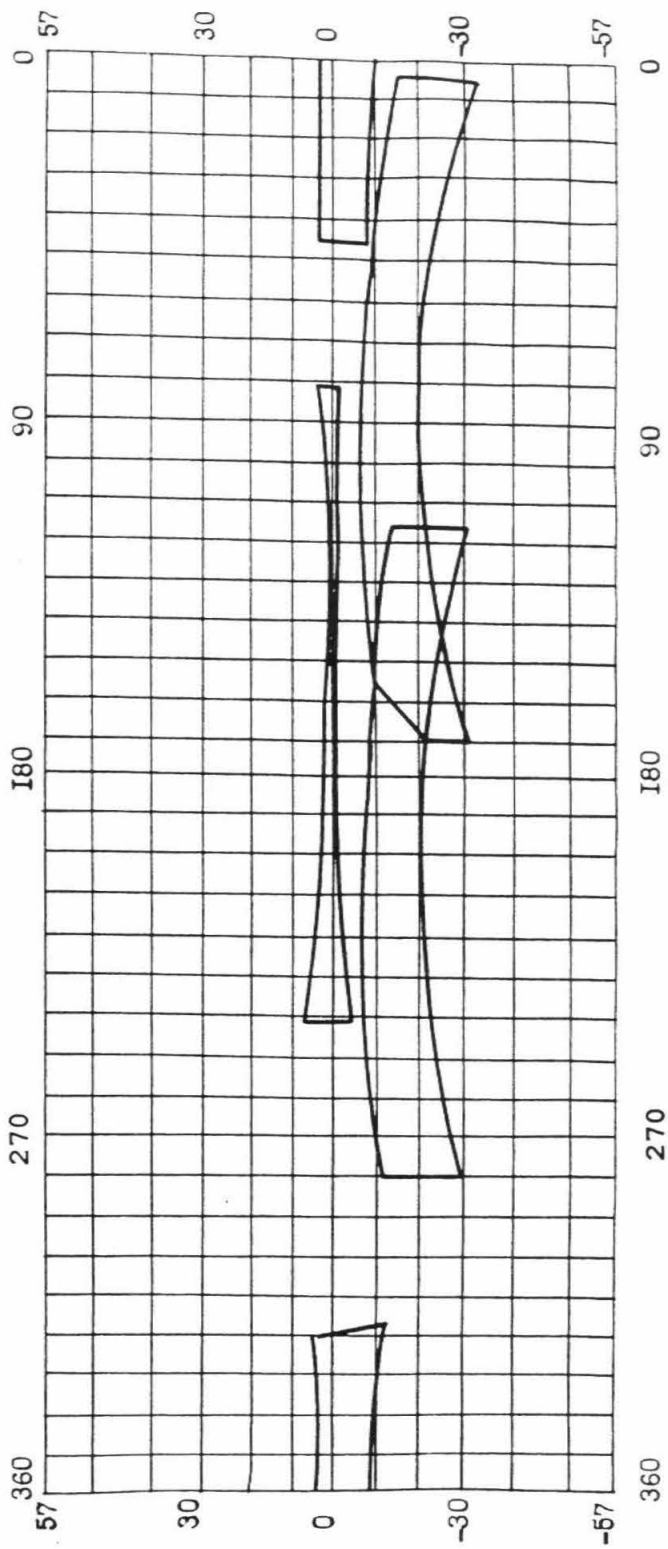

Figure 2.4: Coverage of the surface of Mars by the four Termoskan panoramas.

During the February 11 session (panorama 1), the Phobos spacecraft was in an elliptical transfer orbit with a minimum distance to the observed planet of only 1150 km. The thermal emission and reflected light profiles exhibited longitudinal gaps of varying sizes between scan lines. Each scan in the North - South direction, however, maintained full coverage and resolution, which was 300 m/pixel. The remaining three sessions were taken from a circular orbit closely similar to that of the moon Phobos with an altitude of 6300 km. For these panoramas, line and frame scanning correspond; therefore, there are not significant gaps between scan lines, and geometrical distortions primarily occur only because of the sphericity of the planet. Each of the two observing sessions on the 26th of March lasted one hour. This interval was sufficient for Termoskan to cover the Martian surface from limb to limb. Atmospheric limb studies are discussed in Chapter 5. Also in these two sessions, Termoskan imaged the shadow of Phobos on the surface of Mars as discussed and analyzed in Chapter 6.

2.4 The Data Files

The Termoskan instrument was built and operated by the Institute of Space Devices Engineering (ISDE) in Moscow. In April 1990, ISDE delivered the Termoskan data set to Caltech in the form of 23 digital files. These 23 files were incorporated, essentially as delivered, onto the Planetary Data System (PDS) Phobos '88 CD-ROM and are referred to here as the raw data set (PDS DATA_SET_ID = PHB2-M-TS-2-THERM/VIS-IMGEDR-V1.0). They are described in Appendix 2 which is taken from material provided to the PDS for inclusion on the CD-ROM [*Betts*, 1992]. The only significant difference between the CD-ROM raw data set and the one that was delivered by ISDE to Caltech is that I mirror flipped some files. This was necessary because some of the image files were delivered to Caltech with Mars appearing as it would in a mirror.

The delivered raw data set contained many other complexities that hampered analysis, such as irregular length panorama fragments, dropped lines, and misalignment of

the thermal and visible channels in both lines and samples. I altered these original files to produce a set of more readily usable and scientifically coherent edited files. These files [*Betts*, 1992] were also included on the PDS Phobos '88 CD-ROM. To produce these files, I combined the raw file fragments into the eight whole panoramas (four thermal and four visible); added blank lines to correct geometrically for dropped lines; and adjusted for misalignment of the thermal and visible channels in both lines and samples.

This edited data set was used for the analyses presented in this thesis. Appendix 1 lists all the data files and naming conventions from the CD-ROM. Appendix 2 includes the data set descriptions I prepared for the PDS CD-ROM for both the raw and edited files. Readers interested in actually using the data, or just after a more detailed understanding of the creation of the edited data files, their organization, and their complexities are urged to read Appendix 2. Particularly for the edited data set, note the data set description. It discusses how the files were created. Also, see the confidence level notes, which present information about noise within the data, both periodic and random, and about accuracy of alignment.

2.5 Contrast in the Visible and Thermal Channels

A conspicuous attribute of the Termoskan panoramas is the much lower contrast in the photographic displays of the visible channel versus the thermal infrared. Indeed, this difference is even more striking when viewed in the unstretched digital data, for example, in Figure 5.2. A major factor contributing to the low visible contrast in the visible is the zero phase angle nature of the observations. Shadows on the Martian surface arising from large-scale relief and from topographic slopes were not visible.

In addition, Viking data analyses emphasized how atmospheric dust and other aerosols will cause a lack of surface contrast at visible wavelengths [e.g., *Thorpe et al.*, 1979]. Thus, scattering by dust and ice crystals in the Martian atmosphere also may contribute to the very low surface contrast in the visible channel. The difference in

contrast between the visible and infrared channels implies that the visible wavelength optical depth is probably significantly larger than the thermal infrared optical depth. This is consistent with the results of *Toon et al.* [1977], *Pollack et al.* [1979], *Martin et al.* [1979], and *Zurek et al.* [1982] Their Mariner 9 and Viking analyses imply visible to infrared optical depth ratios for this season of order 2 or greater.

Analyses of limb profiles and of Phobos shadow images, discussed in Chapters 5 and 6, respectively, show that instrumental scattering in the Termoskan optics was negligible. Rocket propulsion products and induced vibrations always pose the threat of fine dust contamination of space optics. Thus an in-flight demonstration of the absence of instrumental scattering is very desirable.

Fortunately for scientific studies of Mars surface, the thermal emission channel yielded very high contrast data. This attribute is clear not just in the photographic renditions, but in the actual digital data as, for example, in Figures 2.7, 2.8, and 2.9. This circumstance reflects in part the excellent qualities of the instrument itself. The Modulation Transfer Function of the entire Termoskan system must have been very high in order for abrupt pixel-to-pixel variations in signal to be recognized. In addition, the bulk of Mars' atmospheric scattering at visible wavelengths probably arises from particles in the half micron or less range [*Clancy and Lee*, 1991]. These are too small and too cold to be discernible emitters in the 8 to 13 micron region (except at the limbs, where path lengths are greater). Furthermore, the dominantly high-sun observational conditions of the Termoskan images enhance the visibility of thermal differences arising from albedo, texture, and slope variations. Modelling studies predict variations of tens of Kelvins.

2.6 Data Validation: Comparison with IRTM

Determining the absolute accuracy of the Termoskan thermal data was a critical first step towards understanding the usefulness and believability of the data set. Validation is important for any instrument, but particularly important for one whose life was cut

prematurely short. Understanding the accuracy of the thermal channel proved important for many of the later studies presented here, particularly those that attempt to calculate thermal inertias (e.g., for channels in Chapter 4 and using the Phobos shadow in Chapter 6).

The kinetic temperature of a surface cannot be directly measured by a remote sensing instrument such as Termoskan. Instead, brightness temperatures are derived from the thermal infrared signal assuming black body surface emission. All further references to temperature within this thesis refer to brightness temperature.

In order to independently test the accuracy of the thermal channel, I compared Termoskan brightness temperatures to brightness temperatures from Viking's infrared thermal mapper's (IRTM's) 11 micron channel (9.8 to 12.5 μm). I constrained the IRTM data to match approximately the Termoskan data in season (L_S), longitude, latitude, and local time of day. In selecting the constraints, I had to balance matching those parameters accurately with obtaining a statistically significant number of IRTM points. Some of the largest overlap with IRTM data occurred in panorama 3, upon which I focus here. Figure 2.5 shows the latitudes and longitudes of IRTM points that match points within a section of panorama 3 to within ±10° of L_S and ±30 minutes of surface local time. Presented here are comparisons for two strips within panorama 3. The locations of the centers of the strips are shown superimposed on Termoskan data in Figure 2.6.

Figure 2.7 shows a comparison of IRTM and Termoskan data for a strip of constant latitude that is two degrees wide and centered upon 18°S latitude. In order to compare the two data sets, I degraded the Termoskan resolution to a resolution comparable to Viking. Thus, in Figure 2.7 the dark line represents Termoskan data that have been averaged in 67 x 67 pixel squares (approximately 2° x 2°). The thinner line is a one pixel Termoskan strip for reference. The IRTM data are represented by dots with horizontal error bars. These "error bars" represent the size of the footprint of each IRTM

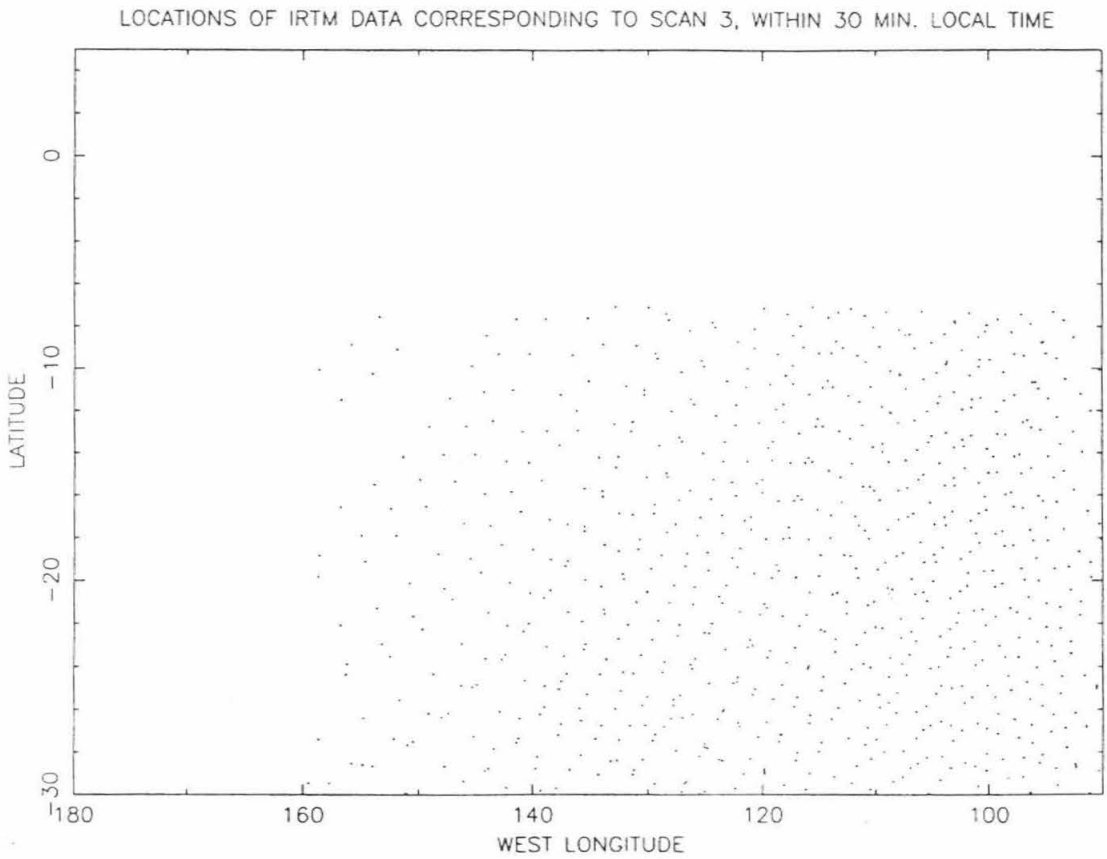

Figure 2.5: Plotted are the locations of the IRTM points which match this section of panorama 3 to within ± 10 degrees of L_S and ± 30 minutes of local time.

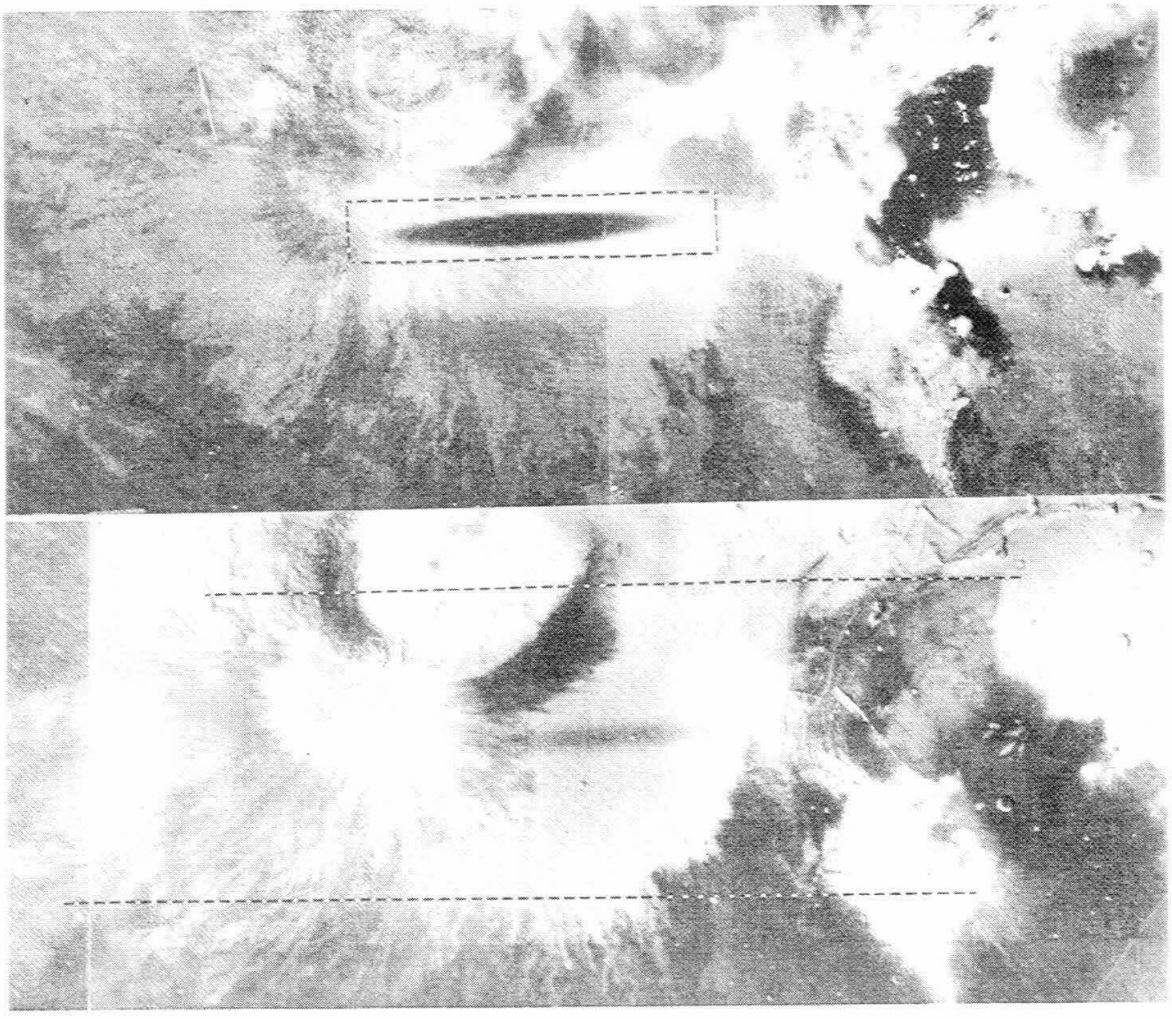

Figure 2.6: Termoskan visible (top) and thermal (bottom) images centered approximately upon 14°S, 117°W. North is top. In all the thermal images in this thesis, darker is cooler. The two lines in the IR data represent the center lines of the strips of data which are compared with IRTM data in Figures 2.7 (southern line) and 2.8. The Phobos shadow used for the analyses in Chapter 6 can be seen within the boxed portion of the visible data and in a similar region in the thermal image.

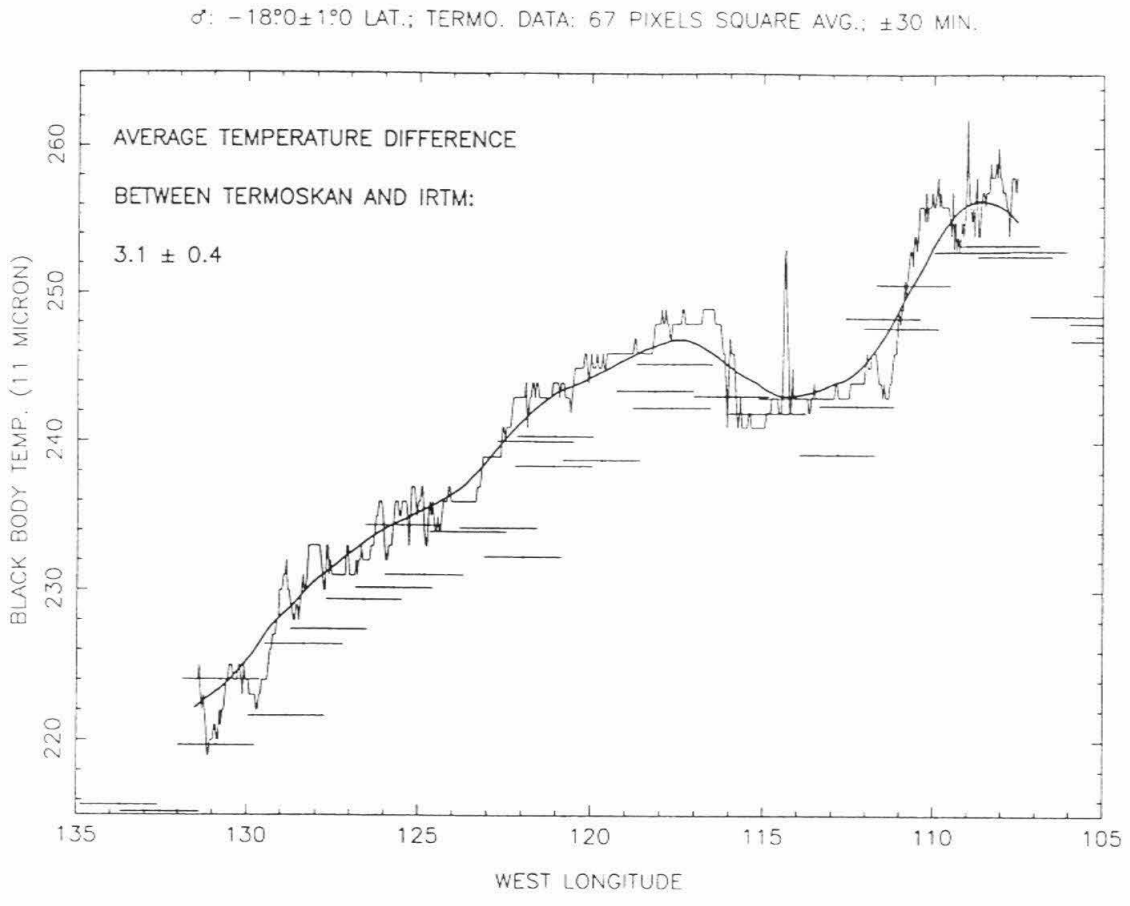

Figure 2.7: Comparison of Termoskan data with analogous IRTM data for a 2 degree wide strip of constant latitude centered on 18°S. The dark line represents a sliding boxcar average of Termoskan data which has been averaged in 2° x 2° squares. The thinner line is a 1 pixel Termoskan strip for reference. The points represent IRTM data with the error bars representing the footprint of each IRTM data point. IRTM data is constrained to match the Termoskan data to within ±10° of L_S and to within ±30 minutes of local time. Local time of day in the data shown ranges from about 8.5 to 10.3 H. After comparing each IRTM point with the averaged Termoskan point of the same longitude, the average temperature difference between Termoskan and IRTM is 3.1 ± 0.4 K with the Termoskan temperatures being warmer. Note how the large scale qualitative features match in the Termoskan and IRTM data. The lower line in the infrared image shown in Fig. 2.6 corresponds to the center of the comparison strip.

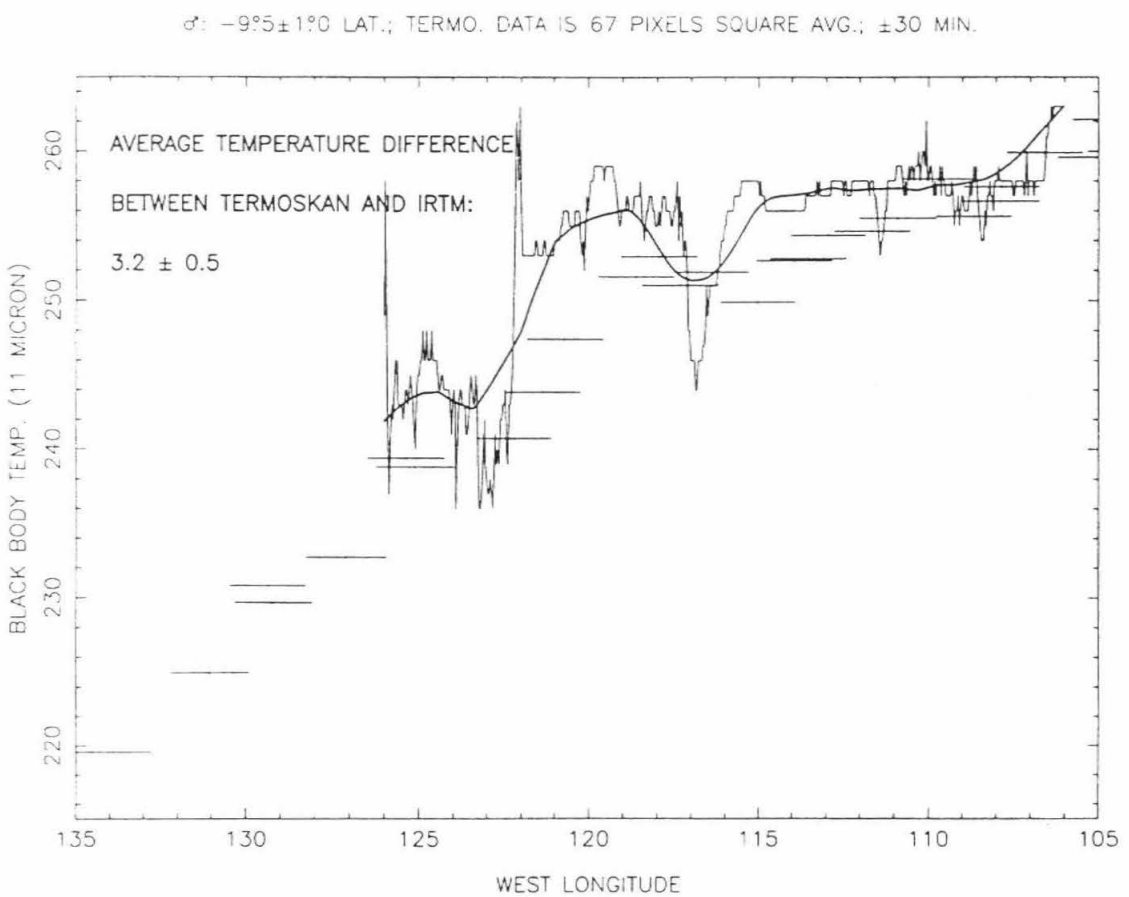

Figure 2.8: Analogous plot to Figure 2.7 for 9.5°S. The upper line in the infrared image shown in Figure 2.6 corresponds to the center of the comparison strip.

data point. Local times of day in these data range from about 8.5 to 10.3 H (24 H = 1 Martian day).

After comparing each IRTM point with the averaged Termoskan point of the same longitude, the average temperature difference between Termoskan and IRTM is 3.1 $\pm$ 0.4 K with the Termoskan temperatures being warmer. Also significant, note in Figure 2.7 that qualitative features match well between the two data sets. Figure 2.8 shows an analogous graph centered upon 9.5°S. For these data the average temperature difference is 3.2 $\pm$ 0.5 K. This result is consistent with the results obtained from the data in Figure 2.7 and from other latitudinal strips that I have examined.

The approximate 3K difference also includes the effects of the somewhat different bandpasses of the Termoskan IR channel and the Viking IRTM 11 μm channel [Kieffer et al., 1977]. The peak of the Termoskan response actually falls between the peaks of the IRTM 9 μm and 11 μm channels. I compared Termoskan with sparsely available IRTM 9 μm data as well. For the regions studied, the IRTM 9 μm brightness temperatures average about 1.5 K higher than the IRTM 11 μm brightness temperatures. Thus, the average temperature difference between Termoskan and the IRTM 9 μm channel is closer to 1 or 2 K. I conclude that the Termoskan brightness temperatures probably differ by no more than 2 K from comparable IRTM data.

One significant cause of the differences between IRTM and Termoskan is the difference in phase angle. IRTM measurements were in general taken at much higher phase angles than the near 0° phase angle Termoskan measurements. In particular, all of the IRTM data shown in Figures 2.7 and 2.8 was taken between 34° and 36° phase. Looking at 0° phase angle, Termoskan observed only the sunlit sides of surfaces and did not observe currently shadowed areas. The IRTM observations, taken at similar times of day, but at much higher phase angles, would have observed shadowed areas. In addition, IRTM would have observed the cooler sides of objects. This is a significant effect particularly for boulders and other large scale roughness for which a diurnal thermal skin

depth is much smaller than the object [*Jakosky et al.*, 1990]. The magnitude of the phase angle induced differences could be a few degrees Kelvin [*Jakosky et al.*, 1990].

Even ignoring possible errors in the decalibrated Viking IRTM data, there are other possible sources of the offset between Termoskan and IRTM. These include any bias in the Termoskan absolute preflight calibration, and any intrinsic difference in Mars' thermal emission between 1976-78 and 1989, including atmospheric effects such as clouds.

Not only are absolute temperature differences very small between Termoskan and IRTM, but also the thermal features in the Termoskan data qualitatively correlate very well with the lower resolution IRTM data, as seen in Figures 2.7 and 2.8. Thus, in both an absolute and a relative sense, I have a high degree of confidence in Termoskan's thermal channel and its calibration.

Termoskan sees thermal variations even at the limit of its spatial resolution. Figure 2.9 again shows Termoskan and IRTM data for 18°S latitude. The three curves represent different degrees of spatial averaging of the Termoskan data. Curve 1 is not averaged, i.e., it is a 1 pixel wide strip; curve 2 has 11 pixels averaged in a north-south direction; and curve 3 has 67 pixels averaged in a north-south direction. None of the curves are averaged in an east-west direction (whereas, Figures 2.7 and 2.8 were). Thermal features remain at the limit of resolution of the 1 pixel curve. For example notice the spike at approximately 115°W longitude (in Figure 2.9). This corresponds to the sunlit rim of a 6 km diameter crater.

2.7 Albedo and Thermal Inertia Determinations

Almost all of the analyses presented in this thesis involve the derivation of thermal properties of the surface, because the power of Termoskan lies in its high spatial resolution in the thermal infrared. Its visible spatial resolution is far worse than that of the viking camera observations. Thus, in terms of visible channel calibration, I am most

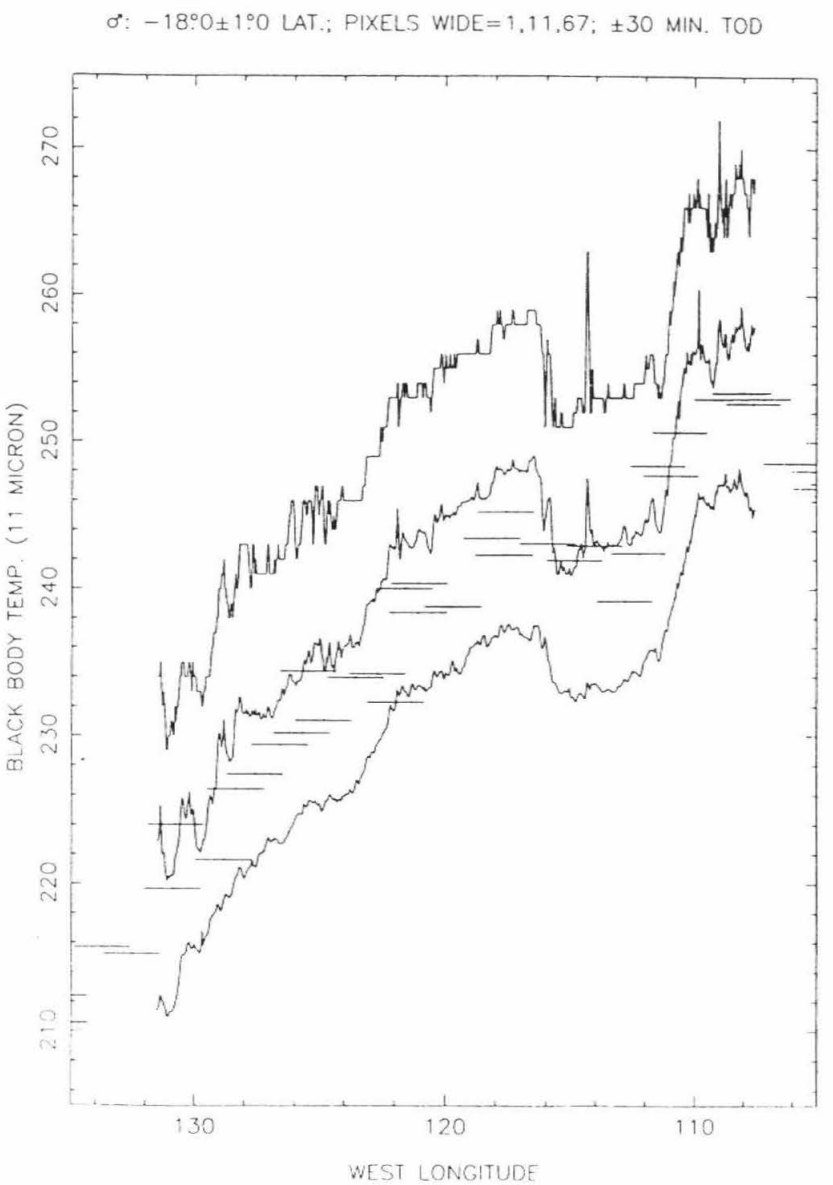

Figure 2.9: The lines represent Termoskan data centered upon -18 degrees latitude. Curve 1 (top) has no averaging; it is a 1 pixel wide strip to which 10 K have been added uniformly to ease comparison with the other curves. Curve 2 (middle) has 11 pixels averaged in a north-south direction. Curve 3 (bottom) has 67 pixels averaged in a north-south direction and has had 10 K subtracted from it. Note that sharp features can be seen in the 1 pixel wide strip that average out at lower resolutions, e.g., the spike at approximately 115°W corresponds to the rim of a 6 km diameter crater.

interested in whether the visible channel signal can be converted to bolometric Bond albedo, which is the parameter necessary for the derivation of thermal properties.

Thermal inertia and bolometric Bond albedo are the two most important physical properties of a planetary surface that determine its diurnal temperature variations. Thermal inertia, a bulk measure of the resistance of a unit surface area to changes in temperature, is commonly used to characterize the insulating properties of planetary surfaces. It is defined as $I = (k\rho c_p)^{1/2}$ where k is the thermal conductivity, ρ is the density, and c_p is the specific heat. Low inertia materials exhibit the largest day-to-night surface temperature variations and the smallest thermal skin depths.

For the martian surface, thermal inertia is often expressed in units of 10^{-3} cal cm^{-2} K^{-1} $sec^{-1/2}$ (e.g., in *Kieffer et al.*, 1977). As a matter of convention, these units are used for thermal inertias throughout this thesis. To convert to SI units (J m^{-2} K^{-1} $sec^{-1/2}$), multiply by 41.86. Several authors (e.g., *Kieffer et al.*, [1977]; *Palluconi and Kieffer*, [1981]; and *Haberle and Jakosky* [1991]) have used brightness temperatures and thermal modelling to derive thermal inertias for the martian surface. These authors used IRTM data from multiple times of day to derive both inertia and bolometric albedo simultaneously.

Termoskan observed only a small area at more than one local time of day and those data are badly foreshortened. Thus, for essentially all the Termoskan data, inertias and albedos cannot be derived independently using observations at two times of day. Therefore, the majority of the Termoskan data require bolometric albedo for thermal inertia determinations. Accurate bolometric albedos are particularly important for deriving inertias from Termoskan data because only daytime observations were obtained. Daytime temperatures are very dependent upon bolometric albedos.

Bolometric (Bond) albedo defines the fraction of incoming solar flux over all wavelengths that is not absorbed by a surface. Surfaces with high bolometric albedos ("bright" surfaces) absorb less incoming solar flux than those with low bolometric albedos

("dark" surfaces). Bolometric Bond albedo for a unit surface element is most simply defined as:

$$A = p\int q(\alpha)d\alpha$$

where p is the total reflectivity of all wavelengths at 0° solar phase angle, α, and $q(\alpha)$ is the variation of reflectivity over all wavelengths with increasing solar phase angle for the surface element. Even the most comprehensive Mars albedo observations are limited by uncertainties in the local variation in q, in wavelength dependence, and in temporal and spatial variations in atmospheric scattering. Termoskan observed only the total visible intensity from Mars surface elements at $\alpha = 0°$. The visible intensity observed included both surface and atmospheric components. Because Termoskan essentially did not observe shadows due to its zero phase angle geometry, the atmospheric contribution cannot be removed using the observed flux in shadowed areas as has been done with other data sets [e.g., *Herkenhoff*, 1989]. In addition to the other difficulties, the visible Termoskan data are largely dependent upon pre-flight calibration. Thus, even approximate estimates of Bond albedo from the Termoskan visible data alone will yield only low confidence results.

Another possible way to gain confidence in bolometric albedos derived from Termoskan data would be tying them to bolometric albedos derived from Viking IRTM solar band measurements. To test this possibility, I compared 1° x 1° averaged Termoskan dn (signal) values with the corresponding 1° x 1° binned albedos of *Pleskot and Miner* [1981]. Comparison strips were limited in latitude and longitude to lessen geometric and atmospheric effects. This increased the chances of tying the Termoskan data to the Viking albedos.

Figures 2.10 and 2.11 show representative examples of the comparisons. Figure 2.10, using data derived from observing session 2, shows a region with relatively large variations in albedo. Note the very high scatter within the data. A least squares fit to the

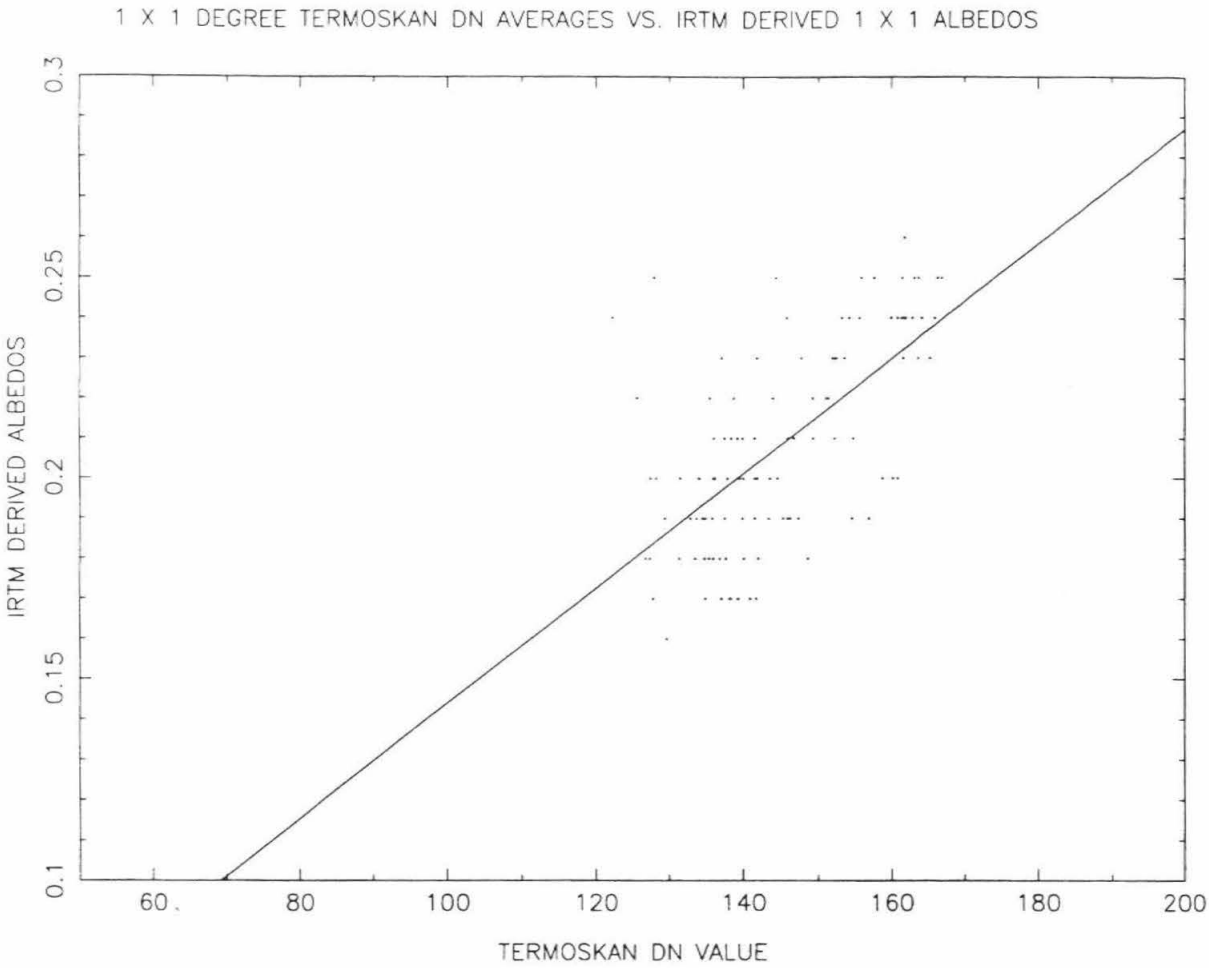

Figure 2.10: Termoskan visible dn vs. IRTM albedos - high contrast. Dots represent Termoskan 1° x 1° averages of visible channel dn (signal) values plotted versus IRTM 1° x 1° bolometric albedos from *Pleskot and Miner* [1981]. The bin centers range from 3.5°N, 42.5°W to 4.5°S, 31.5°W. Note the large amount of scatter in the plot. The line represents a linear least squares fit to the data with the following equation:
Albedo = (0.0009 ± 0.0243) + (0.00143 ± 0.00017) * (dn value).

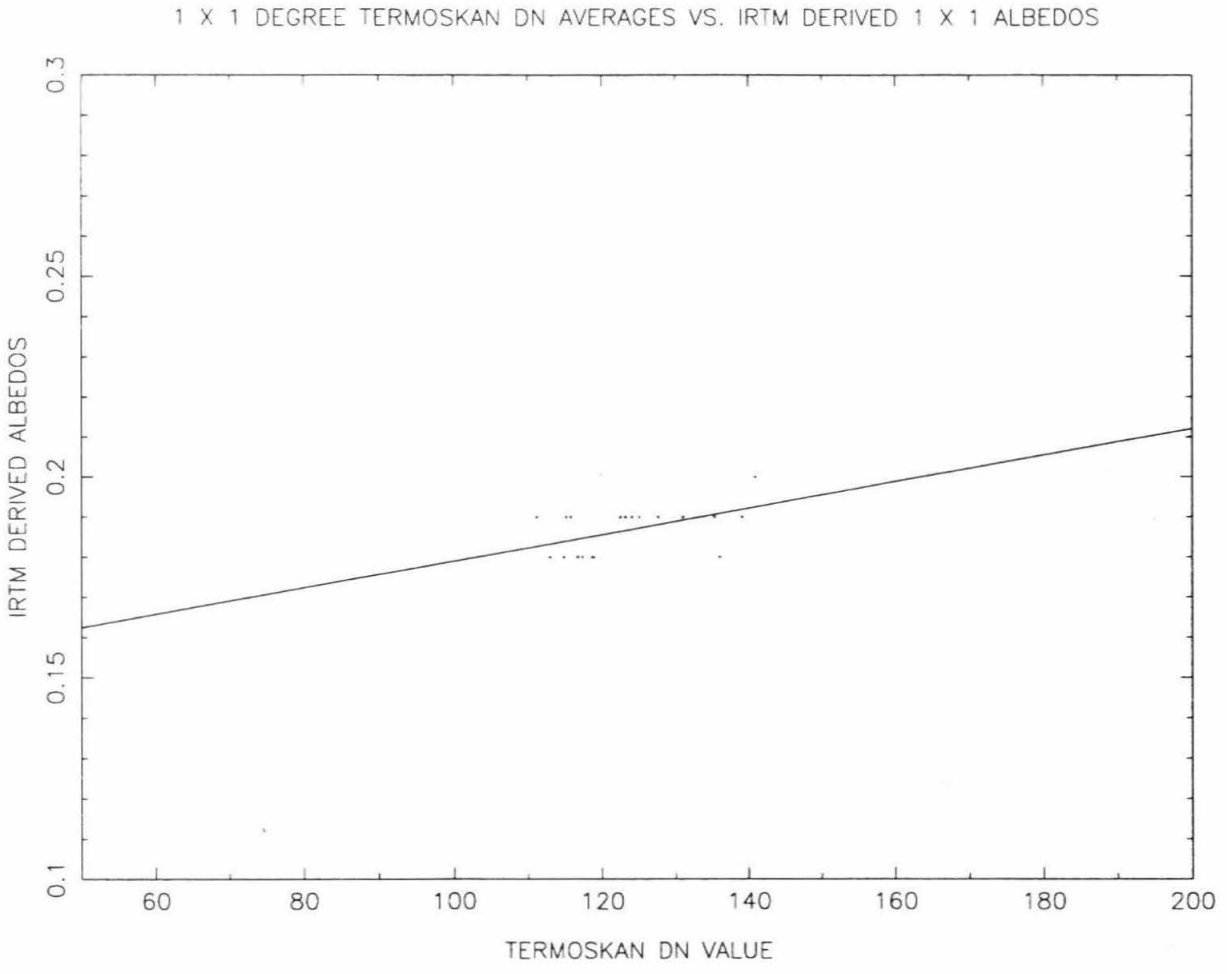

Figure 2.11: Termoskan visible dn vs. IRTM albedos - low contrast. Same as Figure 2.11, but for a different region that has less albedo contrast. The bin centers range from: 14.5°S, 82.5°W to 16.5°S, 76.5°W. The line represents a linear least squares fit to the data with the following equation:
Albedo = $(0.146 \pm 0.016) + (0.00033 \pm 0.00013)$ * (dn value)

data gives a standard deviation in albedos derived from this method of 0.02 Uncertainties of this magnitude will introduce significant uncertainties in the determination of thermal inertias. Figure 2.11 shows a region of low albedo variation, taken from panorama 3, for which the least squares fit is very different from that of Figure 2.10. Accuracy of this least squares fit is hampered by the small albedo variations at the scale of the 1° x 1° bins. The scatter in these and other plots combined with the variety of least squares fits and the uncertainties in the fits leads me to conclude that tying Termoskan data to Viking albedos is potentially very inaccurate at these scales. The ties will be even more inaccurate and uncertain if attempted over larger scales. Thus, although I have not proven the Termoskan data to be intrinsically in error, I conclude that using the Termoskan visible channel on its own or even with generalized ties to Viking data may introduce significant errors in derived absolute bolometric albedos, and significant errors in absolute thermal inertias.

2.8 Implications for Termoskan Studies

Bolometric albedo is nonetheless critical to accurate absolute inertia determinations from Termoskan thermal data due to the day time, single time of day observations of all locations. Therefore, I have focused on significant analyses that can be done with qualitative visible reflectivity comparisons and relative thermal inertias (e.g., Chapter 3, and the qualitative section of Chapter 4).

Because of the limitations of determining absolute thermal inertias from the Termoskan data, the strongest scientific statements can be made about features that clearly show either higher inertia (for example, the fretted channels discussed in Chapter 4) or lower inertia than their surroundings. For the midday surface conditions in most of the data, this involved areas that were either darker in the visible channel and cooler in the thermal infrared (implying higher inertia), or brighter in the visible channel and warmer in the infrared (implying lower inertia). For these types of features, strong statements about

relative thermal inertia can be made. Many new and interesting observations, conclusions, questions, and hypotheses can be put forth with only relative thermal inertias or even with qualitative thermal observations alone (for example see qualitative observations and conclusions in Chapters 3 and 4).

Where diurnal absolute thermal inertia are determined, I use 1° x 1° binned quantitative bolometric albedos from *Pleskot and Miner* [1981]. Combining these albedo variations with the qualitative observations from Termoskan's visible channel has allowed me in some cases to determine if the inertias I derive represent upper or lower bounds (e.g., channel studies in Chapter 4). Lastly, thermal inertias are derived for the upper millimeter of the Martian surface in Chapter 5 using cooling from the shadow of Phobos in a way that does not depend heavily upon albedo. Details of thermal modelling of the Mars surface are discussed in the chapters where modelling is actually used to derive thermal inertias, i.e., Chapters 4 and 6.

Chapter 3

These my sky-robes,
spun out of Iris' woof.
-John Milton

THERMALLY DISTINCT EJECTA BLANKETS

The material in this chapter is taken directly from *Betts and Murray* [1993a], which was published in the *Journal of Geophysical Research - Planets*. I have deleted a small section that described the instrument and data set. This section was redundant with the more detailed descriptions presented in Chapter 2 of this thesis.

3.1 Abstract

Utilizing the Termoskan data set of the Phobos '88 mission I have recognized a new feature on Mars: ejecta blanket distinct in the thermal infrared (EDITH). Virtually all of the more than 100 features discovered in the Termoskan data are located on the plains near Valles Marineris. EDITHs have a startlingly clear dependence upon terrains of Hesperian age, implying a spatial or temporal dependence on Hesperian terrains. Almost no thermally distinct ejecta blankets are associated with any of the thousands of craters within the data set that occur on the older Noachian units. EDITHs also do not appear on the portions of the younger Tharsis Amazonian units seen in the data. The Hesperian terrain dependence cannot be explained by either atmospheric or impactor variations; Noachian and Hesperian terrains must have experienced identical atmospheric and impactor conditions during Hesperian times. Thermally distinct ejecta blankets therefore reflect target material differences and/or secondary modification processes. Not all lobate ejecta blankets are thermally distinct, but all EDITHs correlated with visibly discernible ejecta blankets are associated with lobate ejecta blankets. The boundaries of the thermally distinct areas usually follow closely the termini of the fluidized lobate ejecta blankets, even when the ejecta blankets show a high degree of sinuosity. Thus, the thermally distinct nature of EDITHs must be due to the primary ejecta formation process. The coupling of

these thermal anomalies to morphology is unlike most sharp Martian inertia variations which are decoupled from observed surface morphology. Some thermally distinct ejecta blankets occur near otherwise similar craters that do not have thermally distinct ejecta blankets. Thus, wind patterns or locally available aeolian material cannot provide a single overall explanation for the observed variations. I compiled a data base of 110 EDITH and non-EDITH craters ranging in diameter from 4.2 km to 90.6 km. There are almost no correlations within the data base other than occurrence on Hesperian terrains. I postulate that most of the observed EDITHs are due to excavation of thermally distinctive Noachian age material from beneath a relatively thin layer of younger, more consolidated Hesperian volcanic material. The plausibility of this theory is supported by much geological evidence for relatively thin near-surface Hesperian deposits overlying massive Noachian megabreccias on the EDITH-rich plains units. I suggest that absence of thermally distinct ejecta blankets on Noachian and Amazonian terrains is due to absences of distinctive near-surface layering. Thermally distinct ejecta blankets are scientifically excellent locations for future landers and remote sensing because of relatively dust free surface exposures of material excavated from depth.

3.2 Introduction

Ejecta blankets surround craters on many planetary and satellite surfaces. Lunar and Mercurian deposits have ballistically emplaced ejecta blankets. They appear coarse and disordered near the rim, then gradually thin and smooth out with increasing distance from the crater. Eventually, they blend into fields of secondary craters, rays, and the surrounding terrain [*Shoemaker*, 1962]. On Mars, in contrast, most craters larger than about 4 km in diameter have lobate ejecta blankets with rampart or convex termini. Many craters smaller than 4 km and a small percentage larger than 4 km have lunarlike ballistic ejecta morphology with radial lineations and a thin, irregular boundary [*Strom et al.*, 1992]. At diameters larger than about 50 km, radial lunarlike ejecta morphologies again

dominate [*Pike*, 1980; *Horner and Barlow*, 1988]. A small percentage of craters have lobate blankets with superimposed radial striae. Many blankets are no longer visible due to erosion or blanketing by later deposits.

Formation of distinctive, relatively high relief, Martian lobate ejecta deposits with distinct termini was originally attributed to aeolian modification of lunarlike ejecta blankets [*McCauley*, 1973; *Arvidson et al.*, 1976]. However, flow features evidenced more clearly in Viking images point toward formation by fluidized flow, such as shock-induced fluidization of volatiles in the surface materials [e.g., *Carr et al.*, 1977; *Mouginis-Mark*, 1979; *Barlow and Bradley*, 1990]. Laboratory experiments involving impact into viscous targets have created ejecta blankets similar to those seen on Mars [*Greeley et al.*, 1980; *Gault and Greeley*, 1978]. Laboratory experiments that vary atmospheric pressure and particle size have also reproduced some lobate crater morphologies [*Schultz and Gault*, 1979, 1984]. One of my motivations in studying Martian thermally distinct ejecta blankets in detail is to discern any additional clues to the origin of fluidized ejecta blankets.

Lunar eclipse and lunar nighttime observations show that at least the inner regions of some younger ejecta blankets are thermally distinct (usually warmer than surroundings) [*Shorthill*, 1972]. This is attributed to a greater preponderance of blocks. Newly recognized thermal anomalies associated with Martian ejecta blankets extend further and appear to be more complex in origin.

I have used the high spatial resolution of the thermal infrared/visible Termoskan instrument to carry out the first thermal study of Martian ejecta blankets. Because of insufficient spatial resolution, studies of Viking IRTM data were unable to distinguish any Martian ejecta blankets as thermally distinct from their surroundings (P. R. Christensen, personal communication, 1991). Approximately 100 craters within the Termoskan data have an ejecta blanket distinct in the thermal infrared (EDITH) (e.g., see Figure 3.1). To better understand these features, I have undertaken a threefold analysis: (1) a systematic examination of all Termoskan image data using high-resolution image processing; (2) a

Figure 3.1*a*. Image is from Termoskan's visible channel. Time of day is near local noon. North is towards the left side of the page. Part of Valles Marineris can be seen in the northeast corner. Phase angle is approximately zero for all points. Image was obtained simultaneously with the thermal image shown in Figure 3.1*b*. The dark east-west band is the thermal signature of the passage of the shadow of Phobos. Black vertical lines represent missing lines of data.

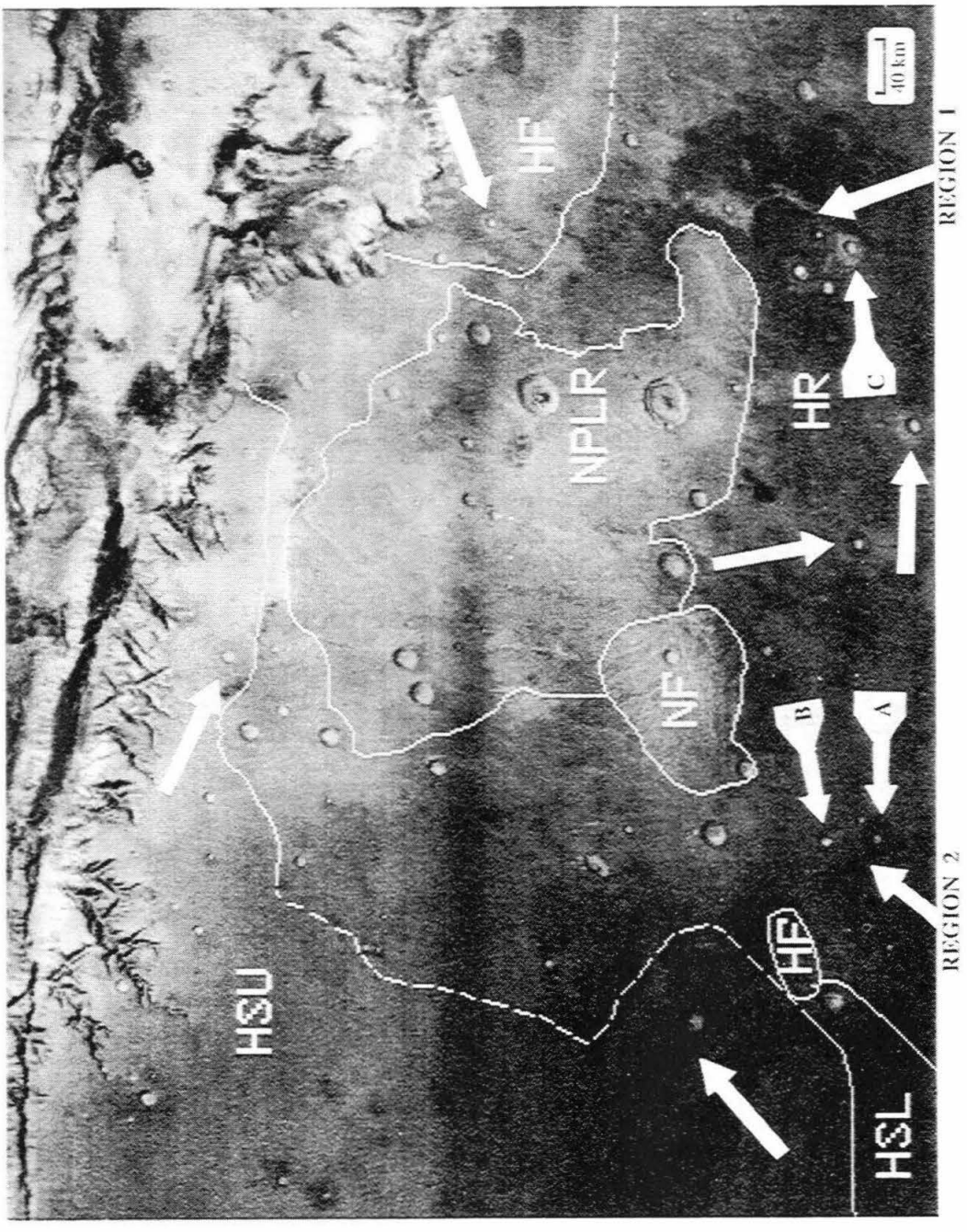

Figure 3.1*b*. Image is from Termoskan's thermal infrared channel. The darker areas are cooler and lighter areas are warmer. Note the thermally distinct ejecta deposits which appear as bright or dark rings surrounding craters in the thermal image (examples denoted by arrows). These deposits are up to 5 K warmer or cooler than their surroundings. White lines indicate geologic map boundaries. Geologic units and boundaries are from *Witbeck et al.* [1991] and *Scott and Tanaka* [1986] with some interpolation between the two. Units shown, from oldest, are Nplr, Noachian plateau ridged unit; Nf, Noachian fractured unit; Hr, Hesperian ridged plains material; Hsl, Hesperian Syria Planum formation, Lower Member; and Hsu, Hesperian Syria Planum formation, Upper Member (see Table 3.2 for more detail). Virtually all of the more than 100 EDITHs observed are situated on Hesperian age plains near Valles Marineris (e.g., Hr, Hsu, and Hf), but not on the older Noachian units (e.g., Nplr and Nf). EDITHs are almost exclusively associated with Hesperian age terrains throughout the data set.

formal study of the systematics of the data by compiling and analyzing a data base consisting of geographic, geologic, and morphologic parameters for a significant fraction of the EDITHs and nearby non-EDITHs (total ejecta blankets 110); and (3) qualitative and quantitative analyses of localized regions of interest. These methods, results, and conclusions are presented in the remaining portions of this paper.

3.3 Properties Associated with Individual EDITHs

On the Hesperian units where EDITHs are present, intensity profiles across different ejecta blankets vary greatly in both the thermal and visible channels (see Figures 3.2 and 3.3). Some of the blankets appear warmer than their surroundings, some appear cooler, and some are not thermally distinct. Some thermally distinct ejecta blankets appear distinct in the visible channel; however, others do not.

The boundaries of EDITHs often closely follow even very sinuous termini of lobate ejecta blankets (e.g., see Figures 3.4-3.7). Thus, the thermal anomalies are strongly associated with the blankets themselves. Those blankets that appear thermally distinct show no consistent pattern of radial thermal variation within each blanket. Many EDITHs are quite uniform in temperature across a given blanket.

Crater interiors often appear warm relative to ejecta and surroundings, as exemplified by the thermal profiles in Figures 3.2 and 3.3 as well as in Figure 3.1. In some cases this is probably due to low inertia material within the craters. However, in all but the flat floors of the largest craters, one must consider the heating effects of slopes and of increased shadowing caused by crater topography. These effects are very difficult to separate from inertia and albedo effects without multiple observations. In this paper I will not comment further on the thermal signature of crater interiors. By contrast, slope and shadow history effects for ejecta blankets are much smaller due to the larger scales and smaller slopes involved.

In order to search for correlations and better understand EDITHs, I compiled a data base of craters and their ejecta which includes quantitative and qualitative information (see Table 3.1). My data base includes 110 craters, most thermally distinct but some not. This set covers all craters larger than 8 km in diameter and most craters larger than 5 km (smallest, 4.2 km; largest, 90.6 km) that are located in the northwest and southwest Coprates subquadrangles (MC-18NW and MC-18SW) and fall within the Termoskan panoramas. Local time of day within this region varies from approximately 1130 to 1330. The craters selected are located between 23.0°S and 8.0°S in latitude and 67.5°W to 90.0°W longitude. This area includes parts of Valles Marineris and several plains and ridged plains units of both Noachian and Hesperian age just south of Valles Marineris. This region was chosen for its many thermally distinct ejecta craters and its variety of geologic units. Many lobate ejecta craters are seen in this region in Viking images even down to subkilometer scales [*Clifford and Duxbury*, 1988].

For each crater in the data base, I have cataloged representative average temperatures for both the ejecta (EJET in Table 3.1) and the area surrounding the ejecta (SURT). Because the relative precision of Termoskan is approximately 0.5 K and the absolute accuracy is better than 3 K [*Murray et al.*, 1991], I have great confidence in relative Termoskan brightness temperatures. In Termoskan's less accurate visible channel, I similarly noted representative *dn* (signal) values for both ejecta (EVIS) and the area surrounding the ejecta (SVIS).

I developed three descriptive thermal parameters, each expressing a somewhat different aspect of the ejecta blankets. First, I assigned a subjective "thermal freshness" parameter (TFR in Table 3.1) describing qualitatively how thermally distinct the ejecta appears relative to the surroundings. Second, I calculated temperature difference (DELT) between the ejecta blanket and the surrounding area using my representative average temperature values. Third, I calculated an approximate time of day corrected temperature for the ejecta alone (ETDS), thus giving a thermal parameter that does not depend upon

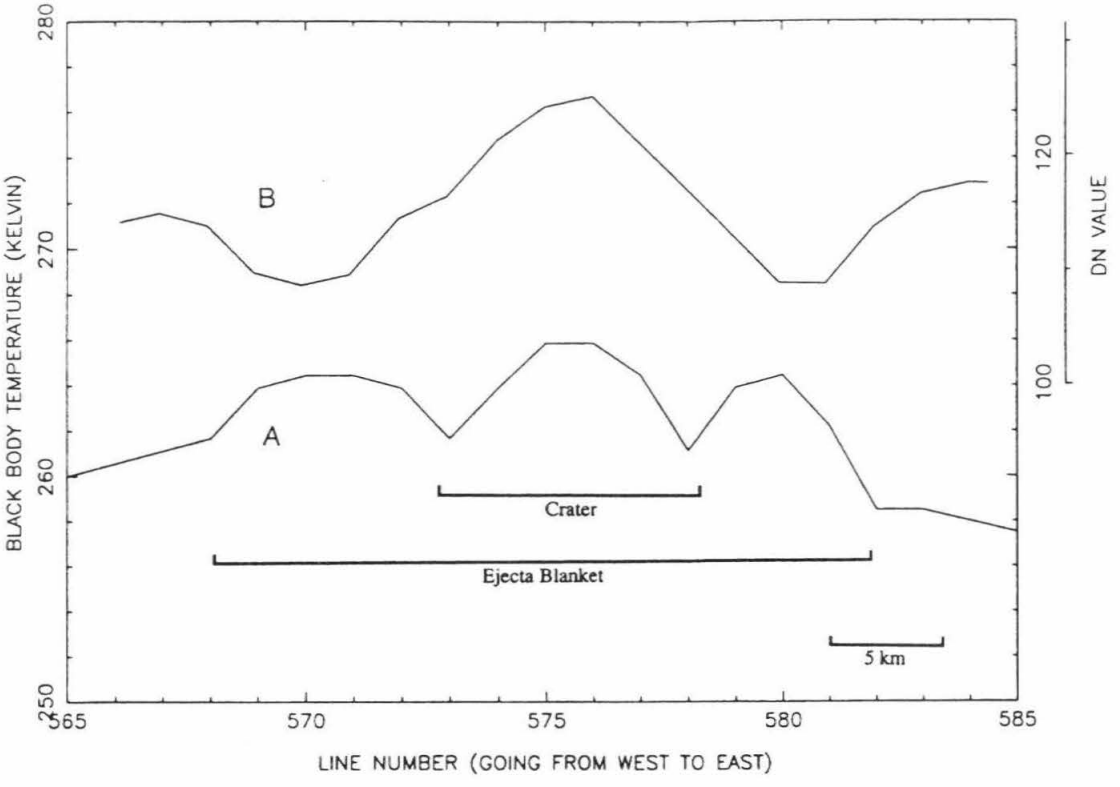

Figure 3.2. West to east Termoskan infrared (curve A) and visible (curve B) profiles across fluidized ejecta blanket and 11.4 km crater located at 18.4°S, 74.0°W (crater 25 in Table 3.1; crater C in Figures 3.1 and 3.4). Note the three peaks in the temperature curve. The outer peaks correspond to the warm (relative to surroundings) ejecta blanket on either side of crater. The central peak corresponds to the warm crater interior. Note the inverse correlation between the temperature of the ejecta blanket and the visible signature, implying that in this case an albedo difference helps explain the warmer ejecta. This inverse correlation exists only in some crater profiles. The crater interior shows correlation between temperature and visible brightness, possibly indicating some degree of low inertia dust mantling in the crater interior.

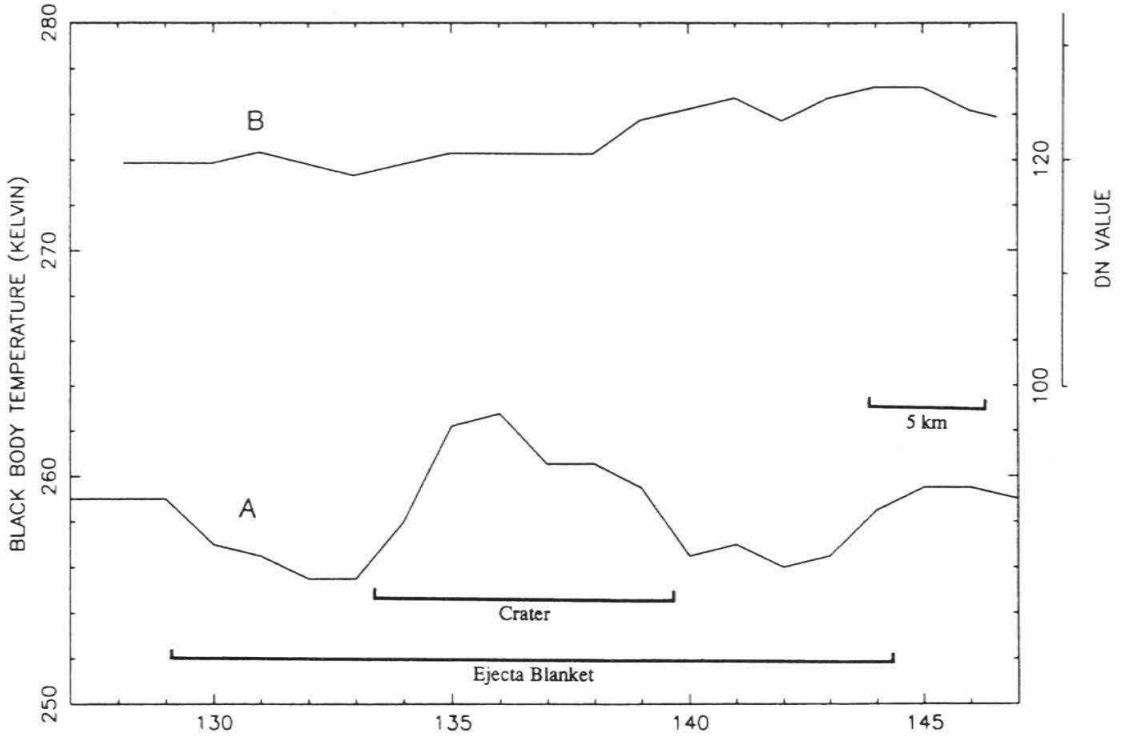

Figure 3.3. West to east Termoskan infrared (curve A) and visible (curve B) profiles across fluidized ejecta blanket and 12.6 km crater located at 18.5°S, 88.7°W (crater 1 in Table 3.1; just off the western edge of Figure 3.1). This crater has an ejecta blanket that is cooler than the surroundings. Notice the two dips in the temperature curve that correspond to the fluidized ejecta blanket. Note that for this crater, the visible curve shows very little correlation to the temperature in either the ejecta blanket or crater interior.

ID	LAT	LON	DIA	TYP	EJE	INT	PTDI	UNIT	TPR	EJET	SURT	DELT	ETDS	STDS	EVIS	SVIS	DELV	TOD	ALB	INER	TOPO	RATIO
1	-18.53	88.72	12.60	Rc	SL	Pk	0.00	Hsu	-3	256.50	259.00	-2.50	-0.72	1.78	126.00	121.00	5.00	11.68	0.18	7.3	6597	2.08
2	-18.28	88.91	5.38	Sc	No	No	0.00	Hsu	-2	256.00	259.00	-3.00	-1.15	1.85	129.00	121.00	8.00	11.67	0.18	7.3	6597	0.00
3	-17.99	89.01	6.10	Sc	No	No	0.00	Hsu	-3	256.00	257.50	-1.50	-1.43	0.07	129.00	120.00	9.00	11.66	0.18	6.9	6176	0.00
4	-18.36	89.29	7.40	Rc	No	No	0.00	Hsu	-3	256.00	259.00	-3.00	-0.94	2.06	128.00	121.00	7.00	11.64	0.17	7.3	6532	2.50
5	-15.48	88.38	5.70	Rc	No	No	0.00	Hsu	-2	257.50	260.00	-2.50	-1.86	0.64	149.00	149.00	0.00	11.70	0.19	6.3	5899	0.00
6	-17.93	84.21	21.50	Sc	No	No	0.00	Hal/Hr/Hsu	2	260.56	258.00	2.56	0.94	-1.62	130.00	130.00	0.00	12.02	0.17	7.3	6106	0.00
7	-17.67	84.05	6.40	Sc	No	No	0.00	Hal/Hr/Hsu	0	260.56	260.56	0.00	0.55	0.55	130.00	130.00	0.00	12.03	0.17	7.3	6106	0.00
8	-16.05	84.60	18.80	Rc	ML	SY	2.60	Hsu	-3	258.00	259.00	-1.00	-2.73	-1.73	148.00	150.00	-2.00	11.98	0.18	7.0	5591	3.61
9	-15.51	84.51	4.30	Rc	SL	No	0.00	Hsu	0	258.50	260.00	-1.50	-2.60	-1.10	150.00	150.00	0.00	11.99	0.18	7.0	5591	0.00
10	-18.73	83.43	7.40	Rc	SL	FP	0.00	Hr	-1	257.50	259.00	-1.50	-2.01	-0.51	125.00	123.00	2.00	12.07	0.17	7.5	6903	1.94
11	-18.54	81.98	11.60	Rc	SL	FP	0.00	Hr	-3	256.50	260.00	-3.50	-3.52	-0.02	123.00	117.00	6.00	12.18	0.20	7.4	6210	2.80
12	-17.85	82.07	8.80	Rc	SL	Pk	0.00	Hr	0	259.50	260.00	-0.50	-0.87	-0.37	124.00	123.00	1.00	12.18	0.17	7.2	5578	2.17
13	-16.38	82.07	19.70	Rc	ML	FP	0.00	Hr	1	263.89	262.78	1.11	2.52	1.41	134.00	134.00	0.00	12.18	0.19	7.2	5019	3.53
14	-16.79	81.20	17.10	Rc	SL	SY	1.20	Hr/Nf	1	262.22	260.56	1.66	0.90	-0.76	132.00	132.00	0.00	12.24	0.19	6.8	5000	2.60
15	-17.06	79.58	10.90	Rc	SL	Pk	0.00	Hr/Nf	2	262.22	260.00	2.22	0.47	-1.75	122.00	132.00	-10.00	12.36	0.19	7.2	5000	2.20
16	-15.76	79.78	11.50	Sc	No	No	0.00	Nf	0	267.08	267.08	0.00	4.47	4.47	139.00	139.00	0.00	12.35	0.19	6.2	5000	0.00
17	-15.83	78.49	20.40	Rc	ML	SY	3.70	Npkr	0	263.33	265.42	-2.09	0.66	2.75	130.00	122.00	8.00	12.44	0.18	6.2	5000	0.00
18	-18.38	77.94	10.60	Rc	SL	Pk	0.00	Hr	-3	260.00	262.22	-2.22	-1.15	1.07	116.00	110.00	6.00	12.48	0.18	7.8	5626	2.20
19	-16.17	77.55	15.70	Rc	SL	SY	2.60	Npkr	0	265.00	265.00	0.00	2.10	2.10	119.00	119.00	0.00	12.51	0.19	7.3	5000	3.14
20	-19.12	76.21	11.60	Rc	SL	SY	2.30	Hr	3	262.78	259.00	3.78	1.65	-2.13	108.00	111.00	-3.00	12.61	0.18	7.8	5698	2.00
21	-15.75	76.33	35.50	Rc	ML	Pk	0.00	Npkr	0	266.67	266.67	0.00	3.24	3.24	120.00	120.00	0.00	12.60	0.18	6.6	5000	4.41
22	-16.71	75.99	8.20	Rc	Pa	FP	0.00	Npkr	-2	263.33	265.42	-2.09	0.46	2.55	122.00	118.00	4.00	12.63	0.18	7.3	5000	2.00
23	-18.04	74.49	9.10	Sc	No	No	0.00	Hr	0	260.00	258.00	2.00	-2.14	-4.14	116.00	116.00	0.00	12.74	0.19	7.7	5163	0.00
24	-17.68	74.36	13.90	Rc	SL	Pk	0.00	Hr	3	260.56	258.00	2.56	-1.94	-4.50	124.00	124.00	0.00	12.75	0.19	7.7	5163	1.54
25	-18.39	73.95	11.40	Rc	SL	FP	0.00	Hr	3	264.44	258.00	6.44	2.59	-3.85	109.00	116.00	-7.00	12.78	0.18	8.2	5473	2.00
26	-17.99	73.84	9.10	Rc	SL	FP	0.00	Hr	3	260.00	258.00	2.00	-2.21	-4.21	120.00	123.00	-3.00	12.79	0.19	8.0	5320	2.29
27	-16.66	73.66	7.00	Rc	SL	Pk	0.00	Hr	2	264.44	260.00	4.44	1.23	-3.21	121.00	126.00	-5.00	12.80	0.19	8.0	5002	2.00
28	-16.25	73.71	4.30	Rc	SL	No	0.00	Hr	2	263.89	260.00	3.89	0.36	-3.53	124.00	128.00	-4.00	12.80	0.19	8.0	5002	0.00
29	-16.06	73.67	4.30	Sc	No	No	0.00	Hr	2	263.89	260.00	3.89	0.36	-3.53	127.00	128.00	-1.00	12.80	0.19	8.0	5002	0.00
30	-15.43	73.01	10.60	Rc	SL	Pk	0.00	Hr	0	265.42	265.42	0.00	1.52	1.52	131.00	131.00	0.00	12.85	0.19	6.9	5000	2.50
31	-17.95	72.03	16.90	Rc	SL	Pk	0.00	Hr	-1	261.67	260.56	1.11	-0.69	-1.80	121.00	121.00	0.00	12.92	0.19	8.0	5621	3.27
32	-16.13	71.05	16.90	Rc	ML	FP	0.00	Hr	0	264.44	264.44	0.00	0.68	0.68	128.00	128.00	0.00	13.00	0.19	7.2	5206	2.80
33	-17.70	70.64	12.60	Rc	SL	Pk	0.00	Hr	2	262.22	260.56	1.66	-0.58	-2.24	127.00	125.00	2.00	13.03	0.19	7.2	5623	2.00
34	-19.21	70.69	5.20	Sc	No	No	0.00	Hr	2	261.11	259.50	1.61	-0.66	-2.27	122.00	122.00	0.00	13.02	0.17	6.9	6142	1.67
35	-19.80	68.98	12.70	Rc	No	No	0.00	Hr	0	263.89	263.89	0.00	2.47	2.47	120.00	120.00	0.00	13.15	0.18	6.5	6183	2.31
36	-18.79	69.13	24.10	Rc	ML	Pk	0.00	Hr	-1	260.00	262.22	-2.22	-2.13	0.09	125.00	125.00	0.00	13.14	0.18	6.5	6017	4.19
37	-18.06	68.52	8.60	Rc	No	No	0.00	Hr	0	262.78	262.78	0.00	0.31	0.31	127.00	127.00	0.00	13.18	0.20	6.6	5875	1.69
38	-17.50	68.23	10.50	Rc	No	No	0.00	Hr	-1	263.33	265.42	-2.09	0.52	2.61	133.00	131.00	2.00	13.21	0.20	6.6	5875	2.06
39	-18.60	67.56	6.20	Sc	No	No	0.00	Hr	-1	260.00	263.33	-3.33	-2.13	1.20	122.00	122.00	0.00	13.26	0.19	6.5	6285	0.00
40	-11.78	90.01	90.60	Dc	No	No	0.00	Hsu	0	265.42	265.42	0.00	4.89	4.89	161.00	161.00	0.00	11.58	0.21	5.5	7825	0.00
41	-10.55	89.92	4.70	Sc	No	No	0.00	Hsu	-1	265.42	266.67	-1.25	4.05	5.30	154.00	154.00	0.00	11.59	0.21	5.4	8290	0.00
42	-10.02	89.78	4.50	Sc	No	No	0.00	Hsu	-2	265.00	266.25	-1.25	3.32	4.57	154.00	154.00	0.00	11.60	0.21	5.4	8290	0.00
43	-11.01	89.62	7.60	Sc	No	No	0.00	Hsu	-1	264.44	266.67	-2.23	3.18	5.41	160.00	160.00	0.00	11.61	0.21	5.4	7607	0.00
44	-9.35	88.83	3.90	Sc	No	No	0.00	Hsu	-1	264.44	265.42	-0.98	2.04	3.02	158.00	158.00	0.00	11.67	0.22	5.1	8681	0.00
45	-10.68	88.67	6.00	Sc	No	No	0.00	Hsu	-2	264.44	265.83	-1.39	2.45	3.84	161.00	161.00	0.00	11.68	0.20	5.4	8271	0.00

Table 3.1. Crater data base of EDITH and non-EDITH craters in the Coprates Southwest (MC-18SW) and Coprates Northwest (MC-18NW) subquadrangles.

Table 3.1. continued.

ID	LAT	LON	DIA	TYP	EJE	INT	PTDI	UNIT	TFR	EJET	SURT	DELT	ETDS	STDS	EVIS	SVIS	DELV	TOD	ALB	INER	TOPO	RATIO
46	-13.54	88.52	19.30	Rc	No	No	0.00	Hsu	0	263.33	263.33	0.00	2.85	2.85	161.00	161.00	0.00	11.69	0.20	5.5	6290	1.60
47	-13.29	88.45	6.10	Dc	No	No	0.00	Hsu	0	263.33	263.33	0.00	2.78	2.78	162.00	162.00	0.00	11.70	0.20	5.5	6290	0.00
48	-9.35	88.45	9.10	Rc	No	No	0.00	Hsu	0	265.00	265.00	0.00	2.40	2.40	159.00	159.00	0.00	11.70	0.22	5.1	8681	0.00
49	-13.47	88.38	7.00	Rc	No	No	0.00	Hsu	0	263.33	263.33	0.00	2.71	2.71	161.00	161.00	0.00	11.71	0.20	5.5	6290	0.00
50	-9.76	88.29	11.30	Rc	DL	sP	1.20	Hsu	0	264.44	264.44	0.00	2.00	2.00	161.00	161.00	0.00	11.71	0.22	5.1	8681	2.14
51	-14.02	87.88	5.70	Rc	No	No	0.00	Hsu	2	261.67	259.50	2.17	1.13	-1.04	160.00	158.00	2.00	11.74	0.18	6.5	5866	1.74
52	-11.25	87.43	6.10	Sc	No	No	0.00	Hsu	-2	262.22	265.00	-2.78	-0.18	2.60	163.00	161.00	2.00	11.78	0.19	5.7	7365	0.00
53	-10.72	87.29	7.80	Rc	No	No	0.00	Hsu	0	265.00	265.00	0.00	2.29	2.29	161.00	161.00	0.00	11.79	0.20	5.7	8071	0.00
54	-8.81	86.62	4.50	Sc	No	No	0.00	Hsu	0	264.44	264.44	0.00	0.74	0.74	153.00	153.00	0.00	11.84	0.21	5.8	8365	0.00
55	-9.04	86.33	13.40	Rc	SL	FP	0.00	Hsu	-1	263.33	264.44	-1.11	-0.48	0.63	155.00	154.00	1.00	11.86	0.20	5.8	8325	2.22
56	-12.82	86.13	4.50	Rc	No	No	0.00	Hsu	-2	257.50	259.50	-2.00	-4.38	-2.38	157.00	157.00	0.00	11.87	0.18	5.9	6462	2.20
57	-8.86	86.06	6.90	Rc	No	No	0.00	Hsu	0	265.83	265.83	0.00	1.90	1.90	153.00	153.00	0.00	11.88	0.21	5.8	8365	0.00
58	-8.65	84.91	10.10	Sc	No	No	0.00	Hsu	0	267.92	267.92	0.00	3.31	3.31	147.00	147.00	0.00	11.96	0.19	6.3	8146	0.00
59	-14.13	84.10	7.50	Sc	No	No	0.00	Hr	0	260.00	260.00	0.00	-2.20	-2.20	160.00	160.00	0.00	12.03	0.18	7.0	5837	0.00
60	-11.79	84.10	6.00	Rc	No	No	0.00	Hr/Hsu	-1	262.78	263.89	-1.11	-0.53	0.58	160.00	160.00	0.00	12.03	0.20	6.0	7110	1.83
61	-9.60	84.10	5.80	Rc	SL	FP	0.00	Hsu	0	266.25	266.25	0.00	1.71	1.71	155.00	151.00	4.00	12.03	0.19	6.3	7982	2.47
62	-9.32	83.82	7.10	Rc	SL	FP	0.00	Hsu	0	266.67	266.67	0.00	2.04	2.04	153.00	150.00	3.00	12.05	0.21	6.1	7798	1.70
63	-11.96	83.72	4.20	Sc	No	No	0.00	Hr	0	265.00	265.00	0.00	1.60	1.60	160.00	160.00	0.00	12.05	0.20	5.7	7066	0.00
64	-8.84	83.16	5.10	Rc	No	No	0.00	Hsu	0	267.92	267.92	0.00	2.84	2.84	150.00	144.00	6.00	12.10	0.21	6.1	8085	2.37
65	-10.90	83.08	9.00	Rc	No	No	0.00	Hr	0	265.42	265.42	0.00	1.28	1.28	160.00	157.00	3.00	12.10	0.21	5.7	7434	1.96
66	-14.75	82.73	21.20	Rc	SL	Pk	0.00	Hr	0	262.78	262.78	0.00	-0.45	-0.45	155.00	155.00	0.00	12.13	0.18	6.7	5625	1.45
67	-9.77	82.35	8.30	Sc	No	No	0.00	Hsu	0	267.50	267.50	0.00	2.60	2.60	152.00	152.00	0.00	12.16	0.23	6.1	7532	0.00
68	-11.29	82.27	5.00	Rc	No	No	0.00	Hr	-2	265.42	266.67	-1.25	1.25	2.50	157.00	157.00	0.00	12.16	0.22	5.7	7154	0.00
69	-12.66	81.64	14.50	Sc	No	No	0.00	Hr	0	265.00	265.00	0.00	1.13	1.13	156.00	156.00	0.00	12.21	0.22	5.6	6920	0.00
70	-11.30	81.41	15.50	Rc	DL	SY	3.10	Nplr/Hr	0	267.50	267.50	0.00	3.01	3.01	155.00	155.00	0.00	12.23	0.24	5.2	7179	3.12
71	-10.26	81.41	14.80	Rc	SL	FP	0.00	Hr	-1	266.67	267.92	-1.25	1.69	2.94	156.00	156.00	0.00	12.23	0.24	5.2	7046	2.68
72	-10.71	81.14	8.60	Rc	SL	FP	0.00	Hr	-1	267.08	267.92	-0.84	2.01	2.85	157.00	157.00	0.00	12.25	0.24	5.2	7046	3.20
73	-12.45	80.70	18.30	Rc	SL	FP	0.00	Nplr	0	267.50	267.50	0.00	3.34	3.34	160.00	160.00	0.00	12.28	0.23	5.6	7038	3.85
74	-10.01	80.48	10.30	Rc	SL	FP	0.00	Hsu	-3	267.50	268.75	-1.25	2.02	3.27	157.00	157.00	0.00	12.30	0.24	5.2	7026	2.78
75	-10.59	80.34	6.00	Rc	No	No	0.00	Nplr	0	267.92	267.92	0.00	2.64	2.64	159.00	159.00	0.00	12.31	0.24	5.2	7026	1.83
76	-12.25	80.27	18.30	Rc	SL	FP	0.00	Nplr	0	267.92	267.92	0.00	3.39	3.39	158.00	158.00	0.00	12.31	0.23	5.6	7038	2.16
77	-10.08	80.09	5.40	Sc	No	No	0.00	Hsu	0	270.00	270.00	0.00	4.45	4.45	157.00	157.00	0.00	12.32	0.24	5.2	7026	0.00
78	-12.90	80.02	6.40	Rc	No	No	0.00	Nplr	0	265.42	265.42	0.00	1.36	1.36	140.00	140.00	0.00	12.33	0.23	5.6	7038	0.00
79	-12.28	79.80	6.20	Sc	No	No	0.00	Nplr	0	267.50	267.50	0.00	3.10	3.10	159.00	159.00	0.00	12.35	0.22	5.7	7066	0.00
80	-13.25	79.75	4.00	Rc	No	No	0.00	Nplr	0	265.00	265.00	0.00	0.87	0.87	135.00	135.00	0.00	12.35	0.20	5.7	6324	0.00
81	-13.06	79.63	5.20	Rc	No	No	0.00	Nplr	0	265.00	265.00	0.00	0.84	0.84	134.00	134.00	0.00	12.36	0.20	5.7	6324	0.00
82	-13.56	79.13	4.50	Rc	No	No	0.00	Nplr	0	266.25	266.25	0.00	2.22	2.22	141.00	141.00	0.00	12.40	0.20	5.7	6324	0.00
83	-13.40	78.21	8.90	Sc	No	No	0.00	Nplr	0	267.08	267.08	0.00	2.81	2.81	140.00	140.00	0.00	12.47	0.20	5.7	5806	0.00
84	-12.40	78.19	4.70	Sc	No	No	0.00	Nplr	0	268.75	268.75	0.00	3.93	3.93	138.00	138.00	0.00	12.47	0.19	5.7	6733	0.00
85	-13.10	78.05	10.70	Rc	SL	Pk	0.00	Nplr	0	267.08	267.08	0.00	2.50	2.50	134.00	134.00	0.00	12.48	0.20	5.7	5806	1.85
86	-11.33	77.97	6.50	Sc	No	No	0.00	Nplr/Hr	0	268.75	268.75	0.00	3.38	3.38	141.00	141.00	0.00	12.48	0.21	6.6	6977	0.00
87	-10.29	77.82	9.90	Sc	No	No	0.00	Hsu	0	268.75	268.75	0.00	2.85	2.85	128.00	128.00	0.00	12.49	0.21	6.6	7449	0.00
88	-13.07	77.28	11.10	Rc	SL	Pk	0.00	Nplr	0	265.83	265.83	0.00	1.11	1.11	134.00	134.00	0.00	12.53	0.18	6.1	5629	1.78
89	-12.11	76.76	11.60	Rc	SL	Pk	0.00	Nplr/Hr	2	267.50	266.67	0.83	2.16	1.33	142.00	142.00	0.00	12.57	0.19	6.1	6325	2.28
90	-10.95	76.72	10.30	Rc	SL	Pk	0.00	Hr	0	267.50	267.50	0.00	1.63	1.63	144.00	144.00	0.00	12.58	0.22	6.6	7313	1.92
91	-13.71	76.55	5.20	Sc	No	No	0.00	Nplr	0	266.67	266.67	0.00	2.09	2.09	137.00	137.00	0.00	12.59	0.19	6.1	5690	0.00

Table 3.1. continued.

ID	LAT	LON	DIA	TYP	EJE	INT	PTDI	UNIT	TFR	EJET	SURT	DELT	ETDS	STDS	EVIS	SVIS	DELV	TOD	ALB	INER	TOPO	RATIO
92	-14.06	76.50	30.00	Rc	SL	sP	5.40	Nplr	0	266.25	266.25	0.00	1.95	1.95	136.00	136.00	0.00	12.59	0.18	6.6	5001	0.00
93	-12.78	75.88	8.60	Rc	No	No	0.00	Nplr/Hr	0	266.67	266.67	0.00	1.70	1.70	138.00	138.00	0.00	12.64	0.18	7.2	6223	2.05
94	-10.87	75.88	7.60	Rc	SL	FP	0.00	Hr	0	266.67	266.67	0.00	0.67	0.67	136.00	136.00	0.00	12.64	0.19	8.0	7181	2.03
95	-13.26	75.75	17.50	Rc	SL	SY	3.10	Nplr/Hr	0	264.44	264.44	0.00	-0.27	-0.27	136.00	136.00	0.00	12.65	0.18	7.2	5415	3.52
96	-9.50	75.50	9.10	Dc	No	No	0.00	Hvl	0	269.17	269.17	0.00	2.39	2.39	111.00	111.00	0.00	12.67	0.21	7.6	6652	0.00
97	-12.24	75.30	4.20	Sc	No	No	0.00	Hr	0	267.08	267.08	0.00	1.49	1.49	120.00	120.00	0.00	12.68	0.18	7.2	6223	0.00
98	-13.86	75.11	4.70	Rc	No	No	0.00	Hr	0	265.00	265.00	0.00	0.45	0.45	131.00	131.00	0.00	12.70	0.18	7.2	5415	1.64
99	-12.81	74.90	9.30	Rc	No	No	0.00	Hf	0	267.08	267.08	0.00	1.95	1.95	121.00	121.00	0.00	12.71	0.16	7.2	6085	2.01
100	-9.62	74.66	5.70	Rc	No	No	0.00	Avm	-1	268.75	270.91	-2.16	1.83	3.99	106.00	106.00	0.00	12.73	0.23	7.6	3308	1.93
101	-13.48	74.39	7.20	Rc	No	No	0.00	Hf	2	266.67	265.00	1.67	1.73	0.06	124.00	124.00	0.00	12.75	0.19	7.2	5246	1.99
102	-13.61	73.11	4.80	Sc	No	No	0.00	Hf	0	266.25	266.25	0.00	1.19	1.19	123.00	123.00	0.00	12.85	0.19	7.4	5179	0.00
103	-14.44	69.96	17.20	Rc	ML	FP	0.00	Hf/Hr	1	267.08	265.83	1.25	1.57	0.32	113.00	113.00	0.00	13.08	0.17	6.7	5344	4.22
104	-8.30	69.96	9.60	Sc	No	No	0.00	Hf	0	269.58	269.58	0.00	1.91	1.91	175.00	175.00	0.00	13.08	0.26	7.6	1295	0.00
105	-14.23	69.60	6.50	Rc	No	No	0.00	Hf/Hr	0	267.92	267.92	0.00	2.97	2.97	114.00	114.00	0.00	13.11	0.17	6.7	5344	0.00
106	-14.94	69.42	8.40	Rc	SL	FP	0.00	Hf/Hr	-1	266.25	267.08	-0.83	1.88	2.71	128.00	125.00	3.00	13.12	0.17	6.7	5344	2.10
107	-8.68	68.61	6.40	Rc	SL	Pk	0.00	Hf	0	268.33	268.33	0.00	0.67	0.67	166.00	166.00	0.00	13.18	0.26	7.6	4480	0.00
108	-14.98	68.23	12.00	Rc	DL	Pk	0.00	Hr	0	266.67	266.67	0.00	2.29	2.29	135.00	135.00	0.00	13.21	0.19	6.7	5572	2.02
109	-9.19	67.63	6.00	Sc	No	No	0.00	Hf	0	268.33	268.33	0.00	0.89	0.89	170.00	170.00	0.00	13.26	0.25	7.4	-195	0.00
110	-9.03	67.53	4.40	Sc	No	No	0.00	Hf	0	268.33	268.33	0.00	0.89	0.89	165.00	165.00	0.00	13.26	0.25	7.4	-195	0.00

Parameters are defined as follows: ID, arbitrary identification number; LAT, latitude; LON, west longitude; DIA, crater diameter (km); TYP, preservational state and general type of ejecta (Rc, lobate ejecta morphology; Sc, no discernible ejecta blanket; Dc, no discernible ejecta and crater almost completely obliterated, rim barely visible); EJE, ejecta morphology (SL, single lobe; DL, double lobe; ML, multiple lobe; No, no classification); INT, interior morphology (Pk, central peak; FP, flat floor pristine; SY, symmetric central pit; sP, central peak topped by small pit; No, no classification); PTDI, central pit diameter (km), 0.00 if no pit; UNIT, geologic map unit, from *Witbeck et al.* [1991] and *Scott and Tanaka* [1986] with some interpolation between the two; multiple units are listed for craters occurring on or near unit boundaries; unit names and descriptions are listed in Table 2; TFR, "thermal freshness", qualitative thermal distinctiveness compared to surroundings (0, not thermally distinct; 3, very distinctive and warmer; -3, very distinctive and cooler); EJET, representative average brightness temperature (K) for ejecta; SURT, same but for surroundings; DELT, EJET - SURT; ETDS, approximate time of day corrected temperature for ejecta = EJET - model temperature (see text); STDS, same but for surroundings; EVIS, representative average visible signal (*dn*) for ejecta; SVIS, same but for surroundings; DELV, EVIS - SVIS; TOD, local time of day; ALB, 1° x 1° binned albedo from *Pleskot and Miner* [1981]; INER, 2° x 2° binned thermal inertia (10^{-3} cal cm^{-2} K^{-1} $s^{-1/2}$) from *Palluconi and Kieffer* [1981]; TOPO, elevation (m) from *U.S. Geological Survey* [1976]; RATIO, ratio of ejecta diameter to crater diameter. Parameters ID, LAT, LON, DIA, TYP, EJE, INT, and PTDI are from N. G. Barlow, submitted report, 1987.

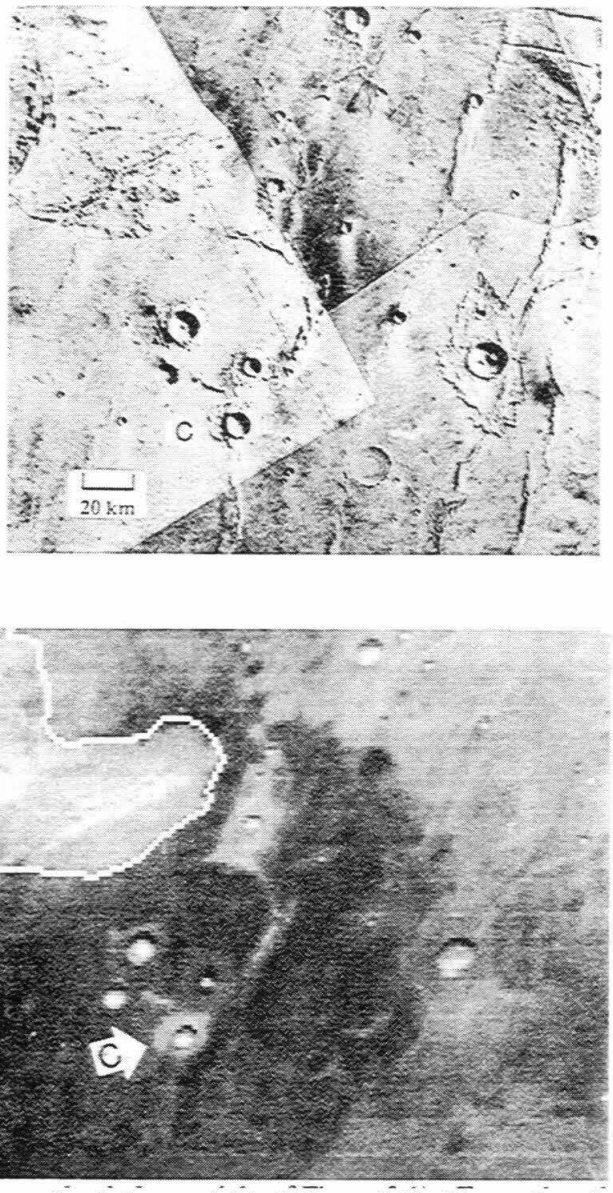

Figure 3.4. Region 1 (seen also in lower right of Figure 3.1): Termoskan thermal image (bottom) and Viking visible photomosaic (top) of an interesting local region of study with four craters near the south rim of an old filled crater, and three craters to the northeast of the old crater. The craters seen outside the old filled crater exhibit ejecta blankets that are significantly warmer than the surroundings. These all are from the group of craters observed which have darker albedo than the surroundings. The craters inside the old filled crater have ejecta blankets which are much cooler than ejecta blankets outside the old filled crater, but still warmer than their surroundings. The only "ejecta blanket" that shows no temperature difference with the surroundings (the southwest crater) is the only crater for which no ejecta blanket can be seen in Viking images. Surviving portions of the old crater rim are also darker in the visible channel and warmer than the surrounding terrain. Also note that the southeast portion of the Noachian plateau ridged unit (Nplr), which appears to the northwest of the old filled crater, is also darker in the visible channel and warmer than surrounding areas. Crater C is an excellent example of thermal boundaries matching ejecta boundaries. The wide thermal anomaly associated with the crater just NE of the large filled crater is a counterexample.

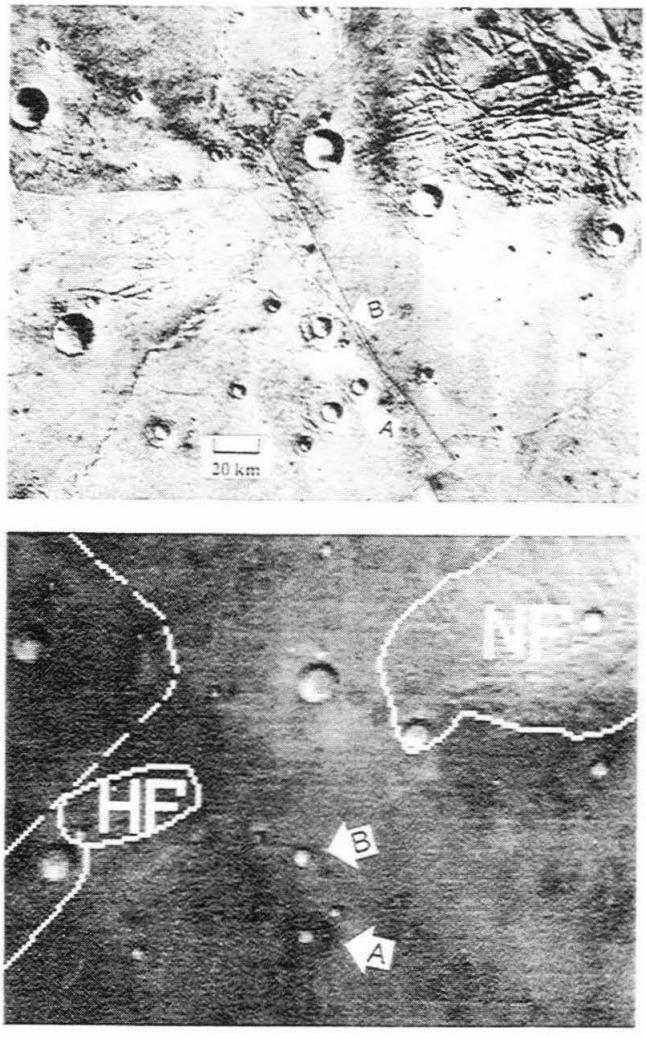

Fig. 3.5. Region 2 (seen also in lower middle of Figure 3.1): Termoskan thermal image (bottom) and Viking visible photomosaic (top) of several nearby craters, one with a thermally distinct ejecta blanket and the others without. In particular, notice the two largest craters, crater A and crater B. Crater A is thermally distinct; crater B is not. They have similar fresh appearing single lobe fluidized ejecta blankets (N. G. Barlow, submitted report, 1987). Both craters are on the Hesperian ridged plains unit (Hr). Crater A (18.54°S, 81.98°W; #11 in Table 3.1) has a very thermally distinct ejecta blanket which is approximately 3.5 K warmer than its surroundings. It has a diameter of 11.6 km and a flat floor pristine interior (N. G. Barlow, submitted report, 1987). It is also distinct in the visible channel, being brighter than its surroundings. Crater B (17.85°S, 82.07°W; 12 in Table 3.1) does not have a thermally distinct ejecta blanket. It has a diameter of 8.6 km and a central peak (Pk) interior morphology. In the visible channel its ejecta blanket is not very distinct, if at all, from the surroundings. There are many smaller craters nearby and none of them appear thermally distinct.

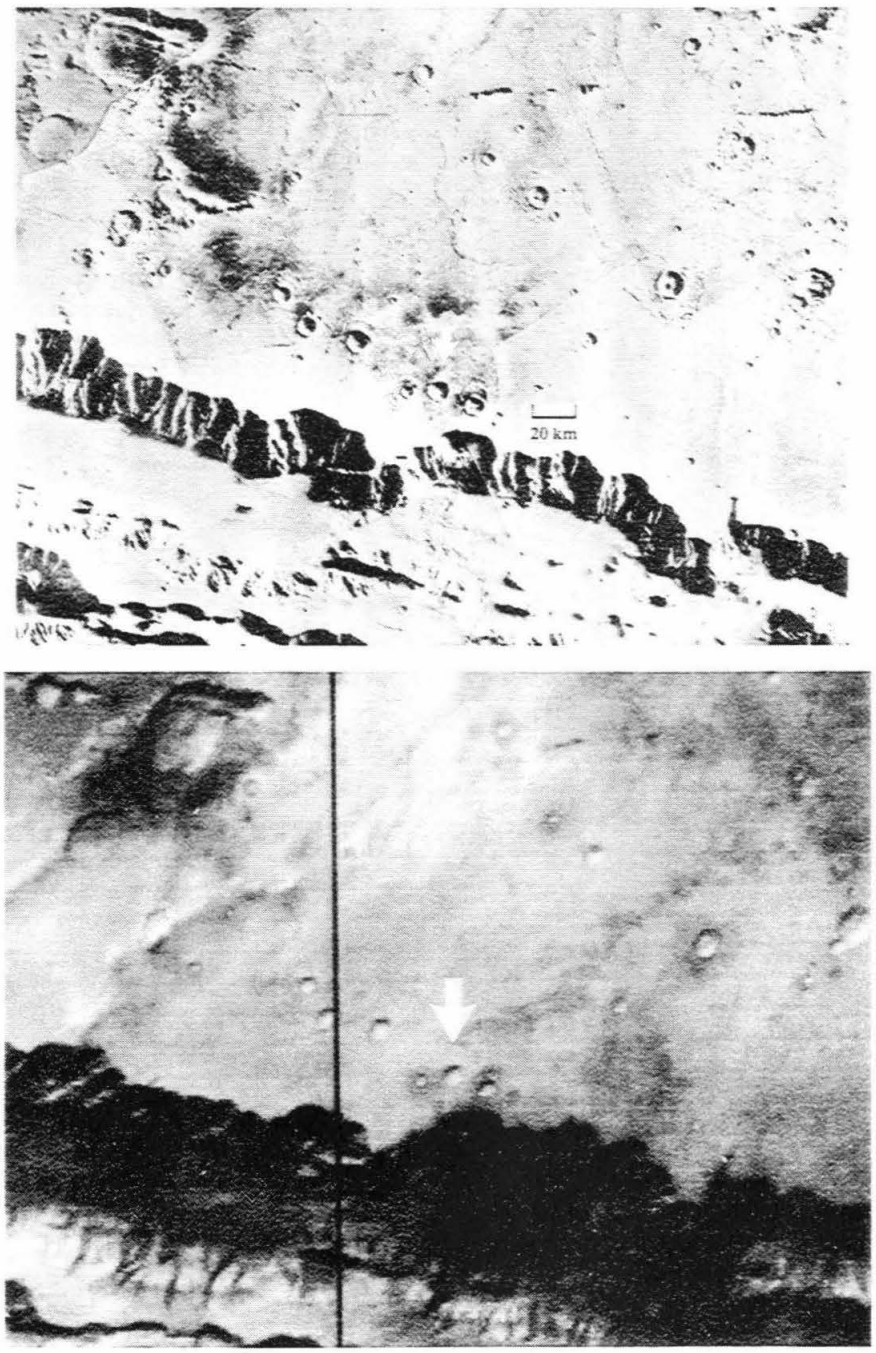

Fig. 3.6. Region 3: Termoskan thermal image (bottom) and Viking visible photomosaic (top) of three nearby almost aligned craters near the north rim of Valles Marineris (diameters 5.8 km, 10.5 km, and 9.8 km). They are centered approximately on 12.5°S, 59.3°W. All three craters have single lobe ejecta morphologies. All occur on the Hpl_3 unit near a boundary with the Hr (Hesperian ridged plains) unit as determined by *Witbeck et al.* [1991]. The largest (middle) crater is the only one of the three that does not have an EDITH. It also has the least fresh ejecta blanket based upon Viking images.

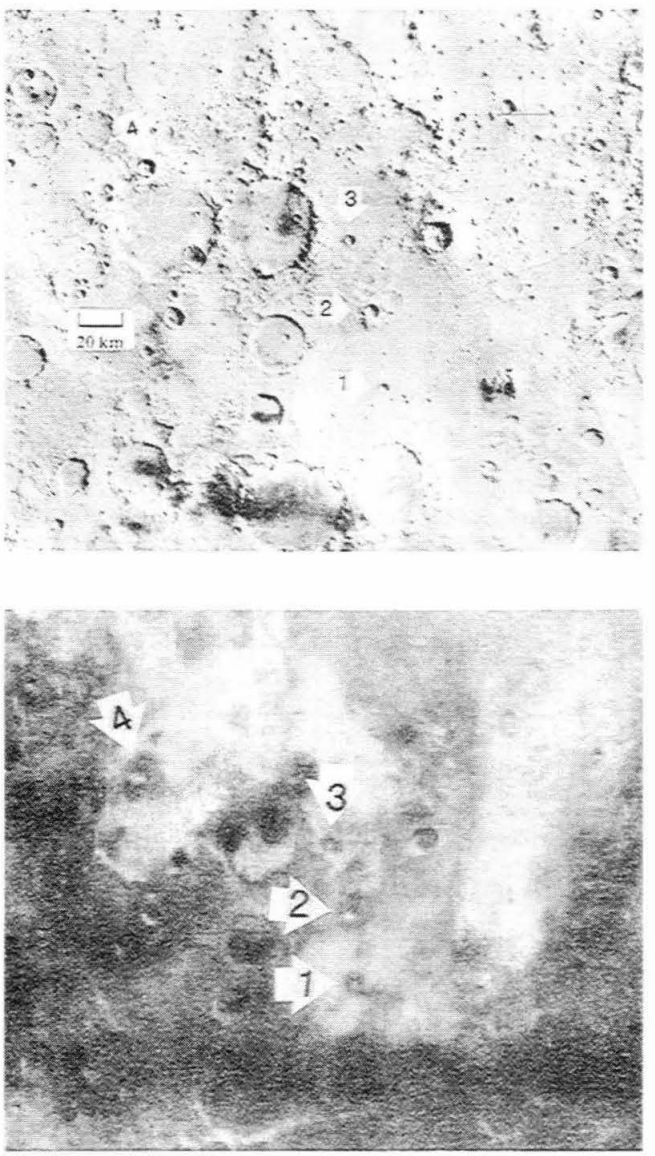

Fig. 3.7. Region 4: Termoskan thermal image (bottom) and Viking visible photomosaic (top) that include the four clearly distinct EDITHs (designated by arrows) of panorama 4. The four EDITHs are approximately centered upon 11.5°S, 197.0°W and are spaced over approximately 150 km. Older highland materials appear to the south (bottom), and younger lowland material to the north. EDITHs all lie near the boundary on lowland terrains (1 and 2 on Hpl_3, 3 on either Hpl_3 or Apk, 4 on Apk, using *Greeley and Guest* [1987]). Notice also the exposed crater rim of a buried crater near EDITH 2 (see text).

the surroundings. To remove the time of day effects to first order, I used a one-dimensional, homogeneous, thermal model of the Mars surface adapted from *Clifford et al.* [1987]. From each ejecta blanket temperature, I subtracted model-derived temperatures for average Mars conditions (inertia 6.5 x 10^{-3} cal cm^{-2} K^{-1} $s^{-1/2}$ and albedo 0.25) for the same time of day, season, and latitude. For comparison, I similarly subtracted model temperatures from surrounding temperatures (STDS). I looked for correlations between each of the three thermal ejecta parameters (TFR, DELT, and ETDS) and the other parameters in my data base.

My three descriptive thermal ejecta parameters showed no correlation with most of the parameters tested. Within the data base as a whole, there are no correlations between temperature difference, time of day corrected ejecta temperature, or thermal freshness with any of the following: crater diameter, ejecta morphology, interior morphology, existence of central pits, longitude, ratio of ejecta diameter to crater diameter, or time of day. The 1° x 1° binned albedo, 2° x 2° binned inertia, and 1° x 1° binned elevation roughly correlate with time of day corrected ejecta temperature on the higher elevation Hsu (Syria Planum Formation, Upper Member) areas but not elsewhere (see Table 3.2 for unit descriptions). These relationships unique to Hsu are discussed below under section 4.

I present the following conclusions and observations based upon my systematic examination of individual EDITHs in the Termoskan data set.

1. On the plains where EDITHs occur, there cannot be uniform blanketing of depth greater than a very few centimeters (the diurnal skin depth) by material younger than the craters. Otherwise, ejecta blankets would not be thermally distinct.

2. In regions with EDITHs there are varying degrees of ejecta blanket degradation at Viking Orbiter camera resolutions. Because there has not been significant blanketing in these regions (based upon conclusion #1), this degradation is probably due to erosion, not deposition.

3. Some thermally distinct ejecta blankets appear distinct in the visible channel as well, implying albedo differences and probable surface compositional differences with the surroundings. Many EDITHs are not visibly distinct, however, leaving textural differences (thermal inertia) as the cause.

4. The thermally distinct nature of EDITHs must be due to the primary ejecta formation process. Two related observations lead us to this conclusion. First, many thermally distinct areas are associated with areas surrounding craters. Second, many of the boundaries of these thermally distinct areas closely follow the termini of ejecta blankets. The dependence of the thermally distinct nature of EDITHs upon the primary ejecta formation process may be direct or indirect. Direct influence would result from either compositional or textural effects of the ejecta material itself. An example of indirect influence would be preferential secondary deposition of low-inertia material on the blankets due to increased roughness.

5. EDITHs are therefore strongly coupled with surface morphology, including those EDITHs that have different thermal inertia than their surroundings. This is significant because most sharp thermal inertia contrasts on Mars are decoupled from morphology.

6. Presence of ejecta blankets alone does not imply the presence of EDITHs. There are many visibly discernible ejecta blankets on Noachian, Hesperian, and Amazonian aged units that do not have EDITHs. At Viking camera resolutions, there are non-EDITH craters that look like EDITH craters. Also, they cover similar size ranges. Furthermore, existence of a lobate ejecta blanket does not imply the existence of an EDITH (only 50 percent of the lobate ejecta blankets on Hesperian terrains are thermally distinct). However, lobate morphology may be required for EDITHs. I cannot yet confirm this because of the absence of any other distinctive ejecta morphology on terrains where EDITHs were observed. Nevertheless, all EDITHs associated with discernible ejecta blankets are associated with fluidized, lobate ejecta blankets. Of the craters classified by

N. G. Barlow (Catalog of large Martian impact craters, submitted as *NASA Contractor Report*, 1987; hereinafter referred to as submitted report, 1987) as having non-discernible ejecta blankets, 30 percent have thermally distinct "ejecta blankets." Thus, these ejecta may or may not show lobate morphologies at higher resolution, and/or they may be partially eroded.

7. The absence of correlations between any of my three temperature parameters and ejecta morphology (single, double, or multiple lobes) implies that any physical differences between different fluidized ejecta morphologies are not capable of causing consistent thermal differences.

3.4 Terrain Dependencies

Virtually all of the more than 100 EDITHs seen in the Termoskan data are located on Hesperian age plains that surround much of Valles Marineris. This region was observed in the third of the four Termoskan panoramas with a resolution of about 1.8 km/pixel. The other three panoramas primarily observed very old (Noachian age) intercrater plains and cratered highland units. Figure 3.8 shows the coverage of each of the panoramas overlain on a simplified low-resolution geologic map of Mars.

There is a startlingly clear correlation of EDITH existence with terrains of Hesperian age, implying spatial or temporal dependence on Hesperian terrains. This is the strongest correlation between EDITHs and any other parameter. EDITHs are present on all the Hesperian age units observed by Termoskan. As exemplified by Figure 3.1, almost no EDITHs are associated with any of the thousands of craters within the data set that occur on the older Noachian units, except five EDITHs clustered near a high contrast albedo boundary in Sinus Meridiani. These five may be the consequence of a very distinctive localized aeolian albedo effect, probably unlike most other EDITHs. Thermally distinct ejecta blankets do not appear on the portions of the younger Tharsis Amazonian units seen in the data. Only four clear thermally distinct ejecta blankets are seen in

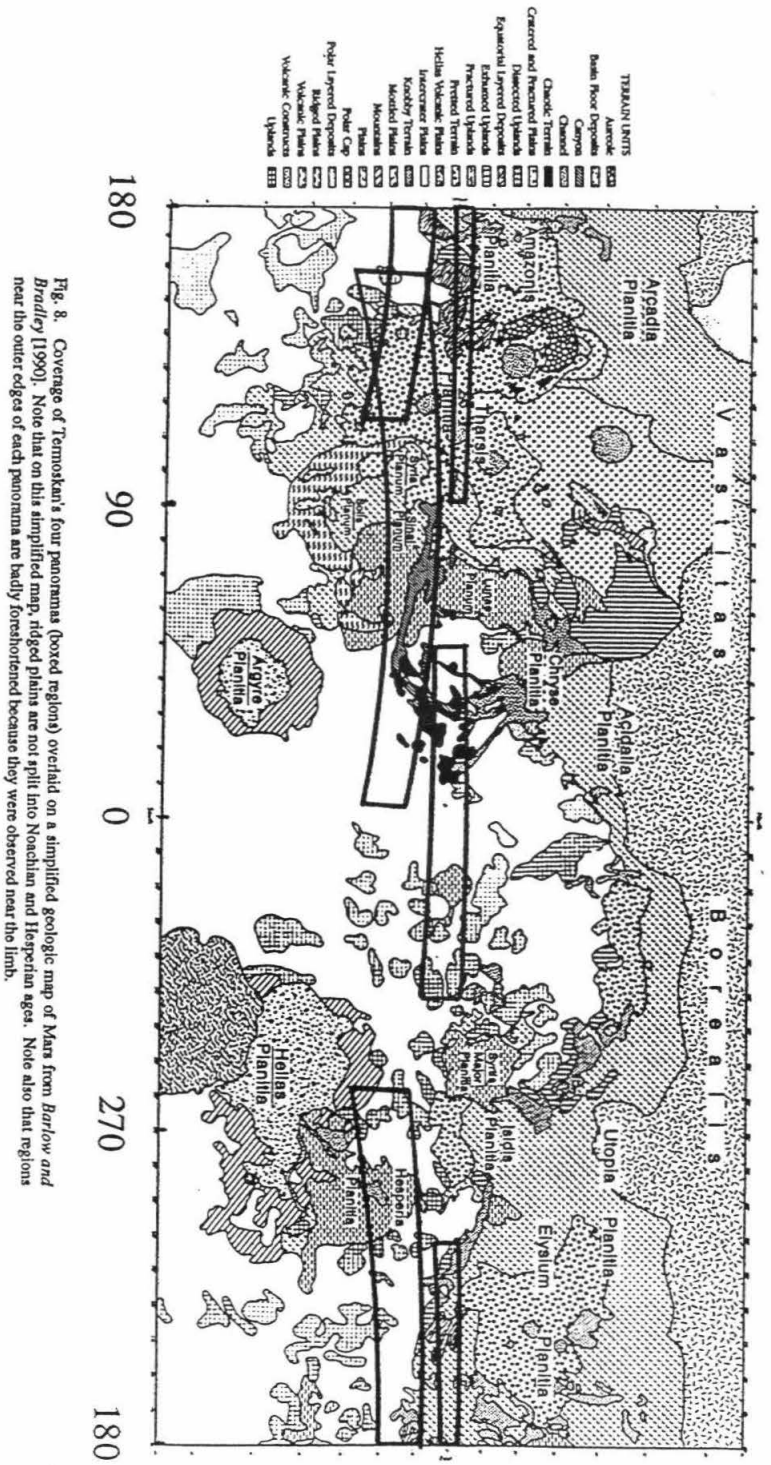

Fig. 8. Coverage of Termoskan's four panoramas (boxed regions) overlaid on a simplified geologic map of Mars from *Barlow and Bradley* [1990]. Note that on this simplified map, ridged plains are not split into Noachian and Hesperian ages. Note also that regions near the outer edges of each panorama are badly foreshortened because they were observed near the limb.

Fig. 3.8. Coverage of Termoskan's four panoramas (boxed regions) overlaid on a simplified geologic map of Mars from *Barlow and Bradley* [1990]. Note that on this simplified map, ridged plains are not split into Noachian and Hesperian ages. Note also that regions near the outer edges of each panorama are badly foreshortened because they were observed near the limb.

panorama 4, and these occur on Hesperian to Amazonian age lowland material near the highland-lowland boundary (see region 4 in section 6). They also occur infrequently and weakly on Amazonian units within Valles Marineris.

Although more subtle than the Hesperian terrain dependence, there are also terrain dependent correlations on the relatively high elevation Hesperian Syria Planum Upper Member (Hsu) unit, but not on the adjacent Hesperian ridged (Hr) unit. These are the two primary EDITH bearing terrains within my data base. Correlations and observations of EDITHs that occur on Hsu but not on Hr include the following. (1) All EDITHs on Hsu, with one exception, have ejecta blankets that are cooler than the surroundings. (2) Time of day corrected ejecta temperature shows strong correlation with time of day corrected temperature of the surroundings. The temperature difference (ejecta - surroundings) of the Hsu craters varies little (in general less than 2 K) even when the absolute temperatures of the surroundings change significantly (approximately 10 K). Therefore, ejecta temperature has a consistent dependence upon the surrounding temperature. (3) Time of

TABLE 3.2. Description of Geologic Map Units

Unit	Name and Interpretation
Apk	Knobby plains material-Probably of diverse origins but appears to have formed mainly by erosion of older units. Knobs are probably erosional remnants but some may be volcanic. Intervening plains may be erosional surfaces or may consist of eolian, mass-wasted, or volcanic materials.
Hsu	Syria Planum formation, Upper member-Lava flows of Syria Planum; erupted from summit area of Syria Planum and from local fractures.
Hsl	Syria Planum formation, Lower member-Similar to upper member but more highly cratered and faulted.
Hpl_3	Plateau sequence, Smooth unit-Probably a complex of eolian, volcanic and alluvial materials.
Hf	Highly deformed terrain materials, Younger fractured material-Probably lava flows. Faults caused by crustal extension; collapse depressions formed by withdrawal of subsurface water or ice. Modified ridged plains material at Nia Fossae (Note: Nia Fossae is the part of this unit that has EDITHs and includes the portion shown in Fig. 1.)
Hr	Ridged plains material-Low-viscosity lava flows; source fissures possibly buried. Ridges may be tectonic or volcanic features.
Npl_2	Plateau sequence, Subdued cratered unit-Dominantly lava flows and eolian material; in "Ladon basin" possibly flood plain deposits from Ladon Valles.
Nf	Highly deformed terrain materials, Older fractured material-Probably impact breccia and volcanic materials.
Nplr	Plateau sequence, Ridged unit-Lava flows erupted from local fractures; ridged produced by volcanic and tectonic processes.
Npl_1	Plateau sequence, Cratered unit-Volcanic materials and impact breccia emplaced during heavy impact bombardment; channels of probable fluvial origin.

Units listed approximately from youngest to oldest, although some are contemporaneous. First letter unit designations imply time-stratigraphic system: A, Amazonian; H, Hesperian; N, Noachian. All units were established by *Scott and Tanaka* [1986] and all interpretations by *Witbeck et al.* [1991] except for Apk unit and interpretation by *Greeley and Guest* [1987].

day corrected ejecta temperature and time of day corrected temperature of the surroundings show some correlations with elevation and latitude. These correlations occur because elevation and latitude in the data base region correlate with inertia, albedo, and each other. Inertias decrease and albedos increase with higher elevation on Hsu, causing higher midday temperatures.

I believe that these correlations, which appear on Hsu but not on Hr, arise from increased dust mantling on the higher elevation Hsu unit, rather than from a bedrock geologic unit variation. Increased dust mantling is consistent with the lower inertias and higher albedos of the Hsu unit. Inertia ranges from 5 to 6 above 6500 m (elevations that occur primarily on Hsu and range up to 9000 m) and from 6 to 8.5 below 6500 m. The Hsu area is near the edge of the Tharsis low inertia region which has been proposed to have a dust covering and to be an area of dust deposition [*Kieffer et al.*, 1977; *Zimbelman and Kieffer*, 1979; *Palluconi and Kieffer*, 1981; *Christensen*, 1986], but still an area with some exposed rocks [*Christensen*, 1982, 1983]. The high elevation regions within my data base have higher inertia (5 as opposed to 2 or 3 in units of 10^{-3} cal cm^{-2} K^{-1} $s^{1/2}$) than Tharsis; however, the Hsu albedo and inertia still probably imply at least some dust mantling, and more than elsewhere within the data base. It would be difficult for an ejecta related mechanism, either primary or secondary, to cause higher brightness temperatures than already occur on this dust mantled region. An increased thickness of dust mantle on both ejecta and surroundings also would help explain the observed reduced temperature difference between surroundings and ejecta. The ejecta still appear thermally distinct either because of differences in the blocks poking through the dust layer or thermal differences showing through a thin dust layer.

3.5 A Layering Explanation

I postulate that most of the observed EDITHs are due to excavation of thermally distinctive Noachian age material from beneath a relatively thin layer of younger, more

consolidated Hesperian volcanic material. The plausibility of this theory is supported by much geological evidence for the EDITH-rich plains units having relatively thin near-surface Hesperian deposits overlying massive Noachian megabreccias. I suggest that absence of thermally distinct ejecta blankets on Noachian and Amazonian terrains is due to absences of distinctive near-surface layering.

Layering is in general important to determining ejecta blanket characteristics [*Oberbeck and Quaide*, 1968; *Head*, 1976; *De Hon*, 1980; *Pike*, 1980; *Greeley et al.*, 1982; *Horner and Greeley*, 1987; *Barlow and Bradley*, 1990], and thus it would not be surprising if it were also involved with EDITHs. The simplest form of my layering explanation is a two-layer model (see Figure 3.9*a*). The top layer (layer 1) is a relatively thin (hundreds of meters) Hesperian age unit consisting primarily of lavas which were probably emplaced as a series of low-viscosity flows. The lower layer (layer 2) is a massive Noachian layer believed to consist of impact breccia.

The majority of EDITHs observed occur on the layered Hesperian plains surrounding Valles Marineris. Indeed, layering in the walls of Valles Marineris, observable in Viking camera images and now also in Termoskan thermal images, is a first-order observation of layering in this region. In addition, the geologic plausibility of my layered model is supported by many lines of evidence in this region for very few hundred meter thick [*De Hon*, 1985; *Frey and Grant*, 1989; *Frey and Grant*, 1990] Hesperian lavas overlying a mechanically weak, Noachian megaregolith layer (my layer 2) [*Tanaka and Chapman*, 1992; *Davis and Golombek*, 1990; *Robinson and Tanaka*, 1988; *MacKinnon and Tanaka*, 1989]. An approximate megaregolith thickness of 2 to 3 km is suggested [*Fanale*, 1976; *Woronow*, 1988; *MacKinnon and Tanaka*, 1989; *Soderblom and Wenner*, 1978; *Davis and Golombek*, 1990]. *Horner and Greeley* [1987] used a two-layer model very similar to ours in this region to explain the increase in crater complexity with decreasing thickness of the Hr unit. They proposed that some property of the lower layer (e.g., increased fracturing during impact or increased volatile content) caused the

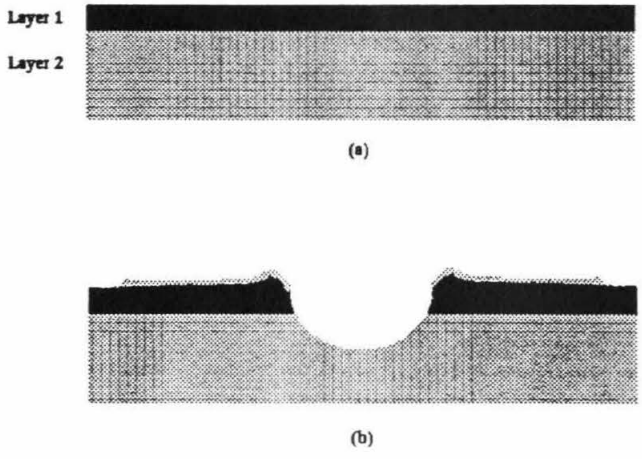

Fig. 3.9. (*a*) Schematic of my layering model before impact. Layer 1 is a relatively thin layer of consolidated Hesperian lavas. Layer 2 is comprised of massive Noachian megabreccia. (*b*) Postimpact view of a fluidized lobate EDITH. Vertical relief of the ejecta blanket is exaggerated. Note the layer 2 material through ballistic ejection and fluidized flow has covered most of the layer 1 ejecta material and contrasts thermally with the layer 1 surroundings.

greater complexity. Likewise, I propose that some physical property of my lower layer causes thermally distinct ejecta blankets.

How does material from layer 2 end up on the surface of an ejecta blanket? Ballistic ejection will invert stratigraphy near the rim of the crater [*Roddy*, 1977; *Stoffler et al.*, 1975] and cover most of the blanket further out with shallow derived material [*Horz et al.*, 1983]. Thus, a sufficiently large impact will cause layer 2 material to overlie layer 1 material near the rim of the crater. Preliminary modeling (B. Ivanov, personal communication, 1992) of fluidized ejecta blanket emplacement on Mars suggests that the layer 2 material may then flow over much of the rest of the ejecta blanket (see Figure 3.9*b*).

EDITHs may directly be the result of inertia and/or albedo differences between layer 2 ejecta material and the surrounding layer 1 material. For example, either pumicelike blocks or very fragmented material from layer 2 could cause the ejecta blanket to have a lower inertia than the layer 1 surroundings. Alternatively, current thermal differences may result from secondary processes such as aeolian deposition or some kind of alteration preferentially acting upon the layer 2 surface. These processes may alter thermal inertia or albedo. In any case, I propose that some property of the layer 2 (Noachian) material causes the eventual thermal contrast with the layer 1 (Hesperian) surroundings.

I attribute the absence of EDITHs on the majority of Noachian and Amazonian terrains to a lack of distinctive near surface layering. Noachian terrains would have layer 2 type material on the surface before a given impact. Thus, the impact would eject material that is sufficiently similar to the surroundings that over time they will be thermally indistinguishable.

The observed absence of EDITHs on the majority of Amazonian units is probably due to the thickness of the terrains which happened to be observed. Most of the Amazonian units observed by Termoskan are central Tharsis volcanics in the Arsia Mons

region. Assuming at least a 2 to 3 km thickness for this region [*Plescia and Saunders*, 1980], the small-diameter Amazonian crater population probably would not have excavated any of the material (possible megaregolith) underlying the Tharsis lavas. Instead these impacts likely excavated only lava materially, physically, and thermally similar to the lava already at the surface.

I note that more than two layers may sometimes play a role in EDITH formation, particularly albedo layers, as hinted at by the occurrence of different albedo layers in some Kasei Valles locations [*Baker and Milton*, 1974; *Scott*, 1991], although not in others [*Tanaka and Chapman*, 1992]. In any case, I find that a layering hypothesis is geologically plausible and explains the vast majority of EDITHs (though a few percent require more complex explanations). In the next section I evaluate some localized regions in light of this theory.

3.6 Interpretation of Localized Regions of Study

I studied four localized regions in greater detail. Figure 3.4 shows and describes region 1, which includes four craters near the south rim of an old filled crater and three craters to the northeast of the old crater. The following explanation of the thermal observations is consistent with my overall layering theory. Impacts outside the larger filled crater formed ejecta blanket surfaces from (layer 2) Noachian material that originated in undisturbed layers beneath a thin layer of Hesperian cover. Due to a presumably thicker Hesperian layer filling the old crater, the impacts inside the old crater rim ejected less of the layer 2 material. Thus, these ejecta blankets are cooler than the blankets outside the old rim, but still distinct and warmer than their surroundings. In this interpretation, the layer 2 material has lower albedo. The old crater rim material and the Noachian material to the northwest may be made of the same layer 2 material.

For this region alone, I could not rule out an alternate theory of preferential trapping of secondary aeolian material due to localized roughness. Darker aeolian

material could have been preferentially trapped by the ejecta blankets, crater rim, and Noachian material due to increased roughness. The blankets inside the crater rim may be different because less of the material that is being preferentially trapped by the rim makes it past the rim. Alternatively, the blankets inside the old rim may have a different degree of roughness than those outside the crater rim. Roughness differences could, however, primarily depend on the excavation of a different lower layer. Preexisting or impact induced roughness may also have caused the wide thermal anomaly associated with the crater to the NE of the large filled crater; however, the exact cause of the extent of this anomaly remains unclear.

My second localized region of study includes several nearby craters, one with a thermally distinct ejecta blanket and the other seven without. Of particular interest are the two largest nearby craters. The larger has thermally distinct ejecta (labeled crater A in Figure 3.5), the other does not (crater B in Figure 3.5). Degree of freshness does not seem to explain the thermal differences. I infer that the largest crater (11.6 km) was the only one in this region that excavated deep enough to reach a physically different layer beneath the Hesperian surface layer. The juxtaposition of these and other similar EDITH/non-EDITH crater pairs (see also region 3 below) implies that neither local wind patterns nor local availability of aeolian material is sufficient on their own to explain EDITH observations.

My third localized region of study (Figure 3.6) is an area on the north rim of Valles Marineris where there are three nearby craters of roughly similar sizes (9.8 km, 10.5 km, and 5.8 km). The largest and "middle" crater is the only one of the three that does not have a thermally distinct ejecta blanket. Thus, excavation of a single lower layer is not alone a sufficient explanation. The middle crater shows the least fresh (presumably oldest) ejecta blanket. Erosional or depositional effects probably removed any thermal distinctiveness.

My fourth region of study involves the only four clear EDITHs in panorama 4 (see Figure 3.7). All of the EDITHs lie on lowland terrains very near the highland-lowland boundary. Two EDITHs (labeled 1 and 2) are situated on a small exposure of Hpl_3, a smooth Hesperian unit (see Table 3.2 for unit descriptions). Based upon exposed rims of buried craters, this unit is thin (a very few hundreds of meters). It is embayed primarily by older Noachian (highland) material (unit Npl_1), implying that the thin Hesperian layering overlies the Noachian unit. Craters 3 and 4 lie on Hesperian and Amazonian terrain near the boundary with the Npl_1 unit. Thus, these four EDITHs are consistent with my layering theory, excavating materially different Noachian material from beneath a thin younger (Hesperian or Amazonian) cover. EDITHs are not observed further from the highland-lowland boundary presumably because of an increasing thickness of Amazonian deposits. Note that EDITH number 4 is somewhat anomalous relative to most EDITHs. Most EDITHs that are cooler than surroundings are visibly brighter or not visibly distinct. In contrast, EDITH number 4 is both cooler and visibly darker than the surroundings. Thus (because of the near midday conditions) this EDITH definitely has a higher inertia than the surroundings.

3.7 Alternate EDITH Hypotheses

Next, I critique several alternatives to my layering theory and show that most of them are unable to explain adequately the presence of EDITHs.

The Hesperian terrain dependence of EDITHs cannot be explained by either atmospheric or impactor conditions. Noachian and Hesperian terrains must have experienced identical atmospheric and impactor conditions during Hesperian times. In addition, the absence of correlations with elevation within the entire data base suggests that EDITH variations are not the result of elevation dependent atmospheric pressure variations. EDITHs must therefore be dependent upon target material and/or distinctive secondary modification of Hesperian terrains.

One possible significant target material property is variation in volatiles. Subsurface volatiles are thought to influence formation of lobate ejecta blankets. The Noachian terrains in my study region near Valles Marineris exhibit similar percentages and morphologies of lobate blankets as the Hesperian units. Also, lobate blankets appear on many of the Noachian terrains seen elsewhere within the Termoskan data. Thus, neither the presence nor the variability of lobate blankets explains the Hesperian EDITH correlation. The ratio of ejecta diameter to crater diameter is thought by several authors to be a measure of the amount of volatiles in the original target material [e.g., *Mouginis-Mark*, 1979; *Kuzmin et al.*, 1988]. Thus, the absence of correlations with this ratio may indicate that neither the degree of fluidization, nor the amount of original volatiles, play major roles in EDITH variability. Central pits are also thought by some to be related to volatiles in the target material [*Rossbacher and Judson*, 1981], yet there are no correlations between central pits and EDITHs.

Crater diameter is thought to be correlated with depth of excavation. Thus, the lack of correlations with crater size indicates that excavations of different material underlying a surface layer of uniform thickness cannot alone explain EDITH variations. However, this does not preclude a variable thickness layered theory, which is more realistic for this region anyway [e.g., *De Hon*, 1985], nor one that introduces secondary effects such as age.

Certain processes are inadequate to explain overall EDITH variations but may be secondary influences. For example, proximity of EDITH/non-EDITH pairs (e.g., region 2 and region 3) rules out local wind patterns and local availability of aeolian material as first-order effects, though not necessarily as second-order effects. Another example is ejecta freshness (age related alteration) which is similarly unsatisfactory as an overall explanation. Many degrees of freshness (as determined by sharpness and distinctiveness in Viking camera images) are observed on Noachian terrains which do not have EDITHs. Even on Hesperian terrains alone, freshness seems incapable of explaining all observations

(e.g., region 2). Freshness does, however, probably function as an important second-order influence (e.g., regions 1 and 3).

Variations in maturity of a duricrust (i.e., degree of bonding of a case-hardened crust) were suggested by *Jakosky and Christensen* [1986] to explain most of the low-resolution thermal inertia variations on Mars. Duricrust variations are not, however, adequate for explaining the higher resolution EDITHs for the following reasons. First, there is no reason duricrust formation should be related to albedo as some EDITHs are. Second, one would expect younger, and thus less mature, ejecta duricrusts to have lower inertia than their surroundings. However, both lower and higher inertia EDITHs are observed. Third, Jakosky and Christensen's proposed time scale for duricrust formation (10^5 - 10^6 years) is too short to explain EDITHs.

Physical change in ejecta material due to the impact process cannot explain Hesperian EDITH variations for two reasons. First, EDITHs are not associated with all ejecta blankets. Second, there is no correlation of EDITHs with impact energy as evidenced by crater sizes. However, preferential physical change in some ejecta material due to impact could result from layering. If one layer, when impacted, metamorphoses or welds more easily than another layer, this difference between layers may manifest itself as a long-term thermal inertia difference.

One alternate hypothesis that I considered thoroughly and did not rule out entirely presumes the Hesperian plains to be smoother than the Noachian plains at a (small) scale important to clastic particle trapping. They appear this way at Viking camera resolutions (of order 100 m on average). The increased Noachian roughness may be due to some age-related factor, such as impact brecciation or other alteration processes. If this is the case, aeolian particles may saltate across the smooth Hesperian units, only being trapped upon rough areas such as ejecta blankets. In contrast, the rougher Noachian terrain may trap saltating material everywhere, not just on ejecta blankets. There are various difficulties with this hypothesis. To explain EDITHs near non-EDITHs, this theory must

rely more heavily than a layering theory on factors such as freshness of ejecta blankets. Also, this theory does not have the layering advantage for explaining the lack of EDITHs on thick Amazonian terrains or the occurrence of Amazonian EDITHs only near the highland-lowland boundary. Presuming that the Amazonian terrains are also rougher than the Hesperian terrains is inconsistent with Viking imaging resolution observations and with age correlated roughness development.

A second alternate hypothesis I considered seriously is that the Noachian unit intrinsically has more material available for local redeposition. *Barlow* [1990] finds that erosion on Mars decreased drastically at the end of the Noachian period, and has probably remained relatively constant at very low rates since that time. Hesperian terrains probably experienced little erosion. In contrast, erosion on Noachian terrains during the Noachian period may have produced ubiquitous sand sized particles. These particles were then available via saltation and creep to blanket ejecta and obscure its thermal signature over time. The Hesperian terrains may look more like Viking Lander sites, i.e., not exhibiting a true regolith, whereas the Noachian terrain may better resemble a true regolith, similar to the lunar surface. Like the Noachian roughness hypothesis discussed above, the Noachian redepositional material hypothesis also has difficulties explaining the lack of EDITHs on Amazonian units. Amazonian terrains should have less erosional products and less developed regolith than Hesperian terrains. Thus, although I cannot firmly rule out either of these last two alternate hypotheses, I believe they are much less plausible than my layering hypothesis.

3.8 Conclusions

In conclusion, I postulate that EDITHs exist on Hesperian units near Valles Marineris because of impact excavation into a thick, more fragmented, materially different Noachian layer beneath a relatively thin layer or layers of Hesperian volcanic material. I also postulate that EDITH variations are primarily controlled by the degree of excavation

of the Noachian layer. However, secondary effects such as degree of erosion of the blankets or local availability of aeolian material probably cause some thermal variations. The thermally distinct nature of the blankets probably results from the ejecta itself, or possibly from secondary aeolian deposits preferentially trapped on the blankets. My layering theory predicts that EDITHs will not generally occur at small crater sizes except where very thin layering exists.

The importance that a brecciated layer has for EDITHs leads to speculation whether this layer is also important for explaining the uniquely Martian phenomenon of fluidized ejecta blankets. Brecciated material will flow more easily than nonbrecciated material. In addition, the breccias' porosity and their origin in what may have been more water-rich Noachian times could have led to ice presence (as suggested by *Tanaka and Chapman* [1992]). The possible importance of such a Noachian brecciated layer to explaining why fluidized ejecta blankets occur so frequently on Mars and so rarely on other bodies is the subject of work in progress.

3.9 Future Missions/Research

EDITHs must be relatively mantle free and exhibit material ejected from depth. Thus, the surfaces of EDITHs are attractive sites for refined observations because these relatively pristine surfaces may offer important clues to understanding fluidized ejecta blankets, the Martian subsurface, and subsurface volatiles. Mars Observer (MO) would have provided an opportunity to observe ejecta blankets on Mars in greater detail with the thermal emission spectrometer (TES), the pressure modulated infrared radiometer (PMIRR), the Mars Observer camera (MOC), and the Mars Observer laser altimeter (MOLA).

TES would have had similar resolution (3 km/pixel) to the Termoskan panoramas used in my analyses, but greater sensitivity and medium resolution infrared emission spectroscopy. TES would facilitate expansion of my EDITH analysis in many ways:

testing whether EDITH terrain dependencies hold on a global scale, providing much greater diurnal and seasonal coverage, providing accurate determination of the relative importance of inertia versus albedo for EDITHs, and allowing us to look for spectroscopic differences between ejecta and surroundings. In addition, TES's spectroscopic measurements could check for increased minerals of hydration that might be expected from volatile-rich emplacement mechanisms.

Using methods similar to those used by *Christensen* [1982, 1983], TES data would also facilitate looking for variations in percentage of rocks and fine component inertia between ejecta blankets and surroundings, between different ejecta blankets, and within each ejecta blanket. Results would indicate whether variations in the fine component inertia or the percentage of blocks are more responsible for the EDITH variations observed. In addition, preferential trapping of certain sized particles could be tested by looking at variations in fine component inertias. Also, if albedo, block percentages, or fine component inertia are seen to vary with time, then I would be led towards aeolian processes contributing to EDITH variations.

PMIRR, with somewhat worse spatial resolution than TES, would have standardly taken nadir thermal observations and obtained surface temperatures, albedos, and inertias. PMIRR would, however, have had detailed simultaneous atmospheric information different from that obtained by TES, which would aid in atmospheric corrections to albedo and inertia.

MOC's maximum resolution of 1.4 meters/pixel resolution would have facilitated the best ever study of ejecta blanket surface detail and horizontal structure. Study of EDITHs will ensure study of more pristine ejecta blanket surfaces. MOC would have been able to detect block albedo differences between ejecta and surroundings for very large blocks. MOC observations of EDITHs also would help to test the role of volatiles in the fluidized ejecta emplacement mechanism. Observed presence of devolatilization features would imply that volatiles were important in the fluidized ejecta emplacement

mechanism [*Mouginis-Mark*, 1987]. MOC data would also constrain the mechanics of fluidized ejecta flow by showing in detail possible flow-related surface features such as striations, ridges, and the size distribution of large boulders.

MOLA profiles, with a vertical precision of about 2 m and horizontal resolution of 165 m, would have provided detailed vertical structural information about EDITHs. Such profile information would be very important for constraining mechanical models of fluidized ejecta flow. In addition, signal shape would have given information about the small scale surface roughness of the blankets.

Termoskan 2 planned for Mars '94 is expected to increase spatial resolution another order of magnitude from most of the Termoskan 1 data. The high spatial resolution will enable study of more small craters to test the prediction that these small craters should not have EDITHs except on very thin Hesperian or possibly Amazonian units.

Finally, I note that EDITHs also may be excellent targets for future landers because EDITHs are not significantly mantled, and material ejected from depth is exposed at the surface.

Acknowledgments. I thank Kenneth Tanaka, David Paige, and William Anderson for timely and thoughtful comments on early versions of the manuscript and Jeff Plescia and Peter Mouginis-Mark for their detailed reviews of my submitted manuscript. I thank Nadine Barlow for providing us with her *Catalog of Large Martian Impact Craters*, and Arnold Selivanov and Margarita Naraeva for assistance with the Termoskan data set. Funding for this research was provided by NASA grants NAGW-1426 and NAGW-2491. Division of Geological and Planetary Sciences, California Institute of Technology contribution 5108.

Chapter 4

If there is but little water in the stream, it is the fault, not of the channel, but of the source.
-St. Jerome

CHANNELS AND VALLEYS

The material presented in this chapter is taken directly from *Betts and Murray* [1993b], which is currently in press at the *Journal of Geophysical Research - Planets*. I have deleted a small section that described the instrument and data set. That section was redundant with the more detailed descriptions presented in Chapter 2 of this thesis.

4.1 Abstract

The Termoskan instrument on board the Phobos '88 spacecraft acquired the highest spatial resolution thermal data ever obtained for Mars. Included in the thermal images are 2 km per pixel, midday observations of several major channel and valley systems including significant portions of Shalbatana Vallis, Ravi Vallis, Al-Qahira Vallis, Ma'adim Vallis, the channel connecting Valles Marineris with Hydraotes Chaos, and channel material in Eos Chasma. Termoskan also observed small portions of the southern beginnings of Simud, Tiu, and Ares Valles and some channel material in Gangis Chasma. Simultaneous broad band visible data were obtained for all but Ma'adim Vallis. I find that most of the channels and valleys have higher inertias than their surroundings, consistent with previous thermal studies of martian channels. I show for the first time that thermal inertia boundaries closely match flat channel floor boundaries. Lower bounds on typical channel thermal inertias range from 8.4 to 12.5 (10^{-3} cal cm^{-2} $s^{-1/2}$ K^{-1}) (352 to 523 in SI units). Lower bounds on inertia differences with the surrounding heavily cratered plains range from 1.1 (46 SI) to 3.5 (147 SI). Atmospheric and geometric effects are not sufficient to cause the inertia enhancements. I agree with previous researchers that localized, dark, high inertia areas within channels are likely aeolian in nature. However, the Termoskan data show that aeolian deposits do not completely fill the channels, nor are

they responsible for the overall thermal inertia enhancement. Thermal homogeneity and strong correlation of thermal boundaries with the channel floor boundaries lead us to favor non-aeolian overall explanations. Flat floors and steep scalloped walls are observed in most regions that show increased inertia. Therefore, I favor fretting processes over catastrophic flooding for explaining the inertia enhancements. Fretting may have emplaced more blocks on channel floors or caused increased bonding of fines due to increased availability of water. Alternatively, post-channel formation water that was preferentially present due to the low, flat fretted floors may have enhanced bonding of original fines or dust fallout. Also of interest, buttes within channels have inertias similar to the plains surrounding the channels. Thus, the buttes were likely part of a contiguous surface prior to channel formation.

4.2 Introduction

Enormous channels and valleys are some of Mars' most intriguing features. Most, including those studied here, are now generally accepted to have been cut by water or ice related processes [*Baker et al.*, 1992; *Baker*, 1982; *Carr*, 1981]. These processes probably included catastrophic flooding and sapping processes. Studies of channels on Mars yield important implications for Mars' geologic, hydrologic, and climatic history.

The Soviet Phobos '88 Termoskan instrument provided the highest spatial resolution thermal data ever for Mars [*Murray et al.*, 1991; *Selivanov et al.*, 1989; *Betts*, 1993], including observations of several large equatorial channels and valleys. Here I present the results of the first detailed study of channels using the Termoskan data. I include: a description of the channels observed, a review of geologic classifications and thermal studies, a description of the instrument and the observations, qualitative results and implications, quantitative thermal inertia determinations and implications, critiques of possible hypotheses, and proposed tests using future missions. The term channel has been widely used for Mars, although it is somewhat erroneous in its usage [*Sharp and Malin*,

1975; *Carr*, 1981]. For simplicity, I use the term channel to refer collectively to features previously classed as channels or valleys.

4.3 Background

4.3.1 Channel Descriptions and Geographic and Geologic Settings

Termoskan observed several large channels near the eastern end of Valles Marineris including: significant portions of Shalbatana Vallis, Ravi Vallis, the channel connecting Valles Marineris with Hydraotes Chaos, and channel material in Eos Chasma. In the same region, Termoskan also observed small portions of the southern beginnings of Simud, Tiu, and Ares Valles as well as channel material in the northern portions of Gangis Chasma. On the other side of the planet, Termoskan observed two major valleys in the Aeolis Quadrangle: Al-Qahira Vallis and Ma'adim Vallis (see Table 4.1). All the channels sections observed by Termoskan cut through ancient cratered terrain of Noachian age [*Scott and Tanaka*, 1986; *Greeley and Guest*, 1987].

TABLE 4.1: Channel Locations, Seasons Observed, and Types

Channel	Channel section observed	L_s	Type
Al-Qahira	20°S, 199°W to 14°S, 195°W	18	Runoff channel [M76]; Longitudinal Valley [B92]; Fretted Channel [C81]
Ma'adim	20°S, 183°W to 16°S, 184°W	18	Runoff channel [SM75]; Longitudinal Valley [B92]; Fretted Channel [C81]
Shalbatana	2°S, 46°W to 5°N, 44°W	6	Outflow channel [SM75]
Hydraotes Channel, Simud, and Tiu Valles	7°S, 36°W to 5°N, 37°W	6	Simud and Tiu: outflow channels [SM75]; the observed portion of Simud: Fretted [S73]
Ravi Vallis	2°S, 44°W to 0°N, 39°W	6	Outflow channel [B82]
Ares Vallis	1°S, 16°W to 5°N, 19°W	6	Outflow channel [SM75]
Eos Chasma	15°S, 44°W to 10°S, 37°W	18	
Gangis Chasma	8°S, 49°W to 7°S, 44°W	6	

Classifications are from the following sources: [S73]: *Sharp* [1973]; [SM75]: *Sharp and Malin* [1975]; [M86]: *Mutch et al.* [1976]; [C81]: *Carr* [1981]; [B82] *Baker* [1982]; and [B92]: *Baker et al.* [1992].

Shalbatana Vallis (see Figure 4.1) appears to emanate from a zone of chaotic terrain at 0°N, 46°W and heads northward. It narrows to a low sinuosity channel with a

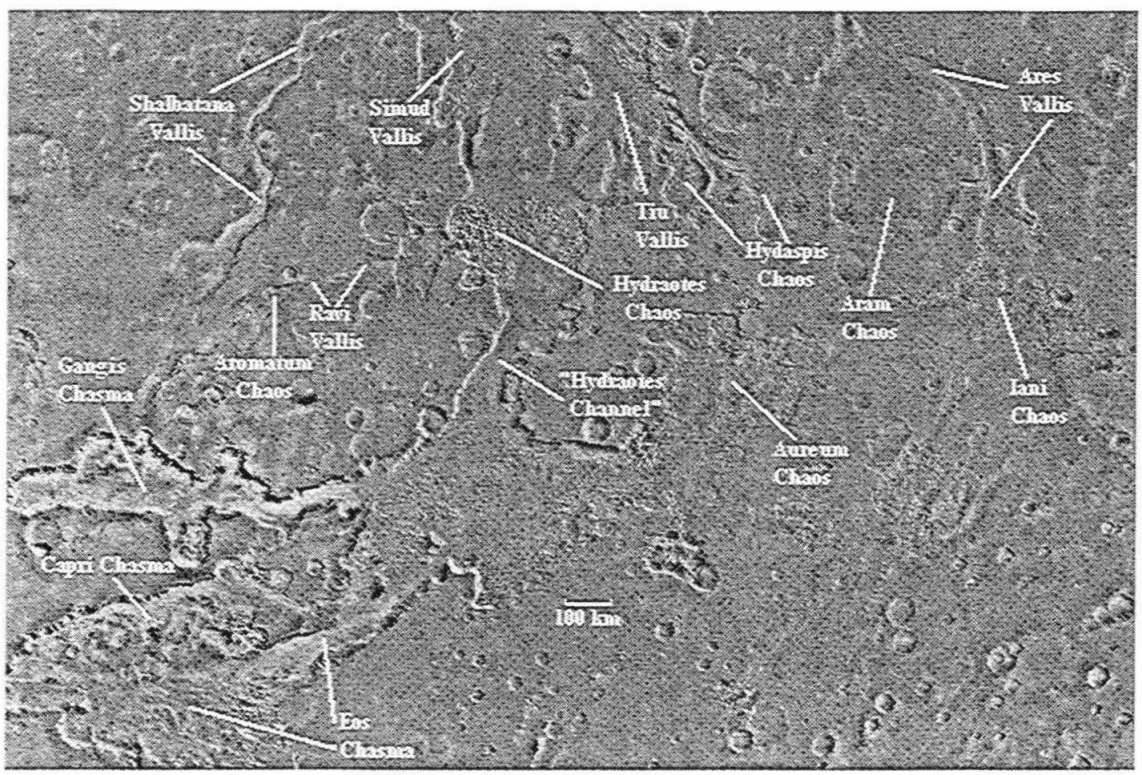

Fig. 4.1. Viking photomosaic (a portion of the file ME00N045 from *USGS* [1991a]) of the channels studied in the eastern Vallis Marineris region centered approximately upon 4°S, 33°W. North is at top in all images. Note that virtually all the channels have smooth flat floors and steep, scalloped walls, suggestive of fretting.

reasonably uniform width of approximately 10 km. It eventually splits into two distributaries. In all, it extends over 1000 km. Termoskan observed approximately the southern 400 km of the channel. Just to the east of Shalbatana is the 300 km long Ravi Vallis, which also emanates from a region of chaotic terrain (Aromatum Chaos). The channel thins and proceeds east, eventually ending in the western portion of Hydraotes Chaos. In contrast with most of the channels discussed here, eastern Ravi has significant amounts of grooved terrain on its floor. In addition, its walls are not as high or as steep as those of the other observed channels.

In addition to Ravi Vallis, several other channels lead either into or out of Hydraotes Chaos (see Figure 4.1). A large, flat channel enters Hydraotes Chaos from Valles Marineris to the South. I will refer to this channel by the unofficial name, Hydraotes Channel. Regions of chaotic terrain occur both to the south and to the north of this channel. Another flat, steep walled channel at the northwest of Hydraotes Chaos begins Simud Vallis. Only approximately 75 km of this channel were observed north of the chaos. In the northeast of Hydraotes Chaos, Termoskan observed about 150 km of a channel (here called Tiu West) that splits around a large butte. This channel then meets another observed channel (here called Tiu East) coming from Hydaspis Chaos to the east. When these sets of channels meet north of the Termoskan coverage, they form Tiu Vallis proper. Small portions of the headward reaches of Ares Vallis were also observed. Most of this part of Ares does not show flat floors, but rather appears scoured and is locally anastomotic [*Sharp and Malin*, 1975]. Simud, Tiu, and Ares, like Shalbatana Vallis, all debouch into Chryse Planitia several hundred km later.

Channel materials were also observed in two of the eastern Valles Marineris Chasma: Eos and Gangis (see Figure 4.1). Flow from these regions presumably headed to the east and eventually northeast in the direction of Hydraotes Channel and Chaos. Only the northernmost part of Gangis was observed. A separate Termoskan panorama shows most of Eos Chasma. Both chasma contain flat, smooth appearing areas classified by

Scott and Tanaka [1986] as Hesperian channel materials. The channel materials are situated next to steep walls, buttes, and at least in Eos Chasma, between regions of chaotic terrain.

Termoskan also observed Ma'adim Vallis and Al-Qahira Vallis, two isolated channels in the Aeolis quadrangle. Termoskan observed the northernmost (distal) 350 km of the 700 km long, gently winding, 15 to 25 km wide Ma'adim Valles. It heads northward until hooking northwest after breaching a 30 km crater. It debouches into another 30 km crater. Ma'adim is unusually old for a large channel [*Baker*, 1982; *Masursky et al.*, 1980]. Ma'adim has steep walls and smooth floors except where benches exist.

Al-Qahira Vallis is located approximately 800 km to the west of Ma'adim. Termoskan observed all 300 km of this channel. It originates from short tributaries, runs mainly east, then turns north and widens as it takes a very straight course. It also has a broad, flat floored main channel and heavy cratering [*Baker*, 1982]. Like Ma'adim, its termination is rather indistinct and shows a marked lack of large scale deposits.

4.3.2 Channel Classifications

Martian channels have been classified by several authors. Table 4.1 summarizes previous geologic classifications for the observed channels. All of the named channels in the eastern Valles Marineris region are classified at least in part as outflow channels [e.g., *Sharp and Malin*, 1975; *Baker et al.*, 1992; *Baker*, 1982; *Carr*, 1981]. These include Shalbatana, Ravi, Tiu, Simud, and Ares. *Sharp and Malin* [1975] define outflow channels as mostly large features that start full-born from localized sources. They are broadest and deepest at their head. Some are scoured and display features characteristic of catastrophic flooding. Many originate from chaotic terrain. Outflow channels are generally accepted to have originally formed by catastrophic flooding, in some cases from release of water from chaotic terrain [*Baker et al.*, 1992; *Carr*, 1986].

Sharp and Malin [1975] classed Ma'adim Vallis as a runoff channel and *Mutch et al.* [1976] classed Al-Qahira Vallis (which was not discussed by *Sharp and Malin*) as a runoff channel. *Sharp and Malin* [1975] define runoff channels as starting small, increasing in size and depth distally and having tributary branches, and crustal control may be strong. *Baker et al.* [1992] class Ma'adim and Al-Qahira Vallis as longitudinal valleys. *Mars Channel Working Group* [1983] distinguished martian valleys from channels by the absence of bedforms indicative of fluvial flow. Longitudinal valleys may have begun as small valleys, then become enlarged by wall retreat as lower courses became deeply incised [*Baker et al.*, 1992].

Whatever caused the original valleys, the wide, flat floors and steep walls with scalloped appearances indicate that a fretting process [*Sharp,* 1973] has been active for Ma'adim and Al-Qahira. This presumably involved sapping of ground water or ice, causing undercutting of the walls. Debris flows, possibly facilitated by ice (as suggested for fretted terrain by *Squyres* [1978]) may have then moved material away from the walls allowing more undercutting erosion to occur. We note, however, that fretting is not a well understood process, but it is morphologically well defined for Mars. *Carr* [1981] actually classes Al-Qahira and Ma'adim as fretted channels.

Fretting also appears to have occurred in the portions of channels observed by Termoskan near eastern Valles Marineris. Again this is based upon the steep walls and flat, smooth floors. In fact, the channel at the northwest of Hydraotes Chaos (leading to Simud) is specifically shown by *Sharp* [1973] as an example of fretted channels next to chaotic terrains. Thus, many of the channels observed show evidence of fretted morphologies. Notable exceptions are eastern Ravi Vallis, southern Ares Vallis, and portions of Tiu East which show rough floors and do not have walls that are as steep. Termoskan observed few classic outflow channel morphologies, although it narrowly missed several north of the area at the eastern end of Valles Marineris. Extension of this analysis to more classic outflow channels using future mission data will be very interesting.

4.3.3 Previous Thermal Studies

Several researchers have undertaken thermal studies of Martian channels and valleys using Viking Infrared Thermal Mapper (IRTM) data. These analyses and the channels studied include: *Christensen and Kieffer* [1979], Kasei, Ares, Shalbatana, Simud, and Tiu Valles; *Zimbelman* [1986] and *Zimbelman and Leshin*, [1987], Al-Qahira and Ma'adim Valles; and *Craddock et al.* [1987 and 1988] and *Craddock* [1987], Dao, Hormakis, Ma'adim, Mangala, and Shalbatana Valles. These studies concluded that many channels and valleys have higher inertia than their surroundings. In their explanations of the inertia enhancements, they emphasized dark, high inertia, presumably aeolian saltation deposits within the channels.

Zimbelman [1986] and *Craddock et al.* [1988] concluded that several centimeter thick aeolian deposits dominate the inertia of the channel floors. At least for the channels they studied, they concluded that thermal observations may not be related to the processes that produced the channels. In contrast, I conclude that thermal observations of much of the channel floors may be sampling some material and textures from the channel floor formation. IRTM studies of channels were limited either by insufficient spatial resolution to resolve the channels or by limited areal coverage of the highest resolution data. In contrast, Termoskan data provides high resolution images with nearly complete spatial coverage (i.e., no gaps or gores).

4.4 Qualitative Analyses

4.4.1 Observations

Termoskan obtained thermal images of several channels in the eastern Valles Marineris region (see Figures 4.2, 4.3, and 4.4), and of Al-Qahira Vallis (Figure 4.5) and Ma'adim Vallis (Figure 4.6). Simultaneous broad band visible channel data were obtained for all but Ma'adim Vallis. All of the channel systems were observed near midday, between 9.87 H and 13.00 H, except Eos Chasma at 15.15 H (where 24 H = 1 Martian

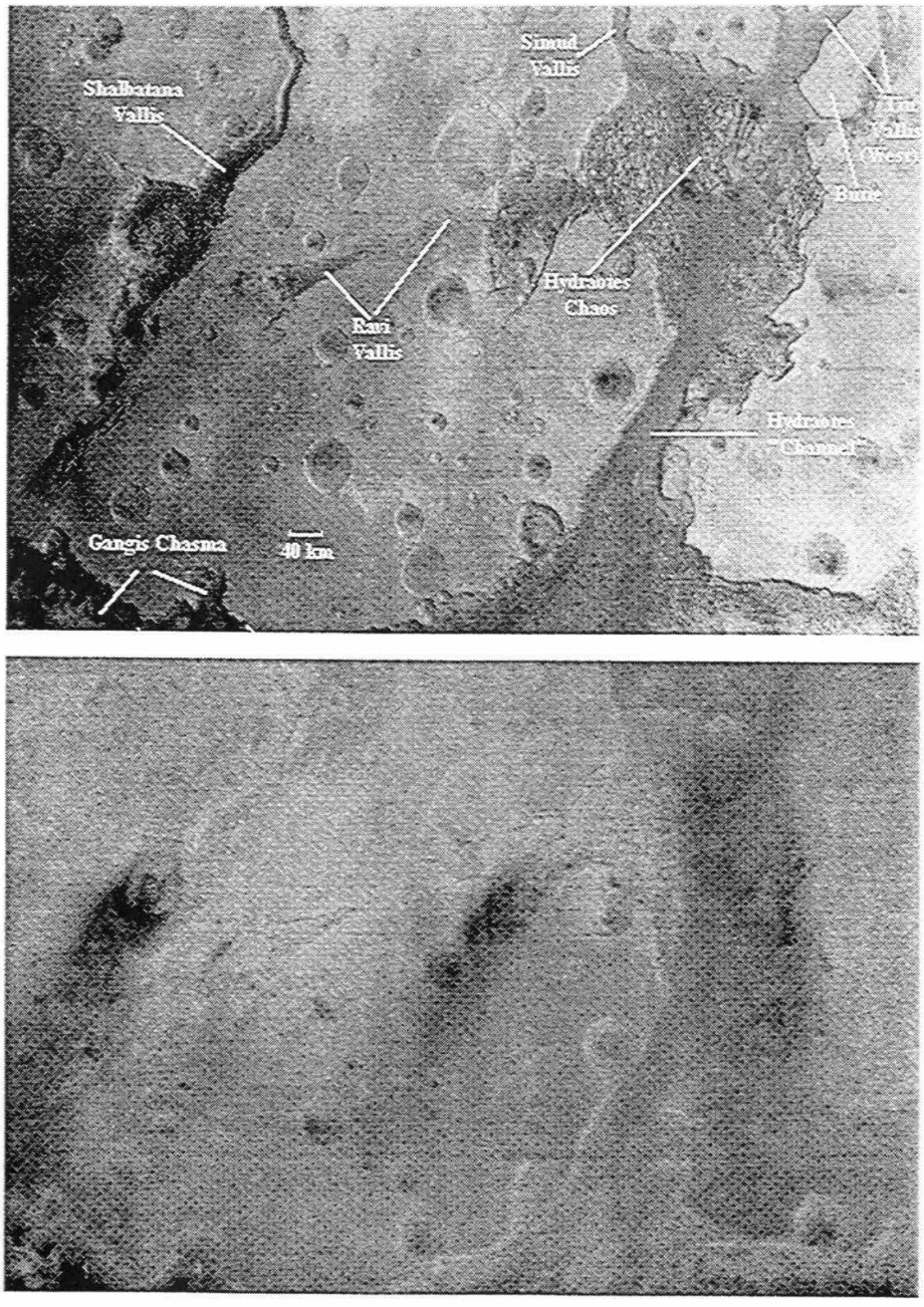

Fig. 4.2. Termoskan thermal (top) and visible (bottom) images centered approximately upon 1°S, 39°W. North is top. In all thermal image shown here, darker is cooler. Shalbatana, Simud, and Tiu Valles all continue for several hundred km north of this image. Note the cool and generally uniform floors of all channels except the eastern (and rough floored) end of Ravi Vallis. Note also that the thermal boundaries closely match the boundaries of the channel floors and depart significantly from albedo boundaries seen in the visible image. Note also the dark, presumably aeolian deposits localized within the southern portions of Shalbatana Vallis and the southwestern portion of Hydraotes Chaos and spreading onto the surrounding plains in both cases. Buttes, including the large labeled one in the northeast of the image, within the channels appear similar in temperature and appearance to the surrounding plains, not the channels.

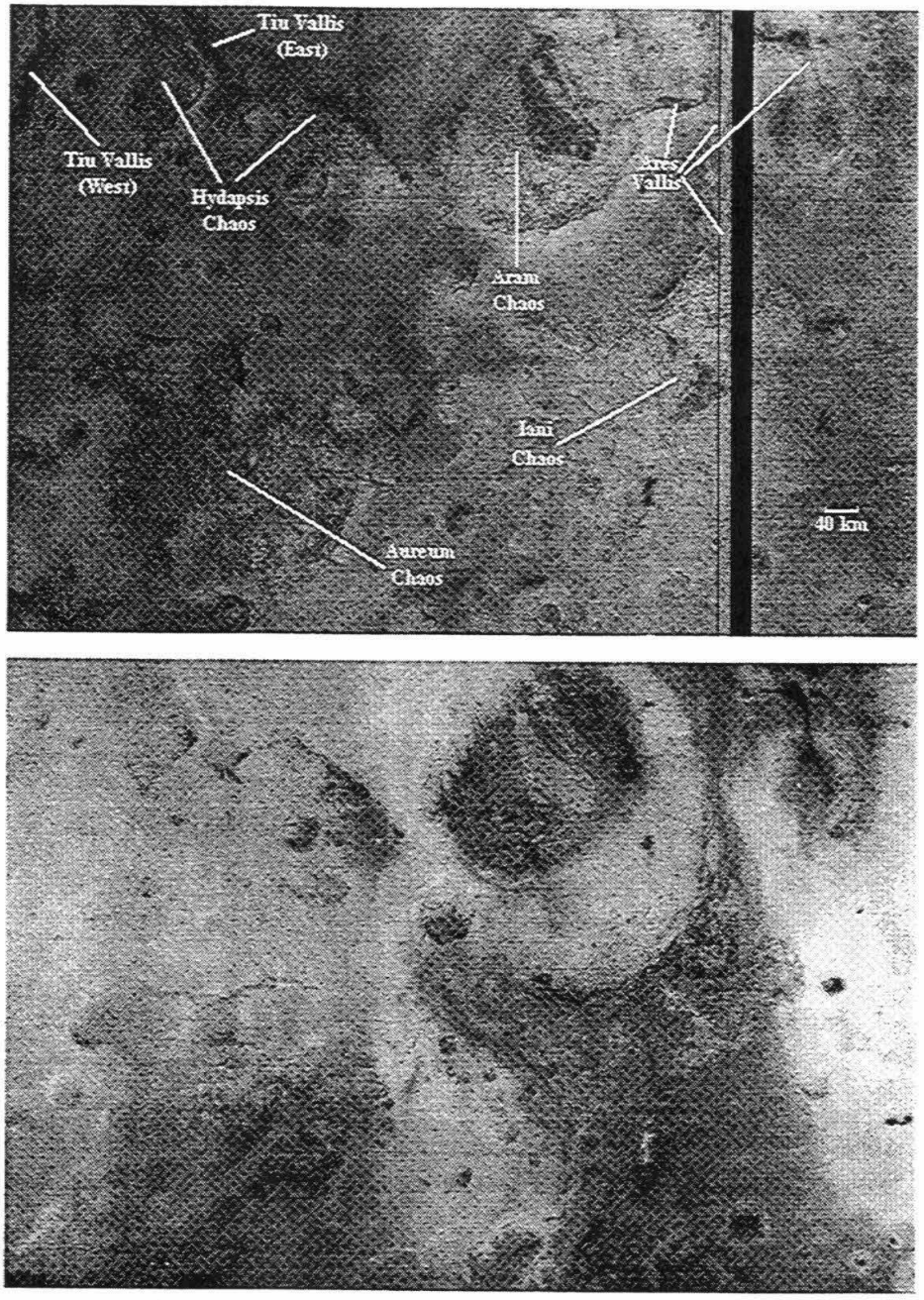

Fig. 4.3. Termoskan thermal (top) and visible (bottom) images centered approximately upon 1°S, 23°W. North is top. Western portion overlaps slightly with Figure 4.2. Vertical black lines have been added where lines were missing in the original data. Note that the central part of Ares Vallis that runs north from Iani Chaos is not thermally distinct from its surroundings. This region shows significant catastrophic flooding bedforms and lacks fretting morphologies. The smaller channels that join the central Ares channel from the west and from the east are in some areas cooler. However, as opposed to most other channels, the cooler areas occur in patches, possibly indicative of aeolian processes.

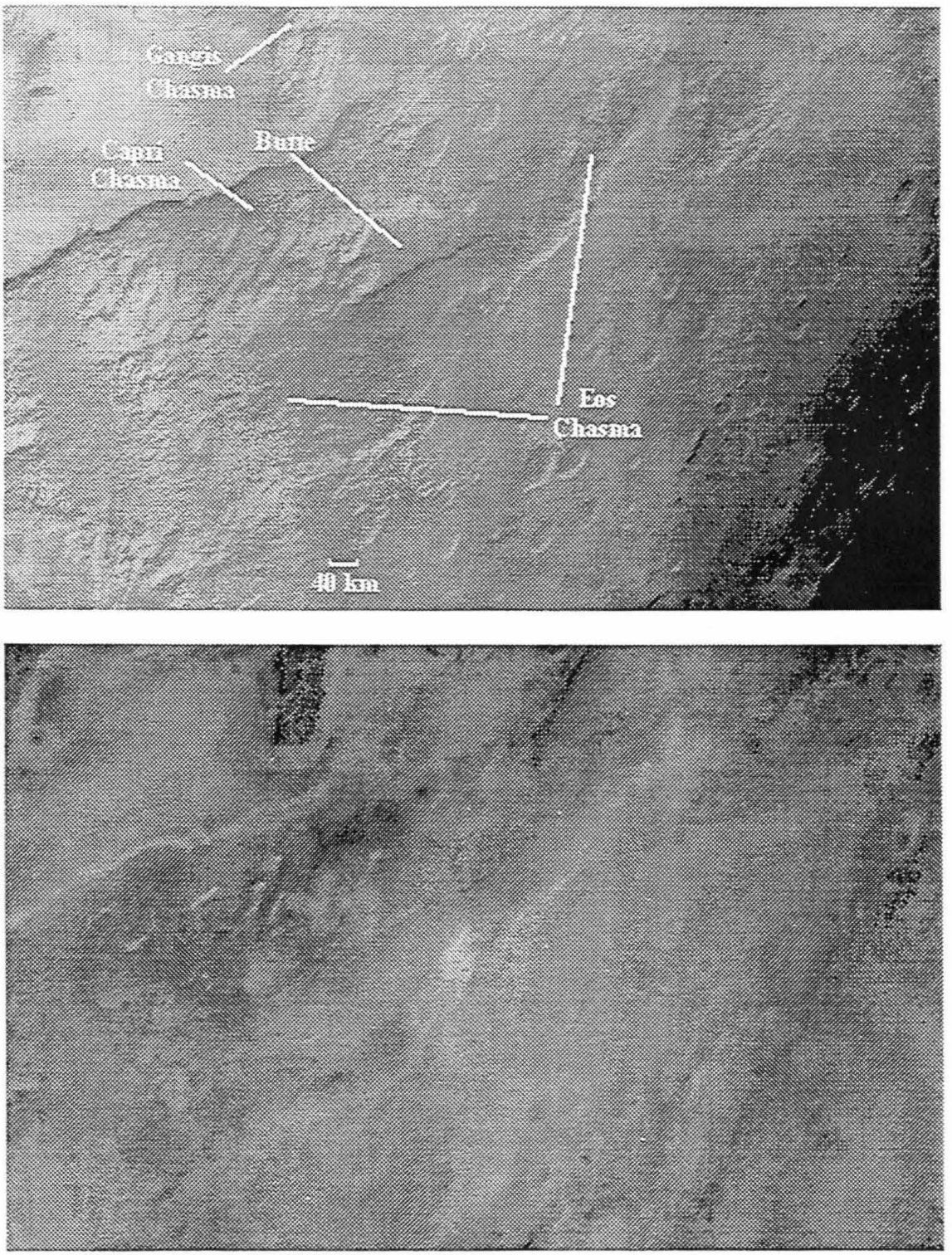

Fig. 4.4. Termoskan thermal (top) and visible (bottom) images showing Eos Chasma and centered approximately upon 14°S, 41°W. Within Eos Chasma, flat floored channel floor materials [*Scott and Tanaka*, 1986], for example south of the labeled butte, are cool relative to surroundings.

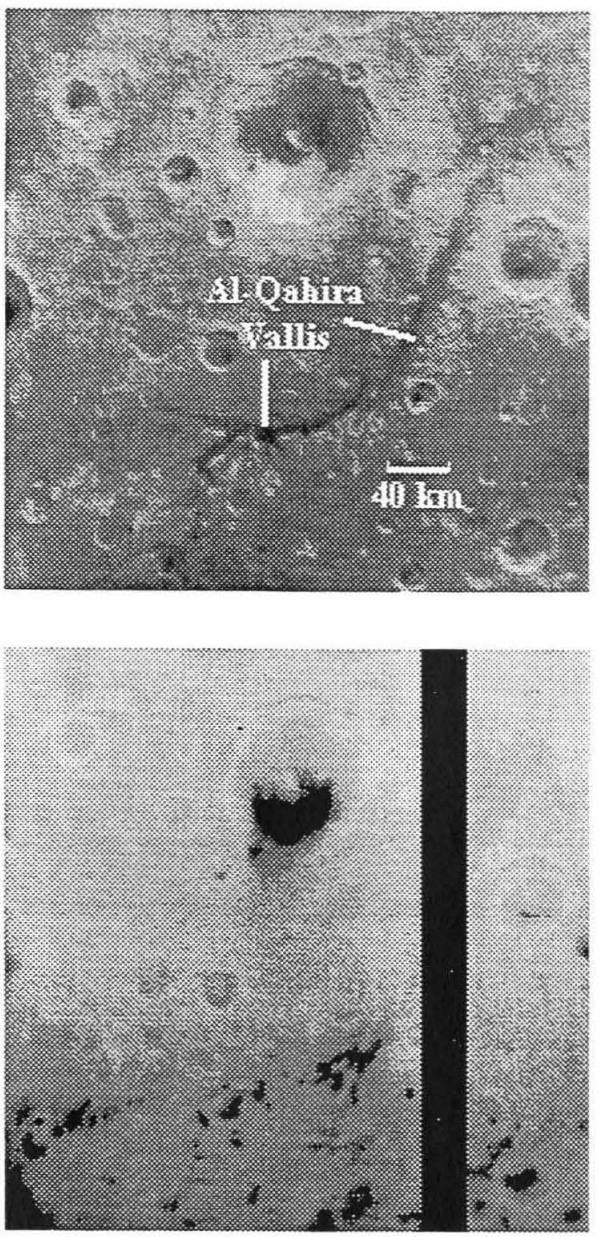

Fig. 4.5. Termoskan thermal (top) and visible (bottom) images showing Al-Qahira Vallis and centered approximately upon 17°S, 197°W. Vertical black lines have been added where lines were missing in the original data. Al-Qahira Vallis shows smooth broad floors, a tributary pattern, and a straight, possibly structurally controlled, northern section. Note dark, presumably aeolian, material localized in the southern portions of the valley and on the surrounding plains, and in the large crater to the northwest of the valley. The channel floors appear cooler than the surroundings both where the dark deposits are and where they are not.

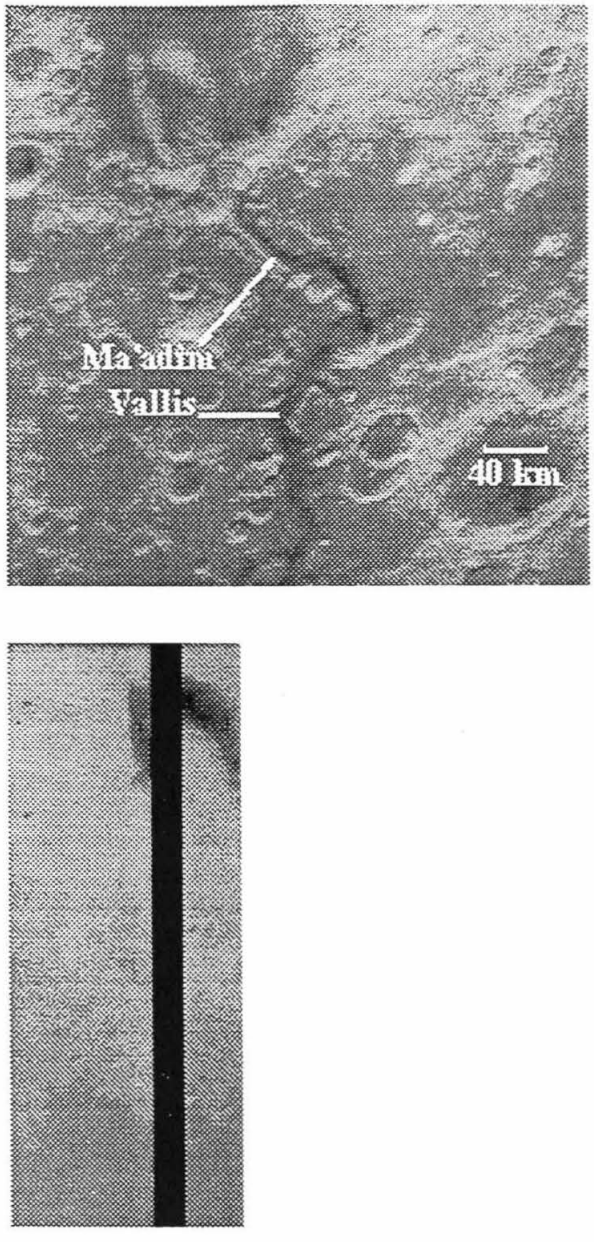

Fig. 4.6. Termoskan thermal (top) and visible (bottom) images showing Ma'adim Vallis and centered approximately upon 17°S, 183°W. Visible data were only obtained in the western portion of this region. Once again, note how cool temperatures follow channel floor. Localized cooler spots may have aeolian causes, but overall cooler channel temperatures probably do not.

day). All were observed with an approximate resolution of 1.8 km/pixel and at nearly 0° phase angle. Mangala Vallis was also observed, but I do not discuss it in detail. The Mangala data are badly foreshortened and interpretation is further complicated by the early morning (post-dawn) and late afternoon (pre-sunset) local times of the observations.

The general characteristics of all the channel observations are summarized in Table 4.2. Termoskan's high resolution images show for the first time that thermal boundaries very closely match channel floor boundaries, usually to within the resolution of the instrument. For these midday observations, the cooler and darker (or similar albedo) channels must have higher thermal inertia than their surroundings. The eastern end of Ravi Vallis and southern Ares Vallis appear different from most of the other channel observations. They do not have flat floors or steep walls, and they appear thermally similar to their surroundings. Thermal distinctiveness within channels is strongly correlated with regions that have morphologies indicative of fretting: flat wide floors and steep, scalloped walls. Comparisons are limited, however, because few other channel types were observed by Termoskan except Ravi and Ares, although many occur elsewhere on the planet.

TABLE 4.2: Summary of Termoskan Channel Observations

Thermal:	Visible:
• Channel floors consistently cooler than surroundings by 3K to 10K	• Channels darker or similar to surroundings
• Thermal boundaries closely follow channel floor boundaries.	• Visible boundaries do not closely match channel boundaries
• Relatively uniform on floors of channels	• Not nearly as uniform as thermal
• Homogeneous floors even in serpentine regions around buttes	• Not homogeneous in serpentine regions around buttes
• Visible boundaries do not closely match thermal boundaries	
• Channel floors cooler than surroundings even outside dark, localized aeolian deposits. Temperature corresponds better to floor boundaries than to dark deposits' boundaries	
• Where benches along walls exist, their temperatures are between those of the flat channel floors and those of the surroundings	
• Tributaries generally appear thermally distinct from their surroundings	
• Landslides and ejecta blankets appear thermally similar to surrounding channel floors, although they are just at the limit of resolution of the Termoskan data, so this observation is guarded	

4.4.2 Implications

I can draw the following conclusions from the qualitative observations listed in Table 4.2:

1. The floors of all the channels observed consistently have higher inertia (implying coarser material, more bonded material, or more rocks) than their surroundings, consistent with previous studies.

2. Boundaries of thermal inertia (which represents the upper few cm of the surface) closely match channel floor boundaries, particularly for wide, flat floors.

3. Dark, presumably aeolian deposits, do not dominate the inertia of the channels as a whole. This contrasts with conclusions drawn by some previous researchers [*Zimbelman*, 1986; *Craddock et al.*, 1988] whose results were based upon lower resolution, non-imaging IRTM data. In Termoskan observations, channel inertias are still higher than those of the surroundings even outside the localized, dark deposits. The dark deposits are very likely saltation traps for dark sand, similar to the localized intracrater deposits seen near some channels and investigated planet-wide by *Christensen* [1983]. I discuss this more fully in the aeolian explanations section.

4. Channels are examples of features whose inertia correlates well with morphology, which is rare on Mars [*Christensen and Moore*, 1992].

4.5 Quantitative Thermal Inertia Determination

4.5.1 Method

I have used the Termoskan data in combination with thermal modelling and albedo information from Viking to derive thermal inertias for points within channels and for points on the surrounding plains. For Al-Qahira and Ma'adim Valles, I chose approximately ten locations inside and ten outside each channel. For the other, shorter, channel segments, one representative channel point and one representative surrounding point were chosen. Points inside each channel were selected to represent the channel, to

avoid large slopes that would significantly alter inertia determinations, and for Al-Qahira and Ma'adim, to give good coverage over the length of the channel. For each location inside, a paired point devoid of extreme slopes was chosen nearby on the surrounding plains. Areas were determined to be devoid of extreme slopes based upon a lack of apparent sun-facing (bright and warm) or anti-sun-facing (dark and cool) slopes based upon both Termoskan data and Viking Orbiter camera images. For each location, I noted the temperature and visible signal from single Termoskan pixels. These single pixel values generally matched to within 1 K and often to within 0.5 K of the average of a 3 x 3 pixel box (if the box was entirely within the channel). Latitude and longitude were determined from USGS photomosaics. Local time of day was calculated for each point based upon its longitude and the absolute time of the observation.

To derive thermal inertias, I used an adaptation of the *Clifford et al.* [1987] finite difference, homogeneous thermal model of the Mars surface. This model numerically solves the heat diffusion equation using the boundary conditions of thermal equilibrium at the surface and no heat flow across the lower boundary. Physically, this model is identical to the Viking thermal model described by *Kieffer et al.* [1977, Appendix 1], although computationally it differs slightly.

Ideally, thermal inertia is determined from diurnal observations using temperature alone, as was done for example by *Palluconi and Kieffer* [1981] and *Kieffer et al.* [1977]. However, Termoskan acquired only one observation of each of the channels studied. Thus, I use an alternate method that uses a single temperature observation combined with bolometric albedo (similar to what was described by *Kieffer et al.* [1977] and used by *Christensen* [1983] and others). I solve for the inertia, I, in the expression:

$$T_{obs} = T_m + \frac{\partial T_m}{\partial I (I - I_m)} \qquad (1)$$

where T_{obs} is the observed Termoskan brightness temperature. I_m is the standard model inertia of 8.0, which was chosen as a representative midpoint inertia for the channels

studied. T_m is a standard model temperature. T_m was determined by first modelling the surface using an inertia of I_m, an albedo of A_m (discussed below), and the correct martian season (L_S = 6° or L_S = 18°, where L_S is the areocentric solar longitude). The model produced temperature outputs for every .25 H and for every 2° latitude. The temperature outputs were then interpolated for each locations' latitude and time of day to give T_m. To derive $\partial T_m/\partial I$, I used an identical process to derive model temperatures for other values of inertia. I use inertias near I_m (within 1.5 units) to minimize errors in $\partial T_m/\partial I$ caused by the non-linearity of temperature with inertia.

Bolometric albedo (A_m) is required when deriving inertias using single observations. Due to instrument limitations, atmospheric variations, and very limited phase angle viewing geometry, even approximate estimates of bolometric albedo from the Termoskan data have thus far not yielded high confidence results [*Murray et al.*, 1991; *Betts*, 1993]. Thus, I use bolometric albedos from the 1° x 1° binned albedos of *Pleskot and Miner* [1981]. I averaged adjacent bins along the course of the channels. Generally, the albedos varied by less than .01 for all bins surrounding and including the channels. The albedo values I used in my model for each channel are shown in Table 4.3. Due to its large width, Hydraotes Channel is the only channel for which I could estimate an albedo separate from the surroundings.

Most of the channels are significantly narrower than the 1° x 1° bin size of *Pleskot and Miner* [1981]. Thus, the *Pleskot and Miner* albedos are likely good estimates for the surroundings, but not necessarily for the channels. The Termoskan data show that the channel floors are actually all darker or similar in albedo to their surroundings. Therefore, considering the midday local times of the observations, my model results represent lower bounds for the channel inertias. Similarly, I determine lower bounds for the inertia differences between channels and surroundings. For the albedos, inertias, and times of day involved, I found that a decrease in model albedo of .01 would cause a derived inertia increase of approximately 0.4. Due to its large width, we were able to estimate an albedo

from *Pleskot and Miner* [1981] for Hydraotes Channel of approximately 0.17 versus surrounding albedos of approximately .20 to .21. Hydraotes Channel also showed the largest difference in visible signal (DN) between channel and surroundings of any of the channels except within dark, localized aeolian splotches. Thus, a .04 decrease from the albedos used represents an approximate lower bound on channel albedos. This corresponds to an approximate upper bound on channel inertia increases over derived inertias due to this effect of 1.6.

4.5.2 Results

My quantitative results back up the qualitative conclusion that all locations on the channel floors have higher inertias than the surroundings. Figure 4.7 and Table 4.3 show my derived average inertias and results from previous IRTM studies. Lower bounds on typical channel thermal inertias range from 8.4 to 12.5 (352 to 523 in SI units). The lower bounds on the average inertia difference between the channel floors and the surroundings varied from 1.1 (46 SI) for Simud Vallis to 3.5 (147 SI) for Hydraotes Channel. My derived inertias for the surroundings are in good agreement with the corresponding 2° x 2° binned inertias of *Palluconi and Kieffer* [1981] with the average inertia difference (Termoskan derived inertia - *Palluconi and Kieffer* inertia) between paired points being +0.3 with a standard deviation of 0.8.

For Al-Qahira and Ma'adim Vallis, where Termoskan obtained significant length coverage, there are no systematic differences in inertia with distance along the lengths of each channel. Also, there is no correlation between channel widths and inertia, as reported for some other channels [*Craddock* et al. 1988; *Christensen and Kieffer*; 1979].

Also of interest are buttes ("islands") seen prominently in Hydraotes Channel and in Eos Chasma. These include the 70 km x 140 km butte at 3°N, 32°W between Hydraotes Chaos and Tiu Vallis (Figure 4.2). Although surrounded by channels, the

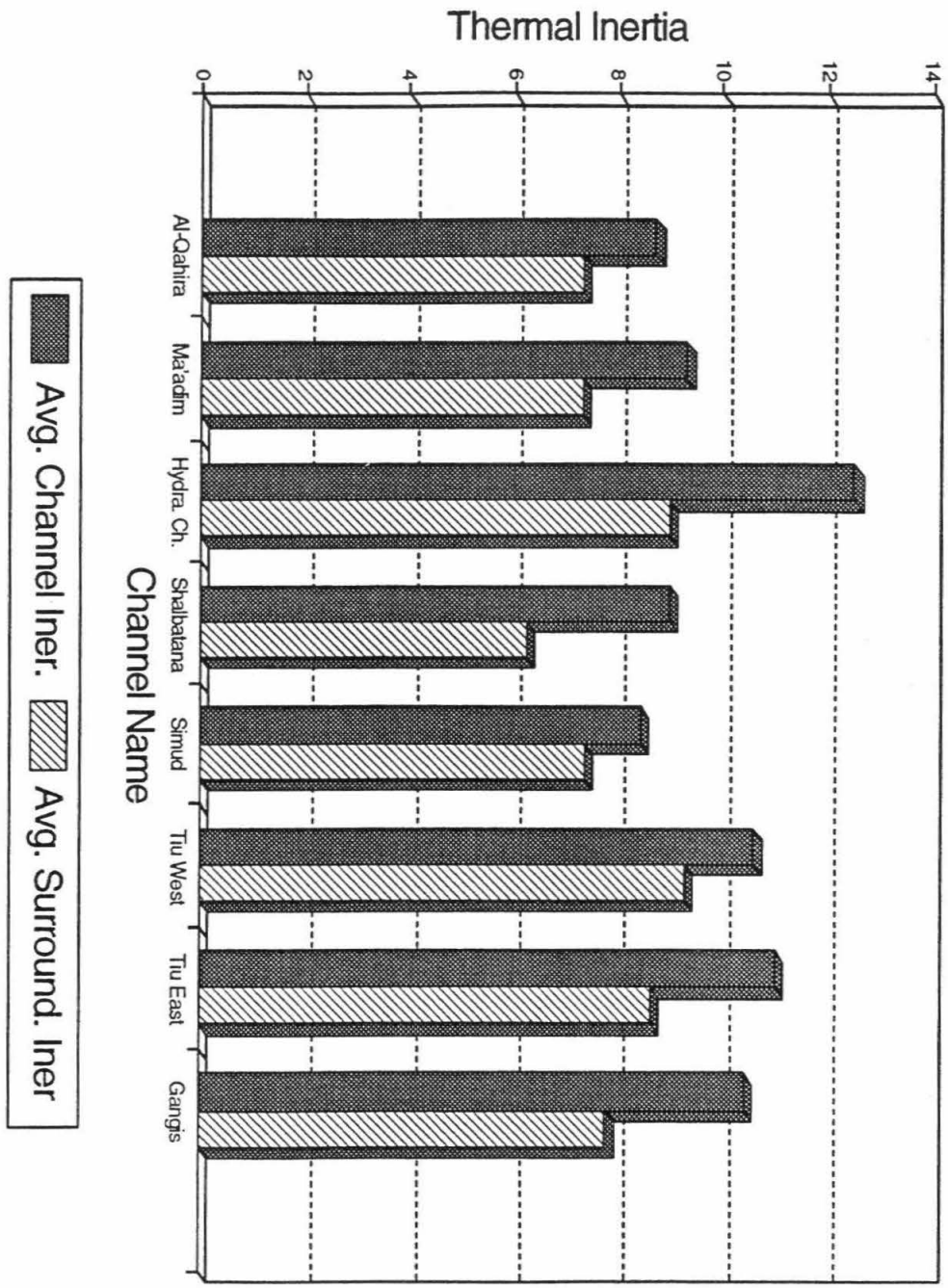

Fig. 4.7. Inertias derived from Termoskan data for thermally distinct channels and the associated surrounding plains. Derived inertias for Eos Chasma and surroundings are not shown because they are unreasonably high due to the afternoon cooling effect (see Table 4.3 for further explanation). Also not shown are Ares and Ravi Valles which are mostly similar in inertia to their surroundings.

Table 4.3: Derived Inertias, Summary of Results from Previous Studies, and Model Albedos Used

Channel	Chan. I	Surr. I	Delta I	Previous Channel Results from Thermal Studies	Ch. A	Su. A
Al-Qahira	8.7 (0.9)	7.3 (0.4)	1.4 (0.8)	[Z86]: In combination with Ma'adim: 3.5-12.5 with mode 8.	.21	.21
Ma'adim	9.3 (0.9)	7.3 (0.4)	2.1 (0.8)	[Z86]: In combination with Al-Qahira: 3.5-12.5 with mode 8.	.21	.21
Shalbatana	9.0	6.2	2.8	[CK79]: 7-8+, thermally distinguishable south of 10°N. [C88]: 9-12, not correlated with dark materials; rock abundance as high as 14 percent.	.24	.24
Hydraotes Channel	12.5	9.0	3.5	[CK79]: 12-13 near chaos. [PK81]: near 11, although most of the bins sample significant portions of the surrounding plateau as well. [C86]: Relatively high rock abundance, > 14percent in some places, although not well resolved from surroundings.	.17	.20
Simud Vallis	8.4	7.4	1.1	[CK79]: 8-10; thermally distinguishable S. of 10°N.	.24	.24
Tiu West	10.6	9.3	1.3	[CK79]: 11-12; thermally distinguishable S. of 10°N.	.22	.22
Tiu East	11.0	8.6	2.4	[CK79]: 10-11; thermally distinguishable S. of 10°N.	.24	.24
Gangis Chasma	10.4	7.8	2.6		.19	.19
Eos Chasma	19.9	15.6	4.4		.17	.17

Abbreviated column headings are as follows: Channel I, derived channel inertias (10^{-3} cal cm^{-2} K^{-1} $sec^{-1/2}$, multiply by 41.86 for SI units); Surr. I, derived inertias for the surroundings; Delta I, average inertia difference between paired points in channel and outside channel; Chan. A, albedo used for channel in thermal model; Surr. A, albedo used for surroundings in thermal model, from *Pleskot and Miner* [1981].

Numbers in parentheses represent standard deviations, presented to give an idea of the range in inertias. These do not represent errors, since the data were collected for several points within the channels and on the surroundings that actually have different inertias.

Previous results are from the following sources: [CK79]: *Christensen and Kieffer* [1979] (note that inertia numbers were read off their contour plots based upon 1/2° x 1/2° bins, whereas descriptions are derived from their text); [PK81]: *Palluconi and Kieffer* [1981] (data from 2° x 2° bins); [C86] *Christensen* [1986]; [Z86]: *Zimbelman* [1986], includes portions of the channels that were not observed by Termoskan; and [C88]: *Craddock*, [1988]; includes portions of the channels that were not observed by Termoskan.

Channel I and Delta I are probably lower bounds (see text).

Almost all derived surroundings inertias agree to within 1 unit of those derived by *Palluconi and Kieffer* [1981] for the corresponding 2° x 2° bin.

Derived inertias for Eos Chasma are probably much too high due to the so-called afternoon cooling effect, in which the surface of Mars is observed to cool much faster in the afternoon than predicted by thermal models of the type used here [*Jakosky*, 1979; *Ditteon*, 1982]. Eos Chasma, observed at 15.2 H, was the only channel observed after 13 H, and hence the only channel for which this was a major factor. For reference, the *Palluconi and Kieffer* [1981] inertia for the area modelled as the Eos Chasma surroundings was 9.2, versus the 15.6 derived here.

Inertias were not derived for Ravi or Ares Valles because they generally appear similar to their surroundings.

buttes have inertias similar to the plains surrounding the channels. This is consistent with the results found by *Christensen and Kieffer* [1979] for a 20 x 90 km butte within Kasei Vallis. Thus, as they concluded for the Kasei Vallis region, my results imply that the buttes were part of a contiguous surface prior to channel formation. The processes that led to the development of the butte and plateau surfaces probably acted prior to channel formation. Less likely, the buttes and plateaus may be currently modified by a similar process. However, this process would have to have affected them despite the presence of the channels and without affecting the surface properties of the channels.

4.6 Why Do Channels Have Higher Inertia?

4.6.1 In General

The Termoskan data are consistent with *Christensen and Kieffer's* [1979] idea (developed for Kasei Vallis) that one process, possibly associated with channel formation, increased the inertia throughout the channels. A second, probably aeolian, process concentrated a coarse, low albedo component in certain areas. Here I assume that the low albedo localized areas are indeed aeolian in nature. I find the more general inertia enhancements to be strongly associated with fretting. I postulate that the inertia enhancements were caused either by the original fretting process or by a secondary process involving preferential bonding of fines due to an increased availability of water. Before discussing fretting in more detail, I first consider alternate origins of the apparent overall inertia enhancement: atmospheric or geometric effects, aeolian causes, or catastrophic flooding causes.

4.6.2 Atmospheric and Geometric Effects

Two atmospheric effects will increase the apparent inertia of a surface with decreasing elevation [*Christensen and Kieffer*, 1979]: an increase in surface conductivity with increasing pressure and an increase in apparent inertia with increasing thermal opacity due to atmospheric dust. Over a range of elevations representative of one of the most extreme channel-surrounding elevation differences (-2 km to 1 km in Hydraotes Channel), the apparent thermal inertia will change due to pressure variation from 6.3 to 6.8 for a surface whose actual inertia is 6.5 at 0 km [*Kieffer et al.*, 1973]. With a visible opacity of 0.3 at -2 km and a scale height of 10 km, the apparent inertia could increase from 6.5 at 1 km to 6.8 at -2 km [*Haberle and Jakosky*, 1991]. Thus, although these effects may accentuate temperature differences, they are too small to explain solely the observed inertia differences.

What about differential shadowing due to the walls? I conclude that this is not a major effect. Increased morning and late afternoon cooling in the channels due to shadowing also is not a major effect. Because of the shadowing effects of the walls, sunrise will occur later and sunset earlier in channels than on the surrounding plains. This will cool the channel floors. However, observationally, I infer this is probably not significant for the channels studied because the channel floors are cooler than the surroundings no matter what their orientation, east-west or north-south. Theoretical modelling shows that for the widths (tens of km) and depths (few hundred m and in rare cases up to 3 km based upon *USGS* [1991]) of the channels studied, the decrease in overall energy received at the surface due to this effect is very small because of the low sun angles and small amounts of time involved. Specifically, I calculated the decrease in energy received at the surface to be less than 0.1percent for the worst case scenario: using the largest height to width ratio observed (approximately 1/10) and a north-south running channel.

Observing geometry combined with roughness of the surrounding plains versus the channels could possibly explain the observations, although the explanation is quite strained. It requires the surrounding plains to have higher average slopes and more large scale roughness than the channel floors. The slopes facing the sun, and thus the warmest slopes, were also the slopes that faced the Termoskan instrument. Thus, rougher surroundings would have appeared warmer. However, IRTM observations found channels to have higher inertias, and IRTM obtained nighttime observations and multiple phase angle observations. Thus, the temperature variations observed by Termoskan are likely not caused by the "smoothness" of the channels alone.

4.6.3 Aeolian Increase of Average Particle Size

Visible wind streaks and intracrater splotches in the areas surrounding the channels and GCM surface wind predictions [*Greeley et al.*, 1993] indicate that aeolian processes

have been and are probably still active in the channel regions studied here. In addition, the channels may focus winds or create them preferentially due to differential heating of walls versus the floors [*Craddock et al.*, 1988], although this is less likely for the widest channels. I agree with previous studies that localized dark splotches and streaks within the channels are probably aeolian sand deposits [*Christensen and Kieffer*, 1979; *Zimbelman*, 1986; *Craddock et al.*, 1988]. The question remains, however, whether aeolian processes are responsible for the enhanced inertia of the rest of the channels. Possible aeolian causes include: 1 - small scale deposition, i.e., between rocks, but not burying all rocks; 2 - large scale depositional blankets; and 3 - deflation, i.e., wind induced removal of fine material, exposing higher inertia material. Because a blanket of suspension (dust) sized particles within a channel would cause a lower inertia, not the observed higher inertia, I consider only saltation sized particles.

The thermal homogeneity of the channel floors argues against any type of aeolian process, short of a uniform sand sea, causing the channel inertia enhancement. Aeolian processes on earth and as observed on Mars inevitably cause spatial heterogeneity. This is consistent with having localized, dark deposits within channels. Based upon Earth analogs, most of the saltating material will keep moving until it reaches and piles up in lower wind velocity / adverse slope traps such as the observed dark deposits. The exact correlation of inertia with flat floor bottoms is also inconsistent with an aeolian explanation. One would expect an aeolian process to spread some of its thermal signature onto terraces or against walls. That is exactly what is observed in the visible with some localized dark deposits that do spread out onto the surrounding plains (e.g., see southern Shalbatana Vallis and also Hydraotes Channel in Figure 4.1). Aeolian explanations, whether depositional or deflational, are also inconsistent with the thermal homogeneities in serpentine regions of the channels, such as around buttes in northern Hydraotes Chaos.

A several centimeter thick sand blanket within the channels, although perhaps consistent with the thermal homogeneity, is inconsistent with other observations. One

would expect a complete sand blanketing to spread somewhat to the surroundings. Also, the visible heterogeneity seen in some places may be inconsistent with a sand sea. Dune features are also not obvious throughout the channels in Viking images, although resolution is a problem.

Preferential aeolian deflation within the channels also seems inadequate to explain the overall inertia enhancement, although it may play some role. As with aeolian deposition, one would expect aeolian deflation to cause greater thermal heterogeneity, particularly in serpentine channel regions. Any topographic obstacle or channel bend would presumably affect the amount of deflation and eventual deposition of particles. An even greater difficulty with aeolian deflation as a sole explanation is that to match the observations, it must uniformly strip flat floors, but not buttes, benches, or the surroundings. Then, even if aeolian deflation has taken place, what remains on the surfaces of the floors? Deflation could not have been too effective stripping the channels down to rock. The inertias are far below the inertias of at least 30 or 40 expected for bare rock on Mars. Although rock abundances for some channels are higher than average Mars, they are still probably less than 20percent [based upon *Christensen*, 1986; *Craddock et al.*, 1988]. Thus, even deflation would have to leave significant fines behind. This could be accomplished by bonding of the fines, some kind or armoring of the surface by rocks, or a self-limiting stripping process where a natural limit is reached on the amount of saltating fine material that can be stripped away [M. C. Malin, personal communication, 1993]. However, one still has difficulty explaining thermal homogeneity and flat floor thermal correlation, including in serpentine regions.

4.6.4 Channel Formation Processes: Fretting vs. Flooding

Two categories of channel formation processes may have resulted in channel inertia enhancement: catastrophic flooding or fretting. Both are consistent with the thermally distinctive characteristic of the channel floors.

Most of the thermally distinct portions of observed channels have flat, wide floors devoid of large scale bedforms. Steep, sometimes scalloped, walls are also associated with most thermally distinct channels. These morphologies are indicative of fretting [*Sharp*, 1973]. Channel sections that are not particularly thermally distinct, such as eastern Ravi and southern Ares have bedforms indicative of catastrophic flooding, but not fretting [*Sharp and Malin*, 1975; *Baker*, 1982]. Thus, I favor a fretting over a catastrophic flooding cause of the inertia enhancement.

Fretting here refers to wet or dry sapping, mass wasting, and possible debris flow [*Sharp*, 1973], although we emphasize that it is not a well understood process. For example, *Baker and Kochel* [1979] identified a whole range of mass movement, slope, and periglacial features associated with scalloped and fretted channel margins. Significantly, these features did contrast with the suite of cataclysmic flood bedforms found on the floors of some channels. Fretting is morphologically well defined for Mars, and it does contrast with channels showing well defined catastrophic flooding bedforms. Thus, whatever the exact fretting processes, fretted morphologies do appear to be associated with the channels showing enhanced inertias in this study. Although catastrophic flooding undoubtedly occurred in some of these channels, fretting likely followed. Only the last significant process to affect the channels will affect the upper few centimeters that are sensed by diurnal thermal measurements.

Chaotic terrain is often associated with nearby fretted areas, such as in the Hydraotes Chaos region. Chaotic terrain may represent an intermediate stage that in some cases was eventually smoothed to form fretted areas [*Sharp*, 1973]. It often has enhanced inertia (e.g., in Hydraotes Chaos) as observed both in the Termoskan data and in IRTM data [e.g., *Christensen and Kieffer*, 1979]. These inertia enhancements could be related to early stages of fretting.

Fretting as a general cause of channel inertia enhancements may be consistent with IRTM thermal studies of channel regions not observed by Termoskan. *Christensen and*

Kieffer [1979] found Simud, Tiu, and Shalbatana Valles to have inertia enhancements south of 10°N, but not north of there. To the north, these channels show increased catastrophic flooding bedforms on their floors such as grooves, and they do not commonly have steep, scalloped walls. *Christensen and Kieffer* found that higher inertia on the floor of Ares Vallis was most apparent north of 10° N and in a region near 7°N. Some of these portions of Ares are not obviously fretted, but most do not show obvious catastrophic flooding floor features as do the least thermally distinct portions south of about 6°N [*Sharp and Malin*, 1975].

Kasei Valles, found by *Christensen and Kieffer* [1979] to have enhanced inertia, was classed as a modified fretted channel by *Sharp and Malin* [1975]. Although it may show significant catastrophic flooding features in certain regions, it was likely last modified in most regions by fretting type processes [*Baker*, 1982]. *Craddock et al.* [1988] reported that Mangala Vallis did not appear thermally distinct from its surroundings. It shows significant catastrophic flooding floor features over much of its length [*Sharp and Malin*, 1975; *Baker*, 1982]. Thus, although it is speculative to extend a fretting explanation to a wider range of channels without higher resolution thermal data, IRTM data do seem generally consistent with a fretting explanation. Future missions' more global coverage will allow a more thorough testing of the generality of the fretting hypothesis.

Fretting could have increased channel inertias either by increasing the average rock abundance versus the surroundings or by preferentially increasing the bonding of fine particles. I consider these two possibilities in turn.

Increased rock abundance. An increased areal percentage of rocks (in the form of boulders, cobbles, gravel, or even pebbles) could be the cause of the channel inertia enhancement. Rocks may have been emplaced as debris derived from fretting, although it would have been challenging to both transport the rocks several km to several tens of km and still preserve a relatively uniform thermal inertia floor signature. However,

particularly given the uncertainty of the fretting process, this may have been possible. IRTM data indicated that rock abundances were higher for some channels including Shalbatana Vallis [*Craddock et al.*, 1988] than for the surrounding terrains. The percentages of rocks found, although high for Mars, are still nowhere near a complete covering of the surface. Thus, a finer clastic component still must play a significant role in determining inertia.

Bonding of fine materials. Variations in maturity of a duricrust (i.e., degree of bonding of a case-hardened crust) were suggested by *Jakosky and Christensen* [1986] to explain most of the low resolution thermal inertia variations on Mars. Areas where fines have been more efficiently bonded will have higher thermal inertias due to increased thermal conductivity. Duricrusts were observed at the Viking Lander sites [*Binder et al.*, 1977; *Mutch et al.*, 1977]. Water and/or salts were proposed as the agents of duricrust formation [Jakosky and Christensen, 1986]. Fretting may have increased bonding of fine materials within the channels due to increased presence of water and possibly brines either initially or secondarily.

Whether of primary or secondary origin, water for the bonding of materials was likely more accessible on the low, flat channel bottoms than on the surrounding plateaus or on the intermediate inertia benches. Bonding is also largely consistent with thermal variations strictly following the channel bottoms, even in serpentine regions. The absolute inertia values of the channels are consistent with values that could be obtained by bonding fine materials in combination with some rocks on the surface. The channel inertias are similar to somewhat higher than inertias in the areas of the Viking Landers (approximately 9 and 8 [*Kieffer*, 1976]). The lander sites showed relatively thin duricrusts as well as relatively high percentages of rocks [*Binder et al.*, 1977; *Mutch et al.*, 1977].

In addition to being consistent with the idea of *Jakosky and Christensen* [1986] that most inertia variations on Mars are due to variations in duricrust maturity, increased bonding in channels is also consistent with *Christensen's* [1986] finding that most thermal

inertia variations on Mars are due to variations in the fine component inertia, not the percentage of blocks. This theory does not explain the increased rock abundances found in some channels, but it is consistent with findings that regions with higher rock abundances generally have higher fine component inertias [*Christensen*, 1986].

Increased water or brines on channel floors may have come from the initial fretting due to sapping water flow or ice flow. This would require that the fines already be present on the surface at the time of channel floor formation and that the bonded material survive since the time of channel formation, which is difficult considering the long time since formation and the relative activity of the surface. In particular, dust storm fallout must be dealt with. One possible scenario is that aeolian deflation strips the new dust fallout off over time. This combined theory of aeolian deflation is favored over deflation alone because the surroundings can be stripped simultaneously, but the result re-exposes the bonded material. Thus, the channel alone does not have to be preferentially stripped and a relatively uniform surface will be exposed. There is an alternative that does not require the original surface to be preserved and that keeps many of the attractive features of a bonding theory.

Water may have been preferentially present on fretted channel floors after initial channel floor formation. Fretting may have emplaced water or ice near the surface, or the uniform floor level of fretted channels may represent the original depth of frozen ground [*Sharp*, 1973]. Processes acting over long time scales such as evaporation, adsorption and diffusion, or some other process may then have provided water at the very surface that accentuated the bonding of fines. The actual material bonded could have been original or could have been dust that was deposited over time in the channels as a result of dust storm fallout. Post floor formation bonding would be consistent with the apparent Termoskan observation that landslides and ejecta blankets appear thermally similar to the surrounding channel floors. However, these features are just at the limit of Termoskan's

resolution, so this observation will have to be confirmed with future higher resolution missions.

Thus, post floor formation bonding avoids some of the difficulties involved with preserving an original surface. The theory is somewhat speculative, however, given uncertainties on how this mechanism would act and at what rates. Whatever the actual process, the association of water with the formation of the channels and the location of channel floors closer to water and ice tables argue for the hydrologic plausibility of a preferential bonding explanation.

4.7 Summary and Conclusions

Utilizing the Termoskan data, I conclude that channels on Mars generally have higher inertia than their surroundings, consistent with IRTM studies. For the first time, I observe that the thermal inertia boundaries very closely match flat channel floor boundaries. Atmospheric and geometric effects are not sufficient to cause the inertia enhancement. I agree with previous researchers that localized, dark, high inertia areas within channels are likely aeolian in nature. I disagree with some researchers that aeolian deposits fill the channels or are responsible for the overall thermal inertia enhancement. Small scale aeolian deposition or aeolian deflation may play roles in the inertia enhancement. However, largely because of the thermal homogeneity of the channel floors, I favor alternate explanations.

Fretting or catastrophic flooding may have emplaced more rocks on channel floors or caused increased bonding of fines due to the presence of water. I favor fretting processes over flooding due to the flat floors and steep scalloped walls in most regions that show inertia enhancements. Alternatively, post-channel formation water that was preferentially present due to the low, flat fretted floors may have enhanced bonding of original fines or dust fallout. Future missions should be able to distinguish between competing theories of inertia enhancement. The possibility that the flat channel floors owe

their high inertia to water related bonding of fines argues for high priority for these sites in future exploration.

The tragic loss of Mars Observer (MO) occurred while this paper was being revised. We have still chosen to include a discussion of MO instruments and their potential contribution to the study of channels and valleys because the comments will be generally applicable to whatever analogous instruments fly on future missions. The Mars Observer Camera's (MOC) unprecedented high resolution (up to 1.4 m/pixel [*Malin et al.*, 1992]) would have enabled channel floor surface morphologies indicative of aeolian, flooding, or fretting processes to be recognized. These morphologies may include: dunes, water flow morphologies, large boulders, and some mass wasting features. The Mars Observer laser altimeter (MOLA) profiles, with a vertical precision of about 2 m and horizontal resolution of about 300 m [*Zuber et al.*, 1992], would have complemented MOC by providing detailed topographic information and some roughness information that will show how flat and smooth the floors really are and how steep the walls are, allowing slope versus angle of repose comparisons for the walls. The high resolution stereo camera (HRSC) on Mars '94 will obtain both high resolution imaging and topographic information.

Also on Mars Observer, the thermal emission spectrometer (TES) [*Christensen et al.*, 1992] and the pressure modulator infrared radiometer (PMIRR) [*McCleese et al.*, 1992], via global thermal inertia and albedo coverage, would have given insight into the origin of the channel inertia enhancements. The correlation of channel inertia enhancements with fretted morphologies versus purely catastrophic flood morphologies would have been tested globally. TES also would have contributed significantly to understanding the small scale cause of the enhancements via rock abundances and fine component inertias in 3 km/pixel maps derived using multi-wavelength methods similar to *Christensen* [1983; 1986]. Thus, increased rock theories could be directly compared with increased fine component processes, whether larger particles or bonding. TES spectral

mapping would have indicated compositional differences between channels and surroundings.

Termoskan 2 on M94 is expected to increase spatial resolution another order of magnitude from most of the Termoskan 1 data. The high spatial resolution targeted upon channels will enable tests of whether the thermal signal remains uniform at those resolutions. In addition, Termoskan 2 can observe more channels of varying morphologies elsewhere on Mars. Observations of small craters and their ejecta and landslides will test inertia enhancement theories and time scales.

The Omega imaging spectrometer on M94 should give important near IR spectral information about the channels. In particular, Omega will facilitate mapping of trace amounts of hydrated minerals as was done at lower resolution for other Mars regions with the Phobos '88 ISM instrument [*Erard et al.*, 1991]. I would expect enhanced hydration signatures for the channel floors if significant bonding has taken place. Thermally distinctive channel floors also represent interesting locations for future landers due to their unique history and the probable surface presence of material from various stratigraphic layers and locations.

Acknowledgments. I thank Philip Christensen and Vic Baker for thoughtful reviews of the submitted manuscript, and Michael Malin for helpful discussions. Funding for this research was provided by NASA grants NAGW-1426 and NAGW-2491. Division of Geological and Planetary Sciences, California Institute of Technology contribution 5287.

Chapter 5

Sunward I've climbed, and joined the tumbling mirth
Of sun-split clouds --and done a hundred things...
John Gillespie Magee, Jr.

MISCELLANEOUS TOPICAL STUDIES

This chapter presents several miscellaneous topical studies that are smaller in scope than those presented in Chapters 3 and 4. These studies are also not as in depth, complete, or detailed as those in Chapters 3 and 4. Nonetheless, they have yielded interesting information worthy of documentation and discussion. The first section presents results from atmospheric limb studies that identified thermal morning limb brightening, visible cloud features, and significant visible atmospheric scattering to very high altitudes. Most of this material was originally presented in *Murray et al.* [1991]. Interpretations in this section were significantly aided by discussions with Prof. David Paige of UCLA and with Dr. Michelle Santee and Dr. David Crisp of JPL.

Section 5.2 presents a discussion of the one major location in the data where the highland-lowland boundary was observed. Section 5.3 presents a brief description and plausible interpretations for fine structure thermal features that appear to emanate from the caldera of Arsia Mons. It presents a brief, generalized discussion of fine thermal structure and thermal boundaries throughout the data set.

5.1 Atmospheric Limb Studies

Three of the four visible and thermal panoramas include the morning limb, and one includes the evening limb as well. The limb profiles of March 26 have a vertical resolution of approximately 3 km/pixel, which approaches that of the Viking Orbiter Camera [*Jaquin et al.*, 1986]. The limb profiles from the February 11 panorama have a vertical resolution of about 1.3 km/pixel in the N-S direction and are somewhat coarser in the E-W direction. They are confused by large gores in the data as discussed in Chapter 2. Termoskan limb

profiles provide information about the vertical structure of Mars' atmosphere. Significant features are seen in both thermal and visible limb profiles.

Figure 5.1 shows morning limb thermal and visible images from the first of the March 26 observing sessions (panorama 3). Contrast in the images has been stretched to enhance limb features. Figure 5.2 shows a single morning limb profile taken from those images, both in the visible (dashed curve) and infrared (solid curve). The data numbers for each channel are plotted as a function of the elapsed time from the beginning of the scan. The Termoskan observations began off the morning limb when the instrument was activated. They then moved across the limb and onto the surface of Mars. Figure 5.3 shows a second morning limb profile also taken during the third observing session.

The absolute time of the limb crossing is not available accurately enough solely from trajectory information to identify the pixel corresponding to the position of the physical limb. That would require 1-3 km absolute orbital knowledge. Not only is this an unrealistic goal, but also much of the geometry data was not passed on to the Termoskan team. Furthermore, the spacecraft rocked slightly about the anti-solar direction in response to its attitude control system (see Figure 6.6). These slow deviations (which were not monitored during the data-taking session) introduce only an insignificant distortion into the Termoskan images. Yet, the absolute time the Termoskan field of view crossed the limb may be uncertain by 10 or 20 seconds due to this slow deviation from the precise anti-solar direction. Analogous problems in determining the absolute location of Phobos' shadow are discussed in Chapter 6. From the analysis presented here, I believe the physical limb was encountered near the point where the infrared signal was first detected. This places the limb crossing at about 26 seconds - close to the beginning of the infrared signal.

Morning thermal limb brightening is evident in thermal images (Figure 5.1) and in the individual limb profiles shown in Figures 5.2 and 5.3. It is also observed in the higher resolution data from February 11. Limb brightening in thermal emission usually arises

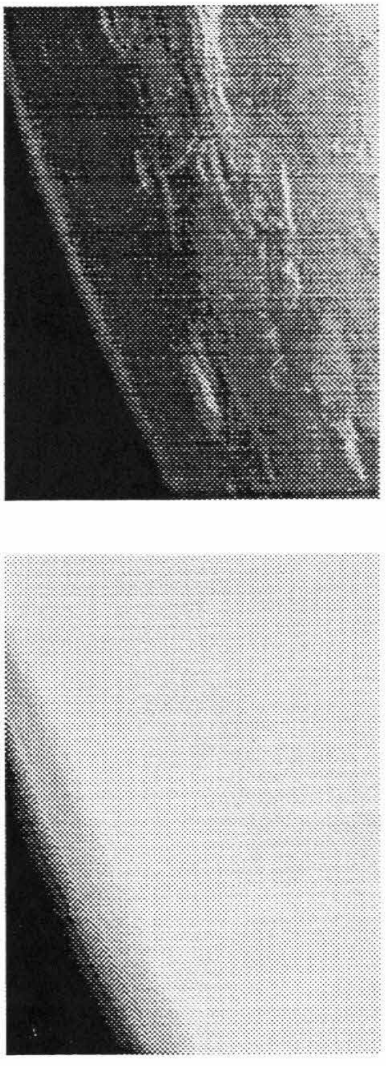

Figure 5.1: Termoskan thermal (top) and visible (bottom) images showing the morning limb from the third set of panoramas. North is top. Data has been stretched to enhance contrast at the limb at the expense of surface features. Note the limb brightening in the thermal channel, i.e., the bright (warm) layer the limb.

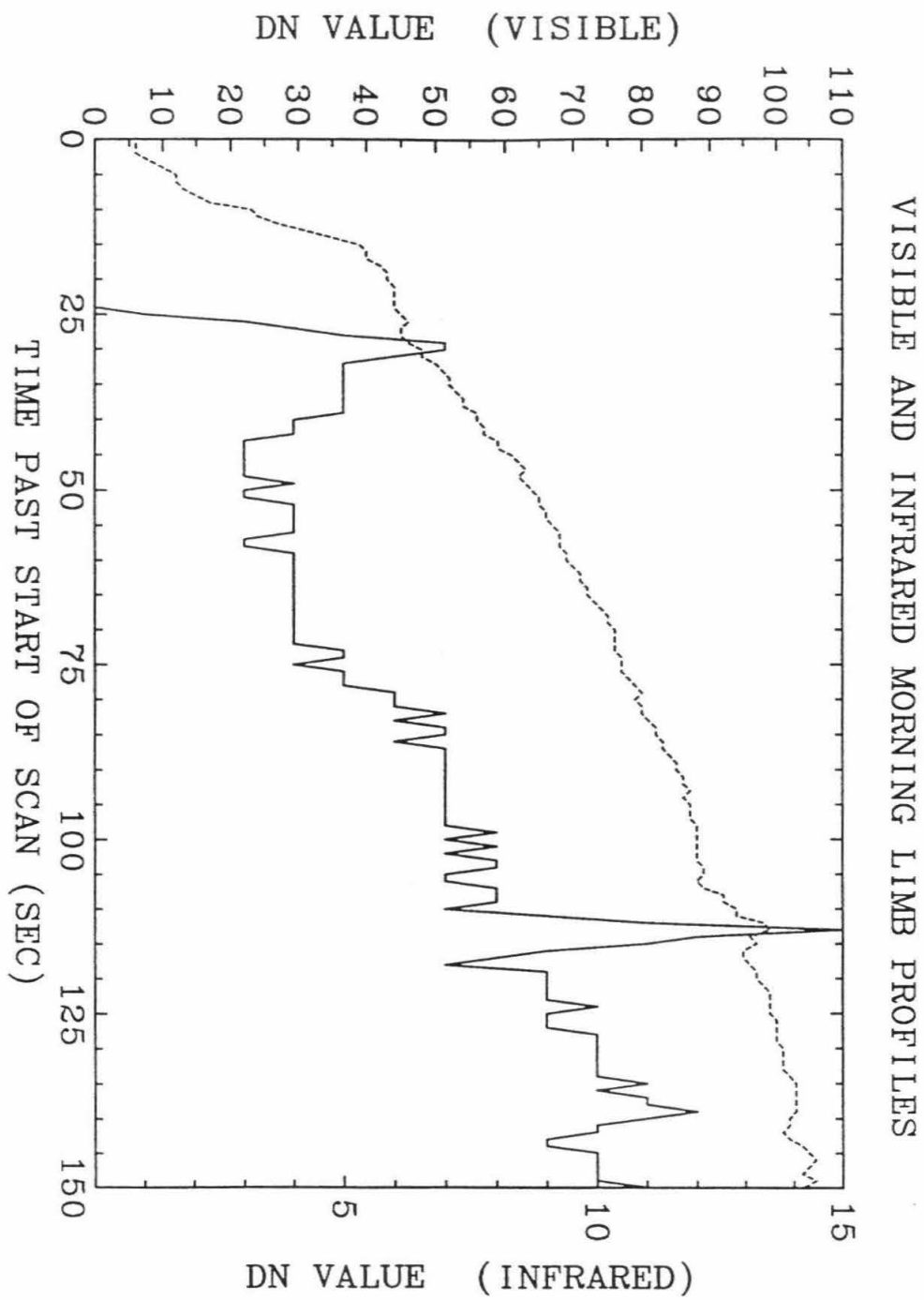

Figure 5.2: A single morning limb profile for both the visible (dashed curve) and the infrared (solid curve) channels. The solid limb was encountered at approximately 26 seconds after the start of the scan. Note the IR limb brightening seen at 26 seconds and the crater rim seen at 113 seconds.

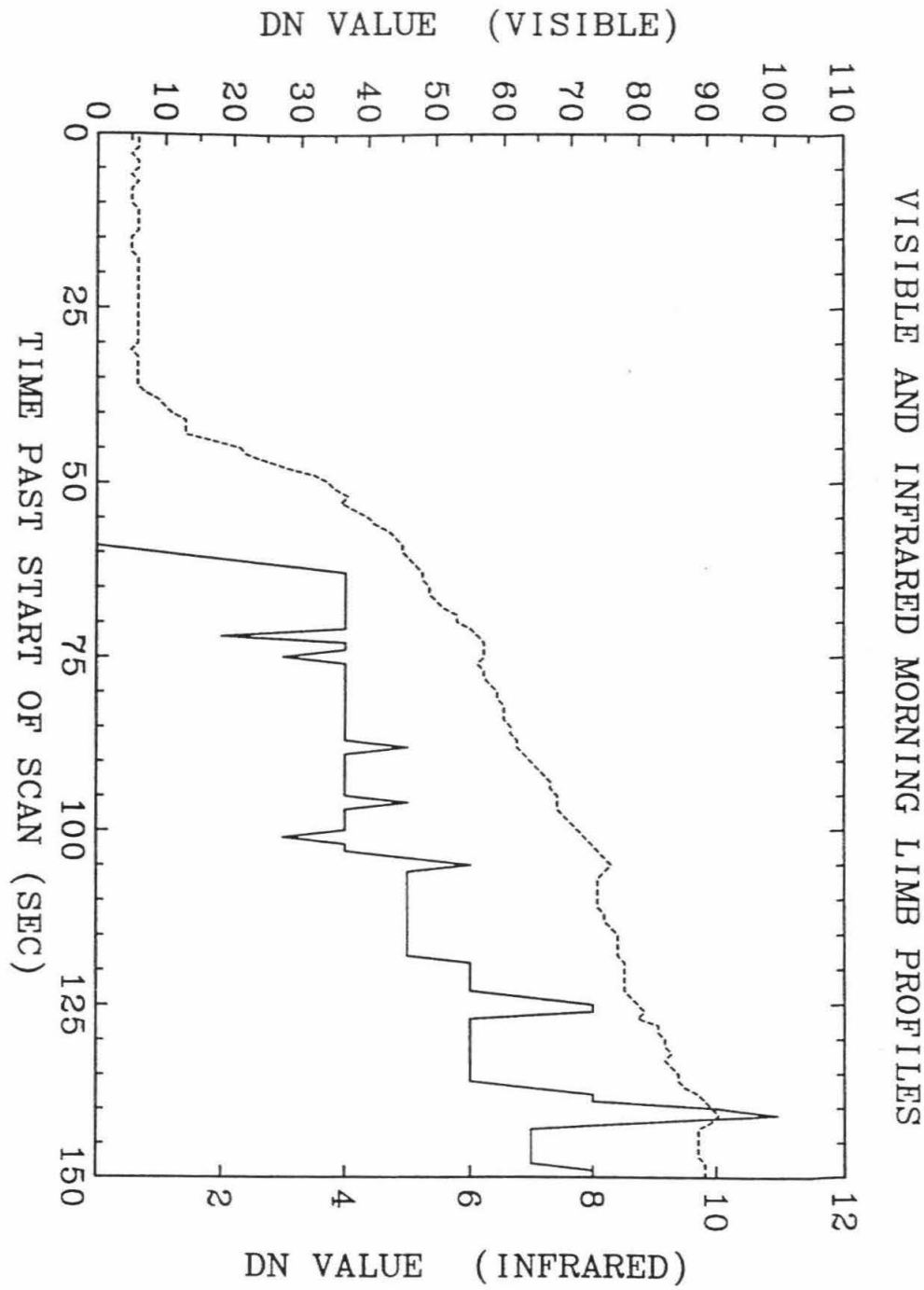

Figure 5.3: Another 1 pixel wide morning limb profile for both the visible (dashed curve) and the infrared (solid curve) channels. Note that in this IR profile, the signal levels off rather than dropping from the limb brightened peak.

from viewing a partially transparent atmosphere containing a temperature inversion. It is difficult to imagine a plausible purely surface origin, though in theory it is possible. An atmospheric effect is my preferred explanation, particularly since the limb brightening occurs over a very large range of latitudes. In the present case, a discernible peak in thermal brightness just off the limb means the dawn atmosphere was warmer than the surface. Furthermore, the atmosphere must have contained a sufficient abundance of thermally emitting particles (dust or ice) to supply the needed flux. Mars' atmospheric gases are nearly transparent at Termoskan's spectral passband. Mariner 9, Viking Orbiter, and Viking Lander observations together suggest that this requirement could be satisfied near the morning terminator by a diurnal predawn ice-crystal fog which often forms [*Jakosky*, 1985]. In addition, some abundance of dust particles is always to be expected in the Mars atmosphere.

The high emissivity of Mars' surface allows it to cool more efficiently during the night than can the gas-dominated atmosphere. An early-morning atmospheric temperature inversion results. This effect is accentuated because the atmosphere "sees" sunlight before the surface. I infer that the sharp peak in thermal emission corresponds to the maximum atmospheric path length sensed just before limb crossing. Once the limb was crossed, Termoskan sensed a decreasing fraction of emission from the warmer atmosphere and an increasing fraction from the colder surface. The composite signal began to decline in magnitude from the peak, or remained constant (as in Figure 5.3). As the scan continued, the emission angle from the surface decreased. The instrument continued to sense less of the warm atmosphere. Then the thermal emission signal began to increase again as the scan progressively viewed warmer and warmer morning areas of the surface.

To test this concept quantitatively, David Paige used a delta-Eddington spherical shell model developed for the Mars Observer PMIRR limb sounder. He found that a water ice haze with a scale height of 5 km (isothermal atmosphere at 200 K, surface at 175 K) could produce a thermal brightness signature matching the one in Figure 5.2

[*Murray et al.*, 1991]. A similar abundance of dust particles also could produce the same result. The thermal profiles in Figure 5.2 and Figure 5.3 differ in degree of limb brightening. This could result from either a local difference in the temperature profile between the atmosphere and the surface or a local difference in the opacity of the atmosphere. Temperature and opacity effects cannot be separated using only one channel.

As seen in Figures 5.2 and 5.3, the visible channel morning limb profiles have significantly different shapes than the thermal profiles. The visible radiance increased for about 24 seconds before the onset of the first infrared signal. This relationship implies the presence of visible scatterers in the atmosphere to about 70 km above the physical surface, which is well above the region where Termoskan sensed tangible thermal emission. This result is consistent with the conclusion in Chapter 2 that the visible optical depth is significantly larger than the infrared optical depth and the particles in the atmosphere are smaller than the infrared wavelengths. Note that the visible channel profiles appear very similar to Viking camera profiles presented in *Jaquin et al.* [1976].

Figure 5.4 shows image data and Figure 5.5 displays profile data from the evening limb crossing of panorama 3. Time on the horizontal axis refers to a local data file. It is not tied into the full panorama. Here the situation is reversed from the morning limb: a peak in brightness was recorded in the visible but not in the infrared channel. Viking observations show the existence of large scale transient early morning atmospheric phenomena, but do not predict similar effects on the evening limb. Furthermore, because the surface absorbs sunlight much more efficiently than the atmosphere, it is much warmer at the end of the day. Thus, surface emission overwhelms emission from atmospheric particles near the evening limb. (Note the differences in DN scale between morning and evening scans). Therefore, no limb brightening is observed in the thermal emission from the evening limb.

The extent of the visible profile for the evening limb implies at least 60 km of scattering atmosphere. Figure 5.6 shows a second evening limb profile also taken during

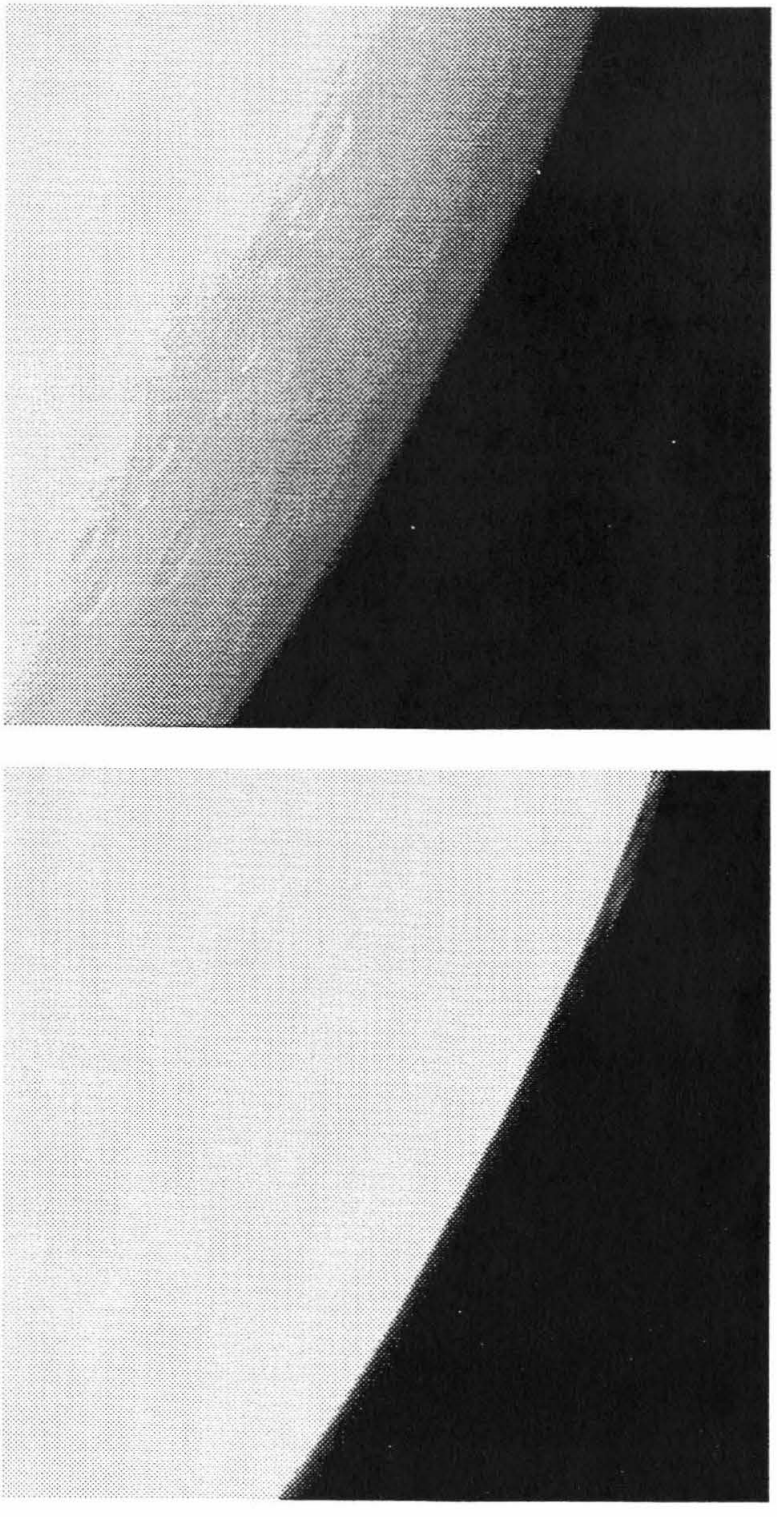

Figure 5.4: Termoskan thermal (top) and visible (bottom) images showing the evening limb from the third set of panoramas. Data has been stretched to enhance contrast at the limb at the expense of surface features. Note the absence of limb brightening in the thermal channel. Also, note the bright, high altitude cloud features that can be seen in the visible channel.

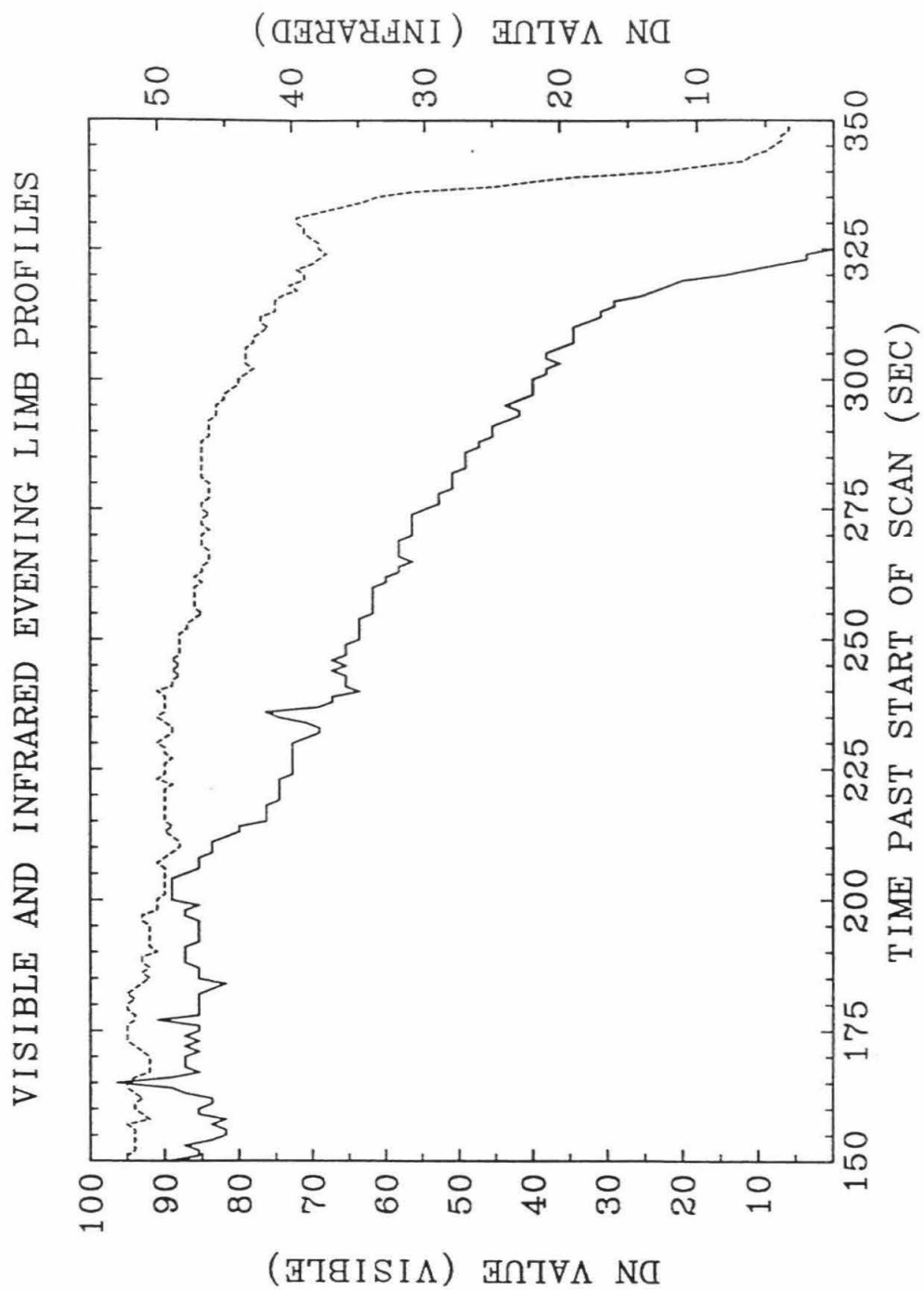

Figure 5.5: A single evening limb profile for both the visible (dashed curve) and the infrared (solid curve) channels. Note that the times on the horizontal axis are local to the particular data file and do not represent actual times along the scan. Notice there is no IR evening limb brightening.

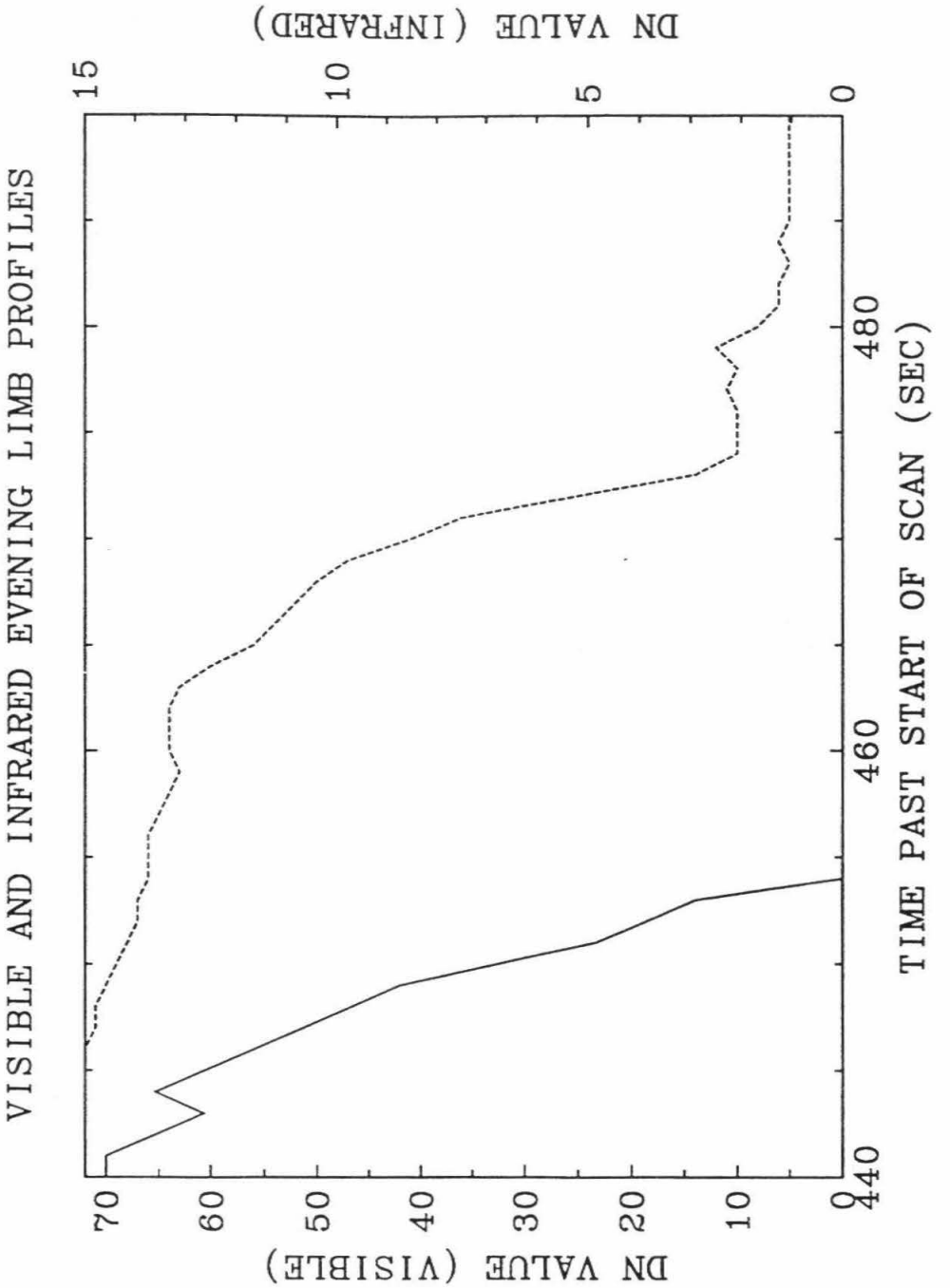

Figure 5.6: Another single evening limb profile seen this time on a different scale. Again times are local to the particular data file. Note the peak in visible brightness at 479 seconds which is a distinct cloud feature (seen also in the Auguste experiment).

panorama 3. The peak in visible brightness at 479 seconds corresponds to a distinct cloud feature. Because this cloud and the higher one seen in Figure 5.6 are so sharply defined, there can be no significant scattered light problem in the optics of the instrument. These stratospheric cloud features may correlate with those observed by Phobos '88 AUGUST experiment [*Blaumont*, 1991].

5.2 The Highland-Lowland Boundary

One of the fundamental questions about Martian geologic history concerns the origin of the crustal dichotomy between the ancient cratered highlands in the south and the northern lowland plains. Theories to explain the dichotomy range from mantle convection [*e.g., Wise et al.*, 1979] to giant impacts [*e.g., Wilhelms and Squyres*, 1974]. Understanding the nature of the current highland-lowland boundary is obviously of importance for testing different theories. Termoskan observed the boundary in a portion of the Aeolis Quadrangle (MC-23), giving us the first ever high resolution thermal imaging of the boundary region (See Figure 5.7). These images show the boundary to be thermally distinct.

IRTM derived thermal inertias indicate that the highlands generally have higher inertia than the lowlands at the 2° x 2° scale [*Palluconi and Kieffer*, 1981]. *Zimbelman and Leshin* [1987] found similar results using a non-imaging, geographically limited set of the highest resolution IRTM data (best resolution 2 km x 5 km). They concluded that thermal inertias in this region are more strongly controlled by location of the terrain within either the northern plains or the southern highlands than by other properties intrinsic to specific geologic units. The Termoskan data also indicate that the highlands have higher inertia. They also go beyond Viking data by giving a detailed look all along the boundary in this region and an idea of the thermal sharpness of the boundary.

Termoskan data observed the boundary from 170°W to 205°W longitude. In this region, Termoskan observed a latitude range from approximately 8°S to 20°S. The

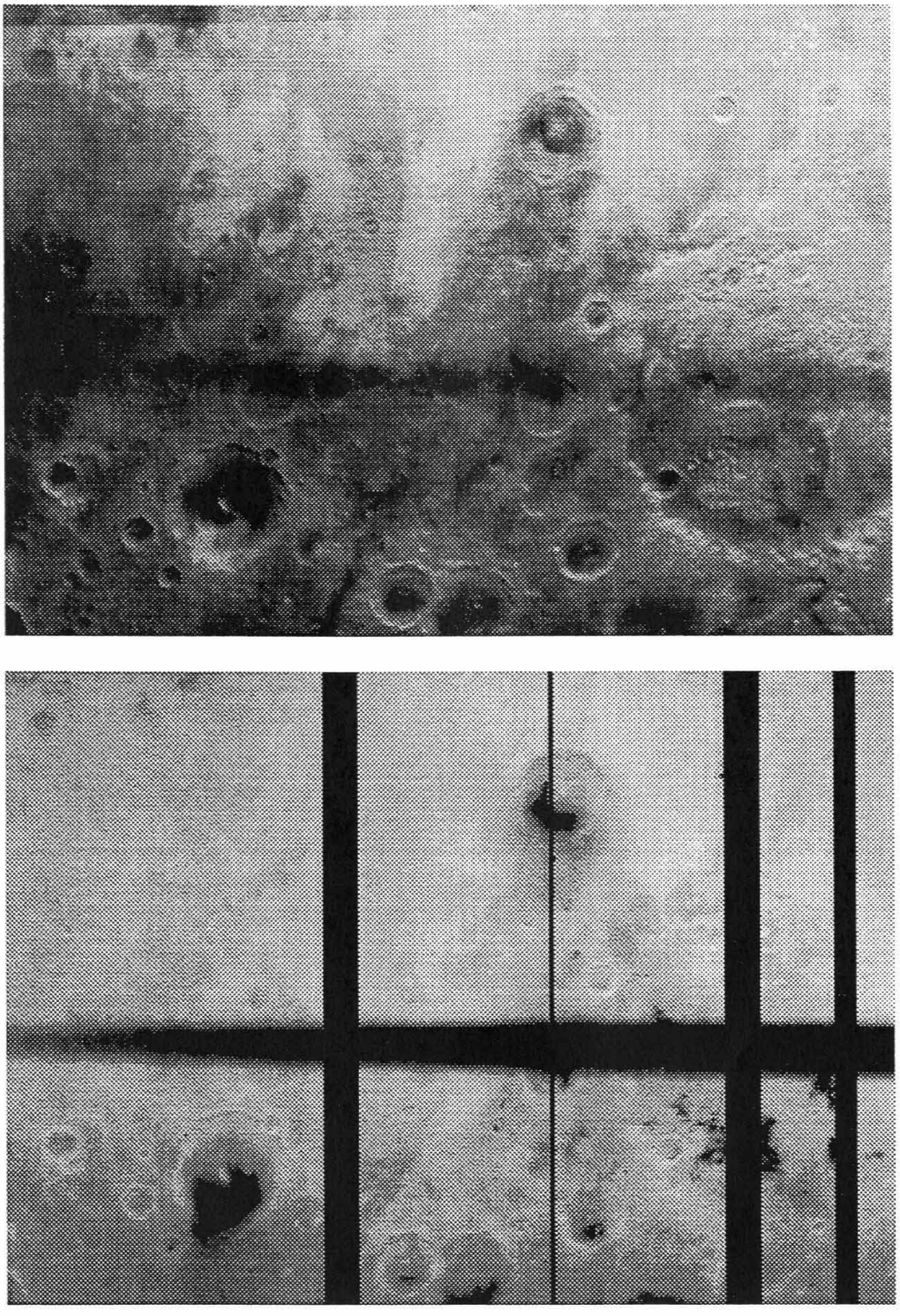

Figure 5.7: Termoskan Thermal (top) and visible (bottom) images showing part of the highland-lowland boundary region. North is top. Images are centered approximately upon 14°S, 191°W. Note the warmer lowland regions in the northern portion of the image (the lowlands have fewer craters, indicating younger age), and the cooler heavily cratered highlands in the southern portions. The thermal boundary very closely follows the geologic boundary. The dark east-west streak is the shadow of Phobos.

lowland side of the boundary is distinctly warmer than the nearby highland material for most of the area observed (see Figure 5.7). The thermal boundary very closely matches the geologic boundary zone [as mapped by *Greeley and Guest*, 1987]. In the visible channel there is generally no distinct boundary, but the lowlands tend to be either brighter or similar to the highlands. Thus, for the midday observing conditions these observations imply that the lowlands have a lower thermal inertia than the highlands. This is consistent with the IRTM derived *Palluconi and Kieffer* [1981] inertias for this region.

The exact nature of the thermal boundary is variable over the range of the highland-lowland boundary observed. In some areas the boundary is very sharp with a 3 K temperature jump in 4 km or less. In these areas the boundary can't be defined any sharper than 4 km (2 pixels) because usually there is a northward sun heated scarp which fills one pixel. I avoid drawing thermal conclusions about scarp pixels due to the uncertain magnitude of the slope heating effects. In other locations, the thermal "boundary" is smeared over 50 km or more. Usually, even where there is a sharp (few km) initial boundary, the temperature continues to increase for many tens of km into the lowlands.

In summary, the highland-lowland boundary in the Aeolis Quadrangle appears strongly correlated with a high-low thermal inertia boundary. The sharpness of that boundary varies from less than 4 km to more than 50 km. Whether there is a "sharp" boundary or smooth boundary, inertias continue to decrease gradually for many tens of km into the lowlands. Thus, whatever process caused the current lower inertia of the upper centimeters of the lowlands acted strongly near the boundary in some places. In all cases, it gradually acted more and more further into the lowlands.

5.3 Fine Thermal Structure: Arsia Mons

The flanks of Arsia Mons show much fine thermal structure as seen Figure 5.8 and as roughly mapped from the Termoskan data by *Crumpler et al.* [1990]. The far reaching finger-like thermal/visible structures extending radially from the caldera appear warmer

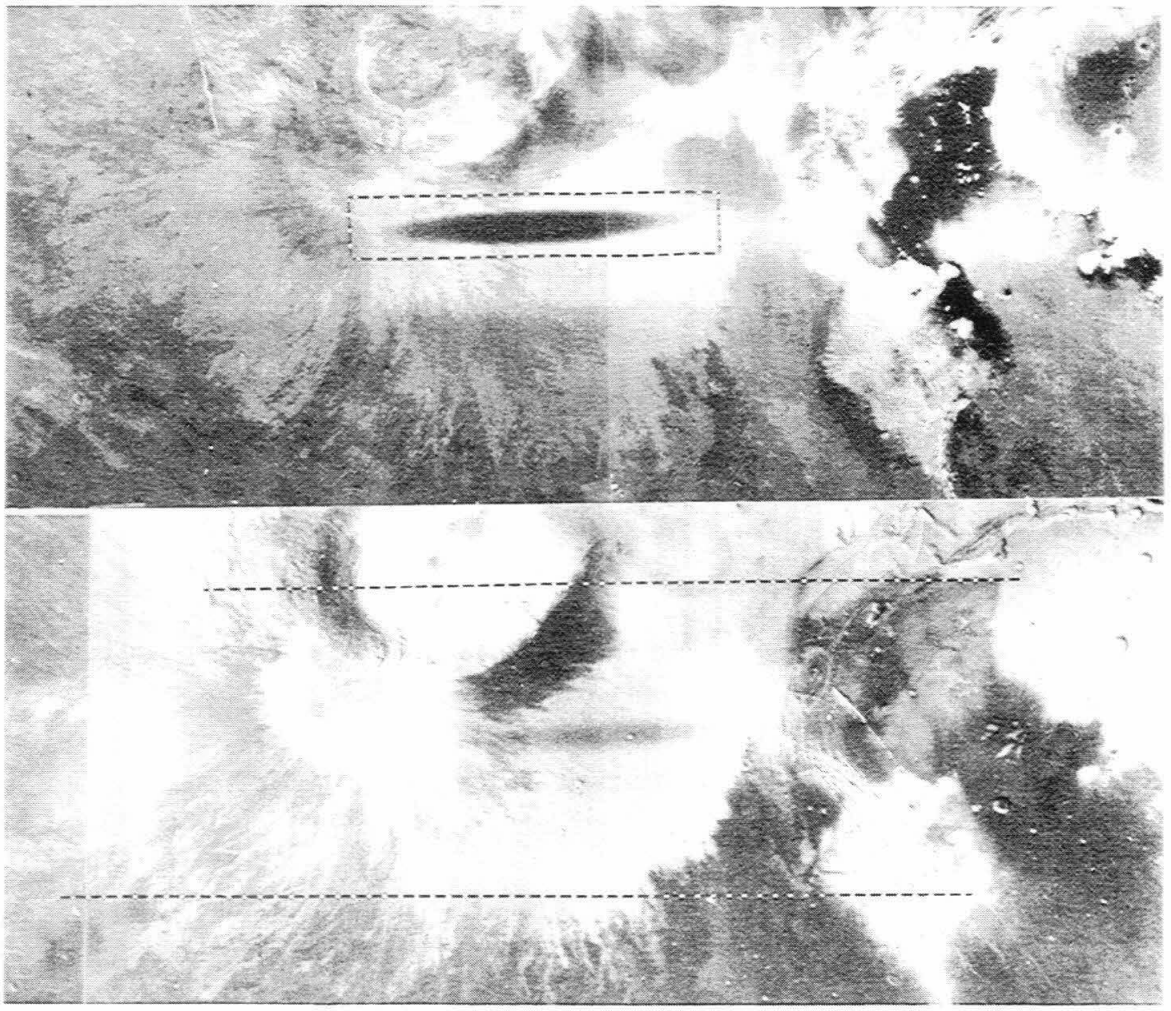

Figure 5.8: Termoskan visible (top) and thermal (bottom) images showing Arsia Mons and its flanks. Note the fine thermal structure emanating from the caldera that corresponds to flow units [*Crumpler et al.*, 1990]. The thermal inertia difference may be primary or secondary.

and brighter than the surrounding terrain. These finger-like features may correspond to the ends of a flow unit, as mentioned by *Crumpler et al.* [1990]. The brighter, warmer fingers that appear to have emanated either in or near the caldera have lower inertia than the region that they have flowed into.

It is surprising to find fine thermal structure corresponding to flows in this region of low inertias [*Palluconi and Kieffer*, 1981], low rock abundances [*Christensen*, 1986a], and presumed current dust deposition [*Kieffer et al.*, 1977; *Zimbelman and Kieffer*, 1979; *Palluconi and Kieffer*, 1981; *Christensen*, 1986b], although much of the region is radar bright [*Muhleman et al.*, 1991]. There are several possible explanations: 1 - physical differences in the flows themselves cause the difference as suggested by *Crumpler et al.* [1990]; 2 - the surface rock abundances on the flows, possibly due to the flows themselves, differ on the lower and higher inertia units; 3 - different properties of the flow units cause a preferential trapping of aeolian material on one unit as opposed to the other; 4 - the greater age of the higher inertia unit has allowed more time for the bonding of fines; or 5 - the lower topography of the higher inertia unit has induced greater bonding of fines due to greater availability of water from subsurface or other sources. Although it is difficult to separate these processes with available data, the low inertias and low rock abundances in the region lead me to favor explanations that involve secondary, presumably aeolian, material, possibly covering a radar bright substrate, i.e., explanations 3, 4, or 5.

This region is a good example of two significant general features within the Termoskan data. First, fine thermal structure is seen at the limit of resolution of the data. This is true even of panorama 1 with its 300 m/pixel resolution. This argues against any type of general aeolian blanketing in the regions observed. Before Termoskan, there were some questions about whether we would see significant thermal structure at these scales. The Termoskan results bode well not only for Termoskan analyses, but also for Mars Observer TES and Mars '94 Termoskan 2. In some cases fine thermal structure may be unrelated to local geology. However, in cases such as these apparent flow features, it is

related to the geology. Fine thermal structure does not appear everywhere in the data. Most of the ancient cratered highlands that were observed in the fourth observing session appear remarkably bland in the thermal.

Second, as can be seen in Figure 5.8, the individual low inertia fingers that probe the higher inertia material are part of a much longer thermal inertia boundary that extends for hundreds of km encircling southern Arsia Mons. Several large scale, relatively sharp thermal inertia boundaries are seen in the data. These include the highland-lowland boundary discussed in the last section and a boundary cutting across Syria Planum. Although these boundaries may have had different origins, Termoskan has provided new clues about them by identifying their sharpness at or near the Termoskan resolution.

Chapter 6

Dancing with my shadow,
and letting my shadow lead.
-Warrant

THE SHADOW OF PHOBOS ON MARS

This chapter describes analyses of Termoskan observations of the shadow of Phobos on Mars. Most of the shadow observations discussion (Section 6.2) appeared in *Murray et al.* [1991]. Here, I present three models of the shadow induced cooling of the Martian surface. Model 1 and its results were presented originally in abstracts *Betts et al.* [1990a; 1990b] and then formally published with several other preliminary Termoskan analyses in *Murray et al.* [1991]. That model and its results are presented in much greater detail here. Models 2 and 3, their descriptions, and their results have not yet been published, but I intend to submit them for publication in the near future.

Section 6.1 introduces the shadow observations and analyses. It also gives some historical background. Section 6.2 describes the shadow observations and the nature of the shadow on the surface. This is followed by a section describing in detail the three thermal models, including the inputs that were used from the Termoskan data. Section 6.4 compares the Termoskan thermal data with the model results to derive thermal inertias. Section 6.5 discusses the results, and the last section of this chapter discusses the three other shadow occurrences and potential for future Phobos shadow research. Readers who are not interested in the details of the models may wish to read at least the Introduction (Section 6.1) before skipping to the results (6.4) section. Obviously, reading the observations section (6.2) and the model description section (6.3) will enhance overall understanding.

6.1 Introduction

Mars' moonlet Phobos orbits Mars in an eight hour, circular, nearly equatorial orbit at an altitude of approximately 6300 km. During the time periods surrounding the Martian

equinoxes, Phobos casts a completely penumbral shadow on the surface of Mars' equatorial regions during portions of each orbit. A passing of the shadow would be viewed by an observer on the surface as a partial eclipse lasting roughly 20 seconds. Termoskan obtained the first ever thermal images of Phobos' shadow on the surface of Mars. Simultaneous visible images were also obtained.

Termoskan observed the shadow of Phobos on the surface of Mars during two of its four panoramas. There are four distinct shadow occurrences. Presented here is my analysis of the best observed and least complicated occurrence (shown in Figure 6.1). For this shadow occurrence, I have combined the observed decrease in visible illumination of the surface with the observed decrease in brightness temperature to calculate thermal inertias of the uppermost tenths of a millimeter of the Martian surface. I use three progressively more complicated thermal models. My preferred model (#3) combined with the data implies values of thermal inertia (roughly .9 to 1.4) that are significantly lower than those originally derived from Viking IRTM measurements (2 to 3.5) [*Palluconi and Kieffer*, 1981]; however, they are similar to those implied for IRTM data by *Haberle and Jakosky's* [1991] thermal model that includes increased atmospheric re-radiation. Note that the IRTM derived inertias are diurnally derived and are sensitive to centimeter depths. The shadow derived inertias sample the upper tenths of a millimeter of the surface. Thus, if layering exists at all, it is not very significant.

These Phobos shadow studies have an interesting historical background. Tomas Svitek and Bruce Murray at Caltech suggested attempted observations of the shadow to the Soviets long before the Phobos '88 spacecraft reached Mars. They noted that the orbit of the spacecraft was highly advantageous, being equatorial and very nearly that of the moon Phobos. The Soviets indicated that the observations were too complicated and that perhaps they would be considered after the primary mission was completed. However, the spacecraft failed before the primary mission was over. Nonetheless, essentially by chance, Termoskan obtained observations of the shadow as part of routine observations.

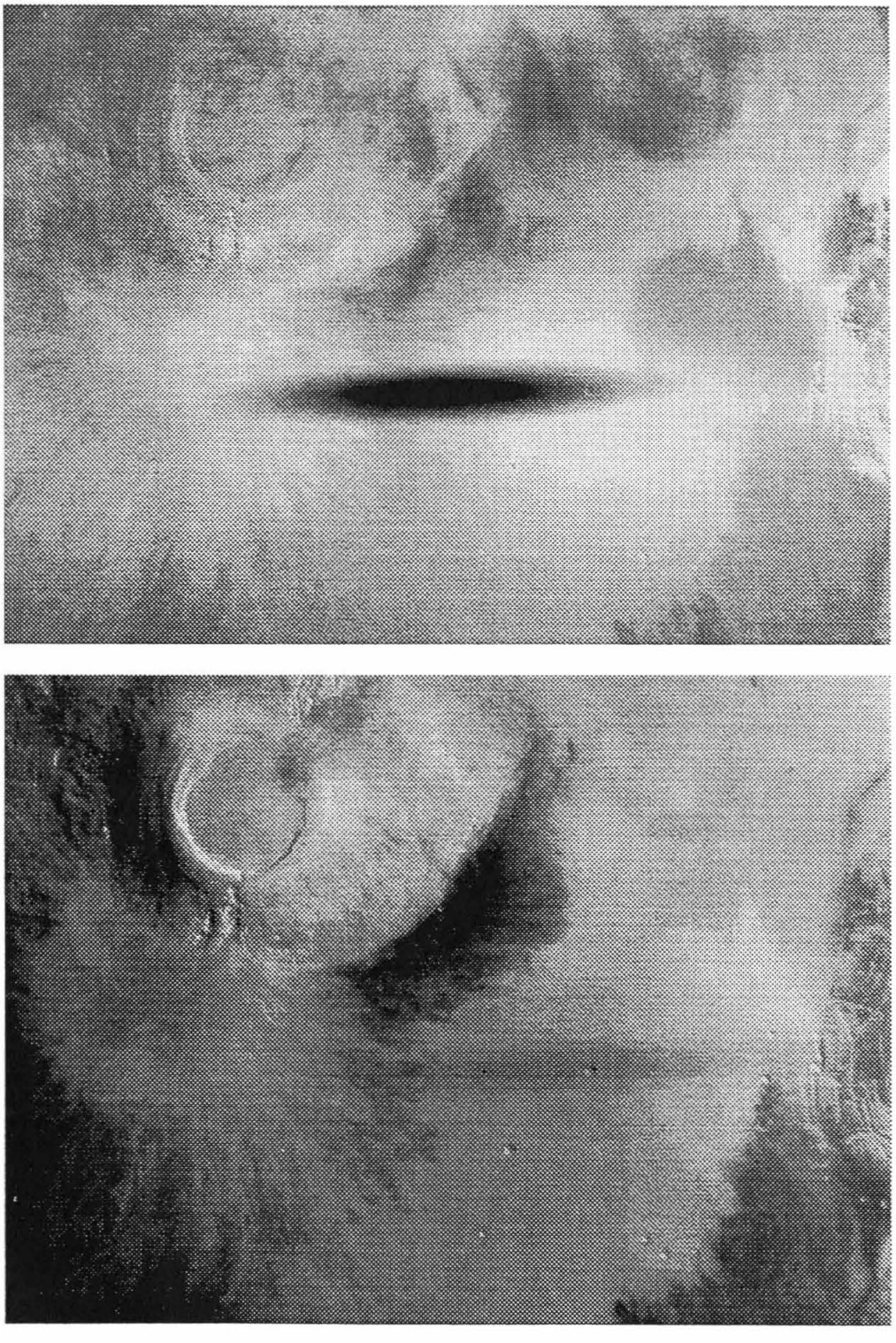

Figure 6.1: Phobos shadow images. Termoskan visible (top) and thermal (bottom) images showing the analyzed Phobos shadow occurrence on the flanks of Arsia Mons. Note that the shadow is observed first (further West) in the visible, then later (to the East) in the thermal. This is due to the delay in cooling after the onset of the shadow.

The similarity of the spacecraft to Phobos' orbit combined with Termoskan's anti-solar orientation (zero solar phase angle) conspired to put Termoskan's instantaneous field of view near the location of the shadow as it traveled across Mars' surface. However, because the spacecraft and moon were not actually in the same place, this orientation alone would have missed observing the shadow. "Fortunately," the spacecraft, and hence Termoskan, rocked slightly back and forth. Thus, Termoskan's instantaneous field of view rocked into and out of observing the shadow. This fortuitous combination of factors has allowed a unique analysis of the cooling from the shadow. This analysis gives never before available insight into the nature of the upper millimeter of Mars' surface in selected locations.

Tomas Svitek, working with Bruce Murray, did initial modelling and analysis of the shadow. I then independently produced a thermal model that reproduced Svitek's preliminary results. This model evolved just slightly into the form that is described as Model 1 here.

Since the time that the initial results were published in *Murray et al.* [1991], I have created two more detailed and realistic models. Here I present those models and their results for the first time. Model 2, my non-isothermal model, does not assume that the pre-eclipse temperatures are constant with depth as Model 1 did. *Haberle and Jakosky* [1991] compared theoretical considerations to *Betts et al.*, [1990a]. They concluded that atmospheric effects are less important for eclipse derived thermal inertias than for diurnally derived thermal inertias. To test atmospheric effects, I created Model 3 by adding a downward atmospheric flux term to Model 2.

6.2 The Shadow Observations

The Arsia Mons shadow occurrence analyzed here is shown in the images in Figure 6.1. East-West and North-South visible intensity and temperature profiles across the shadow are shown in Figures 6.2-6.5. Note the close correspondence of the North-

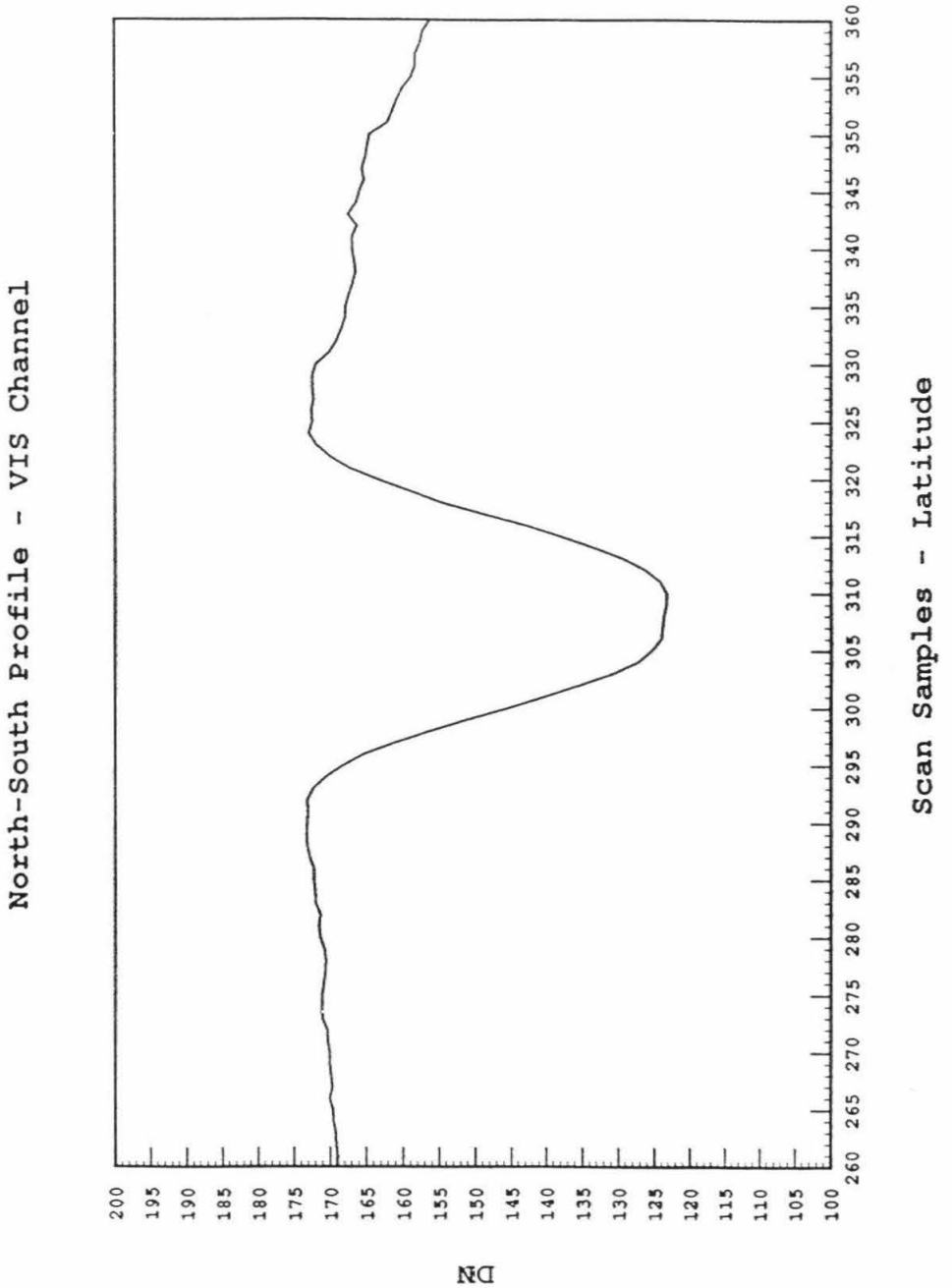

Figure 6.2: North-South profile - VIS channel. Reflectance from Martian surface as measured by Termoskan's visible channel. The curve plotted is an average of ten scan lines centered on the darkest portion of the Phobos shadow (14°S, 117°W). Note the high ratio of signal to noise.

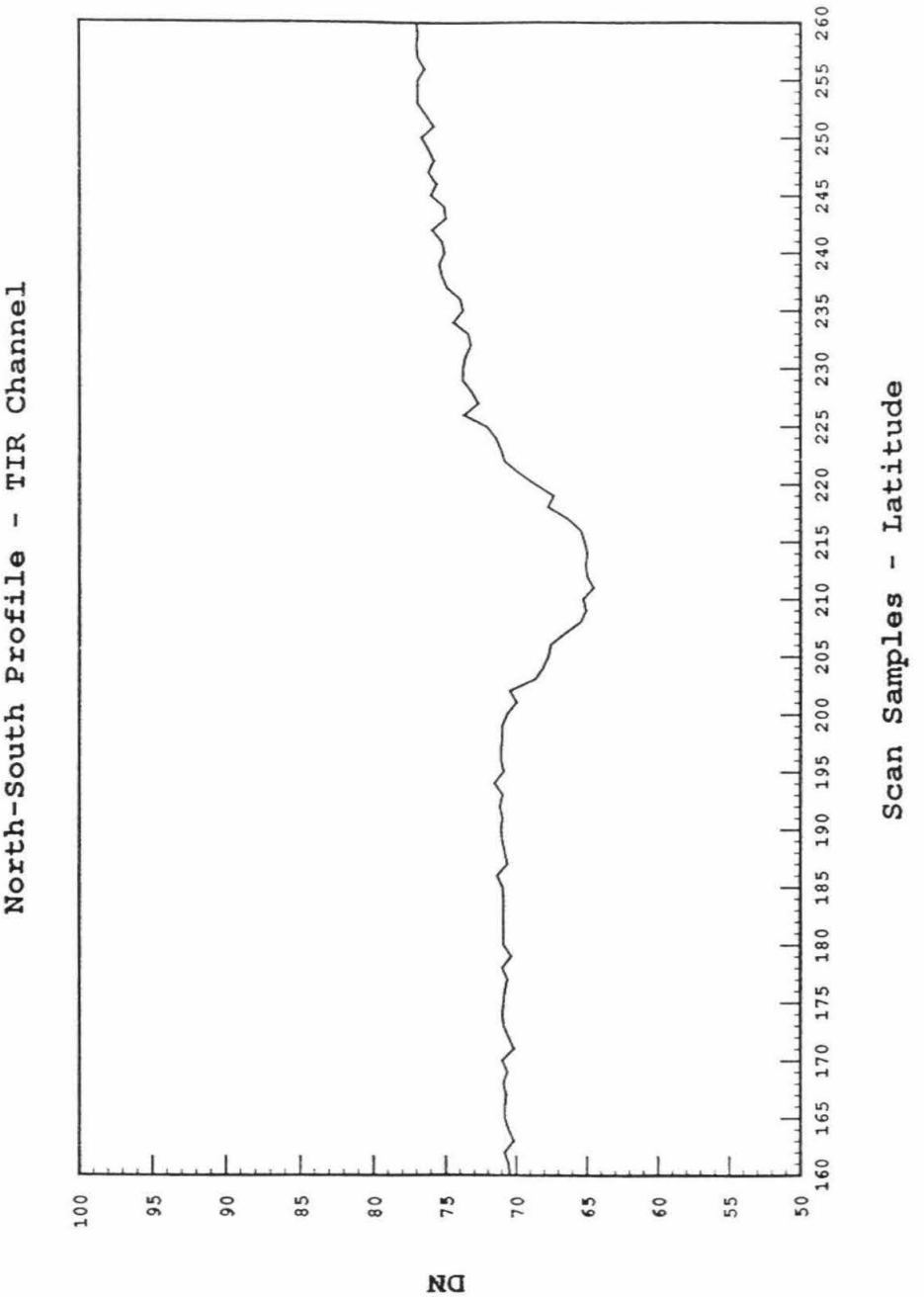

Figure 6.3: North-South profile - TIR channel. Thermal emission from Martian surface as measured by Termoskan's thermal infrared channel. The curve plotted in the figure is an average of ten scan lines centered on the coldest portion of the shadow (14°S, 116°W). Note the lower ratio of signal to noise compared with the visible channel. Also note the very regular 1 DN noise variations in every eighth pixel.

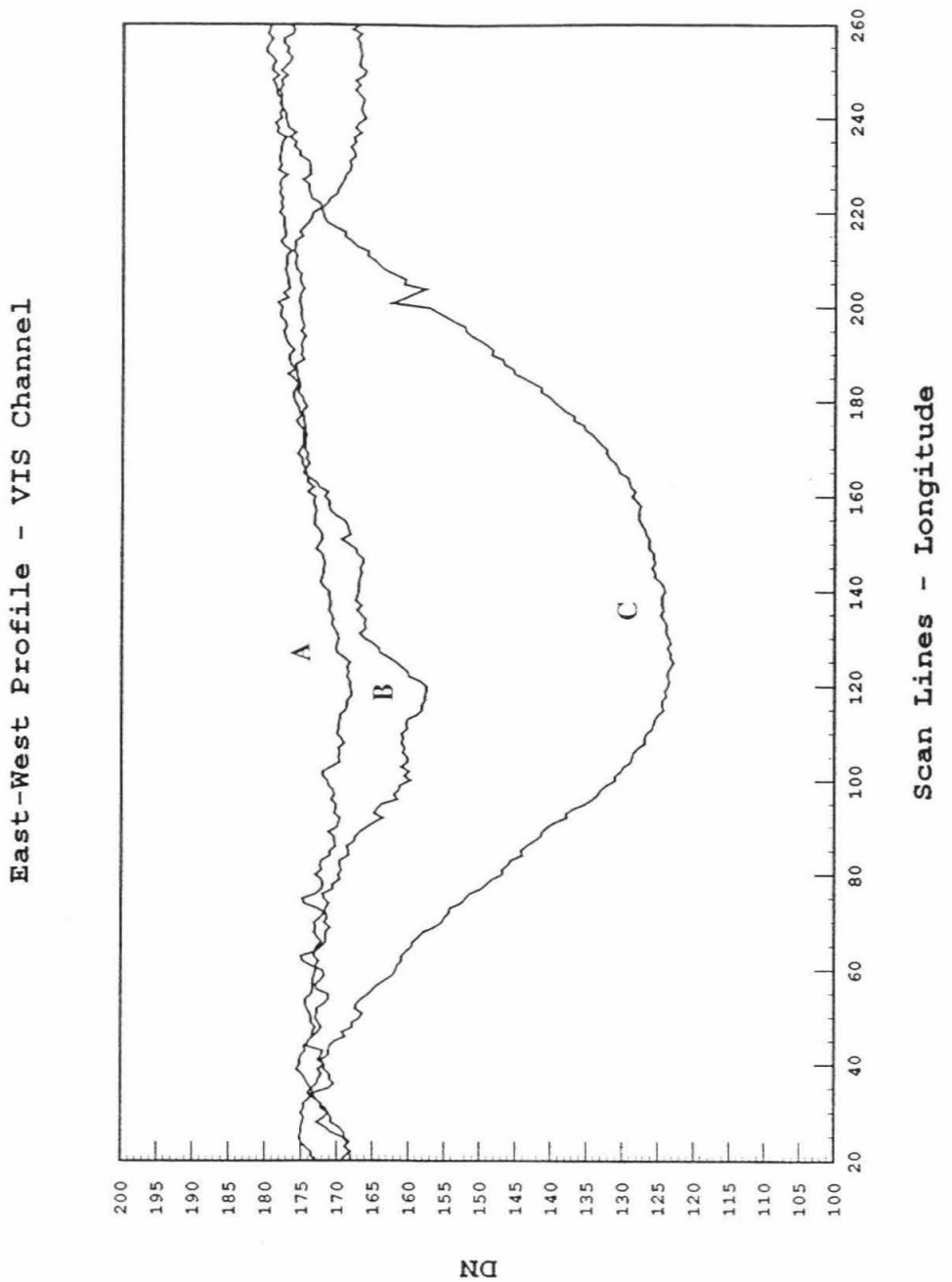

Figure 6.4: East-West profile - VIS channel. Reflectance from Martian surface as measured by visible channel on Termoskan. The curves in the figure are again an average of ten scan lines. Profile A is retrieved from just outside (south) of shadow region (15°S). Profile B is the same but just north of shadow (13°S). Profile C goes straight through the middle of the shadow area.

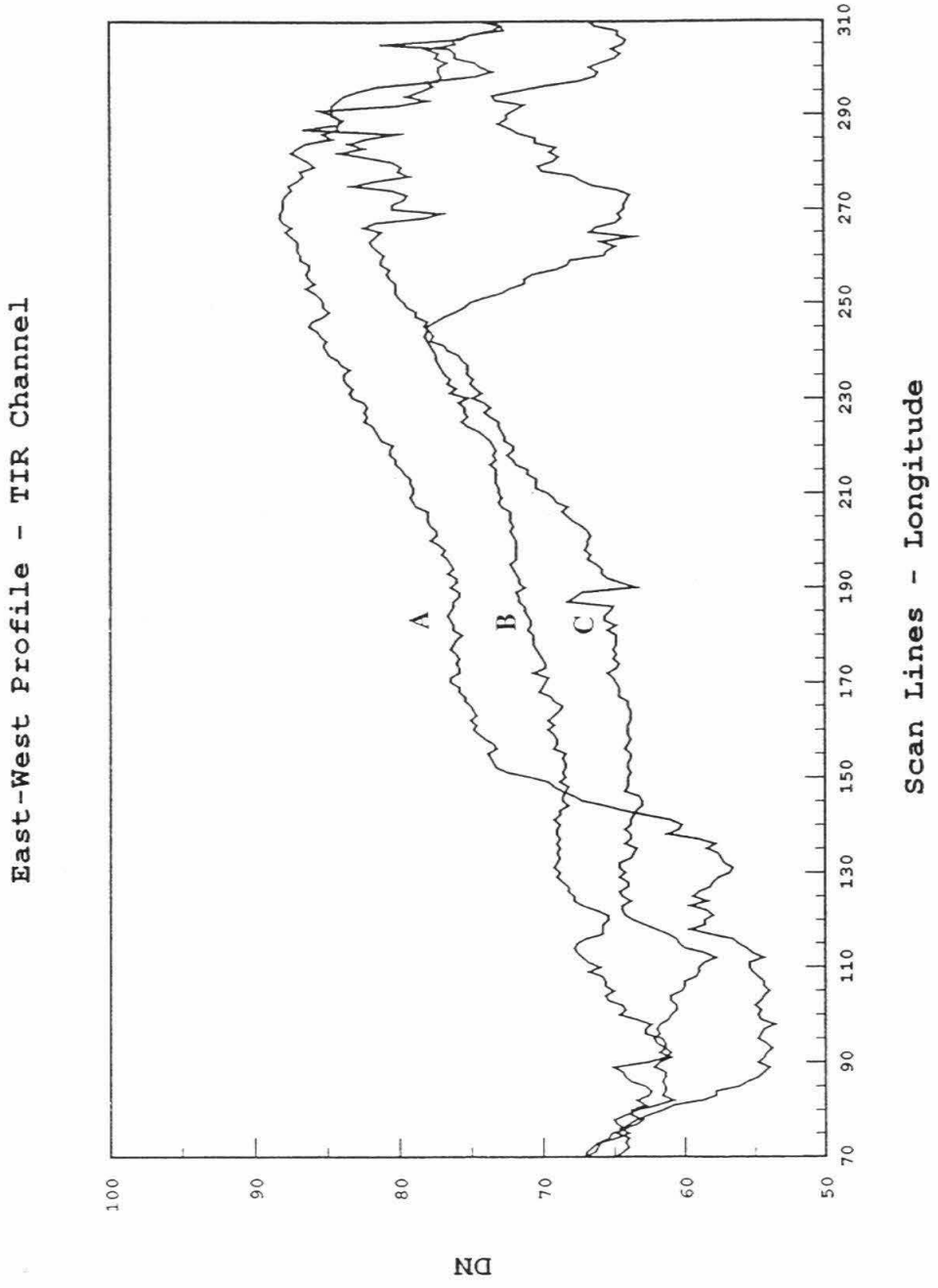

Figure 6.5: East-West profile - TIR channel. Thermal emission from Martian surface as measured by the thermal infrared channel. The curves in the figure are an average of ten scan lines. Profiles A, B and C are retrieved from the same regions as in the previous figure. Note the general trend of increasing temperatures towards east.

South dimension of the shadow in both the visible and infrared. This is an important independent demonstration of the absence of significant visible or infrared light scattering in the Termoskan instrument.

There are seven factors that influence the shadow's shape and intensity. First is the geometric shape of Phobos. Phobos is in synchronous rotation about Mars, was illuminated nearly end on (except near the limbs), and exhibited a nearly circular cross section of about 21 km in diameter. A second effect is distortion due to projection onto the spherical surface of Mars. Phobos' orbit is equatorial and its shadow was being projected to only 14°S latitude at the time of Termoskan's observations. Thus, this effect was minor except near the limbs. Third is the distance from Phobos to where the shadow intersected Mars' surface. This distance changed only an insignificant amount over the time scale of the observation. Similarly, local topography could cause a significant distortional effect only if the shadow crossed through very major topographic relief, e.g., Valles Marineris. Fifth is the penumbral effect. The shadow of Phobos is always completely penumbral, deepest at its center, and diminishing toward the edges. Sixth, atmospheric scattering further diffuses the shadow, smoothing the profile and reducing its maximum depth while increasing its size over the purely penumbral effect. All of the above mentioned effects will influence any observations of Phobos' shadow.

In our observations, there is a further effect on the apparent shape of the shadow: the relative motion of the spacecraft's field of view with respect to Phobos' shadow. Termoskan is a scanning instrument and the geometry of the observation was unusual. Phobos and the spacecraft were nearly coorbiting at the time of observation. Termoskan looked in the anti-solar direction - the same direction Phobos' shadow was projected. Therefore, Termoskan's line scanning system tended to follow the shadow on the surface, causing an apparent elongation of the shadow in the panorama. Furthermore, there was modulation of the apparent shadow because of a slight E-W rocking motion of the spacecraft. Figure 6.6 shows telemetry data taken before and after the observing session.

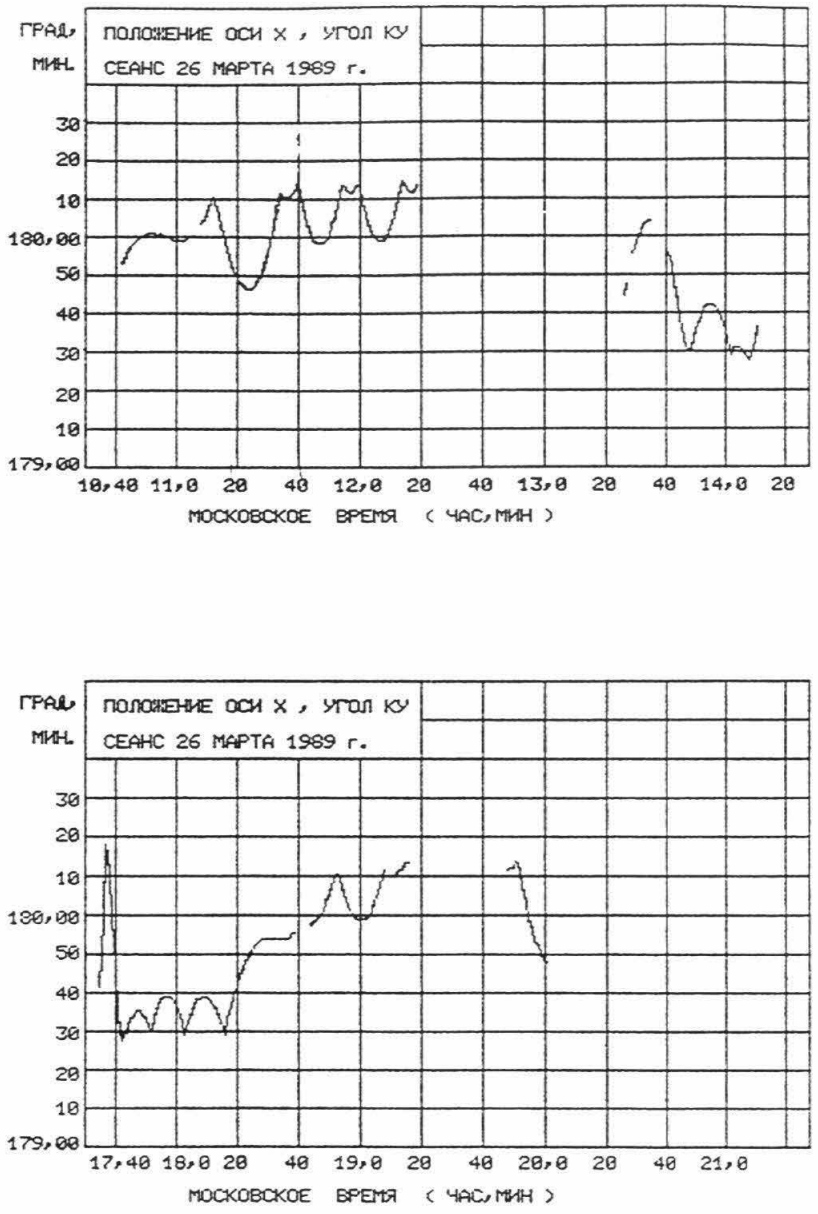

Figure 6.6: Deviations of the spacecraft's field of view from looking anti-solar. The horizontal axis is given in Moscow Time (hour, minute). The vertical axis measures the deviation from the anti-solar direction (180°) in degrees and minutes. These telemetry data were taken before and after the Termoskan panoramas. The upper graph corresponds to the time just before and just after the first March 26 panorama. Similarly, the lower graph is for the second March 26 panorama.

It depicts the magnitude of the rocking motion as function of time. In Figure 6.1, the field of view rocked first past the beginning of the shadow, then progressively through the shadow, and finally past the end of the shadow. Thus, an apparently elliptical shadow appears first in the visible. Subsequently, there is a band of cooling in the infrared channel resulting from the shadow's passage.

I assumed the E-W rocking motion to be uniform over the brief shadow observation shown in Figure 6.1. I also assumed that the N-S shadow length was unaffected by the rocking. Then, I calculated angular rocking motion by comparing the additional E-W shadow length (in seconds) to the N-S length. The angular rate found is 3 x 10^{-5} radians/second, in good agreement with the spacecraft data of Figure 6.6.

6.3 Thermal Models of the Eclipse Cooling

In order to derive thermal inertias from the eclipse observations, I modelled the cooling of the surface for several thermal inertias and compared the results to the observed cooling. I present here descriptions and results from three different, but related, models: Model 1, the Isothermal Model, which assumes that initially all depths are at the same temperature; Model 2, the Non-Isothermal Model, which utilizes an initial temperature with depth profile derived from the *Clifford et al.* [1987] diurnal thermal model; and Model 3, the Non-Isothermal Atmospheric Model, which adds a downward atmospheric flux term to Model 2. All three models are presented here for comparison and completeness. Model 1 was used to produce the results in *Murray et al.* [1991]. Model 2 improves on Model 1. Model 3 is the most complete model because it includes atmospheric re-radiation; however, the amount of atmospheric flux is highly dependent upon poorly known atmospheric conditions at the time of the observations. Thus, it is useful to consider Model 2 separately from Model 3.

All of the models solve the heat equation:

$$\partial T/dt = (1/\rho c)\, \partial(k(\partial T/\partial z))/\partial z \qquad (1)$$

where T is temperature, t is time, ρ is density, c is specific heat, k is thermal conductivity, and z is depth. This equation is solved using the same numerical method used by the *Clifford et al.* [1987] diurnal model described in Appendix 4. This is essentially the same model described earlier by *Kieffer et al.* [1977]. However, modelling the eclipse rather than diurnal and seasonal temperature variations requires several important differences between the eclipse models and the overall *Clifford et al.* model. Parameters such as the time scales used and inputs such as the decrease in visible flux with time in the eclipse must be changed. Where possible, I use the actual Termoskan data to make these changes, rather than relying on theoretical calculations. For example, I use the Termoskan visible data to derive the decrease in absorbed solar flux with time. Using the data where possible decreases the potential error introduced by poorly known factors such as the complex geometry including spacecraft rocking, atmospheric effects, and uncertainties in albedos.

All of the models produce model temperatures as a function of time in eclipse for a given value of thermal inertia. Thermal inertias are determined by first running a model for several values of thermal inertia. Then, model temperatures are compared with Termoskan data temperatures to find inertias for given values of time eclipsed. This comparison is discussed in the next section (Section 6.4).

In the rest of this section I describe the three models by pointing out their differences with the *Clifford et al.* [1987] model described in Appendix 4. In the first five points below, I present the elements that apply to all three models. Then, in the last two points, I address the differences in the three models. Hence, the following are the eclipse model features that are different from the *Clifford et al.* [1987] model:

1. *Time Scales (Depth Scales).* I have adjusted all time related variables to account for the 23-second eclipse time scale, rather than diurnal time scales. In particular, the interval between iterations was changed from several minutes to 0.001 seconds. Models with smaller iteration times were tested but showed no appreciable difference with the

models run with 0.001 second iterations. Note that the iteration time, along with the modeled inertia, determines the thickness and depths of the model compartments based upon finite difference stability criteria (see Appendix 4 for more details).

2. *Use of Orbital Information and Albedos.* Neither Mars orbital information nor albedo information is used in the eclipse models. How these are avoided will become more clear in the specific discussions of elements below. I generalize this point here to emphasize these major differences with the *Clifford et al.* [1987] model. Note that although the eclipse models do not use orbital information or albedo information directly, Models 2 and 3 do use them indirectly because I run the *Clifford et al.* [1987] model to generate the initial temperature with depth profiles. Errors in albedo will only introduce very minor errors when used in this indirect fashion.

3. *Downward Atmospheric Flux term.* The downward atmospheric flux term (variable name FF) is set equal to 0 rather than 2 percent of the noontime solar insolation. Models 1 and 2 have no downward atmospheric flux and model 3 incorporates it elsewhere within the model.

4. *Initial Surface Temperature.* Rather than calculating this from orbital and albedo considerations, the initial (pre-eclipse) surface temperature is assigned a value of 255 K. This is a representative Termoskan temperature for regions just outside the shadow.

5. *Relative Insolation as a Function of Time.* In order to model the cooling as a function of time eclipsed, the model needs a description of the total absorbed insolation as a function of time within the eclipse. For Models 1 and 2 this is equivalent to the absorbed solar insolation as a function of time. For Model 3 this includes atmospheric as well as solar insolation as discussed more fully in point 7 below. I derive the shape of the insolation versus time function from the visible data and the magnitude from the thermal data. In point 7 below I consider the magnitude of the pre-eclipse insolation used, which differs for each of the three models.

Here I discuss the shape of the insolation versus time function. I use this same relative insolation function in all three models. To find the relative insolation I did the following: A - calculated the duration of the eclipse for a point on the surface; B - derived a function that connects location within the shadow in the data to the amount of time that location has been in eclipse; C - used the visible channel eclipse profile to fit the decrease in absorbed solar insolation as a function of location within shadow; and D - combined B and C to derive relative insolation as a function of time in eclipse. These steps are accomplished in the following manner:

A. Combining the maximum width of a North-South profile, the orbital speed of Phobos, and the rotational speed of Mars gives an eclipse duration of just under 23 seconds.

B. I assumed the E-W rocking motion to be uniform over the brief Arsia Mons shadow observation. This assumption is justified both by the short duration of the observation and by the smoothness and shape of the E-W visible shadow profile (Figure 6.4). Thus, I was able to develop a linear relation between the number of lines into eclipse and the time a location had been in eclipse using the observed E-W size of the shadow (approximately 180 lines) and the eclipse duration calculated above (approximately 22.6 seconds). So, for example, the 90th line after the beginning of eclipse had been in some form of eclipse for approximately 11.3 seconds.

C. The next step was to determine the relative decrease in solar insolation as a function of location within the shadow. I assumed that the visible channel signal was linearly proportional to visible flux, consistent with the visible detector's characteristics and with all approximate flux calibrations of the visible channel. Thus, the E-W visible channel signal profile shown in Figure 6.4 should approximate the visible flux decrease within the shadow. I used this profile to quadradically fit the relative decrease in solar insolation within the shadow as a function of location within the shadow. Note that in the darkest part of the shadow the flux decreased by approximately 30 percent. The

advantage of using the visible channel profile instead of theoretical calculations of the flux decrease is that it already incorporates some atmospheric effects as well as geometric distortion due to the spacecraft rocking. Position within the visible channel can be directly correlated with position within the thermal channel to within approximately 1 pixel (Chapter 2 and Appendix 2).

D. Combining B and C gives the relative absorbed solar insolation as a function of time eclipsed, f(t). This function can vary from 0 to 1, where 1 represents the pre-eclipse insolation.

The only remaining step for modelling the insolation is to get an absolute pre-eclipse absorbed solar insolation that this relative function can be mated with. This is discussed separately below in point 7. First, I discuss the initial temperature with depth profile used because that will be important for point 7.

6. *Initial Temperature with Depth Profile.* Model 1 is isothermal before the onset of eclipse with all depths set to 255 K to match the pre-eclipse surface temperature.

Models 2 and 3 utilize more realistic non-isothermal pre-eclipse temperature with depth profiles. As mentioned, establishing a reasonable estimate for this temperature with depth profile is the only place in the models where either albedo or Mars orbit information are used. Even here, they are used indirectly. Before each run of either Models 2 or 3, I ran my adaptation of the *Clifford et al.* [1987] diurnal model utilizing the appropriate season (L_S = 18°), approximate latitude (14°S), and approximate albedo (0.27) (taken from the 1° x 1° binned bolometric albedos of *Pleskot and Miner* [1981]). Using the diurnal model output corresponding to the local time of day of the eclipse (about 10 H), I estimated the pre-eclipse temperature as a function of depth with a linear approximation:

$$TEMP(J) = ITEMP - TOP(J) * (T_{sd} - T_{fd}) / DEPTH_d \qquad (2)$$

where TEMP(J) is the temperature of the Jth compartment, ITEMP is the initial surface temperature, i.e., 255 K, TOP(J) is the depth of the top of the Jth eclipse depth compartment, T_{sd} is the surface temperature in the diurnal model, T_{fd} is the temperature

of the first depth compartment in the diurnal model, and $DEPTH_d$ is the depth of the first depth compartment in the thermal model. Note that this pre-eclipse temperature with depth profile depends upon the thermal inertia used in the diurnal model. Thus, for each value of inertia run in the eclipse model, I first modeled that inertia in the *Clifford et al.* [1987] diurnal model. This gave me new values of T_{sd}, T_{fd}, and $DEPTH_d$ to use in equation (2) and the eclipse model.

7. *Pre-eclipse Absorbed Insolation.* Finally, we need the value of the pre-eclipse absorbed insolation to use with the relative function found in part 5 above. To do this I use the surface equilibrium boundary condition discussed in Appendix 4, in *Kieffer et al.* [1977], and elsewhere:

$$[S(1-A)(\cos i)]/R^2 + F_a = \varepsilon\sigma T^4 - k(dT/dz) - L(dM/dt) \qquad (3)$$

Individual variables are described in Appendix 4. The terms on the left represent the total absorbed insolation, i.e., what we need to know for pre-eclipse conditions. The first term on the left is the absorbed solar insolation. The second term on the left represents the downward infrared atmospheric flux that reaches the surface. This thermal infrared flux is assumed to be absorbed completely by the surface. The first term on the right is the surface emission. Here I assume the emissivity, ε, to be 1 as was done by *Kieffer et al.* [1977]. The second term on the right is the surface conduction term. The third term on the right is the term representing latent heat from carbon dioxide sublimation or condensation. The temperatures involved in this shadow analysis are far above the carbon dioxide condensation temperature, so this term will be zero.

The three models differ in which terms are ignored in calculating the total absorbed insolation. All ignore the carbon dioxide latent heat term, which should be zero. Model 3 only ignores this term. Model 2 also ignores the atmospheric term, and Model 1, the latent heat, atmospheric, and conduction terms.

In principal, the total absorbed insolation could be calculated directly in any of these models from the terms on the left side of equation (3). Instead, I choose to solve for

the total insolation by finding the terms on the right side. There are three reasons to do this. One, by more explicitly using the Termoskan data, I avoid uncertainties in albedo, and the orbital geometry, and I significantly reduce the effects of atmospheric scattering. Two, utilizing the same initial surface temperature, 255 K, that is already used in the pre-eclipse temperature profile will result in greater initial consistency within the model. Three, in Model 3, to calculate the terms on the left side, I also would need to directly calculate the atmospheric downward flux. This would be very difficult to do accurately due to the poor knowledge of the state of the Martian atmosphere at the time of the observations. By using the surface emission and conduction terms to determine the total insolation, I avoid these problems.

I summarize the differences between my three eclipse models in Table 6.1. Here I describe in detail the differences in the insolations used. In Model 1, which ignores the atmospheric, conduction, and latent heat terms, the pre-eclipse absorbed insolation, PREINSOL, is approximated by σT^4, where σ is the Stephan-Boltzman constant and T is a representative value of the surface temperature derived from the data itself (255 K).

Non-eclipsed surface temperatures, and the corresponding non-eclipsed absorbed insolations, will change over the region covered by the eclipse and differ from 255 K; however, the short duration and small area covered by the eclipse keep these variations small. Also, as I discuss more in the next section, I use temperature drops within the eclipse rather than absolute temperatures for comparison with the model to minimize errors caused by insolation or initial temperature errors in the model.

Ignoring the conduction term, k(dT/dz), in Model 1 is consistent with the initial isothermal assumption in this model which implies dT/dz = 0. The insolation as a function of time, INSOL, combines PREINSOL with the relative flux decrease as a function of eclipsed time, f(t), that was derived from the visible channel data in step 5. Thus, for Model 1:

$$\text{INSOL} = (\text{PREINSOL}) * (f(t)) \qquad (4)$$

TABLE 6.1: Summary of Eclipse Model Differences

Model #	Pre-eclipse Temperature with Depth	Includes Atmospheric Flux	PREINSOL	INSOL
1	Isothermal	No	σT^4	PRESOLARINSOL * f(t)
2	Non-Isothermal	No	σT^4 - k(dT/dz)	PRESOLARINSOL * f(t)
3	Non-Isothermal	Yes	σT^4 - k(dT/dz)	ATMINSOL + PRESOLARINSOL * f(t)

PREINSOL = Pre-eclipse total absorbed insolation = PRESOLARINSOL when there is no atmospheric downward flux.
INSOL = Total insolation as a function of time in eclipse.
PRESOLARINSOL = Pre-eclipse absorbed solar insolation.
ATMINSOL = Absorbed atmospheric insolation.
f(t) = Relative absorbed solar insolation (on a scale of 0 to 1) as a function of time in eclipse.

Model 2 differs from Model 1 by approximating the pre-eclipse absorbed insolation, PREINSOL, by:

$$\text{PREINSOL} = \sigma T^4 - k(dT/dz) \quad (5)$$

Note that including the conduction term here is consistent with the non-isothermal initial conditions of this model. After the initial temperature profile with depth is derived for this model as described in step 6 above, dT/dz is approximated by Taylor expansions of the first three depth steps and their temperatures as discussed in Appendix 4. Note that for the mid morning Arsia eclipse observation, dT/dz is negative. Thus, PREINSOL will be larger in Model 2 than in Model 1. The total insolation as a function of time, INSOL, is found in Model 2 in the same way as in Model 1, using equation (4).

Model 3 determines the value of PREINSOL in the same manner as Model 2, using equation (5). Model 3 differs by assuming PREINSOL to be composed of an atmospheric component (downward infrared flux) in addition to the solar component. Thus, in terms of equations, Model 3 differs from Model 2 in the calculation INSOL. The relative flux drop as a function of time derived in step 5 is based upon the visible channel which sensed only the solar flux drop. The downward atmospheric infrared flux should remain very nearly constant during the eclipse because all of the atmosphere contributes, not just the small portion that is eclipsed. Even the eclipsed portion of the atmosphere should put out nearly the same amount of IR flux because eclipse cooling of the

atmosphere should be slight. Thus, I assume that the absorbed downward atmospheric flux, ATMINSOL, remains constant throughout the eclipse, whereas the absorbed solar insolation, PRESOLARINSOL, will vary with eclipse time as described by the function f(t) that was derived in step 5. Thus, rather than using equation (4) as Models 1 and 2 did, Model 3 uses:

$$INSOL = ATMINSOL + PRESOLARINSOL * f(t) \quad (6)$$

Here, PREINSOL, which is what I derived from the surface emission and conduction terms in equation (5), represents the combination of ATMINSOL and PRESOLARINSOL, i.e.,

$$PREINSOL = PRESOLARINSOL + ATMINSOL \quad (7)$$

ATMINSOL will depend strongly upon the amount of dust in the atmosphere as well as to some extent the elevation of the surface. In order to conveniently model different values of ATMINSOL, I define ATMINSOL as a fraction, ATMFRAC, of PRESOLARINSOL. Thus,

$$ATMINSOL = ATMFRAC * PRESOLARINSOL \quad (8)$$

Combining equations (6), (7), and (8) gives an equation dependent upon only PREINSOL and ATMFRAC:

$$INSOL=(ATMFRAC*PREINSOL)/(1+ATMFRAC)+PREINSOL/(1+ATMFRAC)*f(t) \quad (9)$$

which reduces to equation (4) when ATMFRAC = 0. So, using equation (9), the model can be run for several values of ATMFRAC to determine the effects of different amounts of downward atmospheric flux.

6.4 Comparison of Data with Models

To best compare Termoskan observed eclipse temperatures with model results, I used temperature drops within the eclipse rather than absolute temperatures. Variations in absolute temperature are observed outside the eclipse due to variations in albedo, inertia, and time of day. These factors also will effect the observed temperatures within the

eclipse. To minimize these effects, I did two things to the data used for comparison. First, for points within and outside the shadow, I averaged 10 pixel (in the East-West direction) by 1 pixel strips. Second, the data I compare with models are estimated temperature drops within the eclipse. I find these temperature drops by averaging the temperatures of points to either side (North and South) of the shadow and then subtracting the temperature observed in the middle of the shadow. Using these temperature drops rather than absolute temperatures is particularly effective at removing time of day effects. Also, because the area happens to be reasonably bland thermally, gradual albedo and diurnal inertia variations are also removed. In addition, by using temperature drops, I reduce the effects of atmospheric scattering, which should act approximately equally inside and outside the shadow.

To plot the data versus the model curves, these temperature drops were subtracted from 255 K, the pre-eclipse temperature used in the models. Figure 6.7 shows the data plotted versus Model 1 curves. Figure 6.8 shows an analogous plot for Model 2, Figure 6.9 shows curves for Model 3 with ATMFRACTION = 20 percent, and Figure 6.10 shows curves for Model 3 with ATMFRACTION = 10 percent. Most of the data fall between inertias of 0.85 and 1.2 (in units of 10^{-3} cal cm^{-2} $s^{-1/2}$ K^{-1}) for Model 1, between 1.0 and 1.55 for Model 2, between 0.75 and 1.2 for Model 3 with a 20 percent value of atmospheric flux, and 0.9 and 1.35 with a 10 percent value.

6.5 Discussion

The results show that non-isothermal Model 2 raises the derived inertias from the less realistic isothermal Model 1. Adding atmospheric downward flux in Model 3 reduces the derived inertias. First, I consider why in general the differences in the models cause these effects. Then, I consider the models' implications for the surface of Mars.

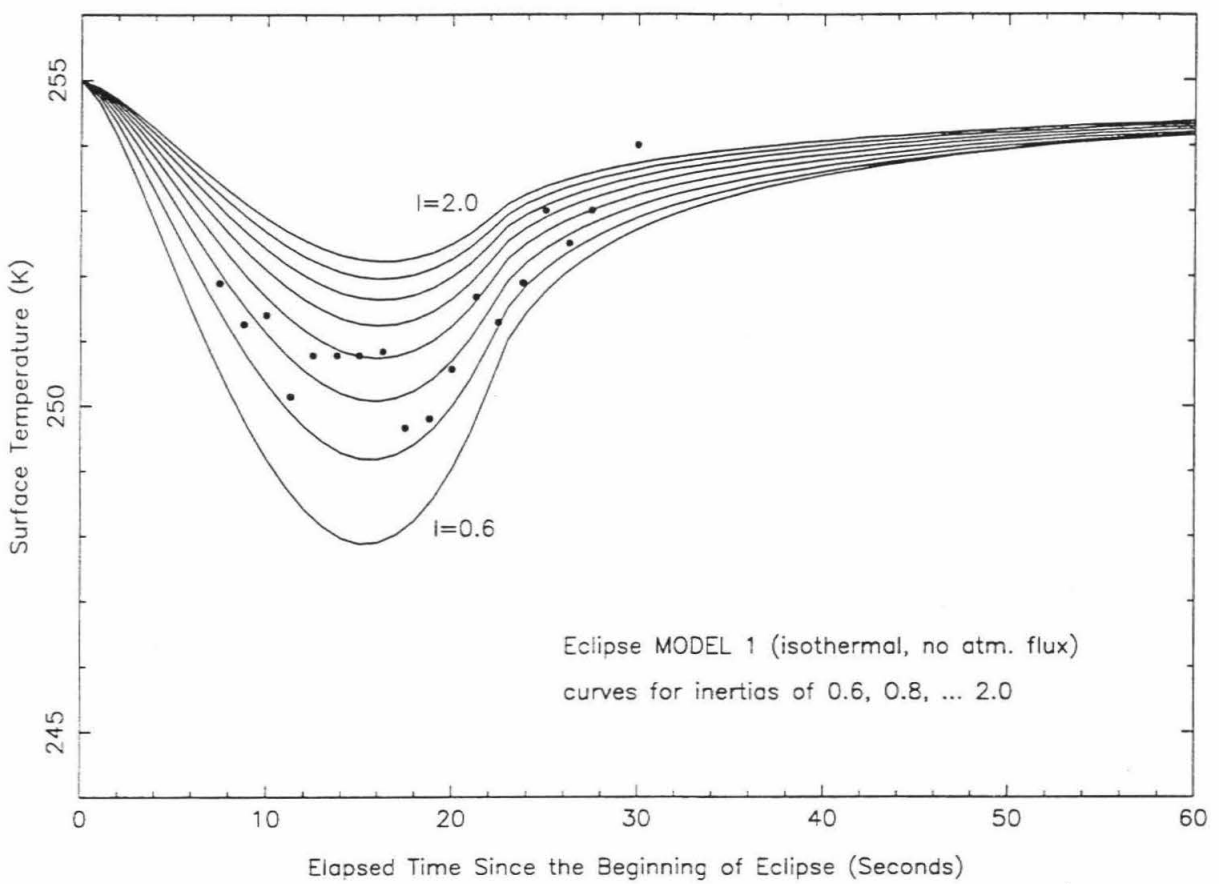

Figure 6.7: Eclipse Model 1 Results. The lines in this plot are model surface temperatures for various thermal inertias (from 0.6 to 2.0). The dots are observational data retrieved from thermal infrared channel. They are derived from 10 line averages of temperature drops at the center of the shadow relative to comparable points outside the shadow. The temperature drops have been subtracted from 255 K to facilitate comparison with our model results. We chose 255 K for the model because it is a typical temperature from the region surrounding the shadow. Most of the experimental data values fall between model curves corresponding to thermal inertias of 0.85 to 1.2 (in units of 10^{-3} cal cm^{-2} $s^{-1/2}$ K^{-1}). Results are the same as those presented in *Murray et al.* [1991].

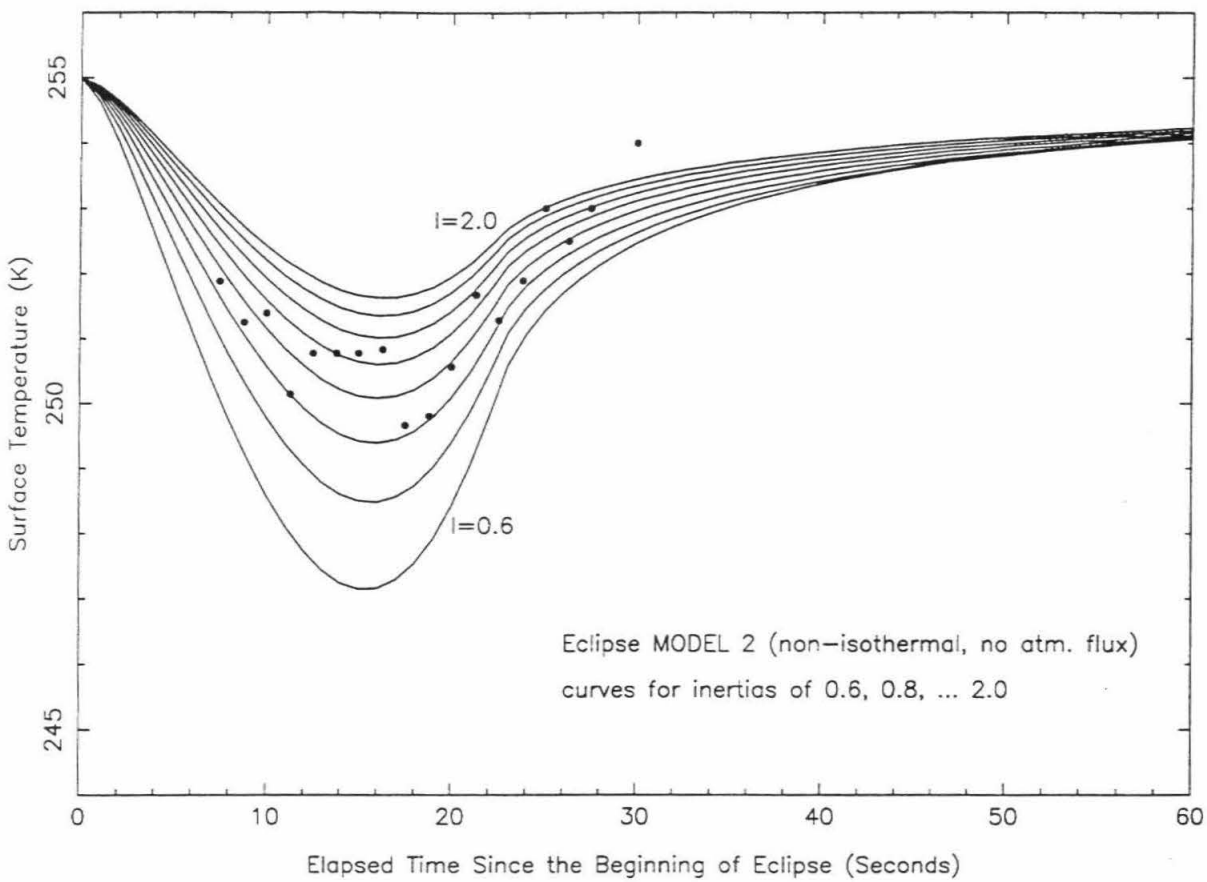

Figure 6.8: Eclipse Model 2 Results. Same as Figure 6.7 but for Model 2 results. Model 2 added non-isothermal with depth pre-eclipse conditions to Model 1. Most of the observational data values fall between model curves corresponding to thermal inertias of 1.0 to 1.55.

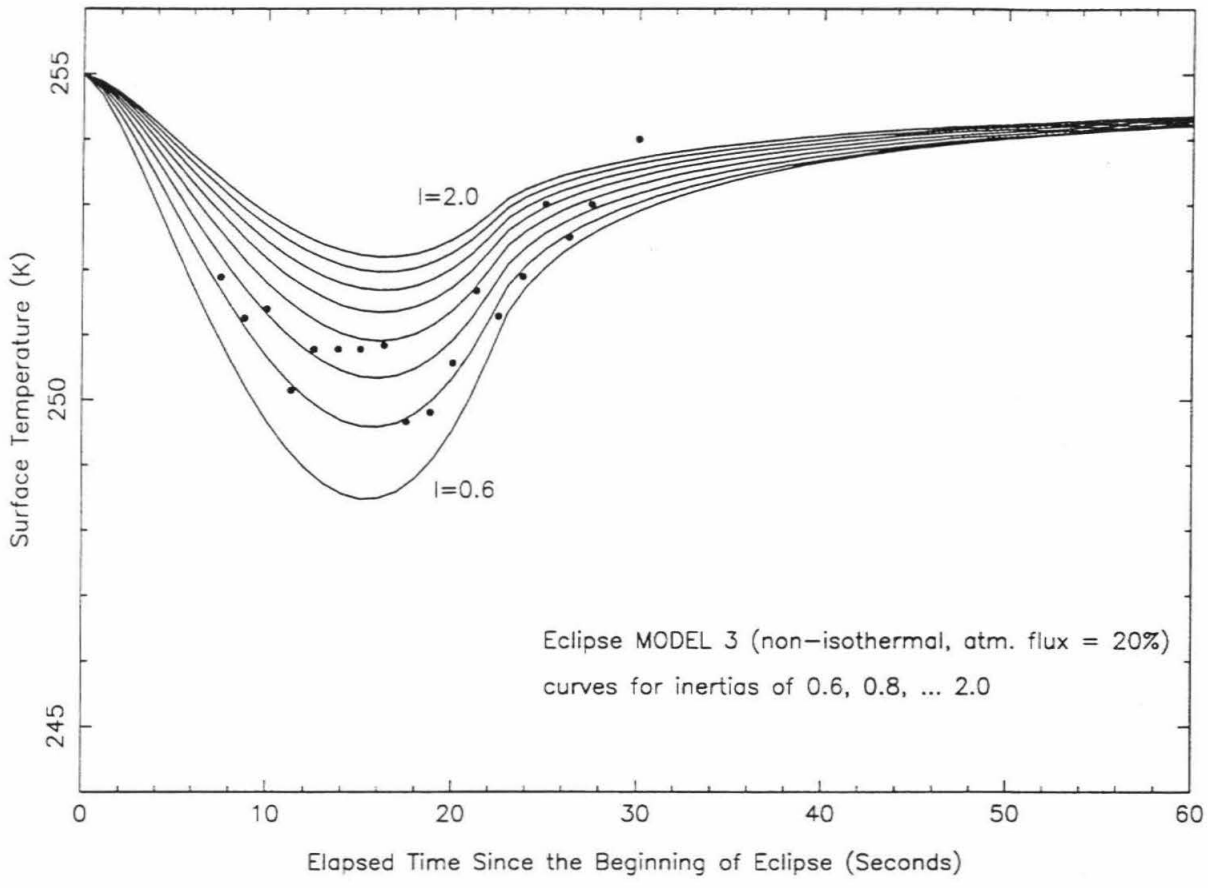

Figure 6.9: Eclipse Model 3, Atm. Flux = 20 percent. Same as Figure 6.8 but for Model 3 results. Model 3 added atmospheric downward flux to Model 2. The curves plotted here are for a downward atmospheric flux of 20 percent of the absorbed pre-eclipse solar flux. Most of the observational data values fall between model curves corresponding to thermal inertias of 0.75 to 1.2.

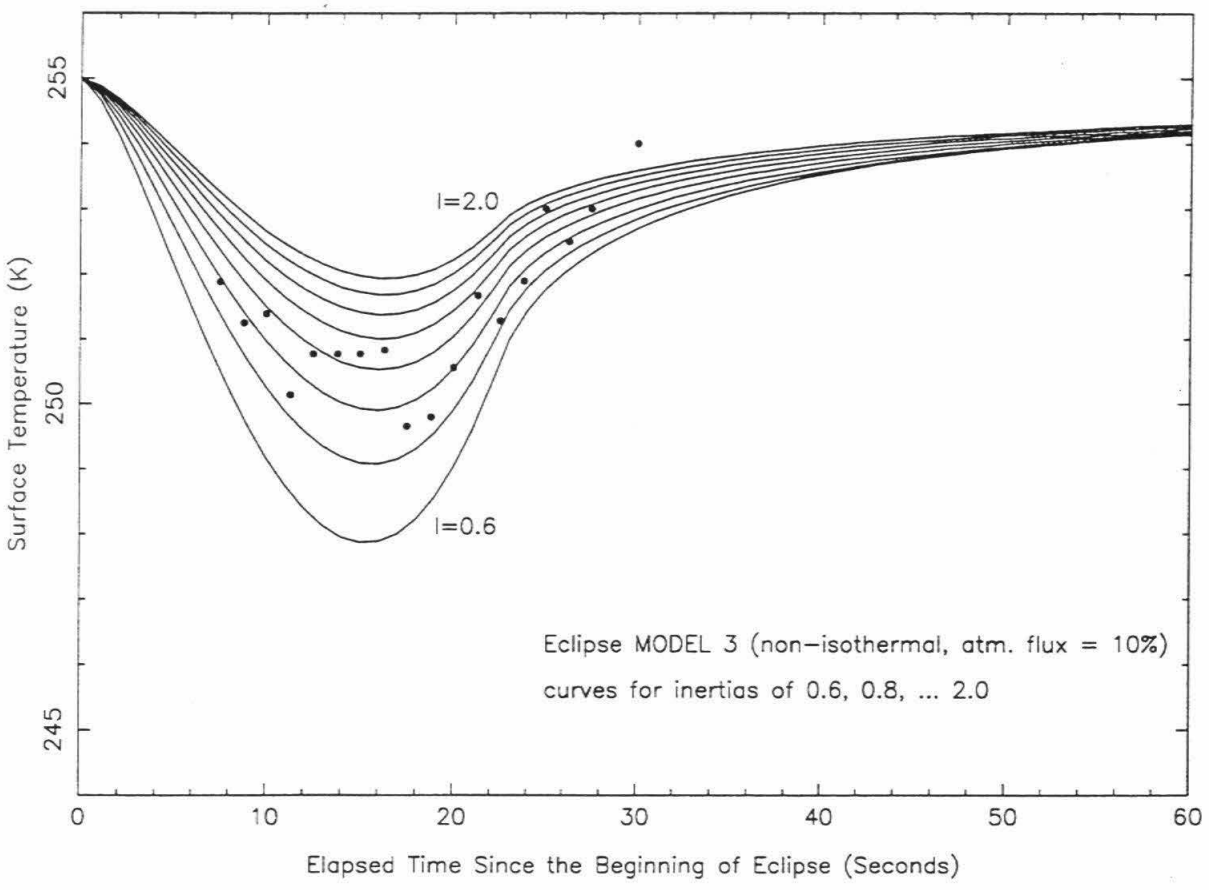

Figure 6.10: Eclipse Model 3, Atm. Flux = 10 percent. Same as Figure 6.9 but with 10 percent downward atmospheric flux. Most of the observational data values fall between model curves corresponding to thermal inertias of 0.9 to 1.35.

6.5.1 Model Differences and Realistic Inertias

Including the non-isothermal, initial temperature versus depth profile in Model 2 allows the model surface to cool more quickly. For these low inertias this dominates the opposite simultaneous effect that results from the additional pre-eclipse insolation which is due to including the conduction term in equation (5). Overall, the faster cooling causes higher inertias to be derived in Model 2 than in Model 1.

The atmospheric downward flux added in Model 3 stays constant throughout the eclipse, and thus keeps the total insolation higher throughout the eclipse. This causes the surface to cool more slowly. Thus, including more downward atmospheric flux causes lower inertias to be derived.

Model 3 should be the most realistic model because it includes both non-isothermal starting conditions and downward atmospheric flux. The next question is what value of atmospheric flux in Model 3 is the most realistic. This is hard to answer precisely, but fortunately the range of most likely possibilities does not affect my eventual scientific conclusions. The atmospheric flux depends upon the atmospheric optical depth which is not well known for the time of the observations. Analyses of data from other Phobos '88 instruments has given answers that range from optical depths of about 0.2 to 0.6, with the most favored values somewhere near the middle of that range. According to modelling by *Haberle and Jakosky* [1991, Figure 4], for this range of optical depths and the local time of day of the observations, the atmospheric flux will range from 6 percent to 11 percent of the solar flux. Thus, the 20 percent model run shown in Figure 6.9 is probably an extreme and should give lower bounds on inertias. Even the 10 percent run shown in Figure 6.10 probably gives inertias that are somewhat low. This is particularly true because the shadow was observed on a surface roughly 9 km (almost 1 scale height) above the 6.1 mbar reference altitude used for the *Haberle and Jakosky* figure that the flux percentages

quoted here came from. Atmospheric flux contributions will be reduced at higher altitudes.

The Model 2 runs, which do not have any atmospheric flux contribution, should give inertia upper bounds. The real values should lie between the Model 2 and Model 3-20 percent values and are probably a little higher but not too far from the Model 3-10 percent values. Thus, inertias of 0.9 and 1.4 probably bracket the majority of the eclipse derived inertias in this shadow region. Ironically, because the non-isothermal effects nearly balance the atmospheric effects for these inertias, these are nearly the same values as the Model 1 results reported in *Murray et al.* [1991] and *Betts et al.* [1990] reported previously from the Model 1 results.

6.5.2 Implications for the Martian Surface

The inertias derived from all the models are consistent with dust sized particles. Assuming a homogeneous surface, inertias of 0.9 to 1.4 imply particle sizes of approximately 5 to 10 microns [*Haberle and Jakosky*, 1991; *Kieffer et al.*, 1973; *Jakosky*, 1986]. The implication that dust covers most of the surface in this region is consistent with previous studies that have proposed that the Tharsis region has a dust covering and is currently an area of dust deposition [*Kieffer et al.*, 1977; *Zimbelman and Kieffer*, 1979; *Palluconi and Kieffer*, 1981; *Christensen*, 1986b]. It is also reasonably consistent with the low rock abundances (about 5 percent) in this region [*Christensen*, 1982, 1983].

For the very low inertias involved in this study, diurnally derived inertias are sensitive to thermal skin depths of 1 or 2 cm. Due to the short duration of the eclipse relative to the length of a Martian day, the eclipse based inertia determinations are sensitive to thermal skin depths of only a few tenths of a millimeter. Comparison of inertias derived by the two methods can indicate the degree of layering within the upper cm of the surface.

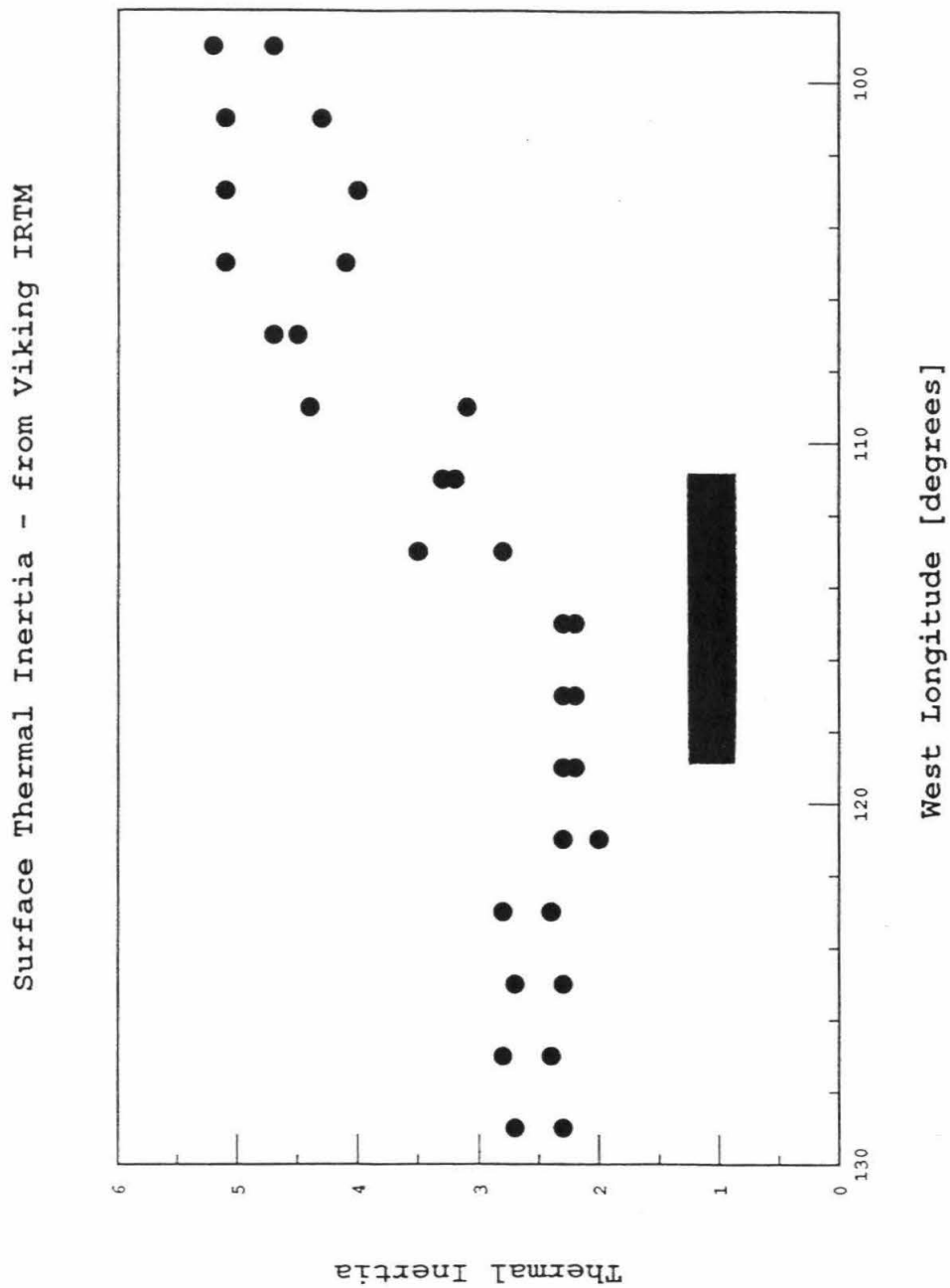

Figure 6.11: Eclipse Region IRTM Inertias. The filled circles represent binned 2° latitude x 2° longitude thermal inertias derived from Viking IRTM measurements by *Palluconi and Kieffer* [1981]. Their inertias are plotted versus longitude for bins centered on 13°S and on 15°S. The shadow center was at approximately 14°S and the region studied was contained between 110°W and 120°W.

Our preferred model inertias are lower by factors of 1.5 to 4 than those derived by *Palluconi and Kieffer* [1981] from Viking IRTM data (see Figure 6.11). This relationship alone would imply layering of lower inertia material over higher inertia material (note that higher inertia is a relative term here as both sets of inertia imply dust sized material, and both are low even for Mars). *Palluconi and Kieffer* inertias imply particle diameters for a homogeneous surface of approximately 20 to 40 microns [*Haberle and Jakosky*, 1991; *Kieffer et al.*, 1973; *Jakosky*, 1986], or two to eight times the sizes implied from eclipse modelling.

Haberle and Jakosky [1991] determined that the 2 percent noontime solar insolation value used for the atmospheric downward flux in the *Kieffer et al.* [1977] thermal model, which was the basis for several later models including *Palluconi and Kieffer* [1981], underestimated the downward atmospheric flux. They determined proposed corrections to *Kieffer et al.* [1977] type inertias depending upon the optical depth of the atmosphere. In suggesting corrections to the *Palluconi and Kieffer* [1981] inertias, they use typical optical depths for the periods analyzed by *Palluconi and Kieffer*: namely, optical depths ranging from 0.3 to 0.5 with the primary one they use being 0.4. A representative *Palluconi and Kieffer* inertia for the shadowed region is 2.4. Using the suggested *Haberle and Jakosky* corrections, this inertia becomes 1.34 for an optical depth 0.2 and 0.81 for an optical depth of 0.4.

Thus, the *Haberle and Jakosky* corrected *Palluconi and Kieffer* inertias agree to within the uncertainty of the corrections with our model results for the shadowed region. Therefore, if layering exists at all, it is probably not as significant as was first thought. This agrees qualitatively with what *Haberle and Jakosky* [1991] concluded based upon the *Betts et al.* [1991] results and theoretical determinations that atmospheric effects will be less important for eclipse derived thermal inertias than for diurnally derived thermal inertias. Indeed, my modelling shows that for the inertias involved, atmospheric

downward flux has considerably less effect upon eclipse derived inertias than upon diurnally derived inertias.

The few tenths of a millimeter sampled by eclipse cooling measurements should present a fair representation of the surface that is sensed by optical and near-infrared instruments. Thus, for the region studied, it is unlikely that optical and near-infrared instruments would sample any significant amount of bare (not covered by dust) rock surfaces.

6.5.3 Summary

In summary, combining our preferred eclipse model with the Termoskan thermal data implies inertias for the Arsia Mons shadow occurrence that mostly fall within the range 0.9 to 1.4. These inertias correspond to dust with particle sizes of 5 to 10 microns for a homogeneous surface. The presence of dust at the surface is consistent with previous theories of Tharsis as a current area of dust deposition. Finally, the similarity of these derived inertias to *Haberle and Jakosky* [1991] corrected *Palluconi and Kieffer* [1981] inertias implies there is very little, if any, layering of the upper tenths of a millimeter versus the upper couple centimeters. Thus, most of the upper couple centimeters is likely composed of unbonded, few micron dust particles.

The findings here obviously do not preclude layering or higher inertias elsewhere. Questions of geographic variability of the upper millimeter of the surface can be addressed to some extent in the future using the three other Termoskan observed occurrences of the Phobos shadow.

6.6 Other Shadow Occurrences/Future Research

The Arsia Mons shadow occurrence analyzed in this thesis was the simplest of four separate shadow occurrences observed by Termoskan. The four occurrences, their locations, and their basic differences are summarized in Table 6.2. All are centered roughly on 14°S latitude. The three shadow occurrences not analyzed here offer unique

TABLE 6.2: Phobos Shadow Occurrences within the Termoskan Data

ID #	Scan #	Location	W. Longitudes Covered	Times of Day Covered (H)	Notes
1	3	Flanks of Arsia Mons	110° to 120°	9.3 to 10.1	Analyzed here.
2	3	S. of Western half of Valles Marineris	75° to 105°	10.5 to 12.7	
3	4	Eastern end is in the crater Herschel	228° to 255°	7.4 to 9.5	No cooling apparent in thermal data.
4	4	North of Ma'adim Vallis	172° to 210°	10.8 to 13.8	No visible channel data for eastern end of shadow. Dropped lines in visible data that does exist.

All shadow occurrences are centered approximately upon 14°S latitude.

opportunities for future analysis, but they are more complicated than the Arsia Mons occurrence.

All of the other shadow occurrences show less cooling than observed in the Arsia shadow occurrence. This implies that they have higher inertias. The newly developed Models 2 and 3 will be particularly valuable for modelling these other occurrences because the conduction effects that are not included in Model 1 are particularly important for regions with higher inertia.

The other three occurrences are also all longer than the Arsia occurrence, i.e., they cover a wider range of longitudes. This means that a wider range of local times of day, surrounding temperatures, and albedos were observed. Further complicating analyses, other E-W visible shadow profiles do not appear as smooth and symmetric (smoothly darkening, then brightening) as the Arsia shadow profile shown in Figure 6.4. Also, the greater length of the apparent shadows implies that the spacecraft rocking motion was slower. Thus, it is less clear that the assumption of uniform rocking of the spacecraft is valid.

There are also idiosyncrasies associated with individual shadow occurrences. Termoskan stopped taking visible data part way through occurrence 4. The visible data that does exist is missing some lines of data. Because the "end" of the shadow was not observed, it will be harder to associate location within the shadow with time eclipsed.

Occurrence 3 shows no apparent cooling in response to the shadow. This obviously will inhibit any direct inertia determinations. However, by making assumptions about what level of cooling could be detected in the Termoskan data, I should be able to place some lower bound on the inertia required to cause this. In the future I will attempt to model the other shadow occurrences within the limitations that they present.

Due to their orbits, the Mars Observer (MO) spacecraft would have had, and the Mars '94 (M94) spacecraft will have, more difficulty obtaining thermal observations of the Phobos shadow. Mars Observer would have been in a nearly polar orbit and Mars '94 will be in an orbit with an inclination of roughly 50°. The Phobos shadow on the surface of Mars only occurs in the equatorial regions and travels roughly west to east. Thus, chance Phobos shadow observations are less likely to happen from the Mars '94 orbit than they were from the Phobos '88 orbit. Nonetheless, although challenging, they still can be obtained with proper planning and targeting. If the shadow is observed by Termoskan 2 Mars '94, the models developed in this thesis can be used to learn about the upper mm of the Martian surface in different regions. Lastly, I note that recently proposed Russian Phobos sample return mission could easily obtain several observations of the Phobos shadow viewing in the anti-solar direction when near Phobos.

Chapter 7

And, while with silent, lifting mind I've trod
The high untrespassed sanctity of space,
Put out my hand, and touched the face of God.
-John Gillespie Magee, Jr.

SUMMARY OF CONCLUSIONS, AND THE FUTURE

This chapter presents a summary of the major thesis conclusions and some implications and proposed studies for future missions. The major thesis conclusions are presented in Section 7.1. Discussion of the future is split into proposed future Termoskan research (Section 7.2) and implications and proposed studies for Mars Observer (MO), Mars '94 (M94), and other future missions (Section 7.3). This latter section includes a set of proposed sites originally selected for intercomparison of Mars Observer instrument data, but which will be useful for any future mission where orbital data sets are intercompared. Also included are proposed studies designed originally for Mars Observer and proposed studies for Mars '94 and other future missions. Much of the MO material was prepared before the tragic loss of MO. I still include a reduced form of this material because it should be useful for whatever analogous instruments fly on future missions.

7.1 Summary of Major Conclusions

The Termoskan instrument of the Phobos '88 space mission acquired the highest spatial resolution thermal data ever obtained for the surface of Mars. This high resolution thermal data, combined with simultaneous visible data, facilitated a number of never before possible studies that were presented in this thesis.

Overall, the Termoskan data has shown that Mars is thermally a very interesting place at resolutions ranging from 300 m/pixel to 3 km/pixel. Mars shows significant variations in thermal properties even at the 300 m/pixel scale. This implies the absence of a global dust layer thicker than about one cm. Termoskan's higher spatial resolution has enabled the recognition of new features such as thermally distinct ejecta blankets and new insights into previously studied features such as channels and valleys. Termoskan's

observations bode well for future instruments such as Termoskan 2 on Mars '94 and instruments that resemble the thermal emission spectrometer on MO.

Comparison of Termoskan thermal data with Viking IRTM data shows good agreement between the two. Thus, Termoskan temperature data should be quite adequate for determination of thermal inertias. Conversion of Termoskan visible data to bolometric albedo is problematic, however. Fortunately, qualitative thermal and visible analyses, quantitative thermal inertia determinations tied to Viking albedos, analyses of atmospheric profiles, and analysis of the shadow of Phobos on Mars have all yielded interesting new conclusions about Mars. The major conclusions are summarized here.

I have recognized a new feature on Mars: ejecta blanket distinct in the thermal infrared (EDITH). EDITHs have a startlingly clear dependence upon terrains of Hesperian age. They show no consistent correlation with any other factor. I postulate that EDITHs exist on the observed Hesperian units because of impact excavation into a thick, more fragmented, materially different Noachian layer beneath a relatively thin younger layer or layers of Hesperian volcanic material. I suggest that absence of thermally distinct ejecta blankets on Noachian and Amazonian terrains is due to absences of distinctive near-surface layering. I also postulate that EDITH variations are primarily controlled by the degree of excavation of the Noachian layer. However, secondary effects such as degree of erosion of the blankets or local availability of aeolian material probably cause some thermal variations. The thermally distinct nature of the blankets probably results from the ejecta itself, or possibly from secondary aeolian deposits preferentially trapped on the blankets. Thermally distinct ejecta blankets are excellent locations for future landers and remote sensing because of relatively dust free surface exposures of material excavated from depth.

Termoskan observed several channel and valley systems on Mars at the highest spatial resolution ever. I find that most of the channels and valleys have higher inertias than their surroundings, consistent with previous thermal studies of martian channels. I

show for the first time that thermal inertia boundaries closely match all flat channel floor boundaries. Lower bounds on typical channel thermal inertias range from 8.4 to 12.5 (10^{-3} cal cm^{-2} $s^{-1/2}$ K^{-1}). Lower bounds on inertia differences with the surrounding heavily cratered plains range from 1.1 to 3.5.

I agree with previous researchers that localized, dark, high inertia areas within channels are likely aeolian in nature. However, thermal homogeneity and strong correlation of thermal boundaries with the channel floor boundaries lead me to favor non-aeolian overall explanations, in contrast with some IRTM researchers. Small scale aeolian deposition or aeolian deflation may play some role in the inertia enhancement. Flat floors and steep scalloped walls are observed in most regions that show increased inertia. Therefore, I favor fretting processes over catastrophic flooding for explaining the inertia enhancements. Fretting may have emplaced more blocks on channel floors or caused increased bonding of fines due to increased availability of water. Alternatively, post-channel formation water that was preferentially present due to the low, flat fretted floors may have enhanced bonding of original fines or dust fallout. Also of interest, buttes within channels have inertias similar to the plains surrounding the channels. Thus, the buttes were likely part of a contiguous surface prior to channel formation.

Termoskan observed morning and evening limbs of Mars. Morning limb brightening is observed in the thermal channel, but not in the visible channel. The thermal morning limb brightening is likely due to a water ice or dust haze that is warmer than the surface at the time of the observations. A water ice or dust haze with a scale height of 5 km could match the observations. Visible scattering is observed to be significant on morning and evening limbs out to 60 or 70 km. In addition, localized high altitude stratospheric clouds are observed in the visible channel. They may correspond to those detected by the Phobos '88 Auguste experiment.

The Termoskan data show that highland-lowland boundary in the Aeolis Quadrangle appears strongly correlated with a high-low thermal inertia boundary. The

sharpness of that boundary varies from less than 4 km to more than 50 km. In all cases, inertias continue to decrease gradually for many tens of km into the lowlands.

Termoskan observed fine thermal structure on the flanks of Arsia Mons and elsewhere. On Arsia Mons the structure apparently correlates with lava flow units. The cause may be primary or secondary, with secondary causes favored in this thesis. This structure is just one example of interesting and significant thermal variations seen at the limit of Termoskan's spatial resolution. The associated boundary and other sharp large scale boundaries are often sharp down to the limit of Termoskan's resolution. These variations and boundaries, including in the very low thermal inertia Arsia Mons region, imply that a uniform dust layer thicker than about one cm cannot exist.

Termoskan obtained the first ever thermal images of Phobos' shadow on the surface of Mars. Simultaneous visible images were also obtained. I analyzed an occurrence of the shadow on the flanks of Arsia Mons. I combined the observed decrease in visible illumination of the surface with the observed decrease in brightness temperature to calculate thermal inertias of the uppermost tenths of a millimeter of the Martian surface. Most of the derived inertias fall within the range 0.9 to 1.4. These inertias correspond to dust with particle sizes of 5 to 10 microns for a homogeneous surface. The presence of dust at the surface is consistent with previous theories of the Tharsis region as a current area of dust deposition. Viking IRTM derived inertias are diurnally derived and are sensitive to centimeter depths, whereas the shadow derived inertias sample the upper tenths of a millimeter of the surface. The shadow derived inertias are significantly lower than those originally derived from Viking IRTM measurements (2 to 3.5) [*Palluconi and Kieffer*, 1981]. However, they are very similar to *Haberle and Jakosky's* [1991] atmospherically corrected *Palluconi and Kieffer* [1981] inertias. Thus, if layering exists at all, it is not very significant.

7.2 Future Termoskan Research

The Termoskan data set has yielded important new information about Mars. Several other Termoskan research projects beyond the scope of this thesis promise to yield even more. Some, such as Phobos shadow surface studies, continue work presented in this thesis. Others, including comparisons with other data sets, are only marginally related. However, all represent what I consider to be worthwhile follow-ups to this thesis. They could be carried out by me or by others using the data and information presented in this thesis. I summarize proposed future Termoskan studies here.

7.2.1 The Phobos Shadow: Surface Inertias

In addition to the occurrence analyzed in this thesis, Termoskan observed three other occurrences of the Phobos shadow on the surface of Mars. Although all are more complicated (as described in Chapter 6), approximate thermal inertias of the upper millimeters of the surface should still be able to be derived for each of these occurrences. This can be done using the eclipse cooling models of Chapter 6 combined with careful consideration of the observational complexities of each occurrence.

7.2.2 Determining the Atmospheric Dust Load

The dust loading of the martian atmosphere at the time of the Termoskan observations represents an important point in our understanding of the atmospheric dust cycles on Mars and secular changes. Determination of the dust loading at that point and time is a unique analysis that can be done with Phobos '88 spacecraft instruments. Attempted determinations made from other instruments on the spacecraft have thus far yielded inconsistent results, arguing for the usefulness of doing the problem with Termoskan data.

It may be possible to use the shape of the Phobos shadow in the visible channel to determine the atmospheric dust loading at the time the Termoskan observations (early 1989, corresponding to very early martian northern spring). If there were no atmospheric

scattering, then the shadow would be well defined with sharp "corners" in the profile at the onset of eclipse and at the point when all of Phobos was in front of the Sun as seen from the Martian surface. The actual shadow profile is smoothed and rounded and spread out compared to the non-scattering ideal (as seen in Figure 6.3). By using a numerical scattering model of the martian atmosphere (e.g., *Yung*, 1976) in a computer model that also takes into account the geometry involved, model shadow profiles can be produced. The zero phase angle observations simplify the geometry somewhat.

By comparing these model profiles to the actual profiles, the dust loading of the atmosphere as described by its optical depth can in principal be determined. Parameters such as particle size, distribution with height, and single scattering albedo may have to be assumed based upon existing estimated values for martian atmospheric dust. It is possible that some of these parameters can be constrained based upon the shadow shape as well. Comparing results for the different shadow occurrences will give a check of the internal consistency of the method. Doing the same analysis using Viking visible images will give a check of the general validity of the method. The morning and evening limb profiles also contain information about the atmosphere that can be independently compared with the shadow results.

7.2.3 Aeolian Studies

Aeolian processes are currently active on Mars and have been proposed as the cause of many of the thermal inertia variations on Mars [e.g., *Christensen and Moore*, 1992]. Thus, although I have identified two morphologic features (ejecta blankets and channels) whose primary thermal nature is likely not of aeolian origins, most of the thermal variations on Mars are still thought to have aeolian causes. The first part of this study would be to analyze and characterize aeolian features using the Termoskan data set alone. Types of aeolian features observed within the data include: relatively high inertia, presumably aeolian sand intracrater deposits, the largest of which were studied with IRTM

data [e.g., *Christensen*, 1983]; wind streaks, which were studied at length in the visible [e.g., *Veverka et al.*, 1981] and the largest of which were studied using IRTM data; miscellaneous aeolian appearing splotches; and what appear to be regional aeolian deposits and erosional surfaces.

The second part of the study would involve comparison of the Termoskan data with Viking visible images and Viking IRTM data to look for temporal variations that have occurred since Viking. Temporal variations, particularly those involving temporary blanketing, were observed during the time period of Viking observations. Termoskan gives the opportunity to look for changes that occur on the scale of years (between the late 70's and 1989). The analysis could start by looking at Viking data from the same season (very early northern spring) in order to try to eliminate seasonal variations. Then, data can be compared from all seasons to try to distinguish changes that occur on a seasonal scale from those that are really the work of about ten years of aeolian modification. Eventually, the study of these features can be expanded to future missions' data in order to get an even larger spread in time, but with Termoskan serving as a "middle" point.

7.2.4 Radar Stealth Region

Muhleman et al. [1991] found a large (tens to hundreds of km) region west of Pavonis Mons that showed no detectable polarized or depolarized radar return using the highest resolution ground based radar study of Mars to date. They named the region, Stealth. To explain the observations, they proposed a several meter thick ash tuff surface layer devoid of volume scatterers. Termoskan obtained extremely high resolution (0.3 km per pixel) thermal and visible data for part of this region. Termoskan provides one potential test of the ash tuff hypothesis. One would expect an ash tuff that gives virtually no radar return to have very homogeneous thermal properties as well as low thermal

inertia. To assess the thermal inertia homogeneity, the visible channel will need to be carefully anchored to Viking albedo observations to insure accuracy.

7.2.5 Comparison of Termoskan Data with Phobos '88 ISM Data

ISM (Infrared Spectrometer for Mars) was a French near-infrared (VIMS-like) scanning spectrometer flown aboard the Soviet Phobos '88 mission [*Bibring et al.*, 1989 and 1991]. Like Termoskan, ISM obtained a limited number of swaths in the equatorial region before the failure of the spacecraft. The overlap of the Termoskan and ISM coverages is shown in Figure 7.1. The Termoskan data can be compared with the ISM data in order to study possible correlations between composition (ISM) and surface thermal properties (Termoskan). Comparison of these two data sets is particularly powerful because they were obtained at the same exact season and closely in time of day. For example one can look for correlations between low inertia features and strong hydration features that may be indicative of clay rich dust deposits. Similarly, hydration features are of particular interest in looking at the thermally distinct channels seen by Termoskan. The ISM data available in the literature (e.g., *Erard et al.*, 1991) will make for an interesting first comparison with Termoskan. Then, comparison with the digital data can be done.

7.3 Implications for Future Missions

7.3.1 Interdisciplinary Test Sites

In order to do accurate quantitative analyses, it is obviously important to understand the exact calibration of the instruments. In the past, visible photometric accuracy has only been known to within 20 percent at best [*Herkenhoff*, 1989]. Calibration and photometric accuracy of future mission's instruments can be refined through comparisons of similar wavelength data from several instruments. For MO, this would have included MOC, TES, PMIRR, and perhaps MOLA.

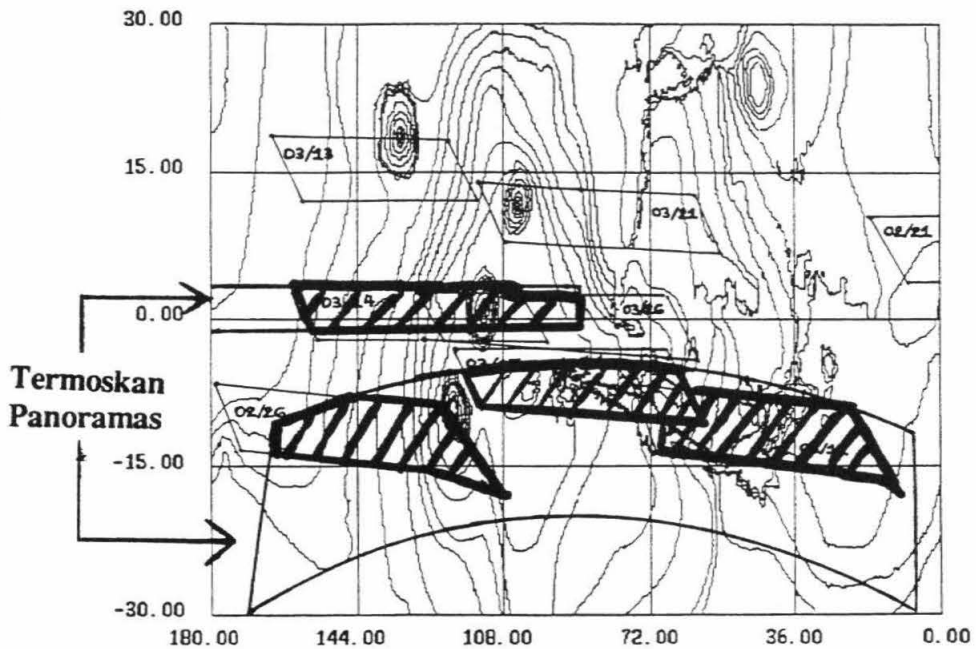

Figure 7.1. Map showing ISM and Termoskan coverage and their overlap in the western hemisphere of Mars. Overlap regions are denoted by diagonal lines. Overlap region includes a thermally distinct ejecta blanket rich region north of Valles Marineris. (Original ISM coverage figure is from *Bibring et al.* [1991].)

The best regions to compare data sets and to do photometry are regions that are free of inherent variations at the scale compared, in other words bland regions as free as possible from albedo, inertia, and topographic variations. I have used the Termoskan data set to search for regions that are "bland" both in the thermal and in the visible. These study regions, or Interdisciplinary Test Sites (IDTS) were to be used by Larry Soderblom's MO Interdisciplinary Science Team which included Participating Scientists Bruce Murray and Ken Herkenhoff. They will still be useful for future missions.

In choosing the Termoskan based IDTS's, I looked through the entire Termoskan data set for sites that appeared bland in Termoskan's thermal and the visible channels. The best IDTS's are shown in Table 7.1. This table also includes sites outside Termoskan's equatorial coverage that were chosen by Ken Herkenhoff based upon Viking data (those sites are designated by V's and the Termoskan sites are designated by P's). Except where otherwise noted in the comments section of the table, all of these sites were bland over at least 1° latitude by 1° longitude. Most were bland out to about 2° x 2°.

Site selection was based upon qualitative and quantitative "blandness." Qualitatively, each site appeared bland to the eye even under hard contrast stretches, lacked obvious craters (at Termoskan's 2 km/pixel resolution), and lacked any other sharp topography that would cause large thermal variations due to slopes. Quantitatively, within 1° x 1° of the center of the site, both thermal and visible dn values varied by less than ± 2 dn, with most pixels varying by ± 1 dn. In the thermal channel, over most temperature ranges, 1 dn corresponds to approximately 1/2 K.

Most of the Termoskan selected sites tend to be on younger terrains, i.e., Amazonian and Hesperian terrains, due to difficulties in finding bland sites on the older Noachian terrains. Although partly due to inherent variability, this terrain bias is largely due to thermal and visible variations caused by the greater number of craters and fractures on Noachian terrains.

PREI	LAT	LON	INER.	ALBEDO	ELEV.	UNIT	MC-
V18	82.5	345.0	8.2	0.25	-1000	Api	1
V16	76.0	320.0	8.2	0.25	-1000	Am	1
V09	55.0	111.0	5.0	0.28	1426	Hal	3
V04	54.0	44.0	13.6	0.11	-3000	Hvm	4
V12	46.0	209.0	6.0	0.27	-1632	Hvm	7
V17	23.0	344.0	2.7	0.29	-112	Hr	12
V15	22.0	319.0	2.4	0.27	1971	Npld	12
V13	18.0	272.0	8.1	0.25	-1998	Hvr	13
V02	8.0	36.0	9.8	0.25	-1459	Hchp	11
P14	3.0	32.0	9.5	0.19	35	Npl1	11
P16	3.0	192.5	3.1	0.27	-1997	Achu	15
V06	2.0	62.0	6.1	0.23	2315	Hr	10
V05	1.0	50.0	6.4	0.25	2402	Npl1	10
V01	-5.0	4.0	7.5	0.15	1123	Npld	19
P15	-5.5	12.5	7.8	0.25	154	Npl1	19
P08	-9.0	87.5	5.8	0.21	8460	Hsu	18
V10	-9.3	120.5	1.8	0.27	13944	At6	17
P13	-9.5	191.5	3.0	0.28	233	Apk	23
P06	-10.0	104.5	3.3	0.27	8197	Hsu	17
P10	-11.5	50.0	6.9	0.16	1895	Hpl3	18
P11	-13.5	248.5	6.2	0.18	3485	Hr	22
P05	-14.0	108.5	3.1	0.24	8242	Hsu	17
P03	-14.5	116.0	2.2	0.27	8232	At5	17
P09	-15.0	67.5	6.3	0.19	5626	Hr	18
P04	-15.0	108.5	3.1	0.24	8213	Hsu/Nf	17
P07	-16.0	105.0	5.3	0.20	8370	Hsu	17
P01	-17.5	146.5	2.7	0.30	3565	AHt3	16
P12	-18.0	205.5	6.2	0.19	2963	Hr	23
P02	-21.0	141.5	4.0	0.25	4804	AHt3	16
V07	-26.0	77.0	8.1	0.15	7000	Hr	18
V14	-37.0	299.0	7.9	0.29	-4809	Ah8	28
V03	-50.0	38.0	9.1	0.24	1000	Nple	26
V11	-50.0	170.0	7.0	0.24	5030	Hr	24
V08	-75.0	98.0	8.2	0.25	-1000	Hdu	30

Table 7.1. Interdisciplinary Test Sites: PREID, temporary identification numbers assigned to sites, numbers starting with P are from Termoskan data and those starting with V are from Viking data; LAT, latitude; LON, West longitude; INER, thermal inertia from 2° x 2° binned thermal inertias from *Palluconi and Kieffer* [1981]; ALBEDO, 1° x 1° binned albedos from *Pleskot and Miner* [1981]; ELEV., elevation data in meters from *USGS* [1976], as appears in the Mars Consortium data set; UNIT, geologic unit from *Scott and Tanaka* [1986], *Greeley and Guest* [1987], or *Tanaka and Scott* [1987] (USGS maps I-1802 A, B, and C, respectively); MC-, Mars quadrangle number as defined by the USGS; COMMENTS, miscellaneous comments, with the initial V or P indicating the sites were chosen based upon Viking or Phobos data respectively, and G-BS indicates that ground-based spectrophotometry data is available for that location, and references to Ter. refer to Termoskan, M9 refer to Mariner 9 albedo based maps [*Batson et al.*, 1979], and VO refers to Viking Orbiter based albedo maps (specifically *USGS* [1979], map I-2179); LOCATIONAL COMMENTS, geographical references to the sites location; ADDITIONAL COMMENTS, more miscellaneous comments; T, average temperature (K) of the site in the Termoskan data, not corrected for time of day; VDN, visible channel dn value in Termoskan data, not corrected in any way; TOD, local time of day of the Termoskan observation of the site; PAN, Termoskan panorama number, there were four thermal/visible panoramas, taken 2/11/89, 3/1/89, 3/26/89, and 3/26/89, respectively; LINE, refers to the line number from within that panorama, determined from the versions of the panorama included on the PDS Phobos data CD-ROM test disk [*Betts*, 1992]; SAMP, sample number within that Termoskan panorama; and TDN, Termoskan thermal channel dn value, converted to the temperatures given in column T.

PREI	COMMENTS	LOCATIONAL COMMENTS
V18	V. Polar ice cap	
V16	V. Albedo boundary	
V09	V. Uniform albedo	
V04	V. Uniformly low albedo	
V12	V. Uniformly high albedo	
V17	V. Uniform albedo. G-BS	
V15	V. Uniform albedo. G-BS	
V13	V. Uniform albedo	
V02	V. Uniform albedo, major relief	
P14	P. Slightly less than 1x1 deg. bland	Plateau surr. by channels N. of Hydraotes Chaos
P16	P.	Roughly on Elysium Planitia
V06	V. Uniform albedo, moderate topo. G-BS	
V05	V. Uniform albedo. G-BS	
V01	V. Uniform albedo, moderate topo. G-BS	
P15	P.	Bright area between Meridiani & Margaritifer
P08	P.	
V10	V. High elevation	
P13	P.	E. of crater Reuyl.
P06	P. Alb. patterns may differ in Ter, M9, & VO	Northern Syria Planum
P10	P.	On Aurorae Planum, just N. of Val. Mar.
P11	P.	On Hesperia Planum
P05	P. Hi I, Low A of same boundary as -15, 108.5	Where Syria Planum meets Claritas Fossae
P03	P.	SE of Arsia Mons, on flanks
P09	P.	
P04	P. Low I, hi A side of boundary. <1 deg. bland	Where Syria Planum meets Claritas Fossae
P07	P.	Southern Syria Planum
P01	P.	E. of Mem. Fossae
P12	P. Wind streaks in area in VO & M9	W. of crater Hadley
P02	P. Slightly less than 1x1 deg. bland	
V07	V. Uniform albedo. G-BS	
V14	V. Uniform albedo, low elevation	
V03	V. Uniform albedo (large area). G-BS	
V11	V. Uniform albedo	
V08	V. Uniform albedo, polar	

Table 7.1: Continued

PREI	ADDITIONAL COMMENTS	T	VDN	TOD	PAN	LINE	SAMP	TDN
V18								
V16								
V09								
V04								
V12								
V17								
V15								
V13								
V02								
P14	Closer to 2.75 lat. Channels and crater nearby	259.50	154	11.02	2	496	336	87
P16		258.50	170	9.54	1	685	344	85
V06								
V05								
V01								
P15		268.75	166	12.47	2	1090	53	106
P08		265.00	156	11.77	3	1508	322	97
V10								
P13	Near (1 deg +) high-lowland and alb. bound.	272.27	181	12.27	4	1892	335	114
P06	Darkest part of bright (N) part of Syria Planum	267.50	166	10.50	3	1003	307	103
P10	Closer to 49.7W lon.	258.00	152	14.57	3	2652	298	84
P11		220.00	101	7.88	4	410	266	29
P05	Actual boundary at -14.5. Pts. are .3 deg. away	252.22	135	10.20	3	904	188	73
P03	Small craters exist 1 deg. to either side	250.56	179	9.64	3	796	184	70
P09	Bland nearby, but variegated further away	265.83	135	13.27	3	2137	150	99
P04	Actual boundary at -14.5. Pts. are .3 deg. away	258.50	169	10.20	3	904	170	85
P07	Very bland in Ter.&M9. Alb. bound. in VO	248.75	76	10.46	3	998	120	67
P01	Also appears in Pan 4 near evening limb	190.00	103	7.36	3	104	180	8
P12	Very little bland thermal in this general region	257.50	156	11.19	4	1462	64	83
P02		200.00	110	7.74	3	189	62	13
V07								
V14								
V03								
V11								
V08								

Table 7.1: Continued

Two points, PREID numbers P04 and P05 deserve special mention because they were selected with slightly different criteria in mind. They were picked because they lie on either side of a very sharp and strong albedo and thermal inertia boundary. They are reasonably bland over less than a degree scale, perhaps over 1/2° x 1/2°, but are most interesting because of the boundary that lies between them.

7.3.2 Proposed MO, M94, and Other Future Mission Studies

I conclude my thesis by discussing ways to use future spacecraft to learn more about topics presented in this thesis, and to test hypotheses presented in this thesis. The tragic loss of the Mars Observer spacecraft while I was writing this chapter left me with the question of whether to include proposed studies for MO. I decided to include shortened versions of these proposals because they will be generally applicable to whatever analogous instruments fly on future missions. So, here I discuss proposed studies for MO, M94, and future missions in general. For each instrument discussed, I propose studies that may be useful for resolving some of the questions raised by this thesis. In previous chapters I discussed how future instruments could address issues for the particular chapter topics. Here, I generalize those discussions and add others on an instrument by instrument basis.

In general, Mars Observer would have been, and future missions will be, particularly useful in extending Termoskan studies globally in the thermal IR and in the visible. This will answer important questions such as are EDITHs globally still seen primarily on Hesperian and thin Amazonian areas? Also, are high inertia channel floors globally associated with fretted morphologies as opposed to catastrophic flooding morphologies?

The thermal emission spectrometer (TES) [*Christensen et al.*, 1992] on MO would have been the most analogous instrument to Termoskan, and in many ways the most powerful instrument for answering questions posed by my Termoskan research. Its power

to have answered these questions in addition to the success of the Termoskan analyses themselves argue strongly for a TES like instrument on future missions. TES would have had similar resolution (3 km/pixel) to the Termoskan panoramas used in my analyses, but greater sensitivity and medium resolution thermal infrared emission spectroscopy. Thus, in addition to providing global coverage, TES would have: 1 - through much more accurate albedos and inertias, allowed the separation of the relative importance of albedo versus inertia for EDITHs; 2 - allowed looking for spectroscopic differences between EDITHs and surroundings and between channels and surroundings; these would have included checks for increased minerals of hydration that might be expected from volatile-rich emplacement or large amounts of dust; 3 - contributed significantly to understanding the small scale causes of the inertias via 3 km/pixel rock abundance and fine component inertia maps derived using multi-wavelength methods similar to *Christensen* [1983; 1986]; specifically, TES could have distinguished whether the particle size of fines, the bonding of fines, or the abundance of rocks are responsible for inertia features such as EDITHs and channels; and 4 - results could have been be compared with Termoskan similar resolution results looking for variations on time scales of years.

Limb scans from MO's pressure modulator infrared radiometer (PMIRR) [*McCleese et al.*, 1992] would have allowed additional study of morning thermal limb brightening first observed by Termoskan, as well as stratospheric cloud features. It also would have obtained surface temperatures, albedos, and inertias with somewhat worse spatial resolution than TES.

I combine my discussion of the Mars Observer camera (MOC) with M94's high resolution stereo camera (HRSC) and all future high resolution orbital cameras. High resolution (on the order of meters) cameras will be able to distinguish fine morphologic details. These details will constrain my hypotheses for the emplacement mechanisms that caused thermally distinct ejecta blankets and channels. For example, MOC type resolutions (up to 1.4 m/pixel [*Malin et al.*, 1992]) would enable channel floor surface

morphologies indicative of aeolian, flooding, or fretting processes to be recognized. These morphologies may include: dunes, water flow morphologies, large boulders, and some mass wasting features. The morphologic differences between thermally distinctive features and non-thermally distinctive features can be tested at the scale of meters. High resolution images may actually be able to resolve large blocks, or phase function measurements could indicate their presence indirectly.

Instruments that give accurate fine scale topographic information, such as the Mars Observer laser altimeter (MOLA) profiles [*Zuber et al.*, 1992] and the Mars '94 HRSC, will be important for constraining mechanical models of fluidized ejecta flow and for understanding the current state of the inertia enhanced channels. In addition, signal shape from instruments such as MOLA will give some information about the small scale surface roughness of the ejecta blankets and channel floors versus their surroundings.

The Omega near-infrared imaging spectrometer on M94 will give important near IR spectral information about channels, EDITHs, and the surface in general. In particular, Omega will facilitate the mapping of trace amounts of hydrated minerals as was done at lower resolution for some Mars regions with the Phobos '88 ISM instrument [*Erard et al.*, 1991]. I would expect enhanced hydration signatures for the channel floors if significant bonding has taken place, and perhaps enhanced hydration signatures associated with EDITHs if water was involved in their emplacement.

Termoskan 2, planned for Mars '94, is expected to increase spatial resolution another order of magnitude from most of the Termoskan 1 data. Most aspects of the instrument are planned to be nearly identical to Termoskan. Thus, it will still be unable to deduce rock abundances by using multiple IR bands as was done with IRTM data, will not have an atmospheric band, nor will it be able to do any spectroscopy. However, it should allow several expansions upon the Termoskan data. The inclination, which will be somewhere near 50°, will allow the instrument to be targeted upon many regions of the planet, greatly expanding the Termoskan coverage. This alone can determine whether

some of the hypotheses presented here to explain EDITHs and channel inertia enhancements hold on a more global scale. In addition, more accurate inertias can be determined by observing areas more than once.

The most exciting Termoskan 2 feature is of course the much higher spatial resolution (as good as 150 m/pixel). The high spatial resolution targeted upon channels will test whether the thermal signal remains uniform at those resolutions. Observations of small craters and their ejecta and of landslides will test inertia enhancement theories and time scales. The high spatial resolution will also enable study of small craters to test the prediction that they should not have EDITHs except on very thin Hesperian or possibly Amazonian units. In addition, the higher spatial resolution combined with the greater global coverage will undoubtedly uncover new thermal features, just as Termoskan allowed the discovery of thermally distinct ejecta blankets.

Chance Phobos shadow observations are less likely to happen from the Mars '94 orbit than they were from the Phobos '88 orbit. Nonetheless, although challenging, they still can be obtained with proper planning and targeting. If the shadow is observed by Termoskan 2, the models developed in this thesis can be used to learn about the upper mm of the Martian surface in different regions. A recently proposed Russian Phobos sample return mission could easily obtain several observations of the Phobos shadow viewing in the anti-solar direction when near Phobos.

Finally, I note that EDITHs and inertia enhanced channel floors may be excellent targets for both future remote sensing and future landers. EDITHs are not significantly mantled, and material ejected from depth is exposed at the surface. Thermally distinctive channel floors offer a unique history and probable surface presence of material from various stratigraphic layers and locations.

Appendix 1

Far better is it to dare mighty things
than to take rank with those poor timid
spirits who know neither victory nor defeat.
- Theodore Roosevelt

PDS PHOBOS '88 CD-ROM: THE DATA FILES

This appendix comes from the Termoskan portion [*Betts*, 1992] of the Planetary Data System (PDS) Phobos '88 CD-ROM. For this CD, I created, delivered, and had reviewed a set of edited Termoskan digital data files, the original digital data files, and descriptions and confidence level notes for the instrument and data sets. In this appendix, I include the content of the AAREADME.TXT file which describes my file naming conventions. Also included are directory listings of all edited and raw data files taken directly from the CD-ROM. Finally, I include a sample PDS image label. I prepared a similar label for each of the edited and raw data files. Appendix 2 gives the instrument and data set descriptions and confidence notes, and Appendix 3 contains the spectral calibration characteristics of the Termoskan instrument and data, all of which also appeared on the CD-ROM.

Data File Naming Conventions

The general form of image and label files for the Termoskan data is:
PANvwwxy.zzz
where:
PAN stands for panorama
v = observing session number
1 = 1989-02-11 observing session
2 = 1989-03-01 observing session
3 = First 1989-03-26 observing session
4 = Second 1989-03-26 observing session
ww = Wavelength channel
VI = Visible channel (reflected solar) IR = Thermal infrared channel
x = File group
R = Raw data
E = Edited data, full length panorama in each file
F = Edited data files chopped into smaller fragments (maximum 512 lines)
y = Fragment number for that panorama for the R and F file groups
1 = westernmost file for that panorama
2,3,4... = fragment numbers heading east from fragment 1 Note: y = D for all files in file group E (there are no fragments)
zzz = Image or label file
IMG = Image file
LBL = Label file

For example, PAN2IRED.IMG contains the entire edited panorama for the thermal channel observations taken on 1989-03-01. PAN2IRED.LBL is the corresponding detached PDS label file for that image. PAN3IRR1.IMG contains the westernmost raw thermal image file from the first of the 1989-03-26 observing sessions. PAN1VIF1.IMG contains the westernmost 512 line fragment of the edited visible channel image from 1989-02-11 (equivalent to just the first 512 lines of the PAN1VIED.IMG file).

The file DNTOTEMP.TBL contains the conversion from thermal channel dn values to brightness temperatures.

List of Edited Data Files

```
 Volume in drive E is PHB_1001
Directory of  E:\TERMOSKN\EDIT_IMG
.          <DIR>        5-14-92   4:29p
..         <DIR>        5-14-92   4:29p
PAN1IRED IMG      794624        5-12-92  10:04a
PAN1IRED LBL      1099          5-14-92  11:34a
PAN1VIED IMG      786432        5-12-92  10:05a
PAN1VIED LBL      1100          5-14-92  11:35a
PAN2IRED IMG      929648        5-12-92  10:07a
PAN2IRED LBL      1027          5-14-92  11:36a
PAN2VIED IMG      524160        5-12-92  10:08a
PAN2VIED LBL      1027          5-14-92  11:38a
PAN3IRED IMG      1307948       5-12-92  10:10a
PAN3IRED LBL      1027          5-14-92  11:40a
PAN3VIED IMG      1316736       5-12-92  10:12a
PAN3VIED LBL      1027          5-14-92  11:42a
PAN4IRED IMG      1352956       5-12-92  10:14a
PAN4IRED LBL      1027          5-14-92  11:45a
PAN4VIED IMG      806400        5-12-92  10:16a
PAN4VIED LBL      1027          5-14-92  11:47a
PAN1IRF1 IMG      198656        5-12-92  10:04a
PAN1IRF1 LBL      1001          5-14-92  11:34a
PAN1IRF2 IMG      198656        5-12-92  10:04a
PAN1IRF2 LBL      1001          5-14-92  11:34a
PAN1IRF3 IMG      198656        5-12-92  10:05a
PAN1IRF3 LBL      1001          5-14-92  11:34a
PAN1IRF4 IMG      198656        5-12-92  10:05a
PAN1IRF4 LBL      1001          5-14-92  11:35a
PAN1VIF1 IMG      196608        5-12-92  10:06a
PAN1VIF1 LBL      1000          5-14-92  11:35a
PAN1VIF2 IMG      196608        5-12-92  10:06a
PAN1VIF2 LBL      1000          5-14-92  11:36a
PAN1VIF3 IMG      196608        5-12-92  10:06a
PAN1VIF3 LBL      1000          5-14-92  11:36a
PAN1VIF4 IMG      196608        5-12-92  10:06a
PAN1VIF4 LBL      1000          5-14-92  11:36a
PAN2IRF1 IMG      198656        5-12-92  10:07a
PAN2IRF1 LBL      1001          5-14-92  11:37a
PAN2IRF2 IMG      198656        5-12-92  10:07a
PAN2IRF2 LBL      1001          5-14-92  11:37a
PAN2IRF3 IMG      198656        5-12-92  10:07a
PAN2IRF3 LBL      1001          5-14-92  11:37a
```

PAN2IRF4 IMG	198656	5-12-92	10:07a
PAN2IRF4 LBL	1001	5-14-92	11:38a
PAN2IRF5 IMG	135024	5-12-92	10:08a
PAN2IRF5 LBL	1001	5-14-92	11:38a
PAN2VIF1 IMG	196608	5-12-92	10:08a
PAN2VIF1 LBL	1000	5-14-92	11:39a
PAN2VIF2 IMG	196608	5-12-92	10:08a
PAN2VIF2 LBL	1000	5-14-92	11:39a
PAN2VIF3 IMG	130944	5-12-92	10:08a
PAN2VIF3 LBL	1000	5-14-92	11:39a
PAN3IRF1 IMG	198656	5-12-92	10:10a
PAN3IRF1 LBL	1001	5-14-92	11:40a
PAN3IRF2 IMG	198656	5-12-92	10:10a
PAN3IRF2 LBL	1001	5-14-92	11:40a
PAN3IRF3 IMG	198656	5-12-92	10:10a
PAN3IRF3 LBL	1001	5-14-92	11:40a
PAN3IRF4 IMG	198656	5-12-92	10:10a
PAN3IRF4 LBL	1001	5-14-92	11:41a
PAN3IRF5 IMG	198656	5-12-92	10:10a
PAN3IRF5 LBL	1001	5-14-92	11:41a
PAN3IRF6 IMG	198656	5-12-92	10:11a
PAN3IRF6 LBL	1001	5-14-92	11:41a
PAN3IRF7 IMG	116012	5-12-92	10:11a
PAN3IRF7 LBL	1001	5-14-92	11:41a
PAN3VIF1 IMG	196608	5-12-92	10:12a
PAN3VIF1 LBL	1000	5-14-92	11:42a
PAN3VIF2 IMG	196608	5-12-92	10:12a
PAN3VIF2 LBL	1000	5-14-92	11:42a
PAN3VIF3 IMG	196608	5-12-92	10:12a
PAN3VIF3 LBL	1000	5-14-92	11:53a
PAN3VIF4 IMG	196608	5-12-92	10:12a
PAN3VIF4 LBL	1000	5-14-92	11:44a
PAN3VIF5 IMG	196608	5-12-92	10:13a
PAN3VIF5 LBL	1000	5-14-92	11:44a
PAN3VIF6 IMG	196608	5-12-92	10:13a
PAN3VIF6 LBL	1000	5-14-92	11:44a
PAN3VIF7 IMG	137088	5-12-92	10:13a
PAN3VIF7 LBL	1000	5-14-92	11:45a
PAN4IRF1 IMG	198656	5-12-92	10:14a
PAN4IRF1 LBL	1001	5-14-92	11:46a
PAN4IRF2 IMG	198656	5-12-92	10:14a
PAN4IRF2 LBL	1001	5-14-92	11:46a
PAN4IRF3 IMG	198656	5-12-92	10:14a
PAN4IRF3 LBL	1001	5-14-92	11:46a
PAN4IRF4 IMG	198656	5-12-92	10:15a

```
PAN4IRF4 LBL      1001          5-14-92  11:53a
PAN4IRF5 IMG      198656        5-12-92  10:15a
PAN4IRF5 LBL      1001          5-14-92  11:46a
PAN4IRF6 IMG      198656        5-12-92  10:15a
PAN4IRF6 LBL      1001          5-14-92  11:47a
PAN4IRF7 IMG      161020        5-12-92  10:15a
PAN4IRF7 LBL      1001          5-14-92  11:47a
PAN4VIF1 IMG      196608        5-12-92  10:16a
PAN4VIF1 LBL      1000          5-14-92  11:47a
PAN4VIF2 IMG      196608        5-12-92  10:16a
PAN4VIF2 LBL      1000          5-14-92  11:48a
PAN4VIF3 IMG      196608        5-12-92  10:16a
PAN4VIF3 LBL      1000          5-14-92  11:48a
PAN4VIF4 IMG      196608        5-12-92  10:16a
PAN4VIF4 LBL      1000          5-14-92  11:53a
PAN4VIF5 IMG       19968        5-12-92  10:16a
PAN4VIF5 LBL         998        5-14-92  11:48a
     102 File(s)     0 bytes free
```

List of Raw Data Files

Volume in drive E is PHB_1001
Directory of E:\TERMOSKN\RAW_IMG

.	<DIR>	5-14-92	4:29p
..	<DIR>	5-14-92	4:29p
PAN1IRR1 IMG	524288	5-12-92	9:54a
PAN1IRR1 LBL	993	5-14-92	10:44a
PAN1IRR2 IMG	524288	5-12-92	9:54a
PAN1IRR2 LBL	993	5-14-92	10:44a
PAN1VIR1 IMG	524288	5-12-92	9:55a
PAN1VIR1 LBL	993	5-14-92	10:45a
PAN1VIR2 IMG	524288	5-12-92	9:55a
PAN1VIR2 LBL	993	5-14-92	10:45a
PAN2IRR1 IMG	524288	5-12-92	9:56a
PAN2IRR1 LBL	993	5-14-92	10:41a
PAN2IRR2 IMG	524288	5-12-92	9:56a
PAN2IRR2 LBL	993	5-14-92	10:49a
PAN2IRR3 IMG	262144	5-12-92	9:56a
PAN2IRR3 LBL	991	5-14-92	10:41a
PAN2VIR1 IMG	364416	5-12-92	9:57a
PAN2VIR1 LBL	991	5-14-92	10:49a
PAN2VIR2 IMG	159744	5-12-92	9:57a
PAN2VIR2 LBL	991	5-14-92	10:41a
PAN3IRR1 IMG	262144	5-12-92	9:57a
PAN3IRR1 LBL	991	5-14-92	10:41a
PAN3IRR2 IMG	524288	5-12-92	9:57a
PAN3IRR2 LBL	993	5-14-92	4:05p
PAN3IRR3 IMG	524288	5-12-92	9:58a
PAN3IRR3 LBL	993	5-14-92	10:36a
PAN3IRR4 IMG	524288	5-12-92	9:58a
PAN3IRR4 LBL	993	5-14-92	10:36a
PAN3VIR1 IMG	372480	5-12-92	9:59a
PAN3VIR1 LBL	991	5-14-92	10:37a
PAN3VIR2 IMG	393216	5-12-92	9:59a
PAN3VIR2 LBL	993	5-14-92	10:37a
PAN3VIR3 IMG	393216	5-12-92	9:59a
PAN3VIR3 LBL	993	5-14-92	10:37a
PAN3VIR4 IMG	154368	5-12-92	9:59a
PAN3VIR4 LBL	991	5-14-92	10:38a
PAN4IRR1 IMG	524288	5-12-92	10:00a
PAN4IRR1 LBL	993	5-14-92	10:38a
PAN4IRR2 IMG	524288	5-12-92	10:00a
PAN4IRR2 LBL	993	5-14-92	10:38a

```
PAN4IRR3 IMG      524288      5-12-92  10:01a
PAN4IRR3 LBL      993         5-14-92  10:39a
PAN4IRR4 IMG      524288      5-12-92  10:01a
PAN4IRR4 LBL      993         5-14-92  10:39a
PAN4VIR1 IMG      393216      5-12-92  10:01a
PAN4VIR1 LBL      993         5-14-92  10:43a
PAN4VIR2 IMG      392064      5-12-92  10:02a
PAN4VIR2 LBL      993         5-14-92  10:40a
      48 File(s)              0 bytes free
```

Sample PDS Image Label

```
CCSD3ZF0000100000001NJPL3IF0PDS200000001          =       SFDU_LABEL
PDS_VERSION_ID                                    =       PDS2
RECORD_TYPE                 =       FIXED_LENGTH
FILE_RECORDS                =       3371
RECORD_BYTES                =       388
^IMAGE                      =       "PAN3IRED.IMG"
DATA_SET_ID                 =       "PHB2-M-TS-2-EDITED-
                                    THRM/VIS-IMG-EDR-V1.0"
PRODUCT_ID                  =       "ALL OF PANORAMA 3, THERMAL,
EDITED"
DETECTOR_ID                 =       "THERMAL CHANNEL"
SPACECRAFT_NAME             =       "PHOBOS 2"
INSTRUMENT_NAME             =       TERMOSKAN
TARGET_NAME                 =       MARS
SOFTWARE_NAME               =       "N/A"
START_TIME                  =       1989-03-26T09:11:29
STOP_TIME                   =       1989-03-26T10:11:29
SPACECRAFT_CLOCK_START_COUNT =      "N/A"
SPACECRAFT_CLOCK_STOP_COUNT  =      "N/A"
PRODUCER_ID                 =       "BRUCE H. BETTS"
PRODUCER_INSTITUTION_NAME=          "CALIFORNIA INSTITUTE OF
                                    TECHNOLOGY"
PRODUCT_CREATION_TIME       =       1992-04
OBJECT                      =       IMAGE
 LINES                      =       3371
 LINE_SAMPLES               =       388
SAMPLE_TYPE                 =       UNSIGNED_INTEGER
 SAMPLE_BITS                =       8
END_OBJECT                  =       IMAGE
END
```

Appendix 2

This royal throne of kings, this sceptered isle,
This earth of majesty, this seat of Mars...
-William Shakespeare

DIGITAL DATA DESCRIPTIONS AND CONFIDENCE NOTES

The material in this appendix is taken directly from material which appeared on the Planetary Data Systems (PDS) Phobos '88 CD-ROM. I reference this material as *Betts* [1992]. Here, I describe and give confidence level notes for two data sets that I delivered to the PDS. The first description is for the "raw" data files that were delivered to Caltech by the Institute of Space Devices in April 1990 (DATA_SET_ID = PHB2-M-TS-2-THERM/VIS-IMGEDR-V1.0). The second description is for my edited data files (DATA_SET_ID = PHB2-M-TS-1-EDITED-THRM/VIS-IMG-EDR-V1.0). There are eight edited files corresponding to the four Termoskan observing sessions, each having one thermal and one visible panorama. All of the description is presented in the standard PDS format.

The Raw Data Set

CCSD3ZF0000100000001NJPL3IF0PDS200000001 = SFDU_LABEL RECORD_TYPE
= STREAM PRODUCT_CREATION_TIME = 1992-05-13
NOTE = "Data Set information for Phobos CD-ROM."

OBJECT = DATASET
DATA_SET_ID = "PHB2-M-TS-2-THERM/VIS-IMGEDR-V1.0"

OBJECT = DATASETINFO
DATA_SET_NAME = "PHOBOS 2 MARS TERMOSCAN
THERMAL/VISIBLE IMAGING EDR V1.0"
EVENT_START_TIME = 1989-02-11T10:55:00Z
EVENT_STOP_TIME = 1989-03-26T17:49:50Z
NATIVE_START_TIME = "N/A"
NATIVE_STOP_TIME = "N/A"
DATA_OBJECT_TYPE = IMAGE
DATA_SET_RELEASE_DATE = 1992
PROCESSING_LEVEL_ID = 2
PRODUCER_FULL_NAME = "Yuri Gektin"
PRODUCER_INSTITUTION_NAME = "Institute for Space Device Engineering"
SOFTWARE_FLAG = N
DETAILED_CATALOG_FLAG = N
PROCESSING_START_TIME = 1989
PROCESSING_STOP_TIME = 1989
DATA_SET_DESC = "In February and March, 1989, the
Termoskan instrument on board the Phobos '88 spacecraft of the USSR acquired a limited set of very high resolution simultaneous observations of the reflected solar flux (hereafter referred to as the visible channel) and emitted thermal flux (thermal infrared (IR)) from Mars's equatorial region. These are, so far, the highest spatial resolution thermal data ever obtained for Mars. Four slightly overlapping thermal panoramas (also called scans or swaths) cover a large portion of the equatorial region from 30°S to 6°N latitude. Simultaneous visible panoramas were taken during each of the four observing sessions; due to spacecraft memory limitations, visible channel processing was stopped early relative to the thermal channel for two of the sessions (2 and 4). Thus, the visible channel panoramas are shorter than the thermal panoramas for these sessions.

The instrument was fixed to the spacecraft with the optical axis pointing in the anti-solar direction. As a consequence, all observations are at approximately zero degrees phase angle and only daytime observations were acquired. Scan lines were acquired approximately going from north to south on the planet at a rate of 1 line per second.

In the first session (taken Feb. 11, 1989), the periapse altitude of the spacecraft's elliptical orbit was 1150 km and the resolution at nadir was approximately 300 m per pixel. The thermal and visible channel panoramas from this session exhibit longitudinal gaps of varying size between scan lines. Within each scan line (acquired in the north-south direction); however, full resolution and coverage were maintained. In the remaining three sessions (one taken on March 1, 1989 and two on March 26, 1989), the panoramas were acquired from a circular orbit of altitude 6300 km with a resolution at nadir of approximately 1.8 km per pixel. In these panoramas, line and frame scanning correspond; therefore, there are not significant gaps between scan lines, and geometrical distortions primarily occur only because of the sphericity of the planet.

Each image consists of 384 samples. The number of lines varies depending upon how long the instrument was on in any given panorama. The data is 8 bit data with dn values ranging from 0 to 255 for both the thermal and the visible channels. West is towards the top of each image file and North is to the right.

All of the Termoskan data is contained in the 23 files of this data set. These files were delivered by the Institute of Space Devices Engineering (ISDE) (Moscow) to Caltech (Pasadena) in April, 1990 (except for session 1 which was delivered a few months earlier). The only difference between the files included here and those delivered from the Institute of Space Devices is that I have mirror flipped some of the files (resulting files all with the extension img: pan1irr1, pan1irr2, pan1vir1, pan1vir2, pan3irr1, pan3irr2, pan3irr3, pan3irr4, pan4vir1, and pan4vir2) as necessary. This was needed because some, but not all, of the image files were delivered from ISDE with the images appearing as Mars would appear if you saw it in a mirror.

Each of the thermal channel files in this data set has 512 samples because in addition to the 384 data pixels per line, there are also 126 pixels on one side of the image used for temperature stripes--each stripe representing the dn level for an additional 10 K. The visible channel files each have 384 pixels (except for session 1 which has filler pixels to 512 samples).

Each of these files are fragments of larger panoramas. The pixels in the thermal channel files and visible channel files are not aligned (do not correspond to the same location on Mars) in this data set. See confidence level notes for more details, and see the edited data set for complete panoramas that have been corrected so as to have the thermal data aligned geometrically with the visible channel data."

CONFIDENCE_LEVEL_NOTE = "A given line and sample in the raw thermal files will not correspond to the same location on Mars as the same line and sample in any of the visible channel files. Various quirks within the data and the raw data files that cause misalignment of the thermal and visible images

are taken into account in the edited data set (file names ending in ed) but not in this raw data set. These include the following. Part of the misalignment problem is just due to the different raw files being of different length. In addition there are: offsets at the beginning of the scans, probably caused by data lines added to the files on Earth; dropped (missing) data lines in some of the thermal data and in some of the visible data (in most of the raw data no gaps are left to distinguish these missing lines); 2 to 3 pixel offsets in the N-S direction between the thermal and visible channels (caused at the spacecraft), i.e., pixels need to be added to the beginning of each thermal line to make the thermal samples line up with the visible channel samples.

In addition to the alignment problems, the following occur in the data: noise in every eighth sample of the thermal channel amounting to a positive 1 or 2 dn increase (probably tied somehow into the calibration that was going on at a similar rate); sporadic single pixel spikes that occur occasionally within the data; occasional partial lines which appear corrupted; occasional whole lines with single dn values that appear to preserve geometry, but have no value as data; depending upon the panorama either the first or last of the 384 sample pixels is corrupted in the thermal channel, leaving at most 383 good samples per line; and two bright west-east lines (affecting the same samples in each line) in visible panorama 1 (possibly caused by reflections off the spacecraft?). The thermal channel appears to be very well calibrated to at least 3 K (Murray et al. 1991)."

END_OBJECT = DATASETINFO

OBJECT = DATASETTARG
TARGET_NAME = MARS
END_OBJECT = DATASETTARG

OBJECT = DSPARMINFO
SAMPLING_PARAMETER_NAME = PIXEL
SAMPLING_PARAMETER_RESOLUTION = 1
MINIMUM_SAMPLING_PARAMETER = "N/A"
MAXIMUM_SAMPLING_PARAMETER = 384
SAMPLING_PARAMETER_INTERVAL = 1<SECOND>
MINIMUM_AVAILABLE_SAMPLING_INT = "N/A"
SAMPLING_PARAMETER_UNIT = "N/A" DATA_SET_PARAMETER_NAME
= DN NOISE_LEVEL = "N/A"
DATA_SET_PARAMETER_UNIT = DIMENSIONLESS END_OBJECT =
DSPARMINFO

OBJECT = SCDATASET
INSTRUMENT_HOST_ID = PHB2
INSTRUMENT_ID = TS
END_OBJECT = SCDATASET

```
    OBJECT                          = DSREFINFO
    REFERENCE_KEY_ID                = "MURRAYETAL1991"

    OBJECT                          = REFERENCE
      DOCUMENT_TOPIC_TYPE           = "DATA SET DESCRIPTION,
DERIVATION
          TECHNIQUE, AND ANALYSIS"
      JOURNAL_NAME                  = "PLANETARY AND SPACE SCIENCE"
      PUBLICATION_DATE              = 1991
      REFERENCE_DESC                = "Preliminary Assessment of Termoskan
          Observations of Mars, Planetary and Space Science, Vol. 39, 1991, pp.
          237-265"

                                        OBJECT          = REFAUTHORS
        AUTHOR_FULL_NAME        = "BRUCE MURRAY"

      END_OBJECT                    = REFAUTHORS

    END_OBJECT                      = REFERENCE

  END_OBJECT                        = DSREFINFO

END_OBJECT          = DATASET
```

The Edited Data Set

OBJECT = DATASET
DATA_SET_ID = " PHB2-M-TS-1-EDITED-THRM/VIS-IMG-EDR-V1.0"

OBJECT = DATASETINFO
DATA_SET_NAME = "PHOBOS 2 MARS TERMOSKAN EDITED
THERMAL/VIS IMAGING EDR V1.0"
EVENT_START_TIME = 1989-02-11T10:55:00Z
EVENT_STOP_TIME = 1989-03-26T17:49:50Z
NATIVE_START_TIME = "N/A"
NATIVE_STOP_TIME = "N/A"
DATA_OBJECT_TYPE = IMAGE
DATA_SET_RELEASE_DATE = 1992-005
PROCESSING_LEVEL_ID = 2
PRODUCER_FULL_NAME = "BRUCE H. BETTS"
PRODUCER_INSTITUTION_NAME = "CALIFORNIA INSTITUTE OF TECHNOLOGY" SOFTWARE_FLAG = N
DETAILED_CATALOG_FLAG = N
PROCESSING_START_TIME = 1992
PROCESSING_STOP_TIME = 1992
DATA_SET_DESC = "The first part of this description repeats general information from the raw data description and the latter part refers specifically to this data set. See the raw data set template for more description of the raw data.

In February and March, 1989, the Termoskan instrument on board the Phobos '88 spacecraft of the USSR acquired a limited set of very high resolution simultaneous observations of the reflected solar flux (hereafter referred to as the visible channel) and emitted thermal flux (thermal infrared (IR)) from Mars' equatorial region. These are, so far, the highest spatial resolution thermal data ever obtained for Mars. Four slightly overlapping thermal panoramas (also called scans or swaths) cover a large portion of the equatorial region from 30°S to 6°N latitude. Simultaneous visible panoramas were taken during each of the four observing sessions; due to spacecraft memory limitations, visible channel processing was stopped early relative to the thermal channel for 2 of the sessions (2 and 4). Thus, the visible channel panoramas are shorter than the thermal panoramas for these sessions.

The instrument was fixed to the spacecraft with the optical axis pointing in the anti-solar direction. As a consequence, all observations are at approximately zero degrees phase angle and only daytime observations were

acquired. Scan lines were acquired approximately going from north to south on the planet at a rate of 1 line per second.

In the first session (taken February 11, 1989), the periapse altitude of the spacecraft's elliptical orbit was 1150 km and the resolution at nadir was approximately 300 m per pixel. The thermal and visible channel panoramas from this session exhibit longitudinal gaps of varying size between scan lines. Within each scan line (acquired in the north-south direction), however, full resolution and coverage were maintained. In the remaining three sessions (one taken on March 1, 1989 and two on March 26, 1989), the panoramas were acquired from a circular orbit of altitude 6300 km with a resolution at nadir of approximately 1.8 km per pixel. In these panoramas, line and frame scanning correspond; therefore, there are not significant gaps between scan lines, and geometrical distortions primarily occur only because of the sphericity of the planet. The dark west-east bands in observing sessions 3 and 4 are from the shadow of Phobos. Each image consists of 384 samples. The number of lines varies depending upon how long the instrument was on in any given panorama. The data is 8 bit data with dn values ranging from 0 to 255 for both the thermal and the visible channels. West is towards the top of each image file and north is to the right.

There are three major differences between this data set and the raw data set First, the raw data has been stripped of all non-image samples, leaving 384 samples. Second, all panorama fragments of the raw data files have been recombined so that each of the full length edited files (designated by file names ending with ed) contain one entire panorama (either thermal or visible). Thus, there are eight full length files corresponding to the four Termoskan observing sessions. For ease of display on some systems, each of these full length files has also been chopped into 512 line fragments (with file names ending in f# where # is the fragment number for that panorama). Note that the last fragment file of each panorama may have less than 512 lines depending upon the length of the full length file. Third, data from the visible and thermal channels have been aligned so that a given line and sample in a thermal image should correspond to the same location on Mars as the same line and sample in the corresponding visible channel image.

Various actions were required to align the thermal and visible data files. Three factors affected the alignment of lines between the thermal and visible files. First, there were offsets at the beginning of files, probably caused by data lines added on Earth. This initial offset was determined by comparison of surface features near the beginnings of the panoramas. Then, non-data lines were removed from the beginning of the appropriate file. Second, there are dropped (missing) data lines in some of the thermal data and in some of the visible data. In most of the raw data, no extra lines were added to fill these gaps. Comparison of the same surface features in both visible and thermal raw images on either side of the dropped lines was used to determine

the number of lines missing. This number of black (dn = 0) lines were inserted to represent the missing lines in the edited files. There were rare occurrences of seemingly superfluous dn = 0 lines in the raw data. These lines were removed. Within the raw data set there are also occasional lines with dn = (a constant value not equal to zero). Most of these lines appeared to preserve geometry, so they were left in the edited files.

There was also a constant offset between thermal and visible samples (north-south direction). The offset ranged from 2 to 3 samples but appeared to be constant for any given observing session. This offset was corrected for in the edited data by adding either 2 or 3 dn = 0 samples to the beginning of each line in the thermal channel.

All thermal files within the edited data set have 388 samples per line, with either 2 or 3 leading dn = 0 samples, 384 data samples, and either 1 or 2 trailing dn = 0 samples. All visible channel files have 384 samples per line.

The UT start and stop times given in the full length edited file labels are times at the spacecraft, not earth receive times."

CONFIDENCE_LEVEL_NOTE = "The alignment of thermal and visible edited files should be good to within approximately +/- 1 pixel.

Lengths of the scans derived from the start and stop times and the 1 line per second scan rate do not always agree with the lengths of the scans, probably due primarily to lines added or subtracted at the beginnings and ends of the 'original' (raw) files. However, the magnitude of the difference in all cases is less than five minutes (300 lines) and thus an insignificant error for most applications. In addition, the following confidence notes remain from the raw data: noise in every eighth sample of the thermal channel amounting to a positive 1 or 2 dn increase (probably tied somehow into the calibration that was going on at a similar rate); sporadic single pixel spikes that occur occasionally within the data; occasional partial lines which appear corrupted; occasional whole lines with single dn values that appear to preserve geometry, but have no value as data; depending upon the panorama either the first or last of the 384 sample pixels is corrupted in the thermal channel, leaving at most 383 good samples per line; and two bright west-east lines (affecting the same samples in each line) in visible panorama 1 (possibly caused by reflections off the spacecraft?). The thermal channel appears to be very well calibrated to at least 3 K (Murray et al. 1991)."

END_OBJECT = DATASETINFO

OBJECT = DATASETTARG
  TARGET_NAME = MARS
END_OBJECT = DATASETTARG

```
  OBJECT                          = DSPARMINFO
    SAMPLING_PARAMETER_NAME                =              PIXEL
    SAMPLING_PARAMETER_RESOLUTION                =              1
    MINIMUM_SAMPLING_PARAMETER              =              "N/A"
    MAXIMUM_SAMPLING_PARAMETER                =              384
    SAMPLING_PARAMETER_INTERVAL             =              1<SECOND>
    MINIMUM_AVAILABLE_SAMPLING_INT                =              "N/A"
    SAMPLING_PARAMETER_UNIT = "N/A" DATA_SET_PARAMETER_NAME
    = DN NOISE_LEVEL              = UNK
    DATA_SET_PARAMETER_UNIT = DIMENSIONLESS END_OBJECT =
  DSPARMINFO

    OBJECT                          = SCDATASET
      INSTRUMENT_HOST_ID      = PHB2
      INSTRUMENT_ID           = TS
    END_OBJECT                = SCDATASET

    OBJECT                          = DSREFINFO
    REFERENCE_KEY_ID          = "MURRAYETAL1991"

    OBJECT                          = REFERENCE
      DOCUMENT_TOPIC_TYPE          =  "DATA  SET  DESCRIPTION,
DERIVATION
          TECHNIQUE, AND ANALYSIS"
      JOURNAL_NAME              = "PLANETARY AND SPACE SCIENCE"
      PUBLICATION_DATE          = 1991
      REFERENCE_DESC            = "Preliminary Assessment of Termoskan
          Observations of Mars, Planetary and Space Science, Vol. 39, 1991, pp.
          237-265"

                                        OBJECT          = REFAUTHORS
        AUTHOR_FULL_NAME        = "BRUCE MURRAY"

      END_OBJECT                = REFAUTHORS

    END_OBJECT                = REFERENCE

  END_OBJECT                  = DSREFINFO

END_OBJECT          = DATASET

END
```

Appendix 3

I was unconscious for about an hour and a half,
but I really don't remember any of it.
I'm going to go turn in my thesis now.
-Mark Hofstadter

TERMOSKAN SPECTRAL RESPONSE AND CALIBRATION TABLES

The following spectral response and calibration tables appeared on the Planetary Data System's Phobos '88 CD-ROM [*Betts*, 1992] in the files calib.txt and dntotemp.txt.

```
CCSD3ZF0000100000001NJPL3IF0PDS200000001 = SFDU_LABEL
RECORD_TYPE          = STREAM
PRODUCT_CREATION_TIME  = 1992-05-13
OBJECT               = TEXT
NOTE                 = "Termoskan calibration tables."
END_OBJECT           = TEXT
END
```

TERMOSKAN CALIBRATION TABLES

The accompanying set of four tables provides spectral and intensity calibration information for the Termoskan instrument on the Phobos 2 spacecraft. The tables show the spectral filter response of the Termoskan visual and infrared channels, the conversion between data number (DN) and brightness for the visual channel, and between DN and brightness temperature for the infrared channel. The wavelengths in the filter response tables are expressed in micrometers; the response is given in arbitrary units, with a maximum value of 1.00. The visual channel brightness is expressed in watts per square meter per steradian; the infrared channel brightness temperature is expressed in Kelvins.

Termoskan visible channel spectral characteristic

λ (μm)	Relative Response	λ (μm)	Relative Response	λ (μm)	Relative Response
0.47	0.00	0.71	0.03	0.95	0.44
0.48	0.04	0.72	0.12	0.96	0.36
0.49	0.07	0.73	0.43	0.97	0.26
0.50	0.04	0.74	0.71	0.98	0.18
0.51	0.00	0.75	0.85	0.99	0.11
0.52	0.12	0.76	0.96	1.00	0.04
0.53	0.21	0.77	1.00	1.01	0.02
0.54	0.22	0.78	0.97	1.02	0.00
0.55	0.13	0.79	0.86	1.03	0.01
0.56	0.07	0.80	0.73	1.04	0.02
0.57	0.30	0.81	0.55	1.05	0.03
0.58	0.50	0.82	0.42	1.06	0.04
0.59	0.63	0.83	0.18	1.07	0.04
0.60	0.68	0.84	0.08	1.08	0.03
0.61	0.50	0.85	0.04	1.09	0.03
0.62	0.28	0.86	0.09	1.10	0.03
0.63	0.05	0.87	0.20	1.11	0.02
0.64	0.20	0.88	0.30	1.12	0.02
0.65	0.48	0.89	0.38	1.13	0.02
0.66	0.66	0.90	0.50	1.14	0.01
0.67	0.73	0.91	0.54	1.15	0.01
0.68	0.66	0.92	0.55	1.16	0.01
0.69	0.38	0.93	0.54	1.17	0.00
0.70	0.22	0.94	0.51	1.18	0.00

Termoskan infrared channel spectral characteristic

λ (μm)	Relative Response	λ (μm)	Relative Response	λ (μm)	Relative Response
7.0	0.00	9.2	0.67	11.4	0.90
7.1	0.02	9.3	0.72	11.5	0.85
7.2	0.04	9.4	0.77	11.6	0.78
7.3	0.07	9.5	0.81	11.7	0.60
7.4	0.15	9.6	0.81	11.8	0.47
7.5	0.19	9.7	0.82	11.9	0.41
7.6	0.21	9.8	0.83	12.0	0.36
7.7	0.23	9.9	0.84	12.1	0.29
7.8	0.25	10.0	0.84	12.2	0.25
7.9	0.31	10.1	0.82	12.3	0.21
8.0	0.37	10.2	0.83	12.4	0.18
8.1	0.44	10.3	0.81	12.5	0.15
8.2	0.45	10.4	0.77	12.6	0.13
8.3	0.46	10.5	0.76	12.7	0.11
8.4	0.48	10.6	0.78	12.8	0.08
8.5	0.50	10.7	0.78	12.9	0.07
8.6	0.50	10.8	0.77	13.0	0.05
8.7	0.52	10.9	0.77	13.1	0.04
8.8	0.54	11.2	1.00	13.4	0.02
9.1	0.64	11.3	0.96	13.5	0.02
				13.6	0.00

Termoskan visible response characteristic

DN	Brightness ($W\ m^{-2}\ srad^{-1}$)	DN	Brightness ($W\ m^{-2}\ srad^{-1}$)	DN	Brightness ($W\ m^{-2}\ srad^{-1}$)
10	0.3	80	4.6	150	8.8
20	0.9	90	5.2	160	9.4
30	1.5	100	5.8	170	10.0
40	2.1	110	6.4	180	10.6
50	2.7	120	7.0	190	11.2
60	3.3	130	7.6	200	11.8
70	4.0	140	8.2	210	12.4

Conversion of Thermal Channel DN Values
to Brightness Temperatures:

DN	Brightness Temperature (K)	DN	Brightness Temperature (K)
1	170	46	235
2	175	53	240
4	180	61	245
6	185	69	250
8	190	78	255
10	195	88	260
13	200	97	265
16	205	109	270
20	210	120	275
24	215	133	280
29	220	146	285
34	225	160	290
40	230		

Appendix 4

Mars ain't the kind of place to raise your kids.
In fact, it's cold as hell.
...And all the science I don't understand,
it's just my job five days a week.
-Elton John

THE MARSTHERM THERMAL MODEL

This appendix describes the *Clifford et al.* [1987] thermal model of the Mars surface that was used in Chapters 4 and 6. First, I briefly describe changes that I made to the program. These do not include the major changes I made when utilizing portions of this program in the modelling of eclipse cooling of the Mars surface due to the shadow of Phobos. Those changes are described in Chapter 6. The second and larger portion of this appendix is the detailed description of the MARSTHERM program which was included with the original version of the program I received.

Modifications to the Program

I primarily altered the MARSTHERM input and output to make it easier to use and to tailor it to my needs. I adjusted the input so that the user, either interactively or via a batch file, entered the latitude, inertia, and albedo for a given run of the program. I adjusted season within the program code itself, primarily because Termoskan only observed three distinct "seasons" (L_S = 356°, 6°, and 18°). Thus, I had three versions of the program to run, one for each Termoskan observed time of year. I had the program output temperatures at all depth steps for every 1/8 H (where 24 H = 1 Martian day) over the course of a full Martian day. I created other programs to constrain the output to only one depth step, and to plot temperature as a function of time for one depth, or temperature as a function of depth for several times. In deriving inertias, I would run the program several times, each with a separate inertia value, and all with the appropriate albedo, season, and latitude. Then, for the time of day of the observation, I could match model temperatures to observed temperatures to derive inertias, interpolating where necessary.

In addition to these input and output adjustments, I corrected some bugs in the program that included eliminating a spurious change in the albedo (without ice) in the middle of the program, shortening of a line that was longer than the standardly allowed FORTRAN 77 length, and expanding the Paige corrected double precision time variable definition to all necessary subroutines.

General MARSTHERM Description

What follows is taken from *Clifford et al.* [1987] and was included with the program, except for the correction in equation (8) which was a correction that David Paige made to the program.

The Mars Thermal Model (MARSTHERM) is a FORTRAN 77 program that uses the method of finite differences to compute surface and subsurface temperature variations at any given latitude throughout the martian year. For the sake of computational efficiency, the program utilizes non-constant intervals for both depth and time, increasing program execution speed with only a small loss in numerical accuracy. With only minor changes, the program should be readily adaptable to investigating the thermal behavior of most other planetary bodies.

SUBROUTINE FINDT

The subroutine FINDT determines the temperature distribution of the martian regolith as a function of depth. These temperature calculations are based upon the given physical properties and the value of the surface temperature that is passed to FINDT from the subroutine FNTEMP. The default values chosen for the surface albedo, soil thermal conductivity, density, and specific heat are the same as those adopted for the Standard Viking Thermal Model (Kieffer et al., 1977).

After initializing the variables, a basic time interval is chosen, and the depth interval for the first compartment is determined from that. At all times the time and depth increments must meet the stability criteria:

$$(K*DT)/(C*RHO*DZ^2)<=0.25 \qquad (1)$$

where K is the thermal conductivity, DT is the time increment, C is the specific heat, RHO is the density and DZ is the depth increment. [Note that some authors indicate a numerical stability criteria of 0.5 instead of 0.25. For values between 0.25 and 0.5, the solution will

converge but in an oscillatory fashion. However, for values <= 0.25, the solution is both convergent and non-oscillatory (James et al., 1967; p. 479). Possible complications arising from an inappropriate choice of compartment size and time interval can be illustrated by considering the result of having both a very small compartment and a very long time interval between calculations. Such a combination artificially permits the accumulation of a large quantity of heat within the compartment, thus leading to an excessively high and unrealistic temperature that may be only partially relieved by conduction during the subsequent time step.

The second and third compartments are given the same thickness as the first in order to simplify the treatment of the first derivative term included in the finite-difference version of the surface boundary condition equation in subroutine FNTEMP (See equations 6 and 13). Following the lead of Kieffer et al. (1977), the remaining compartment thicknesses are chosen such that each is a multiple of the previous one (i.e., the fourth compartment is 1.13 times as thick as the third, the fifth, 1.13 times as thick as the fourth, etc.).

The stability criteria given by Eq. 1 permits an increase in the time between calculations as compartment thicknesses become larger with depth; therefore, substantial economies in time can be achieved by increasing the time intervals accordingly. The time intervals are chosen such that each is four times the duration of the previous one (i.e., DT, 4*DT, 16*DT, etc.). For a given compartment, the appropriate time interval between successive iterations is the largest of these calculated intervals that satisfies the stability criteria. Those compartments which share the same time increment constitute a

level. By assigning the time intervals in this way, the compartment temperatures in one level are always updated simultaneously with those in all higher levels. In terms of performance, when compared with a double-precision 400-compartment constant-time and -depth interval model (Appendix A), the CPU time required to run the non-constant interval model amounts to an 88% speed improvement, with a maximum discrepancy in the final numerical results of less than two percent.

Compartment temperatures are initialized by calculating the average annual equilibrium surface temperature. This temperature is calculated on the basis of the previously selected values of latitude (LAT), albedo (A, where .25 is the default value), emissivity (E), and the annually averaged solar flux given by

$$<S>=[SO/4*(1-ECCEN^2)^{1/2}]((1.5-(2*SIN(OBLIQ))/PI)-(1.5-(6*SIN(OBLIQ))/PI)*SIN^2(LAT)) \quad (2)$$

where SO is the solar flux at the semi-major axis of Mars (a), ECCEN is the eccentricity, OBLIQ is the axial inclination of Mars, and LAT is the latitude (Hoffert et al., 1981). After all compartments are initialized to this temperature, the main loop of the program is entered.

The main loop first determines to what depth compartment temperatures will be updated during the current iteration. The first level compartment temperatures are recalculated with each iteration (i.e., each time step DT). Every fourth iteration these calculations are extended to include the compartments of the second level (those with a time interval of 4*DT), and every sixteenth iteration, those of the third level. This method is continued for the remaining levels until by the sixth and final level, temperatures are recalculated only

once every 1024 iterations. For a given iteration, the decision to extend the numerical calculations to a deeper level is made through the use of a multiple IF-THEN-ELSE statement. The MOD(I,4) statement finds the remainder when I is divided by four and therefore determines whether the loop has been repeated some multiple of four times. If not, only the first level is recalculated. If so, the IF statement checks whether the loop has been repeated some multiple of sixteen times, and so on.

The temperatures of the compartments are found using the basic one-dimensional heat conduction equation:

$$dT/dt=k/(rho*c)*d^2T/dz^2 \qquad (3)$$

where T is the temperature of the compartment,t is time, z is the depth, k is the thermal conductivity, rho is the density and c is the specific heat. Finite difference expressions are used for the two derivatives. The expression for dT/dt is found from a Taylor expansion of T(t+dt):

$$T(t+dt)=T(t)+dt*(dT/dt)+(dt)^2/2*(d^2T/dt^2)+...$$

Ignoring all terms of order 2 or higher, we obtain:

$$dT/dt=(T(t+dt)-T(t))/dt. \qquad (4)$$

From Sundqvist and Veronis (1969) we obtained for the second derivative the following expression:

$$(dT/dz_{i+1/2}-dT/dz_{i-1/2})/(0.5*(dz_i-dz_{i-1})) \qquad (5)$$

where

$$dT/dz_{i+1/2}=(T_{i+1}-T_i)/dz_i$$

and

$$dT/dz_{i-1/2}=(T_i-T_{i-1})/dz_{i-1}$$

The expressions for the derivatives are substituted into the heat

equation which is then solved for T(t+dt) (or TEMPDT as it is called in the program) for each of the compartments. Because of the T_{i+1} term in the second derivative, the temperature in the lowest compartment cannot be calculated using this equation since there obviously is no compartment after it. To allow constant readjustment of the lower boundary, the last compartment is assigned the same temperature as the second to last following each iteration (James et al., 1967). This should cause little error provided that the temperatures in the last two compartments are approximately the same. After this last temperature calculation has been made, the time is incremented by the interval dt.

If the elapsed time is greater than or equal to the time at which a printout of the results is required, the subroutine PRINT is called. No permanent record of the results is kept, in order to reduce the required memory space. Results that are not printed out are lost after being used to compute the next set of temperatures. All the new values that have been calculated and stored in the array TEMPDT are then passed to the array TEMP, the subroutine FNTEMP is called to determine the new surface temperature, and then the loop is repeated.

SUBROUTINE FNTEMP

Subroutine FNTEMP determines the surface temperature based upon the time of day and the position of Mars in its orbit and returns that value to subroutine FINDT. The values for the orbital eccentricity and obliquity are from Ward (1979).

FNTEMP first calls the subroutine FNANOM, which computes the appropriate values of the declination and the true anomaly for that

time. With these values, FNTEMP then determines the surface temperature from the equation:

$$S(1-ALBEDO)+K*dT/dz+FF+L*dm/dt=E*STEFAN*T^4 \quad (6)$$

(Kieffer et al., 1977) where S is the solar flux at the position of Mars in its orbit, K is the thermal conductivity, dT/dz is the change in temperature with depth evaluated at the surface, FF is the downward component of atmospheric radiation, L is the latent heat of vaporization of CO_2, dm/dt is the change in the mass of the CO_2, E is the emissivity (which, after Kieffer et al., (1977), is taken to be 1.0), and STEFAN is the Stefan-Boltzmann constant.

The incident flux is found from the equation $S=S_0\cos(i)$, where i is the angle of incidence of the incoming sunlight (measured from the zenith), and where S_0 is given by:

$$S_0=L/(4*pi*R^2) \quad (7)$$

where L is the luminosity of the sun and R is the instantaneous orbital distance of Mars. In the program, the constant SO is equal to S_0 evaluated at a distance equivalent to the semimajor axis, a, of Mars. Thus the solar flux at any other point in the planet's orbit is given by the expression $SO*a^2/R^2$. The ratio a^2/R^2 is called ORBIT in the program, and is given by:

$$ORBIT=(1+ECCEN*COS(ANOM))^2/(1-ECCEN^2)^2 \quad (8)$$

where ECCEN is the orbital eccentricity and ANOM is the true anomaly (Haymes, 1971, p.500). The cosine of the incidence angle (called SUNPOS in the program) is given by the equation:

$$SUNPOS=SIN(LAT)SIN(DEC)+COS(LAT)COS(DEC)COS(H) \quad (9)$$

where LAT is the latitude, DEC is the declination and H is the hour angle (Barkstrom, 1981). H is calculated from the expression:

H=PI*(ABS(1-(T-DAY*SOL)/12*HOUR)) (10)

where T is the time elapsed, DAY is the number of days elapsed, SOL is the length of a martian day and HOUR is the length of a martian hour. The value of H at sunrise and sunset (called HRZN) is also calculated. When the sun is at the horizon, the angle of incidence is 90 degrees; therefore, since cos(90)=0, Eq. 9 can be solved for HRZN giving:

HRZN=ACOS(-TAN(DEC)*TAN(LAT)) (11)

Two IF statements are also included to set HRZN equal to PI if the latitude is such that the sun never rises and to set HRZN equal to 0 if the latitude is such that the sun never sets. If the value of the hour angle is greater than that of HRZN (i.e., the sun is below the horizon) the solar flux is automatically set equal to zero. The net insolation at the martian surface is found from the equation INSOL=S*(1-ALBEDO), where the value chosen for ALBEDO is defined by the user (but which has a default value of 0.25 (Kieffer et al., 1977)). If the surface temperature falls below 149 K, CO_2 begins to condense from the atmosphere, whereupon the albedo jumps instantaneously to 0.65 (Kieffer et al., 1977). The value for FF (which has been dubbed the fudge factor) is also calculated at this time. As noted earlier, FF accounts for heat that is radiated from the atmosphere. It is set equal to two percent of the value of the insolation at noon (Kieffer et al., 1977).

The heat that is conducted from (or to) the martian surface ($k*dT_1/dz$) is calculated using a finite difference approximation for the derivative. As before, Taylor expansions are used for the temperatures in the second and third compartments. The expressions are:

$$T(z+dz)=T(z)+dz*dT_1/dz+dz^2/2*d^2T_1/dz^2+...$$

$$T(z+2*dz)=T(z)+(2*dz)*dT_1/dz+(2*dz)^2/2*d^2T_1/dz^2+...$$

Substituting T_1 for T(z), T_2 for T(z+dz), and T_3 for T(z+2*dz) gives:

$$T_2=T_1+dz*dT_1/dz+dz^2/2*d^2T_1/dz^2+...$$

$$T_3=T_1+(2*dz)*dT_1/dz+(2*dz)^2/2*d^2T_1/dz^2+... \quad (12)$$

By multiplying the first equation by four, subtracting the second and ignoring all terms of third order or higher, one obtains:

$$dT_1/dz=(4*T_2-T_3-3*T_1)/(2*dz). \quad (13)$$

The surface boundary condition (Eq. 6) is then solved for the surface temperature using Newton's method. The values of the equation and its derivative when all terms are pulled to one side and an initial value of the surface temperature are sent to subroutine NEWTON. The process is repeated with the new values calculated by subroutine NEWTON for the surface temperature until the estimated value given by Newton's method is sufficiently close to the preceeding value to assume that it is correct (the program uses a difference of 0.00001). The program then checks whether the latent heat term will be involved. If so, the temperature at the surface is set to 149 degrees, because once the CO_2 snow begins to form, the surface will remain at that temperature until all the CO_2 finally sublimates away. To determine the mass of CO_2 that either condenses or sublimates during the time interval DT, the surface energy balance is solved for dm (kg CO_2 m^{-3}). This amount is then added to the total mass of CO_2 that has already accumulated. Control is then passed back to the subroutine FINDT along with the most recently calculated value of the surface temperature.

SUBROUTINE FNANOM

Subroutine FNANOM calculates the declination of the sun in the sky and the true anomaly of the planet's position in its orbit. It also calculates the corresponding aerocentric longitude for identifying the orbital position of Mars at any given instant. The true anomaly can be found from the equation:

$$TAN(ANOM/2)=((1+ECCEN)/(1-ECCEN))^{1/2}*TAN(EA/2) \quad (14)$$

where ANOM is the true anomaly, ECCEN is the eccentricity and EA is the eccentric anomaly (Haymes, 1971). The eccentric anomaly is found by using Newton's method to solve the equation:

$$MEAN=EA-ECCEN*SIN(EA) \quad (15)$$

where MEAN (the mean anomaly) is used as the initial value of the eccentric anomaly (Barkstrom, 1981). The mean anomaly is found from the equation:

$$MEAN=(2*PI/PERIOD)*(T-TAU) \quad (16)$$

where T is the current time and TAU is the time of perihelion in seconds (Haymes, 1971). Since no value of TAU is specified in the program, the calculations begin with Mars at perihelion.

After both the eccentric and true anomalies have been calculated, the declination of the sun can be found from:

$$SIN(DEC)=SIN(OBLIQ)*SIN(ANOM+OMEGA-PI) \quad (17)$$

where DEC is the declination of the sun, OBLIQ is the obliquity of Mars (the angle between its axis of rotation and the perpendicular to the plane of orbit), and OMEGA is the angular distance between the northern hemisphere autumn equinox and perihelion (Hoffert et al., 1981).

L_S, the aerocentric longitude of the sun, is given by:

LS=(ANOM+PI+OMEGA)*180/PI-(REVS)*360 (18)

The term 180/PI merely converts the L_s from radians to degrees, and subtracting the number of orbital revolutions (REVS) multiplied by 360 keeps L_s between zero and 360 degrees. The values of the true anomaly, declination, and L_s are then passed back to the subroutine FNTEMP.

SUBROUTINE NEWTON

This subroutine solves an equation for a given variable using Newton's method. The value of the equation after all terms have been placed on one side, the value of its derivative, and an initial value for the variable are sent to the subroutine. The subroutine then estimates a new value using the equation:

GUESS=VALUE-X/DX (19)

where X is the equation and DX is the derivative of the equation. If the estimated value is close enough to the initial value (the program currently uses 1E-5), the variable REPEAT is assigned the value of false so that the procedure will not be repeated. The value of the variable is then set equal to the guessed value and that value is returned to the calling subroutine.

SUBROUTINE PRINT

This subroutine prints out the table of results. It can be modified to print out any of the variables in the program. The first time the subroutine is called, the headings for the table of results are also printed, and then the value of FIRST is set to false, to prevent the headings from being printed again. After printing out the

values requested, it calculates the time for the next printout and returns control to subroutine FINDT.

References

Barkstrom, B., 1981. What Time Does the Sun Rise and Set, Byte, pp. 94-114.

Haymes, R.C., 1971. Introduction to Space Science, John Wiley and Sons, Inc., p. 500.

Hoffert, M.I. et al., 1981. Liquid Water on Mars: An Energy Balance Climate Model for CO_2/H_2O Atmospheres, Icarus 47, pp. 112-129.

James, M.L. et al., 1967. Applied Numerical Methods for Digital Computation with FORTRAN, International Textbook Company, pp. 479-484.

Kieffer, H.H. et al., 1977. Thermal and Albedo Mapping of Mars During the Viking Primary Mission, J. Geophy. Res. 82, pp. 4249-4291.

Sundqvist, H. and G. Veronis, 1969, A Simple Finite-Difference Grid with Non-Constant Intervals. Tellus, 22.

Ward, W.R., 1979. Present Obliquity Oscillations of Mars: Fourth-Order Accuracy in Orbital e and I, J. Geophys. Res. 84, pp. 237-241.

Appendix 5

It's been a hard day's night,
and I've been working like a dog.
It's been a hard day's night,
I should be sleeping like a log.
- The Beatles

TIME OF DAY WITHIN THE TERMOSKAN DATA

This appendix describes how to calculate the local time of day for a given longitude within any of the Termoskan panoramas. Local times of day are critical for thermal modelling of the surface. First I describe the generalized program that I wrote to carry out this task. Then I describe simple linear equations that give results accurate enough for thermal modelling purposes.

I wrote a program to calculate the local time of day in the following manner. The absolute start and stop time of each scan is known to within a few seconds (see Table 2.2). So for any line in a panorama, the absolute time that the data line was acquired can easily be calculated using the line number and the fact that one line was taken every second. Thus, for a given observed point on the Martian surface, we know the time at which it was observed to within a few seconds. Finding its longitude using USGS map resources, we are then in a position to calculate the local time of day at that point when it was observed. To do this, I wrote a program that took a longitude, line number, and panorama for inputs. After calculating the absolute time of the observation, it then derived the sub-solar longitude (SSLO) for the time of the observation by using a reference value of the SSLO at 0 UT of that day as given in the *Astronomical Almanac*. Note that absolute time must be handled carefully because panorama start and stop times such as those given in Table 2.2 are times at the spacecraft, whereas times in the *Astronomical Almanac* are ground receive times. These two values differ by approximately 10 to 15 minutes for the Termoskan observations. Using the West longitude (LONG) of the point in question, I had the program calculate the local time of day using the expression:

$$\text{Local Time of Day} = [12.0 - (\text{LONG} - \text{SSLO})/15.0] \bmod 24,$$

where longitudes are West longitudes and local time of day is given in H, where 1 Martian Day = 24 H.

By doing a linear fit to results for several longitudes for each panorama, I derived linear expressions that give local time of day with very minor errors (less than 0.1H) compared to the accuracy required for thermal modelling. These fits also agree with sample results provided by the Institute of Space Devices Engineering in Moscow. Thus, for each scan the following can be used in the equation,

$$\text{Local Time of Day} = m\,(\text{LONG}) + b,$$

where the values of m and b are given in the following table:

TABLE A5.1: Linear Time of Day (in H) Versus Longitude Fits

Panorama	m	b
1 (2/11/89)	0.07143	23.28
2 (3/01/89)	0.07474	13.41
3 (3/26/89)	0.07474	18.31
4 (3/26/89)	0.07474	27.03

Dream to touch the planets,
Live to touch your dreams.
-Anonymous

REFERENCES

Arvidson, R.E.M., M. Coradini, A. Carusi, A. Coradini, M. Fulchignoni, C. Federico, R. Funiciello, and M. Salomone, Latitudinal variation of wind erosion of crater ejecta deposits on Mars, *Icarus*, *27*, 503-515, 1976.

Baker, V. R., *The Channels of Mars*, Univ. of Texas Press, Austin, 1982.

Baker, V. R. and R. C. Kochel, Martian channel morphology: Maja and Kasei Valles, *J. Geophys. Res.*, *84*, 7961-7983, 1979.

Baker, V. R. and D. J. Milton, Erosion by catastrophic floods on Mars and Earth, *Icarus*, *23*, 27-41, 1974.

Baker, V. R., M. H. Carr, V. C. Gulick, C. R. Williams, and M. S. Marley, Channels and valley networks, in *Mars* (Kieffer, Jakosky, Snyder, and Matthews, eds.), 493-522, 1992.

Barlow, N. G., Constraints on early events in Martian history as derived from the cratering record, *J. Geophys. Res.*, *95*, 14,191-14,201, 1990.

Barlow, N.G. and T.L. Bradley, Martian impact craters: Correlations of ejecta and interior morphologies with diameter, latitude, and terrain, *Icarus*, *87*, 156-179, 1990.

Batson, R. M., P. M. Bridges, and J. L. Inge, *The Atlas of Mars: The 1:5,000,000 Map Series*, NASA SP-438, Washington, D. C., 1979.

Betts, B. H., Edited Termoskan and raw data files and descriptions, on the *PDS (Planetary Data System) Phobos '88 CD-ROM*, Vol. PHB_1001, produced in May 1992.

Betts, B. H. and B. C. Murray, Thermally distinct ejecta blankets from Martian craters, *J. Geophys. Res. - Planets*, *98*, 11,043-11,059, 1993a.

Betts, B. H. and B. C. Murray, Thermal studies of Martian channels and valleys using Termoskan data, *J. Geophys. Res. - Planets*, in press, 1993b.

Betts, B. H., T. Svitek, M. L. Santee, B. C. Murray, D. Crisp, D. A. Paige, M. Naraeva, and A. Selivanov, Preliminary quantitative assessment and analysis of Phobos 88 Termoskan observations of Mars (abstract), in *Lunar and Planet. Sci., XXI*, 1990a.

Betts, B. H., T. Svitek, M. L. Santee, B. C. Murray, D. Crisp, D. A. Paige, M. Naraeva, and A. Selivanov, Preliminary quantitative assessment and analysis of Phobos 88 Termoskan observations of Mars, in *Scientific Results of the NASA-Sponsered Study Project on Mars: Evolution of Volcanism, Tectonics, and Volatiles* (Solomon, S. C., V. L. Sharpton, and J. R. Zimbelman, eds.), *LPI Tech Rpt. 90-06*, Lunar and Planetary Institute, Houston, 79-80, 1990b.

Bibring, J.-P., S. Erard, B. Gondet, Y. Langevin, A. Soufflot, M. Combes, C. Cara, P. Drossart, T. Encrenaz, E. Lellouch, J. Rosenqvist, V. I. Moroz, A. V. Dyachkov, A. V. Grygoriev, N. G. Havinson, I. V. Khatuntsev, A. V. Kiselev, L. V. Ksanfomality, Yu. V. Nikolsky, P. Masson, O. Forni, and C. Sotin, Topography of the Martian tropical regions with ISM, *Planet. and Space Sci., 39 (1/2)*, 225-236, 1991.

Bibring, J.-P., M. Combes, Y. Langevin, A. Soufflot, C. Cara, P. Drossart, T. Encrenaz, S. Erard, O. Forni, B. Gondet, L. Ksanfomality, E. Lellouch, P. Masson, V. Moroz, F. Rocard, J. Rosenqvist, and C. Sotin, Results from the ISM experiment, *Nature*, *341*, 591-594, 1989.

Binder, A. B., R. E. Arvidson, E. A. Guinness, K. L. Jones, E. C. Morris, T. A. Mutch, D. C. Pieri, and C. Sagan, The geology of the Viking Lander 1 site, *J. Geophys. Res.*, *82*, 4439-4451, 1977.

Blamont, J. E., E. Chassefiere, J. P. Goutail, B. Mege, M. Nunes-Pinharanda, G. Souchon, V. A. Krasnopolsky, A. A. Krysko, and V. I. Moroz, Vertical profiles of dust and

ozone in the Martian atmosphere deduced from solar occultation measurements, *Planet. and Space Sci., 39 (1/2)*, 175-187, 1991.

Carr, M. H., *The Surface of Mars*, Yale Univ. Press, New Haven, Conn., 1981.

Carr, M. H., Mars: A water-rich planet, *Icarus*, *68*, 187-216, 1986.

Carr, M.H., L.S. Crumpler, J.A. Cutts, R. Greeley, J.E. Guest, and H. Masursky, Martian impact craters and emplacement of ejecta by surface flow, *J. Geophys. Res.*, *82*, 4055-4065, 1977.

Christensen, P. R., Martian dust mantling and surface composition: Interpretation of thermophysical properties, *J. Geophys. Res.*, *87*, 9985-9998, 1982.

Christensen, P. R., The distribution of rocks on Mars (abstract), *Lunar Planet. Sci., XIV*, 109-110, 1983.

Christensen, P. R., The spatial distribution of rocks on Mars, *Icarus*, *68*, 217-238, 1986a.

Christensen, P. R., Regional dust deposits on Mars: Physical properties and global distribution, *J. Geophys. Res.*, *91*, 3534-3546, 1986b.

Christensen, P. R., Eolian intracrater deposits on Mars: Physical properties and global distribution, *Icarus*, *56*, 496-518, 1983.

Christensen, P. R. and H. H. Kieffer, Moderate resolution thermal mapping of Mars: The channel terrain around the Chryse Basin, *J. Geophys. Res.*, *84*, 8233-8238, 1979.

Christensen, P. R. and H. J. Moore, The Martian surface layer, in *Mars* (Kieffer, Jakosky, Snyder, and Matthews, eds.), 686-729, 1992.

Christensen, P. R., D. L. Anderson, S. C. Chase, R. N. Clark, H. H. Kieffer, M. C. Malin, J. C. Pearl, J. Carpenter, N. Bandiera, F. G. Brown, and S. Silverman, Thermal emission spectrometer experiment: Mars Observer mission, *J. Geophys. Res.*, *97*, 7719-7734, 1992.

Clancy, R. T. and S. W. Lee, A new look at dust and clouds in the Mars atmosphere: Analysis of emission-phase-function sequences from global Viking IRTM observations, *Icarus*, *93*, 135-158, 1991.

Clifford, S. M. and E. Duxbury, Sub-kilometer rampart craters in the equatorial region of Mars: Possible implications for the state and distribution of regolith H_2O, MEVTV Workshop on Nature and Composition of Surface Units on Mars, edited by J.R. Zimbelman, S.C. Soloman, and V. L. Sharpton, *LPI Tech. Rep. 88-05*, pp. 44-45, Lunar and Planet. Inst., Houston, Texas, 1988.

Clifford, S. M., C. J. Bartels, and E. P. Rubenstein, The Mars thermal model (MARSTHERM): A FORTRAN 77 finite-difference program designed for general distribution, *Lunar and Planetary Institute*, Houston, 1987.

Craddock, R. A., High resolution thermal infrared mapping of martian outflow and fretted channels, M.S. thesis, Dept. of Geol., Arizona State University, 1987.

Craddock, R. A., R. Greeley, P. R. Christensen, and F. T. Aldrich, Martian channel materials and the formation of channel winds (abstract), *Lunar Planet. Sci., XIX*, 215-216, 1988.

Crumpler, L. S., J. C. Aubele, S. L. Murchie, J. W. Head, S. T. Keddie, P. C. Fisher, J. Plutchak, A. Selivanov, and M. Naraeva, Preliminary analysis of Arsia Mons as characterized by Phobos 2 Termoskan instrument (abstract), Abstracts for the MEVTV Workshop on the Evolution of Magma Bodies on Mars, *Lunar and Planetary Institute*, 16-17, 1990.

Davis, P. A. and M. P. Golombek, Discontinuities in the shallow Martian crust at Lunae, Syria, and Sinai Plana, *J. Geophys. Res., 95* (B9), 14,231-14,248, 1990.

De Hon, R. A., Variations in interior morphology of 15-20 km lunar craters: Implications for a major subsurface discontinuity, *Proc. Lunar Planet. Sci. Conf., 11th*, 2207-2219, 1980.

De Hon, R. A., Ridged plains of Lunae Planum: Thickness distribution revised (abstract), *Lunar Planet. Sci., XVI*, 171-172, 1985.

Ditteon, R., Daily temperature variations on Mars, *J. Geophys. Res., 87*, 10,197-10,214, 1982.

Erard, S., J.-P. Bibring, J. F. Mustard, O. Forni, J. W. Head, S. Hurtrez, Y. Langevin, C. M. Pieters, J. Rosenqvist, and C. Sotin, Spatial variations in composition of the Valles Marineris and Isidis Planitia regions derived from ISM data, *Proc. Lunar Planet. Sci. Conf.*, 21st, 437-455, 1991.

Fanale, F. P., Martian volatiles: Their degassing history and geochemical fate, *Icarus*, *28*, 179-202, 1976.

Frey, H. V. and T. D. Grant, Resurfacing in Coprates and thickness of the ridged plains (abstract), *Lunar Planet. Sci., XX*, 313-314, 1989.

Frey, H. V. and T. D. Grant, Resurfacing history of Tempe Terra and surroundings, *J. Geophys. Res.*, *95*, 14,249-14,263, 1990.

Gault, D.E. and R. Greeley, Exploratory experiments of impact craters formed in viscous-liquid targets: Analog for Martian rampart craters?, *Icarus*, *34*, 486-495, 1978.

Greeley, R. and J. E. Guest, 1:15M Geologic map of the eastern equatorial region of Mars, *U.S. Geol. Surv. Misc. Invest. Map, I-1802-B*, 1987.

Greeley, R., J. Fink, D.E. Gault, D.B. Snyder, J.E. Guest, and P.H. Schultz, Impact cratering in viscous targets: Laboratory experiments, *Proc. Lunar Planet. Sci. Conf., 11th*, 2075-2097, 1980.

Greeley, R., J. H. Fink, D. E. Gault, and J. E. Guest, Experimental simulation of impact cratering on icy satellites, in *The Satellites of Jupiter*, edited by D. Morrison, pp. 340-378, University of Arizona Press, Tucson, 1982.

Greeley, R., A. Skypeck, and J. B. Pollack, Martian aeolian features and deposits: Comparisons with general circulation model results, *J. Geophys. Res.*, *98*, 3183-3196, 1993.

Haberle, R. M. and B. M. Jakosky, Atmospheric effects on the remote determination of thermal inertia on Mars, *Icarus*, *90*, 187-204, 1991.

Head, J. W., The significance of substrate characteristics in determining morphology and morphometry of lunar craters, *Proc. Lunar Sci. Conf., 7th*, 2913-2929, 1976.

Horner, V. M. and N. G. Barlow, Martian craters: Changes in the diameter range for ejecta fluidization with latitude (abstract), *Lunar Planet. Sci., XIX,* 505-506, 1988.

Horner, V. M. and R. Greeley, Effects of elevation and ridged plains thicknesses on Martian crater ejecta morphology, *Proc. Lunar Planet. Sci. Conf. 17th, Part 2, J. Geophys. Res.*, *92*, E561-E569, 1987.

Horz, F., R. Ostertag, and D. A. Rainey, Bunte breccia of the Ries: Continuous deposits of large impact craters, *Rev. Geophys.*, *21*, 1667-1725, 1983.

Jakosky, B. M., The effects of nonideal surfaces on the dervied thermal properties of Mars, *J. Geophys. Res.*, *84*, 8252-8262, 1979.

Jakosky, B. M., The seasonal cycle of water on Mars, *Space Science Reviews, 41*, 131-200, 1985.

Jakosky, B. M., On the thermal properties of the Martian fines, *Icarus*, *99*, 117-124, 1986.

Jakosky, B. M. and P. R. Christensen, Global duricrust on Mars: Analysis of remote sensing data, *J. Geophys. Res.*, *91*, 3547-3560, 1986a.

Jakosky, B. M., G. W. Finiol, and B. G. Henderson, Directional variations in thermal emission from geologic surfaces, *Geophys. Res. Lett.*, *17*, 985-988, 1990.

Jaquin F., P. Gierasch, and R. Kahn, The vertical structure of limb hazes in the Martian atmosphere, *Icarus*, *68*, 442-461, 1986.

Kieffer, H. H., Soil and surface temperatures at the Viking lander sites, *Science*, 194, 1344-1346, 1976.

Kieffer, H. H., S. C. Chase, Jr., E. Miner, G. Münch, and G. Neugebauer, Preliminary report on infrared radiometric measurements from the Mariner 9 spacecraft, *J. Geophys. Res.*, *78*, 4291-4312, 1973.

Kieffer, H.H., T.Z. Martin, A.R. Peterfreund, B.M. Jakosky, E.D. Miner, and F.D. Palluconi, Thermal and albedo mapping of Mars during the Viking primary mission, *J. Geophys. Res.*, *82*, 4249-4291, 1977.

Kuzmin, R.O., N.N. Bobina, E.V. Zabalueva, and V.P. Shashkina, Mars: Estimation of the relative thickness of the relative ice content in upper layers of the permafrost (abstract), *Lunar Planet. Sci., XIX*, 657-658, 1988.

MacKinnon, D. J. and K. L. Tanaka, The impacted Martian crust: Structure, hydrology, and some geologic implications, *J. Geophys. Res.*, *94*(B12), 17,359-17,370, 1989.

Malin, M. C., G. E. Danielson, A. P. Ingersoll, H. Masursky, J. Veverka, M. A. Ravine, and T. A. Soulanille, Mars Observer camera, *J. Geophys. Res.*, *97*, 7699-7718, 1992.

Mars Channel Working Group, Channels and valleys on Mars, *Geol. Soc. Amer. Bull.*, *94*, 1035-1054, 1983.

Masursky, H., L. Dial, Jr., and M. E. Strobell, Martian channels–a late Viking view, *NASA Tech. Memo. 82385*, 184-187, 1980.

McCauley, J.F., Mariner 9 evidence for wind erosion in the equatorial and mid-latitude regions of Mars, *J. Geophys. Res.*, *78*, 4123-4137, 1973.

McCleese, D. J., R. D. Haskins, J. T. Schofield, R. W. Zurek, C. B. Leovy, D. A. Paige, and F. W. Taylor, Atmosphere and climate studies of Mars using the Mars Observer pressure modulator infrared radiometer, *J. Geophys. Res.*, *97*, 7735-7758, 1992.

Mouginis-Mark, P.J., Martian fluidized crater morphology: Variations with crater size, latitude, altitude, and target material, *J. Geophys. Res.*, *84*(B14), 8011-8022, 1979.

Mouginis-Mark, P.J., Water or ice in the Martian regolith?: Clues from rampart craters seen at very high resolution, *Icarus*, *71*, 268-286, 1987.

Muhleman, D. O., B. J. Butler, A. W. Grossman, and M. A. Slade, Radar images of Mars, *Science*, *253*, 1508-1513, 1991.

Murray, B. C., M. K. Naraeva, A. S. Selivanov, B. H. Betts, T. Svitek, V. D. Kharlamov, A. V. Romanov, M. L. Santee, Y. M. Gektin, D. A. Fomin, D. A. Paige, A. S.

Panfilov, D. Crisp, J. W. Head, S. L. Murchie, and T. Z. Martin, Preliminary assessment of Termoskan observations of Mars, *Planet. Space Sci., 39 (1/2)*, 237-265, 1991.

Mutch, T. A., R. E. Arvidson, J. W. Head, K. L. Jones, and R. S. Saunders, *The Geology of Mars*, Princeton, N. J., Princeton Univ. Press, 1976.

Mutch, T. A., R. E. Arvidson, A. B. Binder, E. A. Guinness, and E. C. Morris, The geology of the Viking Lander 2 site, *J. Geophys. Res., 82*, 4452-4467, 1977.

Oberbeck, V. R. and W. L. Quaide, Genetic implications of lunar regolith thickness variations, *Icarus, 9*, 446-465, 1968.

Palluconi, F. D. and H. H. Kieffer, Thermal inertia mapping of Mars from 60°S to 60°N, *Icarus, 45*, 415-426, 1981.

Pike, R. J., Control of crater morphology by gravity and target type: Mars, Earth, Moon, *Proc. Lunar Planet. Sci. Conf., 11th*, 2159-2189, 1980.

Plescia, J. B. and R. S. Saunders, Estimation of the thickness of the Tharsis lava flows and implications for the nature of the topography of the Tharsis plateau, *Proc. Lunar Planet. Sci. Conf., 11th*, 2423-2436, 1980.

Pleskot, L. K. and E. D. Miner, Time variability of Martian bolometric albedo, *Icarus, 45*, 179-201, 1981.

Pollack, J. et al., Properties and effects of dust particles suspended in the Martian atmosphere, *Journal of Geophysical Research, 84*, 2929-2945, 1979.

Robinson, M. S. and K. L. Tanaka, Stratigraphy of the Kasei Valles region, Mars, MEVTV Workshop on Nature and Composition of Surface Units on Mars, edited by J. R. Zimbelman, S. C. Solomon, and V. L. Sharpton, *LPI Tech. Rep. 88-05*, pp. 106-108, Lunar and Planet. Inst., Houston, Texas, 1988.

Roddy, D. J., Large-scale impact and explosion craters: Comparisons of morphological and structural analogs, in *Impact and Explosion Cratering*, edited by D. J. Roddy, R. O. Pepin, and R. B. Merrill, pp. 185-246, Pergamon, New York, 1977.

Rossbacher, L. A. and S. Judson, Ground ice on Mars: Inventory, distribution, and resulting landforms, *Icarus*, *45*, 39-59, 1981.

Sagdeev, R. Z. and A. V. Zakharov, Brief history of the Phobos mission, *Nature*, *341*, 581-584, 1989.

Schultz, P. H. and D.E. Gault, Atmospheric effects on Martian ejecta emplacement, *J. Geophys. Res.*, *84*, 7669-7687, 1979.

Schultz, P. H. and D.E. Gault, On the formation of contiguous ramparts around Martian impact craters (abstract), *Lunar Planet. Sci., XV*, 732-733, 1984.

Scott, D. H., Geologic map of MTM quadrangles 25057 and 25052, Kasei Valles region of Mars, *U.S. Geol. Surv. Misc. Invest. Ser. Map, I-2208*, scale 1:500,000, 1991.

Scott, D. H. and Tanaka, K. L., Geologic map of the western equatorial region of Mars, *U.S. Geol. Surv. Misc. Invest. Ser. Map, I-1802A*, scale 1:15,000,000, 1986.

Selivanov, A. S., M. K. Naraeva, A. S. Panfilov, Yu. M. Gektin, V. D. Kharlamov, A. V. Romanov, D. A. Fomin, and Ya. Ya. Miroshnichenko, Thermal imaging of the surface of Mars, *Nature*, *341*, 593-595, 1989.

Sharp, R. P., Mars: Fretted and Chaotic Terrains, *J. Geophys. Res.*, 78, 4073-4083, 1973.

Sharp, R. P. and M. C. Malin, Channels on Mars, *Geol. Soc. Amer. Bull.*, 86, 593-609, 1975.

Shoemaker, E. M., Interpretation of lunar craters, in *Physics and Astronomy of the Moon*, edited by Z. Kopal, pp. 283-360, Academic, San Diego, Calif., 1962.

Shorthill, R. W., The infrared moon: A review, in *Lunar Thermal Characteristics*, *Progr. Aeronaut. Astronaut. Ser.*, edited by J. Lucas, MIT Press, Cambridge, Mass., 1972.

Soderblom, L. A. and D. B. Wenner, Possible fossil H_2O liquid-ice interfaces in the Martian crust, *Icarus*, *34*, 622-637, 1978.

Squyres, S. W., Martian fretted terrain: Flow of erosional debris, *Icarus*, *34*, 600-613, 1978.

Stoffler, D., D. E. Gault, J. Wedekind, and G. Polkowski, Experimental hypervelocity impact into quartz sand: Distribution and shock metamorphism of ejecta, *J. Geophys. Res.*, *80*, 4062-4077, 1975.

Strom, R. G., S. K. Croft, and N. G. Barlow, The Martian impact cratering record, in *Mars*, edited by H. H. Kieffer, B. M. Jakosky, C. W. Snyder, and M. S. Matthews, pp. 383-423, University of Arizona Press, Tucson, 1992.

Tanaka, K. L. and M. G. Chapman, Kasei Valles, Mars: Interpretation of canyon materials and flood sources, *Proc. Lunar Planet. Sci. Conf., 22nd*, 1992.

Tanaka, K. L. and Scott, D. H., Geologic Map of the Polar Regions of Mars: *U.S. Geological Survey Miscellaneous Investigations Series Map* I-1802C, scale 1:15,000,000, 1987.

U.S. Geological Survey, Topographic map of Mars, *U.S. Geol. Surv. Misc. Invest. Ser. Map, I-961*, 1976. (Reproduced in the Mars Consortium data set.)

U. S. Geological Survey, Mosaicked digital image model (MDIM), on *Mission to Mars: Digital Image Map CD-ROM*, Vol. 1, 1991a.

U.S. Geological Survey, Topographic map of Mars, U.S. Geol. Survey Misc. Geol. Inv. Map I-2179, 1991b.

Wilhelms, D. E. and S. W. Squyres, The Martian hemispheric dichotomy may be due to a giant impact, *Nature*, *309*, 138-140, 1984.

Wise, D. U., M. P. Golombek, and G. E. McGill, Tectonic evolution of Mars, *J. Geophys. Res.*, *84*, 7934-7939, 1979.

Witbeck, N. E., K. L. Tanaka, and D. H. Scott, Geologic map of the Valles Marineris region (east and west halves), Mars, *U.S. Geol. Surv. Misc. Invest. Ser. Map, I-2010*, scale 1:2,000,000, 1991.

Woronow, A., Variation in thickness of ejecta cover on Mars with increasing crater density, MEVTV Workshop on Nature and Composition of Surface Units on

Mars, edited by J. R. Zimbelman, S. C. Solomon, and V. L. Sharpton, *LPI Tech. Rep. 88-05*, pp. 135-137, Lunar and Planet. Inst., Houston, Texas, 1988.

Zimbelman, J.R., Thermal properties of channels in the aeolis quadrangle: topographic traps for aeolian materials, in *Symposium on MECA*, LPI, 112-114, 1986.

Zimbelman, J. R. and H. H. Kieffer, Thermal mapping of the northern equatorial and temperate latitudes of Mars, *J. Geophys. Res.*, *84*, 8239-8251, 1979.

Zimbelman, J.R. and L.A. Leshin, A geologic evaluation of thermal properties for the Elysium and Aeolis quadrangles of Mars, *J. Geophys. Res.*, *92*, E588-E596, 1987.

Zuber, M. T., D. E. Smith, S. C. Solomon, D. O. Muhleman, J. W. Head, J. B. Garvin, J. B. Abshire, and J. L. Bufton, The Mars Observer Laser Altimeter Investigation, *J. Geophys. Res.*, *97*, 7781-7798, 1992.